Myofibroblast Specific cGMP/cGKI Signaling Counteracts Ang II-Induced Cardiac Remodeling

Dissertation
der Mathematisch-Naturwissenschaftlichen Fakultät
der Eberhard Karls Universität Tübingen
zur Erlangung des Grades eines
Doktors der Naturwissenschaften
(Dr. rer. nat.)

vorgelegt von
M. Sc. Melanie Cruz Santos
aus Stuttgart

Tübingen
2023

Gedruckt mit Genehmigung der Mathematisch-Naturwissenschaftlichen Fakultät der Eberhard Karls Universität Tübingen.

Tag der mündlichen Qualifikation:	12.01.2024
Dekan:	Prof. Dr. Thilo Stehle
1. Berichterstatter/-in:	Prof. Dr. Robert Lukowski
2. Berichterstatter/-in:	Prof. Ph.D. Adrian Hobbs

I. Table of contents

II. List of Figures

III. List of tables

IV. List of abbreviation

Abbreviation	Meaning
ACE	Angiotensin-converting enzyme
AMP	Adenosine monophosphate
Ang I	Angiotensin I
Ang II	Angiotensin II
ANP	Atrial natriuretic peptide
AP	Alkaline phosphatase
APS	Ammonium peroxydisulphate
AT_1	Angiotensin II receptor type 1
AT_2	Angiotensin II receptor type 2
BDM	2,3-Butandion-monoxim
BK	Ca^{2+}- and voltage-activated K^+ channel
BNP	Brain natriuretic peptide
BP	Blood pressure
BSA	Bovine serum albumin
BT	Body temperature
BW	Body weight
cAMP	3',5'-cyclic adenosine monophosphate
CF	Cardiac fibroblast
cGK	cGMP-dependent protein kinase
cGMP	3',5'-cyclic guanosine monophosphate
CM	Cardiomyocyte
CMBK-KO	CM-specific BK channel knockout mice
CMF	Cardiac myofibroblast
*cmf*KO	CMF-specific cGKI knockout mice
CNG	Cyclic nucleotide-gated channel
CNP	C-type natriuretic peptide
Col1a2	Fibroblast specific collagen type I alpha 2 chain
CTR	Control animal
dATP	2'-deoxyadenosine 5'-triphosphate solution
dCTP	2'-deoxycytidine 5'-triphosphate solution
dGTP	2'-deoxyguanosine 5'-triphosphate solution
DMA	Dimethyl amiloride
DPBS	Dulbecco's phosphate buffered saline
DTT	Dithiothreitol
dTTP	2'-deoxythymidine 5'-triphosphate solution
EC	Endothelial cells
EDTA	Ethylenediamine tetraacetic acid disodium salt dihydrate
eNOS/NOS3	Endothelial NO synthase
ERK1/2	Extracellular signal-regulated kinase
ET-1	Endothelin 1
ETAR	Endothelin receptor type A
FBS	Fetal bovine serum
FGF-2	Fibroblast growth factor-2
FRET	Fluorescence resonance energy transfer
G	Gauge
GMP	Guanosine monophosphate
GPCR	G-protein coupled receptors
GTP	Guanosine-5'-triphosphate
H&E	Hematoxylin and eosin
HEPES	4-(2-Hydroxyethyl)piperazine-1-ethanesulfonic acid

HF	Heart failure
HFmrEF	Heart failure with mildly reduced ejection fraction
HFpEF	Heart failure with preserved ejection fraction
HFrEF	Heart failure with reduced ejection fraction
HW	Heart weight
i.p.	Intraperitoneal
IFG-1	Insulin-like growthdactor-1
IL-6	Interleukine-6
iNOS/NOS2	Inducible NO synthase
ITS	Insulin-Transferrin-Selenium
JNK	c-Jun N-terminal kinase
KLF5	Krüppel-like factor 5
KO	Knockout
LIF	Leukemia inhibitory factor
LV	Left ventricular
LVEF	Left ventricle ejection fraction
MAPK	Mitogen-activated protein kinase
MI	Myocardial infarction
min	Minutes
miRNA	microRNA
MK2	MAPK-activated protein kinase 2
MMP	Matrix metalloproteinase
NEP	Neprilysin
NEP_i	Neprilysin inhibitor
NGS	Normal goat serum
nNOS/NOS1	Neuronal NO synthase
NO	Nitric oxide
NO-GC	Soluble guanylyl cyclase
NOS	NO synthase
NP	Natriuretic peptide
NPR-C	Natriuretic peptide receptor-C
p.o	Per oral
p38-MAPK	P38 Mitogen-activated protein kinase inhibitor
PCR	Polymerase chain reaction
PDE	Phosphodiesterase
PDE_i	Phosphodiesterase inhibitor
PFA	Paraformaldehyde
pGC	Particulate guanylyl cyclase
PMSF	Phenylmethyl sulphonyl fluoride
PVDF	Polyvinylidene fluoride
RT	Room temperature
s.c.	Subcutaneous
SDS	Sodium dodecyl sulfate pellets
sec	Seconds
SMC	Smooth muscle cells
SNAP	Nitroso-N-acetyl-penicillamine
TAC	Transverse aortic constriction
TAM	Tamoxifen
TEMED	Tetramethylethylenediamine
TGF-β	transforming growth factor β
TGFβR1	TGF-β receptor type 1
TGFβR2	TGF-β receptor type 2
TIMP	Tissue inhibitors of metalloproteinase
TL	Tibia length

Tris	Tris(hydroxymethyl)-amino methane
TUNEL	Terminal deoxynucleotidyl transferase-mediated deoxyuridine triphosphate (dUTP) nick end labeling
VASP	Vasodilator-stimulated phosphoprotein
α-SMA	α-smooth muscle actin

1 Introduction

1.1 Myocardial fibrosis – pathological hallmark of cardiovascular diseases (CVDs)

Despite new therapeutic approaches for the treatment of distinct cardiovascular diseases (CVDs), these conditions remain among the leading cause of death worldwide (McClellan et al., 2019, Vaduganathan et al., 2022). Virtually all CVDs ethnologies are associated with cardiac remodeling, characterized by the development of cardiac hypertrophy and fibrosis, which together accelerate the progression of heart failure (HF) (Travers et al., 2016, Shimizu and Liao, 2016). According to the recently proposed definition, HF represents a clinical syndrome with symptoms evoked by functional and structural cardiac alterations accompanied by elevated natriuretic peptide (NP) levels and/or signs of pulmonary or systemic congestion (Bozkurt et al., 2021). HF can be classified on the basis of the left ventricle ejection fraction (LVEF), including HF with preserved EF (HFpEF: EF ≥50%), HF with mildly reduced EF (HFmrEF; EF 41% - 49%) and HF with reduced EF (HFrEF; EF ≤ 40%) (Bozkurt et al., 2021). In general, HF is characterized by a very poor overall prognosis associated with a high mortality rate within the first five years following initial diagnosis, requiring new therapeutic approaches and strategies for improving the prognosis of this disease (Liu et al., 2017, Shahim et al., 2023, Travers et al., 2022). To address this, recent research strategies are focusing on the control of myocardial fibrosis as a new therapeutic perspective (Travers et al., 2022).

Cardiac fibrosis is a common underlying pathological determinant of CVDs and is characterized by an excessive accumulation of collagen fibers throughout the myocardium (Travers et al., 2016, Gordon et al., 2022). In this context, the phenotype transition of resident cardiac fibroblasts (CFs) into cardiac myofibroblast (CMFs) in the course of pathophysiological stimuli like myocardial infarction (MI) or chronic angiotensin II (Ang II) stimulation is considered to be the critical event accelerating the development of cardiac remodeling (Liu et al., 2021b). Indeed, extensive preclinical studies identified CMFs as the major source of collagen deposition in the injured heart, making the manipulation of this cell type the perfect therapeutic target to prevent, treat or even reverse myocardial fibrosis (Liu et al., 2021b, Aujla and Kassiri, 2021, Travers et al., 2022).

1.1.1 Characteristics of myocardial fibrosis

Fibrosis can be divided into three distinct categories based on its anatomic localization as well as its underlying cause(s) (Zeisberg and Kalluri, 2013, Piek et al., 2016, Anderson et al., 1979). Cardiac stress induced by chronic hypertension results in reactive interstitial fibrosis, defined by an excessive extracellular matrix (ECM) accumulation throughout the myocardium without concomitant loss of CMs. Furthermore, hypertension is linked to the development of perivascular fibrosis characterized by the deposition of collagen fibers in the adventitia of the coronary arteries (Piek et al., 2016). Although myocardial fibrosis implies a worse cardiac outcome and is associated with increased mortality (Wong et al., 2012), the formation of a fibrotic scar is considered a protective function due to a negligible regenerative capacity of the heart (Frangogiannis, 2020). For instance, following MI, the massive loss of cardiomyocytes

(CMs) is replaced by activation of CF and subsequent formation of a collagen-based scar that lacks contractile capabilities but preserves structural integrity of the ventricles, thus protecting the heart from rupture (Frangogiannis, 2020, Kanisicak et al., 2016).

Nevertheless, irrespective from the original cause, the persistent fibrotic response induces detrimental and profound cardiac dysfunction. In this context, increased deposition of ECM leads to both impaired electro-mechanical coupling of CMs, loss of cardiac elasticity and muscle stiffness, ultimately resulting in a decline of cardiac function and an increased risk of life-threatening arrhythmias (Hinderer and Schenke-Layland, 2019, Travers et al., 2016). Interestingly, replacement fibrosis predominantly causes systolic dysfunction, whereas perivascular and interstitial fibrosis are associated with deterioration of diastolic function, with negligible or delayed effects on systolic function (Frangogiannis, 2020). Furthermore, cardiac dysfunction causes a restricted cardiac blood flow associated with markedly impaired oxygen- and nutrient delivery to the myocardium, which in turn can lead to an ischemic damage to the CMs (Bernardo et al., 2010, Piek et al., 2016, Brown et al., 2005, Segura et al., 2014).

Overall, these structural changes indicate an unfavorable physiological environment that holds the potential to further drive CM hypertrophy and cell death thereby promoting the progression of HF (Piek et al., 2016).

1.1.2 Properties and function of CF

The heart consists of four principal cell types, including CMs, smooth muscle cells (SMC), endothelial cells (EC) and CF, with the latter accounting for 40-60% of the cell population in the heart (Baum and Duffy, 2011, Tallquist and Molkentin, 2017). CFs are flat and spindle-shaped cells of mesenchymal origin with the unique morphological feature of lacking a basement membrane (Fan et al., 2012).
The major function of CF involves the maintenance of ECM homeostasis and integrity via the controlled synthesis and degradation of ECM proteins. CF achieve this task not only by the secretion of distinct collagen isoforms (type I, type III), but also through the production of so-called ECM-regulatory proteins (Souders et al., 2009, Fan et al., 2012). Among the latter proteins are matrix metalloproteinases (MMPs), which are responsible for the degradation of collagen and other ECM proteins, as well as their inhibitors, known as tissue inhibitors of metalloproteinases (TIMPs). In this manner, CF ensures tight control of ECM turnover and the maintenance of a functional three-dimensional network for CMs and other cells, thereby preserving the overall functionality and structure of the heart (Souders et al., 2009, Fan et al., 2012, Jabłońska-Trypuć et al., 2016).
Additionally, CFs are suggested to be able to detect and respond directly to mechanical, chemical, or electrical signals in the heart due to their intimate affiliation with the ECM, their direct cell-cell contacts with CM and other cells, and their ability to secrete proinflammatory cytokines in response to cardiac stress (Baudino et al., 2006). These properties justify their designation as sentinel cells (Zhu and Carver, 2012, Díaz-Araya et al., 2015).

1.1.3 Characteristics and function of CMFs

CMFs are a highly specialized cell type that does not occur in the healthy heart but instead emerge from activated CFs during the course of cardiac injury, thereby contributing to multiple functions within pathological processes (Tai et al., 2021). Besides the classic CF property including the production and secretion of ECM proteins (i.e., type I, type III collagens, fibronectin), this cell type also harbors contractile functions enabled by the de novo expression and incorporation of α-smooth muscle actin (α-SMA) into the filamentous fibers (Tai et al., 2021, Darby et al., 1990, Leslie et al., 1991, Petrov et al., 2002). Furthermore, CMFs express periostin, a matricellular protein that accumulates mainly in collagen-rich regions and is involved in the organization of the ECM (Snider et al., 2008, Dobaczewski et al., 2010, Kanisicak et al., 2016). Interestingly, the acquisition of the *Postn* gene expression correlated strongly with an activated CF phenotype following pathophysiological stimuli, making the respective gene product periostin an excellent marker for CMFs (Kaur et al., 2016).
Being the major source of ECM production in the injured heart and possessing contractile properties for wound edge contraction, CMFs are critical for wound closure and preservation of cardiac structural integrity after injury (Tai et al., 2021, Piek et al., 2016). For instance, deletion of CMFs in the early phase of MI led to an increased incidence for left ventricular (LV) rupture and consequently greater mortality in mice, highlighting the importance of CMFs in collagen secretion and formation of a stable scar as a surrogate for CM death (Kanisicak et al., 2016). Once the wound is closed and a mature scar is formed, the CMFs are thought to undergo apoptotic cell death (Desmoulière et al., 1995). One consideration in this context is the shielding of CMFs from mechanical stimuli by the formation of a mature cross-linked matrix, which might inactivate the cells and thereby initiate the course of apoptosis (Dobaczewski et al., 2010, Turner and Porter, 2013). In contrast, CMFs embedded in the scar could still be detected after 17 years in post-MI hearts, raising the notion that the persistent activity of this cell type promotes the fibrotic response, leading to cardiac dysfunction and eventually HF (Willems et al., 1994, Liu et al., 2021b). Besides the properties previously outlined, CMFs secrete a variety of different cytokines and growth factors driving the pathological process further in a paracrine and autocrine manner (Cartledge et al., 2015, Hall et al., 2021). Particular emphasis is placed on the coupling or manipulation of the function and viability of CMs, which will be discussed in more depth in chapter 1.2. Detrimental effects of the persistent activity of CMFs on the long-term outcome has been confirmed in distinct murine disease models. For example, CMF deletion during chronic Ang II exposure or in the subacute phase of MI ameliorated myocardial fibrosis development (Kaur et al., 2016).

Hence, CMF exerts pro-hypertrophic effects on CMs both through increased collagen deposition, leading to an augmented workload of CMs, and through the release of cytokines and growth factors that stimulate CMs in a paracrine fashion. Collectively, these process may eventually result in CM's death, which in turn would cause a progressive deterioration of cardiac function (s., Figure 1) (Piek et al., 2016).

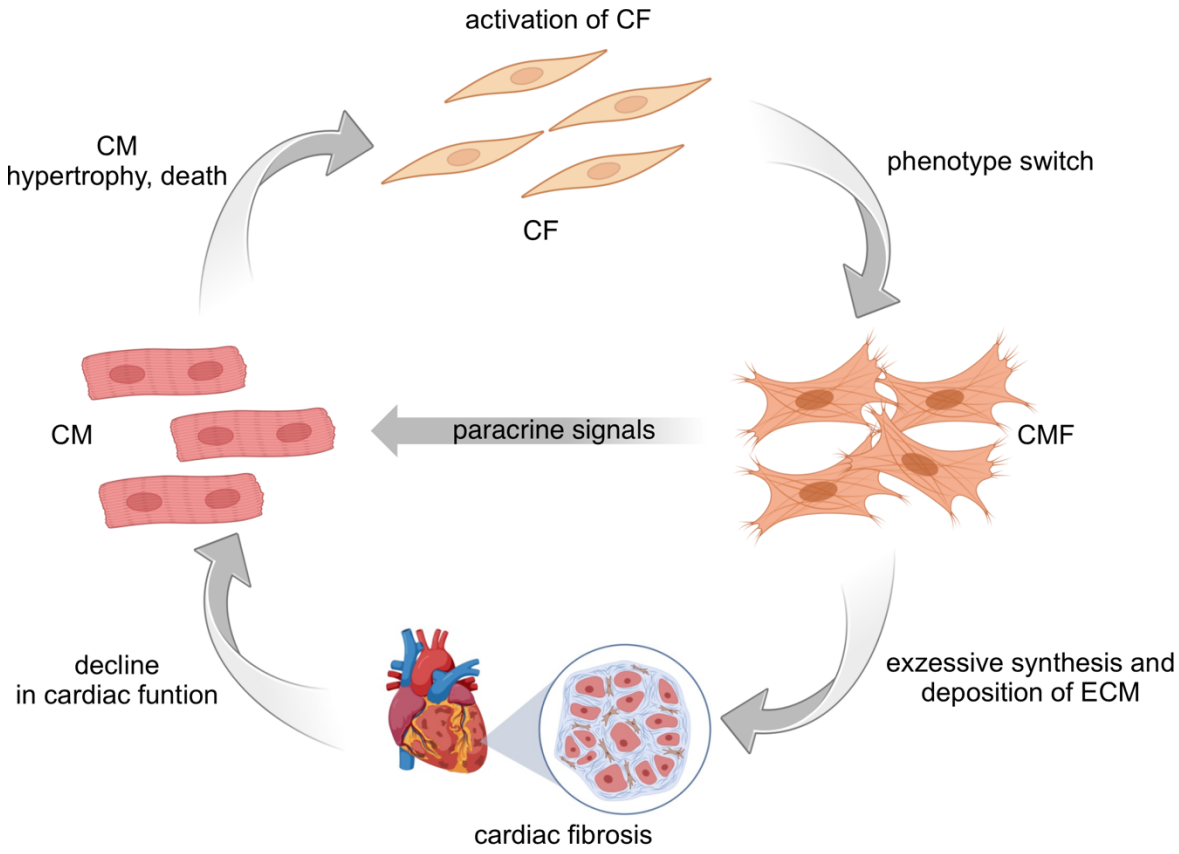

Figure 1:Detrimental effect of CMF activation accelerating cardiac remodeling
Simplified illustration of the effects of CMFs on cardiac outcome, modified from Piek et al. (2016). In response to pathophysiological stimuli cardiac fibroblast (CF) undergo a phenotype switch to cardiac myofibroblasts (CMFs) (Liu et al., 2021b). CMFs themselves secrete both cytokines and growth factors that can directly affect the function and viability of cardiomyocytes (CMs) in a paracrine manner, as well as a large number of ECM proteins leading to the development of cardiac fibrosis (Cartledge et al., 2015, Hall et al., 2021, Kurose, 2021). Both myocardial fibrosis, which is associated with deterioration of cardiac function and impaired nutrient and oxygen supply to the myocardium, and the release of paracrine mediators lead to CM stress and hypertrophy, ultimately resulting in CM cell death. As a consequence, this in turn causes further activation of the resident CFs, thereby restarting the cycle already described and eventually resulting in a progressive deterioration of cardiac function (Piek et al., 2016). Created with BioRender.com.

1.1.4 Signaling pathways driving the differentiation of CF to CMFs

There is a plethora of evidence that Ang II, transforming growth factor β (TGF-β), endothelin 1 (ET-1) and environmental mechanical forces are major inducers of the transition from CF to CMF (s. Figure 2) (Gibb et al., 2020, Davis and Molkentin, 2014, Walker et al., 2004).

The cytokine TGF-β is expressed by a variety of cells including immune cells, macrophages and CF and interacts by binding to its TGF-β receptor type 1 (TGFβR1) and type 2 (TGFβR2) in both an autocrine and paracrine manner (Gibb et al., 2020). TGF-β mediates its functions via the canonical or non-canonical signaling pathway, depending on whether it binds to TGFβR1 or TGFβR2 (Luo and Lodish, 1996, Davis and Molkentin, 2014, Clayton et al., 2020). The implication of the canonical pathway in the differentiation process of CMFs with the

involvement of TGFβR1-mediated phosphorylation of SMAD2/3, which enables its translocation to the nucleus and thus the initiation of gene transcription (Gibb et al., 2020, Davis and Molkentin, 2014), was already demonstrated in distinct experimental concepts: Accordingly, genetically modified mice carrying a constitutively active TGFβR1 mutation in fibroblasts exhibited a pronounced increase in the fibrotic response of the skin and blood vessel walls of the lung and kidney. In-depth analysis of the primary skin fibroblasts revealed that this mutation was associated with a pronounced rise in SMAD2/3 phosphorylation and increased differentiation into myofibroblasts (Sonnylal et al., 2007). Furthermore, disruption of this signaling pathway in CF by deletion of either SMAD3 or both TGFβR1/2 caused a decline in CMF differentiation following TGF-β stimulation *in vitro* in comparison to WT cells. Corroborating these *in vitro* findings, mice lacking SMAD3 or both TGFβR1/2 specifically in *Tcf21*$^{+}$ CF were protected from pressure overload-induced cardiac fibrosis (Khalil et al., 2017). Collectively, these findings highlight the importance of the TGF-β/SMAD3 signaling cascade as crucial mediator of CMF differentiation. As already indicated, studies also confirm the contribution of the non-canonical (SMAD-independent) signaling pathway to CMF differentiation. In this respect, the TGF-β-stimulated mitogen-activated protein kinase (MAPK) signaling branches, in particular c-Jun N-terminal kinase (JNK) and p38 kinase (p38-MAPK), are the most intensively studied (Davis and Molkentin, 2014, Davis et al., 2012, Liu et al., 2007). For instance, mouse embryonic fibroblast lacking MAPK-activated protein kinase 2 (MK2), a specific downstream effector of p38-MAPK, displayed a decline in α-SMA expression levels at baseline and in response to TGF-β stimulation (Sousa et al., 2007). Consistent with these results, deletion of p38-MAPK in *Tcf21*$^{+}$ CF was associated with a reduction in CMF abundance and myocardial fibrosis after MI injury (Molkentin et al., 2017).

Moreover, CF expresses G-protein coupled receptors (GPCRs), including the receptors for Ang II and ET-1 (Alvarez et al., 2011, Booz and Baker, 1996, Hafizi et al., 1998). Interestingly the latter protein is highly expressed and secreted in the hearts of patients with HF and is thought to promote LV remodeling (Tsutamoto et al., 2000, Omland et al., 1994). There is evidence for a functional role of ET-1 in the induction of CF proliferation and conversion into CMFs, whit a recent publication by Duangrat et al. (2023a) demonstrating that these actions occur via the endothelin receptor type A (ETAR)-mediated phosphorylation of extracellular signal-regulated kinase 1/2 (ERK1/2) (Duangrat et al., 2023a, Phosri et al., 2017).

Considerable evidence exists for the induction of Ang II-mediated differentiation from CF to CMFs (Olson et al., 2005, Bai et al., 2013). Ang II is suggested to induce this pro-fibrotic response in part by connecting different signaling pathways as it promotes the TGF-β and ET-1 secretion from CFs (Fujisaki et al., 1995, Duangrat et al., 2022, Rosenkranz, 2004, Gray et al., 1998, Davis and Molkentin, 2014).

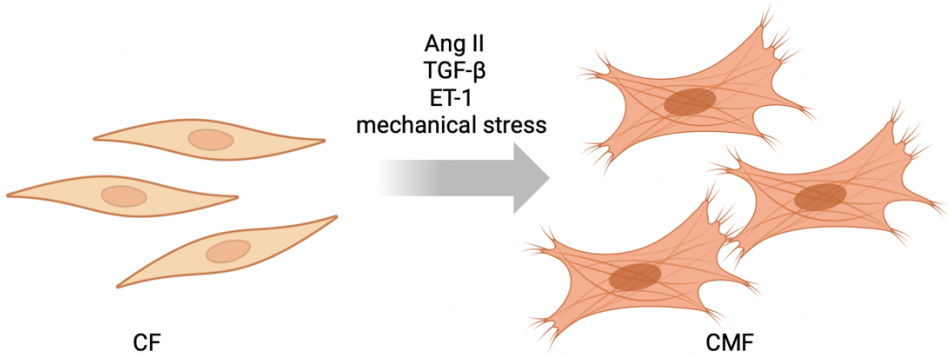

Figure 2: Differentiation of CFs into CMFs upon pathophysiological stimuli
Representative illustration of the CF-CMF transition was modified according to Tai et al. (2021). CFs can be activated to differentiate into CMFs via stimulation with various cytokines such as transforming growth factor β (TGF-β) (Khalil et al., 2017), neuroendocrine factor angiotensin II (Ang II) (Bai et al., 2013), endothelin 1 (ET-1), and mechanical stress (Dalla Costa et al., 2009). Created with BioRender.com.

1.1.5 Ang II in the development of cardiac fibrosis

Ang II represents the major effector molecule of the renin angiotensin-aldosterone system (RAAS), tightly controlling the regulation of the salt and water homeostasis as well as vascular tone (Fountain et al., 2023). Physiologically, low sodium chloride levels, activation of the sympathetic nervous system, or low arterial blood pressure (BP) lead to the release of renin from the granules of juxtaglomerular cells (Patel et al., 2017). Subsequently, the protease cleaves angiotensinogen produced in the liver by hydrolysis of a leucine-valine bond to form the decapeptide angiotensin I (Ang I) (Verdecchia et al., 2008). The cleavage of Ang I by the carboxypeptidase angiotensin-converting enzyme (ACE) to Ang II occurs in the pulmonary capillaries, renal epithelial cells, and ECs (Riordan, 2003, Patel et al., 2017). There are basically two different subtypes of Ang II receptors, namely the angiotensin II receptor type 1 (AT_1) and the angiotensin II receptor type 2 (AT_2), both of which are GPCRs (Guo et al., 2001). While the AT_1 receptor is responsible for mediating classical Ang II functions including vasoconstriction, cell proliferation, and stimulation of renal sodium reabsorption, the role of the AT_2 receptor in the adult organism is less clear (Fatima et al., 2021, Carey and Park, 2006). However, current evidence points towards a strong protective role of the latter receptor, which rather antagonizes the effect of the predominantly expressed AT_1 receptor (Carey, 2005, Fatima et al., 2021, Yang et al., 2012). Initial pharmacological studies using a selective AT_2 receptor agonist demonstrated anti-inflammatory and pro-natriuretic effects as well as improved insulin resistance and metabolism. These effects were associated with beneficial anti-adiposity, antihypertensive and cardioprotective outcomes (Fatima et al., 2021, Hakam and Hussain, 2005, Menk et al., 2015, Shum et al., 2013, Nag et al., 2019).

Besides the vasoconstrictor properties leading to an increase in BP, Ang II also exerts growth-promoting effects on CFs and CMs, leading to cardiac fibrosis and hypertrophy (Sadoshima and Izumo, 1993, Crabos et al., 1994). The relevance of these local effects of Ang II to the pathogenesis of cardiac remodeling processes was demonstrated in a transgenic mouse model overexpressing the human AT_1 receptor specifically in CMs. These mice displayed an

increased development of cardiac hypertrophy and fibrosis culminating in the development of HF, which, however, was independent from BP alterations (Paradis et al., 2000). In particular, the pro-fibrotic action of Ang II can be linked to a very high density of AT_1 receptors on CFs (Booz and Baker, 1996, Hafizi et al., 1998). Corresponding *in vitro* studies found that Ang II is capable of inducing proliferation and ECM-production in CFs as well as promoting the differentiation into CMFs, again underscoring its pro-fibrotic actions (Bai et al., 2013, Chen et al., 2004, Duangrat et al., 2023b, McEwan et al., 1998). For instance, inhibition of the AT_1 receptor by losartan in rat CF attenuated Ang II-induced activation of the TGF-β /SMAD signaling cascade, which in turn abolished the induction of pro-fibrotic genes like *Col1* (Gao et al., 2009).

1.2 Intramyocardial CF/CMF – CM communication

In general, there is ample evidence pointing to an extensive cross-talk between CF/CMFs and CMs via the ECM matrix, direct cell contact and the release of paracrine mediators (Cartledge et al., 2015). In terms the latter, CF/CMFs are capable of producing and secreting a variety of distinct cytokines, including interleukine-6 (IL-6) and TGF-β, each of which can exert a modulatory effect on CM function and viability (s. Figure 3) (Cartledge et al., 2015, Hall et al., 2021).

This hypothesis was strengthened by a publication from Gray and co-workers, in which the intimate interaction between CF and CMs was extensively examined (Gray et al., 1998). In this context, Ang II stimulation of cultured CF induced a pronounced secretion of TGF-β. Subsequent cultivation of the isolated CM in the latter TGF-β enriched conditioned medium resulted in the induction of protein synthesis in CM, representing a surrogate for CM growth (Gray et al., 1998). This outcome was further corroborated in a different study by Cartledge et al. (2015) which investigated the impact of CMF on CM hypertrophy and viability in a co-culture environment that only allowed paracrine exchange. In the latter cultures, CMs presented a great increase in CM dimensions as well as a significant reduction in viability compared to pure CM culture systems. These harmful effects were attributed to the release of TGF-β from CMFs. Taken together, these results suggest a crucial role of TGF-β release from CF in inducing CM-hypertrophy and affecting CM-viability via a paracrine pathway (Cartledge et al., 2015).

According to a publication by Sano et al. (2000), Ang II stimulated CF exhibited an upregulation of IL-6, leukemia inhibitory factor (LIF) and cardiotrophin-1 mRNA expression levels. Cultivation of CM in conditioned medium derived from Ang II stimulated CF, containing the latter cytokines provoked an increased in CM areas via the activation of the gp130-linked signaling pathway. Thus, Ang II mediated release of cytokines from CF was implicated in Ang II-mediated hypertrophy development of CMs (Sano et al., 2000). These results were corroborated by the investigation of a fibroblast-specific p38-MAPK mouse strain in which p38-MAPK was specifically ablated by Cre recombinase expressed under control of the fibroblast-specific collagen type I alpha 2 chain (*Col1a2*) promoter. Conditional p38-MAPK knockout (KO) mice were protected against myocardial injury induced by β-adrenergic stimulation with isoproterenol, as evidenced by attenuated cardiac hypertrophy and less functional deficits.

Supporting *in vitro* experiments revealed a key function of the CF-specific p38-MAPK in the induction of pro-hypertrophic IL-6 release from CF, further highlighting the relevance of CF-to-CM signaling in the development of CM hypertrophy (Bageghni et al., 2018).

The key role of CMFs in cardiac hypertrophy development was substantiated by its regulatory influence on insulin-like growth factor-1 (IGF-1) secretion (Takeda et al., 2010). In this context, the specific depletion of the transcription factor Krüppel-like factor 5 (KLF5) in *Postn*$^{+}$ CMFs, generated by employing a Cre recombinase controlled by the *Postn* promoter, caused a decline in pressure overload-induced cardiac hypertrophy. Additional *in vitro* analyses of cultured CF revealed a direct regulation of IGF-1 secretion by KLF5, which in turn mediates the hypertrophy response in CMs in a paracrine manner (Takeda et al., 2010). Fibroblast growth factor-2 (FGF-2) is another factor with paracrine activity that is secreted by CF/CMF in response to pro-hypertrophic stimuli (Santiago et al., 2014, Faul, 2017). Thus, a global deletion of FGF-2 protected mice from cardiac hypertrophy development in an Ang II-dependent hypertrophy mouse model compared to WT mice. Moreover, the supernatant obtained from Ang II stimulated CF isolated from WT mice was capable of inducing cell growth of cultured CMs, while the conditioned supernatant derived from Ang II stimulated FGF-2 deficient CF failed to induce morphological changes in CMs (Pellieux et al., 2001).

Another novel paracrine mechanism between CF and CM involves the Ang II-induced release of exosomes containing miRNA-21 (miR-21) from CF (Lyu et al., 2015). This apparently occurs via the activation of both AT_1 and AT_2 receptors. Thus, *in vitro* experiments verified that CF-derived exosomes activated MPAKs (i.e., ERK, JNK and p38) in cultured CMs thereby upregulating the RAAS systems including the expression of renin, angiotensinogen and both AT_1 and AT_2 receptors. In mice, administration of GW4869 or dimethyl amiloride (DMA), both exosome release inhibitors, ameliorated fibrosis development and cardiac hypertrophy in response to sustained Ang II exposure. Together, these results imply that Ang II-mediated release of exosomes from CF amplifies the hypertrophic response of CMs to an Ang II challenge (Lyu et al., 2015). *Vice versa*, the release of exosomes from CMs has been found to trigger cardiac fibrosis via CM-to-CF cross-talk (Yang et al., 2018). In a publication by Yang et al. (2018), a high expression of miR-208 was identified in post-myocardial hearts, which was traced back to the release from CMs. While no expression of miR-208 was detectable in CF cultures subjected to Ang II or hypoxia stimulation, a CM-CF co-culture displayed a pronounced rise in miR-208 in CFs. Furthermore, stimulation of cultured CF with the miRNA-208a-containing exosomes led to an increase in proliferation and differentiation into CMFs. However, while infusion of miR208a was able to worsen cardiac function in healthy rats, post-MI rats showed a marked improvement in cardiac function and reduction in cardiac fibrosis after inhibition of miR-208a *in vivo* (Yang et al., 2018).

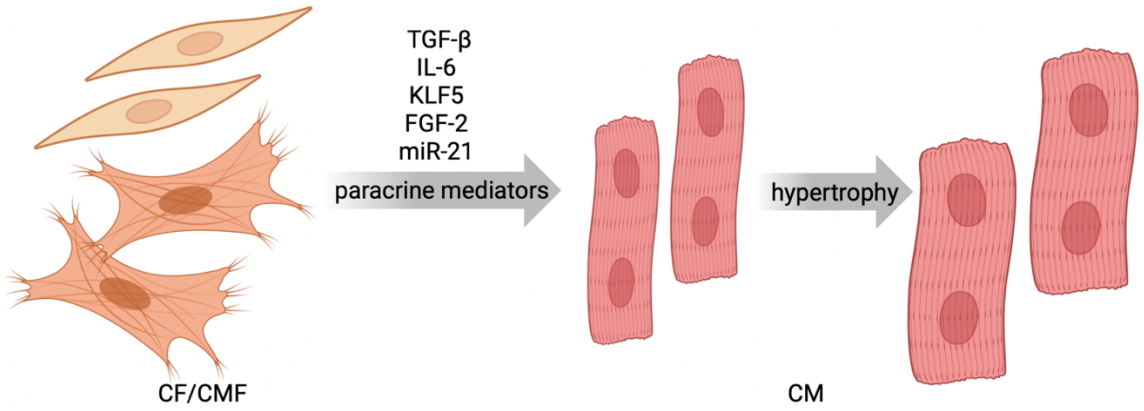

Figure 3: Paracrine communication between CF/CMFs and CM
Paracrine communication between CF/CMFs and CMs, modified from Takeda and Manabe (2011). Cytokines, miRNA, and growth factors secreted by CF/CMFs have been shown to induce CM hypertrophy in a paracrine manner. Only some of these factors have been included in this scheme namely transforming growth factor-β (TGF-β) (Gray et al., 1998); interleukin-6 (IL-6) (Sano et al., 2000); Krüppel-like factor 5 (KLF5) (Takeda et al., 2010); fibroblast-growth factor-2 (FGF-2) (Santiago et al., 2014); microRNA21 (miRNA-21) (Lyu et al., 2015). Created with BioRender.com.

1.3 The NO/cGMP/cGKI pathway

1.3.1 Elements of the cGMP signaling axis

A total of three different isoforms of NO synthases (NOS) are responsible for the endogenous production of nitric oxide (NO) and are expressed in a wide range of tissues. Both neuronal NOS (nNOS/NOS1) and endothelial NOS (eNOS/NOS3) are constitutively expressed (Förstermann and Sessa, 2012). The third isoform represents the inducible NOS (iNOS/NOS2), which is usually not present in resting cells but whose expression can be triggered in response to infection, bacterial lipopolysaccharide and immunostimulatory cytokines in multiple cell types (Aktan, 2004). For the production of NO, the substrate L-arginine is oxidized by NOS involving additional cofactors to produce L-citrulline and NO (Förstermann and Sessa, 2012, Nathan and Xie, 1994). One of these cofactors, important for the enzymatic activity of the three NOS isoforms, is calmodulin. Regarding eNOS and nNOS, calmodulin binding is triggered in response to an increase in intracellular Ca^{2+} concentration, whereas activation of iNOS occurs in a calcium-independent manner (Förstermann and Sessa, 2012, Lee and Stull, 1998).

The NO produced has half-life time of only 3 to 5 sec, cannot be stored, and diffuses from the originating cell to surrounding cells, where it exerts its function by binding to NO-sensitive soluble guanylyl cyclase (GC or NO-GC) (Tuteja et al., 2004, Hofmann et al., 2000) (s. Figure 4). The NO-GC are heterodimers, which explains why two different subtypes can be distinguished on the basis of their composition: i.) NO-GC1 consisting of α_1 and β_1 subunit and ii.) NO-GC2 composed of α_2 and β_1 subunit. After binding of NO to the amino-terminal bound heme of the β_1 subunit, the conversion of guanosine-5'-triphosphate (GTP) to 3',5'-cyclic guanosine monophosphate (cGMP) occurs at the carboxyterminus of the α_1, α_2 or β_1 subunits containing the catalytic site. This justifies the required interaction between an α subunit and

the β_1 subunit to carry out the catalytic activity (Hofmann, 2020). One further pathway leading to NO-independent cGMP generation is via the activation of the transmembrane particulate guanylyl cyclases (pGCs) (s. Figure 4). Altogether, seven distinct subtypes of these pGCs were identified ranging from GC-A to GC-G (Kuhn, 2016). The NPs known as atrial natriuretic peptide (ANP), B-type natriuretic peptide (BNP) and C-type natriuretic peptide (CNP) can promote the synthesis of cGMP by binding to GC-A and GC-B. These NPs have varying affinities for the pGC: ANP and BNP preferentially activate the GC-A, whereas CNP exerts its effect mainly via the GC-B (Potter et al., 2009).

Several effectors have already been identified for the second messenger cGMP, with the most important being cyclic nucleotide-gated (CNG) ion channels and cGMP-dependent protein kinases (cGK) (Hofmann, 2020) (s. Figure 4). CNG channels are mainly expressed in retinal photoreceptors and olfactory neurons and are therefore essentially involved in the signal transduction pathways of vision and olfaction (Kaupp and Seifert, 2002, Biel and Michalakis, 2009, Schmidt et al., 2009). These channels can be activated by either intracellular cGMP- or 3',5'-cyclic adenosine monophosphate (cAMP)-binding, triggering channel opening and subsequent Ca^{2+}-influx that ultimately leads to the induction of Ca^{2+}-dependent processes (Biel et al., 1998, Biel and Michalakis, 2009).
The cGKs are members of the serine/threonine kinase family and are widely distributed in a variety of tissues (Hofmann and Wegener, 2013). Two genes *Prkg1* and *Prkg2* are responsible for the transcription of the enzymes cGKIα, cGKIβ and cGKII, respectively (Hofmann, 2020, Scott, 1991). In terms of structure, the cGKs are composed of a C-terminal catalytic domain and an N-terminal regulatory domain and exist as homodimers held together by a leucine zipper located in the regulatory domain (Hofmann et al., 1992). Moreover, the latter domain incorporates two non-identical cGMP binding pockets, while the catalytic domain comprises the binding sites for Mg^{2+}-ATP and for proteins containing a serine/threonine residue. Binding of cGMP induces a conformational change of the enzyme, resulting in the removal of inhibition of the catalytic domain by the N-terminus. Consequently, this allows phosphorylation of target proteins by transferring a phosphate from ATP to the serine/threonine residue in the catalytic domain (Vallur et al., 2014, Hofmann et al., 2000). While the soluble cGKI is mainly present in platelets, smooth muscle cells (SMC), lung, heart and cerebellum, the membrane-bound cGKII is predominantly expressed in the brain, adrenal glands, kidney and intestinal mucosa (Hofmann et al., 2000, KEILBACH et al., 1992).

The cGMP degradation occurs via phosphodiesterases (PDE), providing tightly controlled regulation of cGMP concentration in cells (Kukreja et al., 2012) (s. Figure 4). The PDEs specifically cleave the 3',5'-cyclic phosphate moiety of cAMP and/or cGMP with the generation then of adenosine monophosphate (AMP) and guanosine monophosphate (GMP) (Francis et al., 2001). A total of 11 different PDE families have been identified so far, which differ strongly in their affinity for cGMP and cAMP (Hofmann, 2020). Overall, only PDE5, PDE6, PDE9 are specific for cGMP, while PDE4, PDE7, PDE8 are dedicated to the degradation of cAMP. The other PDEs (PDE1, PDE2, PDE3, PDE10, PDE11) display composite affinity for cAMP and cGMP (Kukreja et al., 2012). Moreover, PDEs are also crucial elements of the so-called cross-talk between the cGMP and the cAMP signaling pathways. Thus, the PDE2 is also termed

cGMP-stimulated cAMP PDE, since it was shown that an allosteric binding of cGMP to the PDE2 accelerates cAMP hydrolysis by a factor of 10 (Hofmann, 2020, Pavlaki and Nikolaev, 2018). PDE3 is another PDE involved in the cGMP-cAMP cross-talk. In this context, the binding of cGMP to PDE3 causes an inhibition of the PDE3-dependent cAMP breakdown (Pavlaki and Nikolaev, 2018).

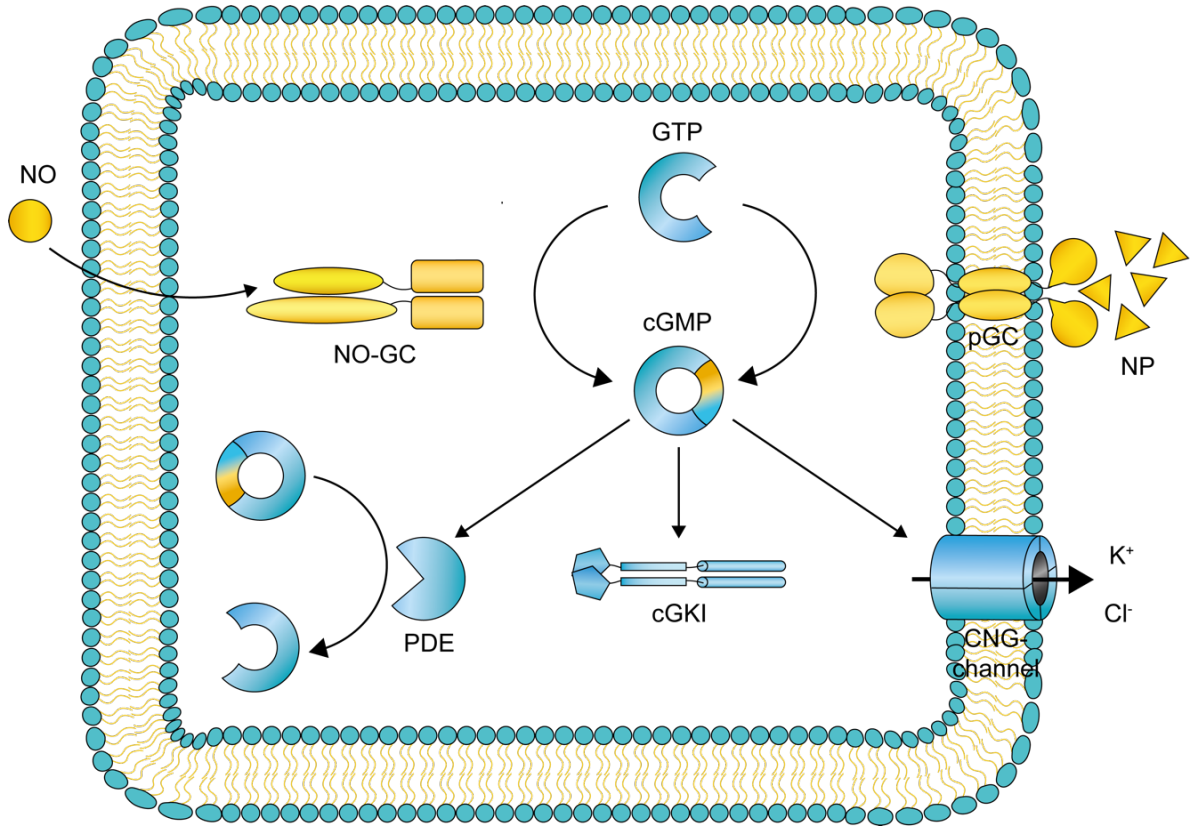

Figure 4: Generation, degradation, and effectors of cGMP
Schematic representation of the generation, degradation, and specific target structure of cyclic guanosine monophosphate (cGMP) modified according to Lukowski et al. (2022). Depicted is the conversion of guanosine-5'-triphosphate (GTP) to cGMP via the soluble guanylyl cyclase (NO-GC) or the particulate guanylyl cyclase (pGC) (Schmidt et al., 2009). Major cGMP effectors comprise the cyclic nucleotide-gated (CNG) ion channels and the cGMP-dependent protein kinases (cGK) (Hofmann, 2020). Tight regulation of intracellular cGMP concentration occurs via phosphodiesterase (PDE), which are responsible for the degradation of cGMP to guanosine monophosphate (GMP) (Soderling et al., 1998).

1.3.2 Role of cGMP signaling pathway in cardiac fibrosis

A plethora of evidence demonstrates an antifibrotic effect of the cGMP pathway in several organ systems including skin, lung, kidney and last but not least, the heart (Sandner and Stasch, 2017). For the latter organ system in particular, body of research ranges from *in vitro* investigations to the use of genetically modified mice and the application of pharmacological agents designed to modulate the cGMP signaling pathway.

In this context, a specific deletion of GC-A in mice resulted in increased BP levels and concomitant development of severe hypertrophy and interstitial fibrosis, all of which reflected characteristics of a human hypertensive heart disease. Moreover, the animals died before

reaching six months of age either due to morphological changes indicating the development of congestive HF or due to aortic dissection (Oliver et al., 1997). Interestingly, double-KO mice lacking GC-A and AT_{1A} receptor displayed considerably lower BP, interstitial fibrosis, and hypertrophy relative to GC-A deficient mice. *Vice versa*, treatment of GC-A KO mice with a subpressor dose of Ang II was observed to exacerbate the cardiac phenotype, whereas this effect was absent in WT mice. Overall, these results suggest that increased cardiac AT_{1A} signaling is partially responsible for the adverse phenotype in GC-A deficient mice and that GC-A opposes AT_{1A}-mediated cardiac remodeling (Li et al., 2002). In line with the preceding findings, a study by Li et al. (2008) revealed enhanced transverse aortic constriction (TAC)-induced hypertrophy development, collagen and CMF accumulations in cardiac sections obtained from ANP-deficient mice. Corresponding *in vitro* experiments provided supporting evidence that ANP was able to counteract TGF-β-induced CF proliferation and collagen production via the GC-A/cGMP cascade (Li et al., 2008).

Besides ANP, CNP is also thought to possess antihypertrophic and antifibrotic effects (Soeki et al., 2005). Investigations of genetically modified mice bearing either a specific deletion of CNP in CMs or in fibroblasts or a global ablation of the (natriuretic peptide receptor-C) NPR-C receptor revealed a comparable exacerbation of pressure overload-induced fibrosis. While treatment of global NPR-C animals with exogenous CNP failed to improve the detrimental cardiac phenotype, WT mice exhibited marked improvement in cardiac structure and functional deficits, ultimately leading to the conclusion that the cardioprotective effects of CNP are mediated via the NPR-C receptor (Moyes et al., 2020). Since NPR-C is considered to be a clearance receptor for natriuretic peptides that lacks GC-activity (Potter and Hunter, 2001), it is likely that this cardioprotective mechanism occurs independent of cGMP. However, there is evidence for an additional CNP-mediated antifibrotic effect via activation of the GC-B receptor (Werner et al., 2023). In this context, ablation of GC-B in *Col1a2*$^{+}$ fibroblasts resulted in a reduction of cardiac fibrosis in response to chronic Ang II exposure. This antifibrotic efficacy was further substantiated *in vitro* by demonstrating that CNP could suppress the pro-proliferative effects of Ang II in cultured murine CF. Moreover, CNP-induced phosphorylation of cytoskeleton-associated vasodilator-stimulated phosphoprotein (VASP) at serine^{239}, the specific target site of cGKI, indicating that the antifibrotic effects mediated by CNP/GC-B in CF occur via the cGMP/cGKI signaling pathway (Werner et al., 2023).

Besides NP/cGMP, also actions of the NO/cGMP signaling pathway have been related to antifibrotic and cardioprotective effects. Thus, NO-GC1 deficient mice exhibited increased perivascular and interstitial fibrosis along with elevated collagen I, periostin and TGF-β mRNA expression patterns in response to chronic Ang II exposure (Broekmans et al., 2020). Stimulation of isolated CF derived from neonatal rats with the NO-donor nitroso-N-acetyl-penicillamine (SNAP) attenuated the Ang II mediated expression of TGF-β, further corroborating the NO-mediated negative effect on cardiac fibrosis progression (Abdelaziz et al., 2001). Further evidence supporting this hypothesis was provided by the fact that applications of the NO-GC stimulator BAY 41-2272 and the NO-GC activator BAY 58-2667 (cinaciguat) at supra-pharmacological doses (10 µmol/l) suppressed the proliferation behavior of CF in response to FCS stimulation *in vitro* (Irvine et al., 2012). Consistent with previous

findings, treatment of rats with the NO-GC stimulator BAY 41-2272 attenuated the profibrotic response to chronic Ang II challenge *in vivo* resulting in a decline in collagen accumulation, lower CMF abundance, and reduced TGF-β and type I collagen expression. Indeed, this antifibrotic effects were attributed to BAY 41-2272-mediated suppression of Ang II-mediated proliferation rate of CF, which was associated with a higher intracellular cGMP concentration (Masuyama et al., 2006). Another NO-GC stimulator riociguat, already approved for the treatment of erectile dysfunction (Hatzimouratidis et al., 2010) and pulmonary hypertension (Rubin et al., 2011), was capable of reversing pressure-overload induced cardiac remodeling in murine hearts (Rüdebusch et al., 2022). This was reflected by reduced hypertrophy development and collagen deposition as well as reduced expression levels of fetal genes including *Nppa*, *Nppb* and *Myh7*. Similar to the aforementioned studies, stimulation of cultured CF with riociguat resulted in a substantial decrease of the Ang II-stimulated proliferation rate compared to CF exclusively treated with Ang II (Rüdebusch et al., 2022).

Perturbations downstream of the cGMP production are also accompanied by severe pathological cardiac dysfunction following myocardial injury. This was confirmed in a study by Frankenreiter et al. (2017), in which mice with a CM-specific deletion of the Ca^{2+}- and voltage-activated K^+ channel (BK) (CMBK-KO), an established downstream target of cGKI, presented a substantial rise in the infarct area following I/R injury compared with control animals. Moreover, treatment of the control animals with riociguat and cinaciguat protected the heart from I/R damage, whereas this cardioprotective outcome was abrogated in the CMBK-KO mice. Analyses of the long-term outcome following MI revealed a pronounced collagen accumulation in the CMBK-KO mice compared to the corresponding control animals, implying that the functional cGMP/cGKI/BK signaling pathway limits cardiac fibrosis and associated cardiac dysfunctions upon myocardial injury (Frankenreiter et al., 2017).

Inhibition of the intrinsic catabolism of cGMP using the PDE5 inhibitor sildenafil improved pressure overload induced CM hypertrophy as well as cardiac function in murine hearts following TAC. Based on these results, it was postulated that the higher intracellular cGMP levels in CMs resulted in increased cGKI activation, which was eventually responsible for the antihypertrophic effects (Takimoto et al., 2005). However, this hypothesis was at odds with a study by Lukowski et al. (2010), which demonstrated that mice lacking cGKI in the CMs did not respond with an amplified remodeling response to TAC or chronic isoproterenol stimulation *in vivo* compared with corresponding WT animals (Lukowski et al., 2010). Initial evidence of a cardioprotective effect of the cGMP/cGKI pathway dependent on the underlying pathophysiological stimulus was obtained in mice with a CM-specific deletion of GC-A (Klaiber et al., 2010). Exposure of these mutants to chronic isoproterenol stimulation resulted in comparable extent of cardiac hypertrophy development compared to control animals. In contrast mice lacking GC-A specifically in CM exhibited a pronounced hypertrophy in response to sustained Ang II stimulation relative to control animals (Klaiber et al., 2010). This apparent dependency on the stress stimuli was further corroborated in CM-restricted cGKI KO mice (Frantz et al., 2011). Although the latter mice displayed no difference in hypertrophy development after chronic isoproterenol or Ang II treatment *in vivo*, cardiac fibrosis was substantially elevated exclusively following Ang II stimulation compared to the control group

(Frantz et al., 2011). Taken together, the function of the cGMP/cGKI signaling pathway in CMs and its importance for the observed cardioprotective effects do not seem to be conclusively elucidated to date. Indeed, the signaling pathway in other cardiac cell types i.e., CMF/CF and EC is assumed to be involved in mediating the cardioprotective outcome (Hofmann, 2020). Interestingly, a recent study using a knock-in mouse model expressing a fluorescence resonance energy transfer (FRET)-based cGMP indicator demonstrated that stimulation with cGMP-enhancing agents (NO, NO-GC stimulator and activator) failed to elevate intracellular cGMP levels in CMs. In contrast, the aforementioned compounds led to an increase in cGMP levels in CF, which was subsequently transferred via gap junctions into CMs (Menges et al., 2019), establishing a novel level of cross-talk between CFs and CMs.

1.3.3 cGMP-enhancing drugs in CVDs

Disturbances of the cGMP signaling cascade have been implicated in various CVDs such as HF, atherosclerosis and hypertension (Kraehling and Sessa, 2017). In this context, cGMP dysregulations are linked to an increased cGMP degradation, decreased synthesis, or impaired downstream signaling and are collectively referred to as cGMPopathies (Petraina et al., 2021). In this sense, cGMP enhancing compounds have been successfully implemented in the treatment of CVDs for several years and therefore represent an ongoing major focus in the development of new therapeutic approaches (Buglioni and Jr., 2016). Here, the first therapeutically employed compounds were the so-called NO-donors (s Figure 5), including nitroglycerine, isosorbide dinitrate (ISDN) and isosorbide mononitrate (IDMN) for the treatment of acute and chronic angina pectoris (Schlossmann and Hofmann, 2005). Moreover, ISDN can be applied as a secondary option in the management of acute HF (Ponikowski et al., 2016, Petraina et al., 2021).

Additional to the latter compounds, novel drugs have been developed with a focus on the direct stimulation of the NO-GC to promote intracellular cGMP synthesis (s Figure 5) (Sandner et al., 2021). This group of agents can be subdivided into two classes, termed NO-GC-activators, and NO-GC-stimulators, with only the latter group being currently employed in the management of congestive HF (Armstrong et al., 2020b, Petraina et al., 2021). Whereas NO-GC activators bind directly to the oxidized, heme-free NO-GC, the NO-GC stimulators interact with the reduced, heme-containing NO-GC and act independently or synergistically with NO (Sandner et al., 2021, Buys and Sips, 2014). The first representative of the NO-GC stimulators to be approved for the treatment of pulmonary arterial hypertension and thromboembolic pulmonary hypertension is riociguat (Petraina et al., 2021, Conole and Scott, 2013). Another clinical trial evaluating the efficacy of riociguat treatment in patients with HF due to pulmonary hypertension caused by LV systolic dysfunction failed to observe a decline in pulmonary arterial pressure compared to the placebo group (Bonderman et al., 2013). However, riociguat exhibited a significant beneficial effect on the cardiac outcome as determined by the cardiac index (Bonderman et al., 2013). Moreover, another clinical trial conducted in patients with HFpEF and pulmonary hypertension revealed that riociguat treatment had a profound beneficial effect on cardiac outcome, marked by an improvement in stroke volume and cardiac index but without causing changes in mean pulmonary artery pressure (Bonderman et al.,

2014). Based on this positive response, the efficacy of long-term treatment with riociguat in patients with pulmonary hypertension associated with HFpEF is currently being investigated (Mascherbauer et al., 2016). Recently another NO-GC simulator termed vericiguat was approved for the therapy of HFrEF. In the pivotal VICTORIA trial, vericiguat showed a successful reduction in the incidence of cardiovascular death and hospitalization compared to the placebo group (Armstrong et al., 2020b, Markham and Duggan, 2021). Despite these encouraging results in the treatment of HFrEF, the incorporation of vericiguat in the treatment of patients with HFpEF in a phase IIb clinical trial failed to improve quality of life as assessed by the Kansas City Cardiomyopathy Questionnaire (KCCQ)- physical limitation score (Armstrong et al., 2020a, Petraina et al., 2021).

In addition to stimulating cGMP production, the intracellular cGMP concentration can be increased by inhibiting the PDEs responsible for the cGMP breakdown (s Figure 5) (Kukreja et al., 2012). Sildenafil and tadalafil belong to the therapeutic group of PDE5 inhibitors and are indicated for the management of erectile dysfunction and pulmonary hypertension (Rubin et al., 2011, Galiè et al., 2016, Hatzimouratidis et al., 2010). Moreover, sildenafil treatment failed to either reduce filling pressure during exercise in the context of diastolic dysfunction after MI or improve exercise capacity in patients with HFpEF (Andersen et al., 2013, Redfield et al., 2013). However, the PDE3 inhibitor milrinone is already successfully applied for the short-term therapy of acute HF (Ponikowski et al., 2014). A recent pilot study demonstrated an improvement in the quality of life in patients with HFpEF treated with a new extended-release version of milrinone (Nanayakkara et al., 2020, Petraina et al., 2021). The PDE9 inhibitor CRD-733 exhibited a significant improvement in major features of HF, including LV hypertrophy and dysfunction in a mouse model (Richards et al., 2021).

Last but not least, the zinc-activated endopeptidase neprilysin (NEP) also influences the cGMP signaling pathway via the degradation of NPs (s Figure 5) (Bozkurt et al., 2023, Nakagawa and Saito, 2022). Furthermore, NEP also breaks down vasoconstrictive peptides such as endothelin and Ang II (Potter, 2011). Based on the latter interaction, the neprilysin inhibitor (NEP_i) sacubitril was used in conjunction with the AT_1 receptor blocker valsartan, preventing the action of the accumulating neurohormone at their receptors (McMurray et al., 2014). Treatment of HFrEF patients with this combination was superior to the therapy with enalapril only, as demonstrated by the significant reduction in cardiovascular deaths as well as HF hospitalizations (McMurray et al., 2014). Based on these breakthrough results, the sacubitril/valsartan combination was approved as a novel first-in-class drug combination termed angiotensin receptor neprilysin inhibitor (ARNI), for the treatment of patients with HFrEF (Nicolas et al., 2023). In contrast to this success, the PARAGON-HF clinical trial failed to demonstrate a beneficial effect of the sacubitril-valsartan combination compared with valsartan alone in patients with HFpEF, as there was no change in the number of hospitalizations nor in the number of deaths from cardiovascular causes (Solomon et al., 2019).

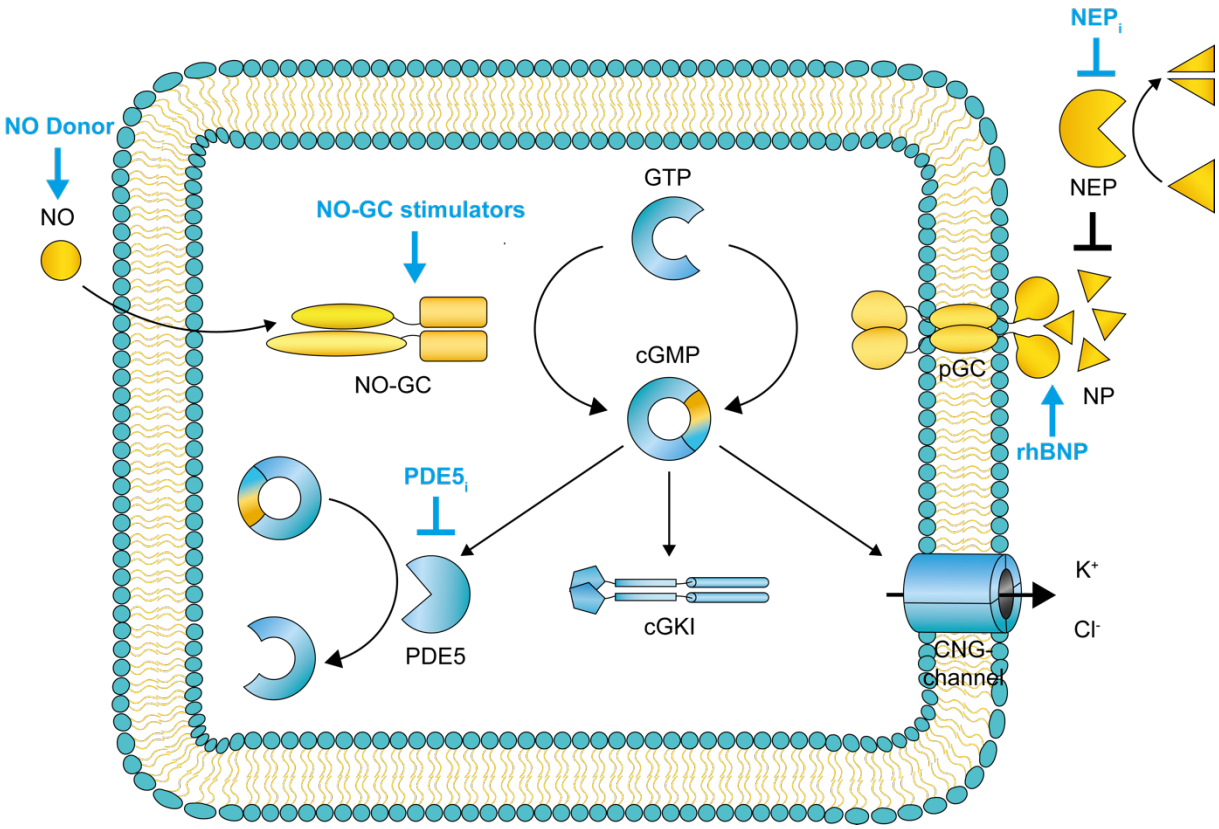

Figure 5: Targets of cGMP modulating compounds
Schematic representation of the cyclic guanosine monophosphate (cGMP) signaling cascade and targets of cGMP enhancing drugs modified from Lukowski et al. (2022). Depicted is the conversion of guanosine-5'-triphosphate (GTP) to cGMP via the soluble guanylyl cyclase (NO-GC) or the particulate guanylyl cyclase (pGC) (Schmidt et al., 2009). Major cGMP effectors comprise the cyclic nucleotide-gated (CNG) ion channels and the cGMP-dependent protein kinases (cGK) (Hofmann, 2020). Tight regulation of intracellular cGMP concentration occurs via phosphodiesterase (PDE), which are responsible for the degradation of cGMP to guanosine monophosphate (GMP) (Soderling et al., 1998). A raise in intracellular cGMP concentration can be achieved by using nitric oxide (NO)-donors, NO-GC stimulators (NO-GC activators) and neprilysin inhibitors (NEP$_i$), as well as by inhibiting cGMP degradation using PDE-inhibitors (PDE$_i$) (Buglioni and Jr., 2016). Another approach involves stimulation of the NP/cGMP signaling pathway by administration of a recombinant human brain natriuretic peptide (rhBNP) (Colucci, 2001, Yoshimura et al., 1991). Nesiritide belongs to the latter therapeutic group and can be administered intravenously as a vasodilator in the treatment of acute HF (Ponikowski et al., 2014).

1.4 Hypothesis and Aim

Although cGMP-modulating agents like vericiguat and NEP_i have provided therapeutic benefits and are in clinical use for HFrEF therapy, the cell type(s) mediating the beneficial response(s) in the heart are largely unclear (Hofmann, 2020). However, considering the available genetic animal-based and pharmacological studies (s. chapter 1.3.2 and 1.3.3), the cGMP cascade in CF/CMFs seems to play an important role affecting CM growth and survival via paracrine mechanisms (Cartledge et al., 2015) and/or by transferring cGMP to this cell type via gap junctions (Menges et al., 2019), although a direct validation of this interesting hypothesis is pending.

To investigate this, the aim of the present thesis was to examine the putative role of cGKI in *Postn*$^+$ CMFs, representing the major cell type contributing to myocardial fibrosis after myocardial injury (Kaur et al., 2016). For this purpose, we generated CMF-specific cGKI-KO mice (*cmf*KO) and corresponding littermate control animals (CTR) by intercrossing the floxed cGKI animals with the tamoxifen (TAM)-inducible *Postn*iCre-mouse line. To induce cardiac remodeling, we implanted osmotic minipumps that released Ang II continuously for over 28 days. By evaluating the cardiac outcome in terms of fibrosis development, extent of hypertrophy, and cardiac function and by monitoring the proliferation behavior of isolated CF/CMF primary cell cultures, we assessed whether the cGMP/cGKI signaling cascade in CMF *in vivo* opposes the adverse remodeling induced by Ang II.

2 Materials and Methods

2.1 Equipment

Name	Reference or Source
Air flow cabinet for laboratory animal husbandry	Uniprotect, Bioscape
Amersham Imager 600	GE-Healthcare
Analytical balance	VWR-124, Sartorius AG
Anesthesia device	Groppler
Anesthetic mask for mice	RACPro, Groppler Medizintechnik
Animal temperature control	TCAT-2LV Controller, Physitemp
Autoclaves	VX-55, Systec VX-120, Systec
Camera (Grid-Assay)	Pco. Panda back-illuminated sCMOS & 10.0 Monochrome w/o IR, Diagnostic instruments
Centrifuge	5417C, Eppendorf
CO_2-Incubator	Hera Cell, Heraeus
Cryostat	Microm HM, Thermo Scientific
Digital caliper	Digitale ABS AOS caliper, Mitutoyo
Digital slide scanner	Pannoramic Flash Desc DX, 3D Histech
Drying oven	FD 115, Binder
Echocardiography for small animals	Vevo2100, VisualSonics
Electrode plates (WB)	Scie-Plas, 30034507
Electrophoresis cell (agarose gel)	Sub-cell, Bio-Rad
Electrophoresis cell (WB)	Mini Protean, Bio-Rad
ELISA-plate reader	Tecan Infinite F200 Pro
Fine surgical instruments for research	FST
Fluorescence microscope	ApoTome, Zeiss Axio Imager Z1, Carl Zeiss
Gel documentation system	BioDoc Analyze, Biometra
Hamilton 50 µl syringe	705N, Hamilton
Ice machine	Ziegra Brucheismaschine
Infrared lamp	IL, Beurer
Inverted transmitted-light microscope	Zeiss Axiovert 200M, Zeiss
Langendorff-perfusion system	Hugo Sachs Elektronik, Harvard Apparatus
Microwave	MWG 800, FiF
Nanophotometer	P 330, Implen
PCR-Thermocycler	Mastercycler Gradient, Eppendorf
Peristaltic pump (CM-Isolation)	REGLO digital, Ismatec
pH-electrode	Blue Line 18 pH, Schott
pH-meter	pH 540 GLP, WTW pH-Meter 761 Calimatic, Knick
Pipette (2,5 µl, 10 µl, 100 µl, 200 µl, 1000 µl, 5 ml)	Research pro, Eppendorf
Pipette controller	Accu-jet pro, Brand
Power supply	EV 231, Consort Standard Power Pack 25, Biometra
Precision scale	BP 2100 S, Sartorius
Pressure transmitter for mice	TA11PA-C10, Data Science Int.
Refrigerated centrifuge	MIKRO 220R, Hettich
Routine stereo microscopes	Leica Microsystems M80 Leica Microsystems EZ5
Safety cabinet	Safe 2020, Thermo Scientific

Small animal scale	LS2000H, G&G
Telemetry system	DataScience Int.
Test tube rotating shaker	3025, GFL
Thermoshaker incubator	Thriller thermo Incubator, Peqlab
Timer	TR118, Oregon Scientific
Ultrapure lab water purification	Purelab flex, Elga Milli-Q Biocell, Milliporea
Universal shaker	S20, CAT
Vortex	Genie 2 G560E, Scientific Industries
Water bath	K10/C10, Thermo Haake TW20, Julabo

2.2 Consumables

Name		Reference or Source	Identifier or Catalog number
Aluminum foil ROTILABO®		2596.1	Carl Roth
Blotting papers ROTILABO®		CL67.1	Carl Roth
Cannula	25 G	300400	BD Microlance
	27 G	302200	BD Microlance
	30 G	304000	BD Microlance
Cell strainer		542040	Greiner
Centrifuge tubes	15 ml	CLS430766	Corning
	50 ml	CLS430291	Corning
Costar® Multiple well plate plates		CLS3526	Corning
Costar® Stripette	5 ml	CLS4050	Corning
	10 ml	CLS4100	Corning
	25 ml	CLS4250	Corning
	50 ml	CLS4500	Corning
Coverslips 18 mm		0111580	Marienfeld Superior
Superfrost™ Plus adhesion microscope slides		J1800AMNZ	Epredia
Gloves nitrile powder-free		290418	Abena
Greiner CELLSTAR® 96 well plates		M0812	Sigma-Aldrich
Grid-500 µm slide		80806-G500	Ibidi
Neubauer haemocytometer		MDH-2N1	Millipore
Pasteur pipettes without cotton plug		4522.1	Carl Roth
PCR tubes 0.5 ml		0030124.537	Eppendorf
Pipette tips, without filter	10 µl	70.3010	Sarstedt
	20-200 µl	70.3030.020	Sarstedt
	1000 µl	70.1187.002	Sarstedt
Precision wipes KIMTECH		AA64.1	Kimberly Clark
Protein LoBind® Tubes		0030108116	Eppendorf
Reaction vials	1.5 ml	CH76.1	Carl Roth
	1.5 ml	CK06.1	Carl Roth
Sealing film Parafilm®		H666.1	Carl Roth
Single-use fine dosage syringes 1 ml		9166017V	B-Braun
TC-treated culture dish 100 mm		430167	Corning
Weighing pan ROTILABO®		1878.2	Carl Roth

2.3 Software

Name	Manufacturer
Axiovision Rel 4.8	Carl Zeiss
BioDocAnalyze (BDA) gel analysis software	Biometra
BioRender	BioRender
CaseViewer	3D Histech
CorelDRAW 24.0.0.301	Corel Corporation
Dataquest A.R.T.3.1	Data Sciences International
Illustrator 27.0	Adobe
ImageJ 1.53v	NIH
Microsoft Office 365	Microsoft
Prism 9.4.1	GraphPad Software
Vevo Lab	VisualSonics
VevoStrain 2100	VisualSonics
Zen Lite 2.6	Zeiss

2.4 Animal models

2.4.1 Animal husbandry

Experimental animals were housed and bred in compliance with the legal provisions of the Animal Welfare Act (Tierschutzgesetz – TSchG) in the Department of Pharmacology, Toxicology and Clinical Pharmacy, Institute of Pharmacy at the Eberhard-Karls University of Tübingen. Animals were maintained in an open, specific pathogen-free (SPF) housing system at controlled room temperature (RT) (22 ± 2°C) and humidity conditions (55 ± 5%) with ad libitum access to standardized food and water. Moreover, a cycle of alternating 12 hours (h) light and 12 h darkness was strictly followed to ensure the animals day-night rhythm. Animal breeding was conducted in a Makrolon® type III cage system by mating 1-2 females and one male mouse, while a maximum of three animals (usually littermates) with the same sex were housed in a Makrolon® type II cage system. In order to encourage the animals‘ natural behavior and welfare, environmental enrichments were provided by equipping the cages with nesting material and an additional shelter (house) (Bayne, 2018). The latter was exceptionally excluded from cages with more than one male mouse due to the potential occurrence of territorial disputes.

For the implantation of both osmotic minipumps (s. chapter 2.6.3) and BP transmitters (s. chapter 2.6.5), the experimental animals were individually kept. Solitary confinement precluded mutual injuries of the animal by opening the suture closure and ensured individual time of rest for each animal to recover from anesthesia. This husbandry was initiated one week preoperatively allowing the animals to acclimatize and was maintained even after the wound healing phase in order to avoid potential territorial conflicts.

2.4.2 Transgenic mouse lines

2.4.2.1 Heterozygous floxed cGKI$^{fl/+}$ mutant mouse

For the generation of mutant mice with a cell-specific cGKI-depletion, the genetically modified cGKI$^{fl/+}$ (PRKG1^{tm2Naw}) mouseline was employed. Thereby, the genomic manipulation is based on the flanking of exon 10 of the *PRKG1* gene by two loxP sites. By applying the Cre/loxP system the excision of exon 10 via the two loxP sequences results in the formation of a KO allele (-) (Wegener et al., 2002). In detail, exon 10 is essentially required for cGKI activity, as it encodes part of the ATP-binding site (Langmesser et al., 2009, Wegener et al., 2002).

2.4.2.2 CMF-specific cGKI knockout mouse

CMF-specific cGKI-KO mice were obtained using a transgenic *Postn*iCre$^{Tg/+}$ (Tg(Postn-icre/ERT2)#Wet) mouse line expressing a Tamoxifen (TAM)-inducible Cre-recombinase (Cre^{ERT2}) controlled by the *Postn*-Promotor (Kaur et al., 2016). The F1 parental generation was produced by crossbreeding heterozygous floxed cGKI$^{fl/+}$ mice (s. chapter 2.4.2.1) with transgenic *Postn*iCre$^{Tg/+}$ animals. In a second mating step, the obtained *Postn*iCre$^{Tg/+}$ x cGKI$^{fl/+}$ mice were again crossed with heterozygous floxed cGKI$^{fl/+}$ animals to generate both CMF-specific cGKI-KO (*Postn*iCre$^{Tg/+}$ x cGKI$^{fl/fl}$; *cmf*KO) and corresponding littermate control (*Postn*iCre$^{Tg/+}$ x cGKI$^{+/+}$; CTR) mice in the F2 generation (s. Figure 6A).

A

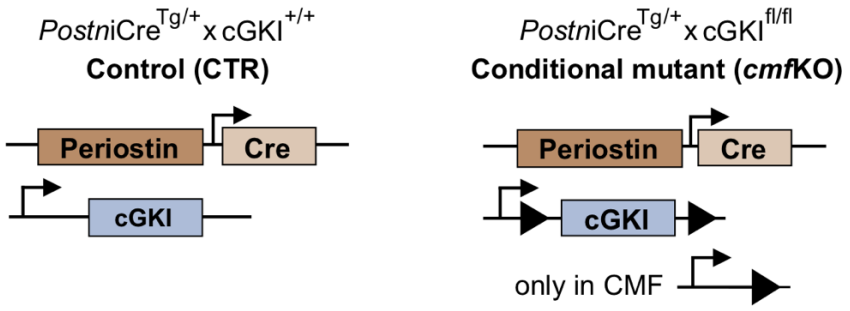

Figure 6: Generation of CMF-specific cGKI (*cmf*KO) and littermate control (CTR) mice
(**A**) The employed transgenic *Postn*iCre$^{Tg/+}$ mouse strain expressing a TAM-inducible Cre-recombinase under control of the *Postn*-promotor provides a targeted approach to specifically examine CMFs (Kaur et al., 2016). Intercrossing transgenic *Postn*iCre$^{Tg/+}$ with heterozygous floxed cGKI$^{fl/+}$ mutant mice in two mating steps resulted in the generation of the CTR (*Postn*iCre$^{Tg/+}$ x cGKI$^{+/+}$) und *cmf*KO (*Postn*iCre$^{Tg/+}$ x cGKI$^{fl/fl}$) animals. In the latter genotype, TAM-induced Cre-mediated excision of the lox-P flanked *PRKG1* locus results in animals lacking cGKI expression specifically in CMFs.

2.4.2.3 Global double fluorescent Cre reporter mouse

To investigate the tissue specificity and efficiency of the Cre-recombination, transgenic *Postn*iCre$^{Tg/+}$ mice were crossed with a global double fluorescent ROSA$^{mT/mG}$ Cre reporter model (B6.129(Cg)-Gt(ROSA)26Sor$^{tm4(ACTB-tdTomato,-EGFP)Luo}$/J) to obtain double transgenic ROSA$^{mT/mG}$ x *Postn*iCre$^{Tg/+}$ experimental mice and corresponding littermate ROSA$^{mT/mG}$ control animals in the F1 generation. The ROSA$^{mT/mG}$ reporter mouseline is particularly suitable and

already well established for such investigations (Figure 7A). Because the mT/mG knock-in construct drives the constitutive and ubiquitous expression of the membrane-bound red fluorescent tandem dimer tdTomato (mT) prior to Cre-recombinase mediated excision of the loxP-flanked mT DNA sequence, while Cre activity results in the expression of the membrane-bound green fluorescent EGFP (mG). Consequently, this mouseline facilitated the specific visualization and distinction of non-recombined (red-fluorescent) and recombined (green-fluorescent) cells (Muzumdar et al., 2007). This principle is illustrated in Figure 7B in the context of the transgenic *Postni*Cre$^{Tg/+}$ mouseline employed within this work.

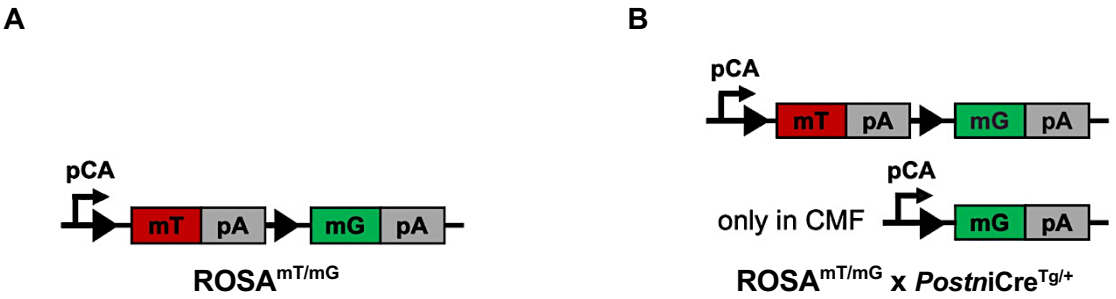

Figure 7: Schematic description of the principle of the double fluorescent ROSA$^{mT/mG}$ mouse
(**A**) The mT/mG construct inserted into the R26 gene locus of the ROSA$^{mT/mG}$ reporter mice consists of a CMV β-actin enhancer promotor (pCA) that drives the expression of the mT/mG cassette (loxP-mT-pA-loxP-mG-pA). In the absence of Cre-recombinase activity, ubiquitous expression of the red fluorescent mT-protein can be detected, as the polyadenylations sequences (pA) promotes the termination of the mT gene transcription preventing formation of mG transcripts (Muzumdar et al., 2007). (**B**) Cre-mediated recombination of the two loxP-sited leads to the excision of the mT DNA sequence allowing the pCA-promotor to drive the expression of the green-fluorescent mG protein. Based on the CMF-specific expression of the employed *Postni*Cre$^{Tg/+}$, the expression of the green fluorescent mG protein is only expected in CMFs derived from double transgenic ROSA$^{mT/mG}$ x *Postni*Cre$^{Tg/+}$ mice. Illustration adapted from Muzumdar et al. (2007).

2.4.2.4 CM-specific cGKI knockout mouse

Animals lacking cGKI specifically in CMs were generated using a transgenic mouseline expressing a constitutive Cre-recombinase under the control of the *myosin heavy chain 6c* (B6.FVB-Tg(Myh6-cre)2182Mds/J; *αMHC*-Cre$^{Tg/+}$) promotor (Agah et al., 1997). By intercrossing transgenic *αMHC*-Cre$^{Tg/+}$ mice with heterozygous floxed cGKI$^{fl/+}$ mutants, the F1 parental generation was obtained. Following a second breeding step of the parental mice (*αMHC*-Cre$^{Tg/+}$ x cGKI$^{fl/+}$) with heterozygous floxed cGKI$^{fl/+}$ mutants, the CM-specific cGKI-KO mice (*αMHC*-Cre$^{Tg/+}$ x cGKI$^{fl/fl}$) and the respective control littermates (*αMHC*-Cre$^{Tg/+}$ x cGKI$^{+/+}$) of the F2 generation were obtained for experiments. The cell specific *αMHC*-driven expression of the Cre-recombinase was already evaluated and confirmed in a previous study by Frankenreiter et al. (2017).

2.5 Mouse-Genotyping

2.5.1 Materials, Reagents and Solutions

Product / Reagent	Reference or Source	Identifier or Catalog number
100 mM 2'-deoxycytidine 5'-triphosphate solution (dCTP)	Genaxxon bioschience	M3019
100 mM 2'-deoxythymidine 5'-triphosphate solution (dTTP)	Genaxxon bioschience	M3021
100 mM 2'deoxyguanosine 5'-triphosphate solution (dGTP)	Genaxxon bioschience	M3020
100mM 2'-deoxyadenosine 5'-triphosphate solution (dATP)	Genaxxon bioschience	M3018
2-Log DNA-ladder	New England Biolabs	32000-S
Agarose	Biozym Scientific	840004
Boric acid	Carl Roth	6943.3
Bromophenol blue	Serva	15375
Ethidium bromide solution	Sigma-Aldrich	E1510
Ethylenediamine tetraacetic acid disodium salt dihydrate (EDTA)	Carl Roth	8043.2
Ficoll 400	Carl Roth	CN90.3
High Pure PCR Preparation Kit	Roche	11796828001
Isopropanol	Carl Roth	9866.2
KAPA Mouse Genotyping Kit	Roche	KK7301
Q5 High-Fidelity DNA polymerase	New England Biolabs	M0491S
Roche Kit High Pure PCR preparation Kit	Roche	11796828001
Tris(hydroxymethyl)-amino methane (TRIS)	Carl Roth	5429.3
Xylene Cyanol	Sigma Aldrich	X4126

Mouseline	Primer	Sequence
*Postn*iCre$^{Tg/+}$	5HA-F	5'-TGC CCC TGT GAT TTC TCT TC-3'
	5HA-R	5'-GGA GCA TCT TCC AGG TGT GT-3'
ROSA$^{mT/mG}$	F1	5'-CTC TGC TGC CTC CTG GCT TCT-3'
	R1	5'-CGA GGC GGA TCA CAA GCA ATA-3'
	R2	5'-TCA ATG GGC GGG GGT CGT T-3'
αMHC-Cre$^{Tg/+}$	F1	5'-ATG ACA GAC AGA TCC CTC CTA TCT CC-3'
	R1	5'-CTC ATC ACT CGT TGC ATC ATC GAC-3'
	F2	5'-CAA ATG TTG CTT GTC TGG TG-3'
	R2	5'-GTC AGT CGA GTG CAC AGT TT-3'
cGKI	F1	5'-CCT GGC TGT GAT TTC ACT CCA-3'
	R1	5'-AAA TTA TAA CTT GTC AAA TTC TTG-3'
	R2	5'-GTC AAG TGA CCA CTA TG-3'

→ Primer lyophilizates are dissolved with dH_2O according to the manufacturer's instructions to a concentration of 100 µM.
→100 µM stock solution is diluted 1:5 to obtain a working solution of 20 µM (ROSA/ *αMHC*-Cre$^{Tg/+}$/cGKI primer) or 1:10 to obtain a working solution of 10 µM (*Postn*iCre$^{Tg/+}$ primer)

EDTA 0.5 M, pH 8.0	
EDTA	0.5 M
dH_2O	ad 1000 ml
adjust pH to 8.0 with NaOH	

2% Agarose gel	
Agarose	2%
1x TBE buffer	100 ml
Ethidium bromide	0.1 µg/ml

10x TBE buffer	
Tris	891 mM
Boric acid	889.53 mM
EDTA 0.5 M; pH 8.0	4% (v/v)
dH_2O	ad 1000 ml

1x TBE buffer	
10x TBE buffer	10%
dH_2O	ad 1000 ml

Xylene Cyanol solution	
Xylene Cyanol	9.28 mM
dH_2O	2 ml
dissolve in the ultrasonic bath	

Bromophenol blue solution	
Bromophenol blue	5.5% (w/v)
dH_2O	2 ml

6x Loading buffer	
Ficoll 400	18% (w/v)
EDTA 0.5 M; pH 8.0	24% (v/v)
10x TBE buffer	60% (v/v)
Bromophenol blue solution	2.6% (v/v)
Xylene Cyanol solution	3% (v/v)
dH_2O	ad 50 ml
→ stir Ficoll 400, EDTA and 10x TBE-Buffer for 1 h at 60°C	
→add the remaining components	

2.5.2 Sample collection and DNA isolation

Numerical identification of the mouse offspring was carried out at the age of three to four weeks by ear punching. These collected biopsies were stored in 1.5 ml reaction tubes at -20°C before being used for the genotyping of the respective animals. DNA extraction from the biopsies was performed using the Roche Kit High Pure PCR preparation Kit according to the manufacturer's instructions. Briefly, the samples were first mixed with 200 µl lysis buffer und 40 µl reconstituted proteinase K, before being incubated overnight at 55°C on a temperature-controlled shaker (500 rpm). After mechanical fragmentation of the biopsies using a 200 µl pipette, 200 µl binding buffer and 100 µl isopropanol were added, thoroughly mixed, and subsequently centrifuged at 13000 *x g* for 5 min. The supernatant was transferred to the buffer reservoir of a filter tube and afterwards centrifuged at RT for 1 minute at 8000 x g, resulting in specific binding of the DNA to the silica column matrix, with the excess buffer being discarded. Purification of the DNA was performed via three consecutive washing steps (once in 500 µl inhibitor removal buffer then twice in 500 µl washing buffer), each followed by another centrifugation step at 8000 *x g* for 1 min. The latter buffer is completely removed by a full speed centrifugation step for 10 sec, before the DNA was eluted via the addition of 50 µl elution buffer and subsequent centrifugation at 8000 *x g* for 1 min. The purified and collected DNA can be stored for a maximum of 24 h at 4°C or for long-time storage at -20°C until further processing.

2.5.3 DNA-amplification by polymerase chain reaction

Exponential amplification of specific DNA fragments was performed by polymerase chain reaction (PCR). This commonly employed standard technique requires a master mix of specific

primers, nucleotides (deoxyribonucleotide triphosphate – dNTPs), and a DNA polymerase in addition to the DNA to be amplified (Garibyan and Avashia, 2013). Depending on the gene segment of interest, corresponding needed primer pairs and DNA polymerase were utilized for distinct master mixes (s. Table 1) and PCR programs (s. Table 2). For each sample, 25 µl of the respective master mix were prepared in a 500 µl PCR reaction tube.

Table 1: PCR Master mix

***Postn*iCre$^{Tg/+}$**	
5x Q5 Reaction Buffer	1X
10 mM dNTPs	200 µM
10 µM primer F/R	each 0.5 µM
DNA	7.5 µl
Q5 High-Fidelity DNA Polymerase	0.02 U/µl
dH_2O	ad 25 µl

***αMHC*-Cre$^{Tg/+}$**	
KAPA PCR Mix	12.5 µl
20 µM Primer F/R	each 0.8 µM
DNA	1 µl
dH_2O	ad 25 µl

cGKI	
KAPA PCR Mix	12.5 µl
20 µM Primer F/R	each 0.8 µM
DNA	5 µl
dH_2O	ad 25 µl

ROSA$^{mT/mG}$	
KAPA PCR Mix	12.5 µl
20 µM Primer F/R	each 0.8 µM
DNA	1.3 µl
dH_2O	ad 25 µl

Table 2: PCR-Program

***Postn*iCre$^{Tg/+}$**		
T1	94.0°C	3 min
T2	94.0°C	30 sec
T3	58.0°C	15 sec
T4	72.0°C	30 sec
Repeat T2-T4		39x
T6	72.0°C	5 min

cGKI / ROSA$^{mT/mG}$		
T1	94.0°C	5 min
T2	94.0°C	30 sec
T3	55.0°C	45 sec
T4	72.0°C	30 sec
Repeat T2-T4		35x
T6	72.0°C	5 min

***αMHC*-Cre$^{Tg/+}$**		
T1	95.0°C	3 min
T2	95.0°C	15 sec
T3	59.7°C	15 sec
T4	72.0°C	15 sec
Repeat T2-T4		30x
T6	72.0°C	5 min

2.5.4 DNA-detection via gel electrophoresis

Gel electrophoresis was subsequently performed in order to separate the amplified DNA fragments according to their molecular size within an electric field (Lee et al., 2012). For this purpose, a 2% agarose gel was prepared by dissolving agarose in 1x TBE buffer (s. chapter 2.5.1) in the microwave under heating. While continuously stirring, the gel was allowed to cool down to RT before ethidium bromide (0.1 µg/ml) was added and the gel was poured to the gel

casting chamber. Immediately afterwards, a comb was inserted into the gel to create sample pockets. Samples for the detection of *Postn*iCre required the addition of loading buffer (s. chapter 2.5.1) in a ratio of 6:1. This buffer consists of bromophenol blue (100 bp) and Xylene Cyanol (800 bp), which enabled the determination of the running distance of the sample throughout the separation process. Since the Kappa Genotyping Mix is already pre-loaded with a dye, the addition of the latter buffer was not required for the other samples. Upon polymerization of the gel, the combs were pulled out followed by the loading of the pockets with either the DNA-ladder allowing the estimation of the size of the DNA amplificates or the samples themselves. The initial applied voltage of 80 V was increased to 120 V for the remaining electrophorese duration of 1-2 h, as soon as the samples had migrated from the sample pockets into the agarose gel. Once the running front had reached the end of the gel, the DNA amplificates were visualized using a UV-detection system owing to the intercalation of the fluorescent dye ethidium bromide with the DNA. By means of the DNA-ladder, the received DNA bands were assigned to specific sizes, thereby enabling the identification of the genotype of a specimen (s. Table 3).

Table 3: Size of the examined DNA amplificates

*Postn*iCre$^{Tg/+}$	553 bp	ROSA$^{mT/mG}$	250 bp	*αMHC*-Cre$^{Tg/+}$	300 bp	cGKI$^{+/+}$	284 bp
		ROSA$^{+/+}$	330 bp	*αMHC*-Cre$^{+/+}$	200 bp	cGKI$^{fl/fl}$	338 bp
						cGKI$^{-/-}$	250 bp

2.6 *In vivo*-mouse models

All animal experiments performed within this thesis were authorized by the responsible local Ethics Committee for Animal Experiments (Regierungspräsidium Tübingen) in compliance with the requirements of the Animal Welfare Act (Tierschutzgesetz - TschG) and the Animal Welfare Ordinance (Tierschutzversuchsverordnung - TSchVersV). Moreover, animal welfare was safeguarded through routine inspections as well as through lively exchanges with the veterinarians and animal protection officers of the Institution for Animal Welfare, Veterinary Service and Laboratory Science of the Eberhard-Karls University of Tübingen.

2.6.1 Materials, Reagents and Solutions

Product / Reagent	Reference or Source	Identifier or Catalog number
1 M acetic acid	Carl Roth	KK62.1
Ang II human	Sigma-Aldrich	A9525
Atipamezole – Nosedorm 5 mg/ml	alfavet	
Buprenorphine – Buprenovet 0.3 mg/ml; 5x1 ml	Bayer	PZN 1498870
Bepanthen Augen- und Nasensalbe	Bayer	PZN 1578681
Fentanyl HEXAL 0.1 mg/ ampule	Hexal	PZN 07524746
Flumazenil – Anexate 0.5 mg/ 5 ml	Cheplapharm	PZN 03488574
Glutaraldehyde (25 %)	Carl Roth	3778.1
Isofluran CP	CP-pharma	798-932
Isotonic NaCl solution 0.9 %	Fresenius Kabi	PZN 02159621
Medetomidine – Dormilan 1 mg/ml	alfavet	

Metamizole – Novaminsulfon 500 mg/ml	1A Pharma	PZN 07387887
Midazolam-ratiopharm 5 mg/ml	ratiopharm	PZN 04921754
Miglyol®812	Caelo	3274
Tissue tape (Leukosilk-Gewebeklebeband)	BSN Medical GmbH	PZN 0397109
TAM	Sigma-Aldrich	T5648
Tergazyme	Sigma-Aldrich	Z273287
Depilatory cream (Veet Men)	Reckitt Benckiser	PZN 4916836
Disinfectant (Octenisept Wunddesinfektion)	Schülke & Mayr	PZN 04804008
Ultrasound gel	Sonogel	4011

Surgical instruments	Reference or Source	Identifier or Catalog number
Bulldog serrefines	FST	18050-35
Dumont #5 forceps	FST	11251-20
Blunt-blunt scissors	FST	14018-13
Extra fine bone scissors	FST	14084-08
Extra fine graefe forceps	FST	11152-10
Extra fine graefe forceps	FST	11151-10
Micro serrefines	FST	18052-01
Needle holder	FST	12565-14
Needle holder with suture cutters	FST	12002-12
Spring scissors	FST	15012-12
Vessel cannulation forceps	FST	00608-11
Vessel dilating forceps	FST	00276-13

TAM-injection solution	
TAM	1 mg
Miglyol	50 µl
→ vortex until a transparent solution is obtained (i.p. injection (21G))	

1% Tergazyme solution	
Tergazyme	1% (w/v)
dH_2O	40 ml

2% Glutaraldehyde solution	
Glutaraldehyde (25%)	2 ml
dH_2O	ad 25 ml

Anesthesia	
Medetomidine (500 µg/kg)	25 µl
Midazolam (5 mg/kg)	125 µl
Fentanyl (50 µg/kg)	25 µl
0.9% NaCl-solution	325 µl
→ prepare freshly → weight-adjusted i.p. injection (25G): 10 ml/kg BW	

Ang II solvent solution	
Acetic acid (1M)	100 µl
0.9 NaCl	10 ml

Ang II stock solution (23 µg/µl)	
Ang II	10 mg
Ang II solvent solution	434.78 µl

Antagonization of the anesthesia	
Flumazenil (0.5 mg/kg)	225 µl
Atipamezole (2.5 mg/kg)	25 µl
0.9% NaCl-solution	200 µl
→ weight-adjusted s.c. injection (25G): 10 ml/kg BW	

2.6.2 Tamoxifen injection

The activation of the TAM-inducible *Postn*iCre-recombinase was carried out according to Kaur et al. 2016, describing the generation and functionality of the employed inducible Cre mouse line (Kaur et al., 2016). For this purpose, 1 mg TAM per mouse was freshly dissolved in 50 µl miglyol daily (s. 2.6.1) and applied i.p. via a syringe (21 G) to one of the lower abdominal quadrants. This treatment was conducted for five consecutive days, by rotating the injection site from one flank to the other daily.

2.6.3 Implantation of osmotic minipumps

For the induction of Ang II-mediated cardiac remodeling, osmotic minipumps releasing Ang II continuously for 28 days were implanted subcutaneously (s.c.) in the left flank of the experimental animals (Kaur et al., 2016). According to the underlying literature, a growth-promoting and profibrotic Ang II-concentration of 2 µg/g/d (diluted in 0.9% NaCl/0.01M acetic acid; s. chapter 2.6.1) was applied (Straubinger et al., 2017, Nakayama et al., 2010, Patrucco et al., 2014).
The surgical procedure of the implantation of the osmotic minipumps was performed as previously described (Straubinger et al., 2017). Prior to the implantation of the osmotic minipumps, the animals were weighed in order to adjust the Ang II concentration specifically to the bodyweight (BW) of the respective mouse by diluting the Ang II stock solution (s. chapter 2.6.1) with the respective solvent (s. chapter 2.6.1). To avoid adhesion of the peptide hormone to the plastic surface, special reaction tubes containing a specific polymer coating (Protein-LoBind Tubes) were utilized for the preparation of Ang II-based solutions. Due to the properties of the employed pump (model 1004), only mice with an initial BW between 20 g and 30 g were included into the study. While the minimal weight restriction was related to the manufacture's recommendations, the Ang II concentration cannot be adjusted to a BW over 30 g owing to a maximal reservoir volume of 100 µl of the pump in conjunctions with the Ang II solubility product. Upon the preparation of 115 µl weight-adjusted Ang II-stimulation solution, the minipumps were filled using a provided blunt tipped 27-gauge (27G x 0.45) filling tube and closed by their flow moderator.
Anesthesia was induced by weight-adjusted intraperitoneal (i.p.) application of a combination of fentanyl (50 µg/kg), midazolam (5 mg/kg) and medetomidine (500 µg/kg) (s. chapter 2.6.1) and maintained throughout the surgical procedure by a continuous inhalation anesthesia with 1.0-2.0% isoflurane/oxygen. Adequate depth of the anesthesia was ascertained by the absence of inter-toe-, eyelid- and corneal-reflexes before the mouse was placed in the prone orientation on a heating surgical plate with an integrated rectal probe, permitting body temperature (BT) to be registered and maintained at 37°C ± 0.5°C during the surgery. To prevent ocular dryness during the operation, an ointment containing dexpanthenol (Bepanthen) was applied to the eyes. Before proceeding with a 1.0 – 1.5 cm skin incision located centrally on the back between both flanks, the fur in the corresponding area was removed with depilatory cream and the skin was disinfected using Octenisept® wound disinfection. With a blunt-blunt scissors, the connective tissue was carefully disrupted, and a small pocket was formed on the left flank of the mouse into which the osmotic minipump was

inserted. Wound closure was performed by 5-8 single knot technique, before anesthesia was antagonized by s.c. application of flumazenil (0.5 mg/kg) and atipamezole (2.5 mg/kg) as well as cessation of isoflurane supply. Intraoperative analgesia was guaranteed by the administration of fentanyl, while postoperatively the animals were treated with metamizole per oral (p.o.) (25 mg/ml drinking water) for five consecutive days. Throughout the experimental procedure, the overall state of health and welfare of the animal was accurately monitored according to predefined evaluation criteria.

2.6.4 Survival curve

Throughout the curse of the distinct treatment regimens (+TAM; +TAM + Ang II), the long-term outcome of both genotypes (CTR and *cmf*KO) was assessed in respect of survival and graphically displayed in a Kaplan-Meier survival curve. The welfare of the animals as well as their overall state of health was continuously monitored and assessed within each experimental group based on defined criteria and early end point definitions developed in cooperation with the corresponding veterinarians. Despite the absence of obvious symptoms beforehand, prolonged Ang II treatment provoked spontaneous death of some animals irrespective of the underlying genotype.

2.6.5 Telemetric blood pressure measurements

To assess Ang II-mediated changes in BP, locomotor activity and heart rate of CTR and *cmf*KO mice, implantable transmitter were utilized providing data acquisition by a telemetric system, as previously described (Straubinger et al., 2017, Längst et al., 2021). Initial anesthesia was achieved by i.p. application of a combination of fentanyl, midazolam and medetomidine as previously mentioned (s. chapter 2.6.3) and was supplemented after 30 min by an inhalation anesthesia using 1.0-2.0 Vol% isoflurane/oxygen for the entire remainder of the surgical intervention. After attaining sufficient anesthetic depth, detected by loss of inter-toe-, eyelid- and corneal-reflex, the mouse was positioned supine on a heating plate equipped with an integrated rectal probe ensuring the maintenance of BT at 37°C ± 0.5°C during the surgical procedure. Drying of the eyes was prevented by the application of dexpanthenol-containing ointment (Bepanthen). The relevant chest region was depilated using depilatory cream and disinfected before a submandibular ventral incision was performed towards the sternum. After exposure of the left common carotid artery (LCCA), a permanent ligation of this artery was performed caudal to the bifurcation into the arteria carotis communis and the arteria carotis externa. A second non-permanent ligation was conducted proximal to the first ligation using a bulldog clamp allowing the fluid-filled catheter to be inserted into the blood vessel through a small incision between the two ligations without bleeding. The catheter was then advanced towards the thoracic aorta and secured in this position with two sutures. Using atraumatic forceps, a pocket was formed in the right flank of the mouse for subcutaneous placement of the transmitter unit. Postoperative analgesia was achieved by the s.c. application of buprenorphine (0.1 mg/kg BW) before the wound was closed with the single knot technique. Anesthesia was antagonized by administration of Flumazenil and Atipamezol s.c. as well as by cessation of the inhalation anesthesia, as previously mentioned (s. chapter 2.6.3).

After the surgery, the animals received buprenorphine at 8-h intervals for 24h, followed by the administration of paracetamol (1.3 mg/ml) via the drinking water for further two days. After a seven-day recovery period, basal measurements were monitored at 15 min intervals for a duration of 5 min for three consecutive days. Immediately after the implantation of the osmotic minipumps releasing Ang II (s. chapter 2.6.3) the BP changes were recorded for the next following 7 days, whereby data acquisition was conducted at the already specified intervals. During the entire experimental procedure, the overall health state of the animal was closely supervised according to predefined evaluation criteria. Upon completion of the telemetric BP measurements, the animal was euthanized using CO_2 and death was ensured by cervical dislocation. The transmitter was removed, relieved of large tissue remnants, and cleaned via several washing steps. This involved first overnight incubation of the transmitter in a 1% tergazyme® solution (s. chapter 2.6.1) before the device was thoroughly rinsed with dH_2O and stored in a 2% glutaraldehyde solution (s. chapter 2.6.1) for 24 h. After another washing step in dH_2O, the catheter was stored in 0.9% sterile NaCl-solution until the next implantation. These data were acquired together with M. Sc. Pharm. Clement Kabagema-Bilan (Department of Pharmacology, Toxicology and Clinical Pharmacy, Institute of Pharmacy, University of Tübingen). Mr. Kabagema-Bilan carried out the implantation of the BP transmitter.

2.6.6 Transthoracic echocardiography

Cardiac morphological and functional abnormalities emerging in response to prolonged Ang II infusion in CTR and *cmf*KO mice were evaluated by non-invasive echocardiography's, as previously described (Frankenreiter et al., 2017, Straubinger et al., 2017). For this purpose, the echocardiography system (VisualSonics Vevo-2100 Ultrasound, Imaging System) provided by the working group of Prof. Meinrad Gawaz (Department of Cardiology and Angiology, University Hospital Tübingen) was employed. Sedation of the mouse was achieved using volatile 1.0 - 2.0% isoflurane/oxygen inhalation anesthesia via a breathing mask. Upon ensuring sufficient depth of anesthesia (loss of inter-toe-, eyelid and corneal reflex), the mouse was restrained supine on a heating plate allowing to detect the BT of the mouse via a rectal probe and to maintain BT at 37°C ± 0.5°C during the investigation process. Moreover, the board was equipped with specific electrode pads that enabled the simultaneously acquisition of an electrocardiogram (ECG) by fixing the paws on the ultrasound gel-covered electrodes. After the depilation of the left thoracic region with depilatory cream, remnants of the cream were carefully removed with water to prevent potential ultrasound artifacts followed by the air-bubble free application of ultrasound gel to the breast. For the acquisition of the parasternal long axis (PLAX), the adjustable heating plate was tilted to the left and rotated by 30° around the anteroposterior axis while the 30-MHz transducer was kept in the vertical position 10° counterclockwise (Pistner et al., 2010). By placing the transducer on the ultrasound gel, the heart was visualized in the two-dimensional brightness mode (B-mode) and subsequent minor adjustments were performed to ensure the course of the aortic outflow and apex in a horizontal lying plane. Additional data was collected in the two-dimensional time mode (M-mode) by placing the M-mode cursor between the apex and the aortic valve (s. Figure 8A). After completion of the examination, the anesthetized mouse was sacrificed by cervical dislocation and the heart was harvested for further histological investigations (s. chapter 2.11).

2.6.6.1 Quantification of LV function with the conventional method

Using the conventional method, global cardiac function was assessed by the automatic determination of manually plotted left ventricle wall dimensions (including the intraventricular septum (IVS) and left ventricular posterior wall (LVPW)) and left ventricular internal diameter (LVID) during systole and diastole in the M-mode view (s. Figure 8B). Based on these length specifications, ejection fraction (EF%) and fractional shortening (FS%) were automatically calculated by the software. M-mode recordings acquired in three distinct plate positions were selected for the quantification of three cardiac cycles respectively. Consequently, all functional parameters for each individual mouse were expressed as an average of nine cardiac cycles.

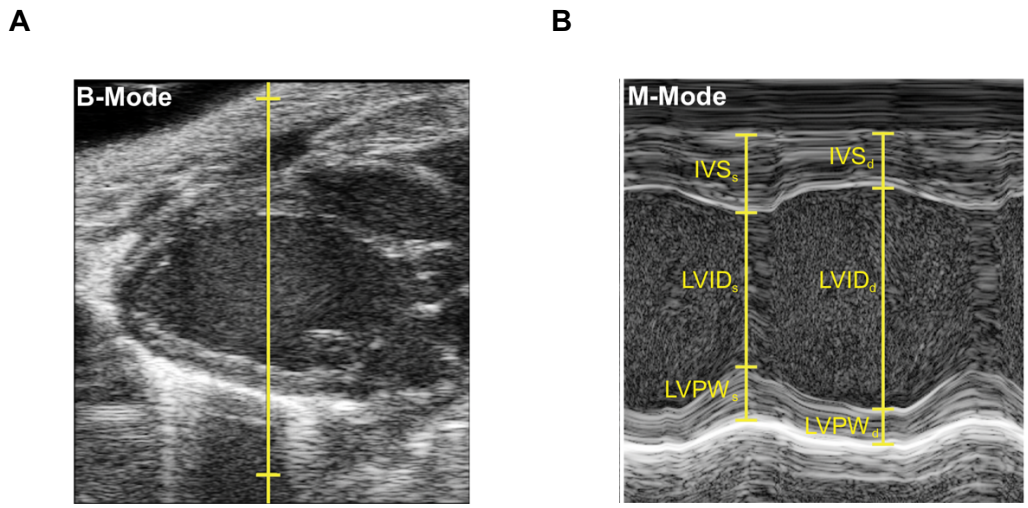

Figure 8: Analysis of cardiac function by conventional M-Mode echocardiography's
(**A**) Representative B-mode image obtained in PLAX view. The yellow highlighted M-mode cursor, divides the heart centrally between the aortic valve and the apex, indicating the position of (**B**) the displayed M-mode image. In this recording, LV wall and LV internal diameter were manually identified during the systole (s) and diastole (d) (shown in yellow). With these points, the software automatically determined the length of the respective parameters for the calculation of the global cardiac function. *IVS:* intraventricular septum, *LVID*: left ventricular internal diameter, *LVPW*: left ventricular posterior wall.

2.6.6.2 Quantification of LV function by ,,Vevo Strain" analysis

Speckle-tracking echocardiography (STE) provides a further option for the evaluation of LV performance, allowing the highly sensitive determination of global and regional functional parameters by integrating the measurement and assessment of LV myocardial deformation (Sato et al., 2022). For this investigations, only high-resolution B-Mode recordings were selected that enabled an automatic detection of three consecutive cardiac cycles by the software ,,Vevo Strain 2100''. Semi-automatic LV wall tracing was performed by setting 10 dots manually along the endocardium and by automatic detection of the epicardium by the software, followed by manual correction if required (s. Figure 9A). For complete acquisition of the LV deformation (strain and strain rate) and wall motion (velocity and displacement), the number of selected dots along the endo- and epicardium were automatically extrapolated to 48 points and displayed as curvilinear data (s. Figure 9B) (Dandel et al., 2009). Furthermore, global

cardiac parameters as EF, FS, and global longitudinal strain (GLS) were evaluated by LV wall tracing from three cardiac cycles and expressed as mean values.

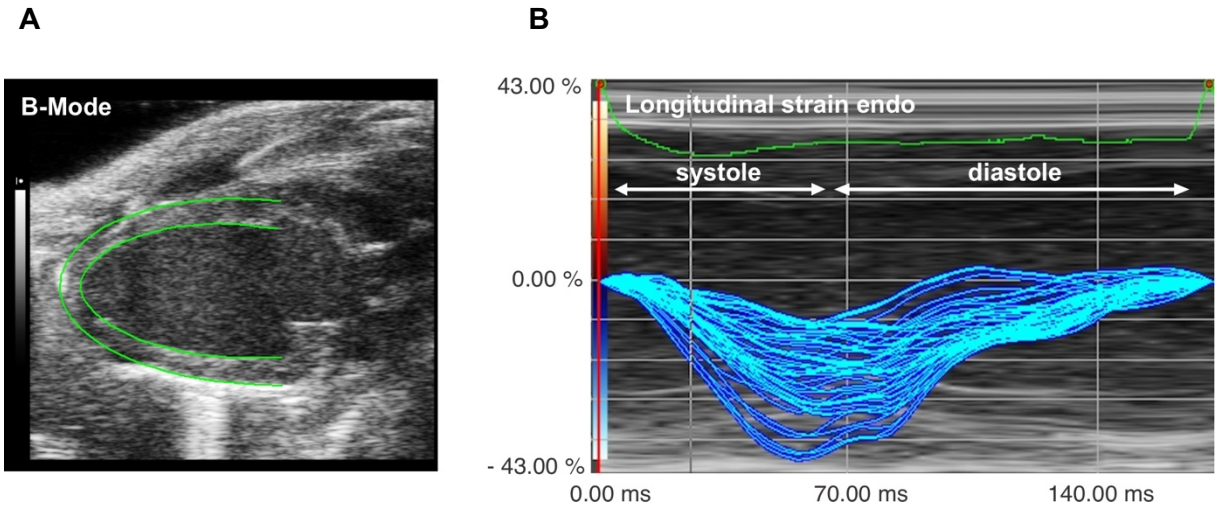

Figure 9: STE-based quantification of LV cardiac function
(**A**) Representative B-Mode image acquired in PLAX view, representing the semi-automatic LV-wall tracing (endocardium and epicardium) captured by means of the 48 points. (**B**) Exemplary illustration of the determined longitudinal strain of the endocardium for each individual point of the respective 48 points as curvilinear data (blue lines) for one cardiac cycle.

The subsequent time-to-peak analysis enabled the evaluation of regional myocardial deformation capacities. For this purpose, eight of the 48 points were combined into one cardiac segment, resulting in a division of the heart into 6 regions shown in Figure 10A. For the three selected cardiac cycles, the strain, stain rate and velocity were plotted as curvilinear data for each cardiac region as well as for the longitudinal and radial wall movement of the endocardium (likewise for the epicardium). Moreover, an average curve was calculated resulting from the mean values of all segmental values at the respective time points (Figure 10B).

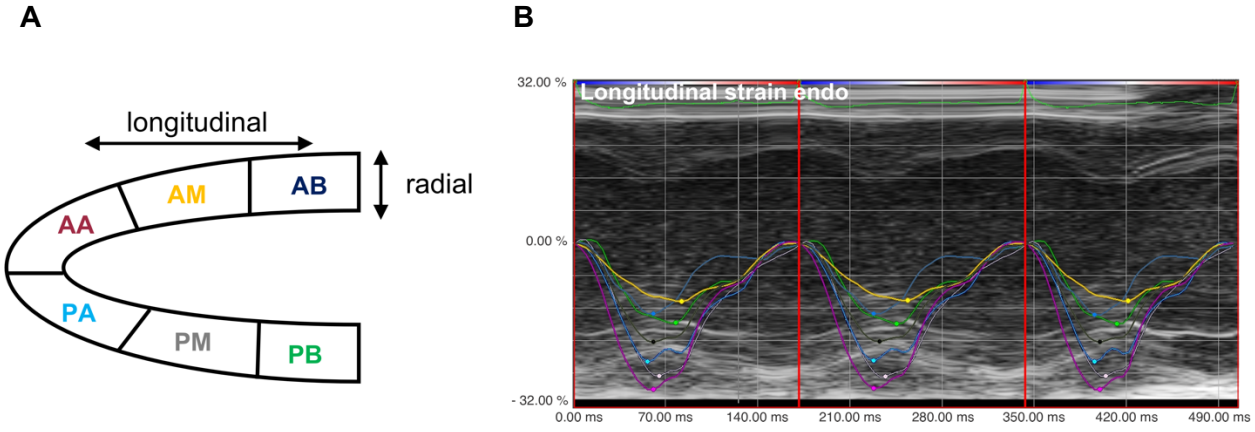

Figure 10: STE-based quantification of regional LV functions
(**A**) Schematic representation of the automatic division of the LV into six segments by the software, modified from Frankenreiter et al. (2017). (**B**) Representative curvilinear data displaying the longitudinal strain of the endocardium within each segment during three cardiac cycles. *AB*: anterior base (blue),

AM: anterior mid (yellow), *AA*: anterior apex (red), *PA* posterior apex (turquoise), *PM*: posterior mid (grey), *PB*: posterior base (green), average curve (black).

2.6.7 *In vivo* experimental set-ups in chronological order

Overall, the *in vivo* experiments performed can be divided into three distinct experimental groups, with the first two experimental arms differing only in the presence or absence of sustained Ang II stimulation. In contrast, the third group underwent additional implantation of BP transmitters. In detail, the first experimental group received only one daily TAM injection (+TAM treatment) for five consecutive days in order to activate the TAM-inducible Cre recombinase under physiological conditions (Figure 11A). The second experimental cohort underwent subcutaneous implantation of osmotic minipumps allowing continuous Ang II release over 28 days to induce cardiac remodeling. Within this set up, the animals received a daily TAM application after one day postoperatively for five consecutive days (+TAM +Ang II treatment) (Figure 11B). At the end of the 28 days, the required experimental investigations were carried out in both experimental groups (+TAM; +TAM +Ang II), whereby e.g., the cardiac output or the morphological changes of the heart were analyzed. Within the third experimental group, the first step involved the implantation of BP transmitters in order to determine basal BP values as well as the Ang II-mediated BP increase. Following a 7-day recovery phase, basal BP levels were monitored for the next three days before the osmotic minipumps were implanted to induce Ang II-mediated cardiac remodeling (Figure 11C). Immediately after the implantation of the osmotic minipumps releasing Ang II the BP changes were recorded for the next following 7 days. In this experimental set-up, the five-day TAM treatment for the induction of TAM-inducible Cre recombinase was also initiated one day after the implantation of osmotic minipumps.

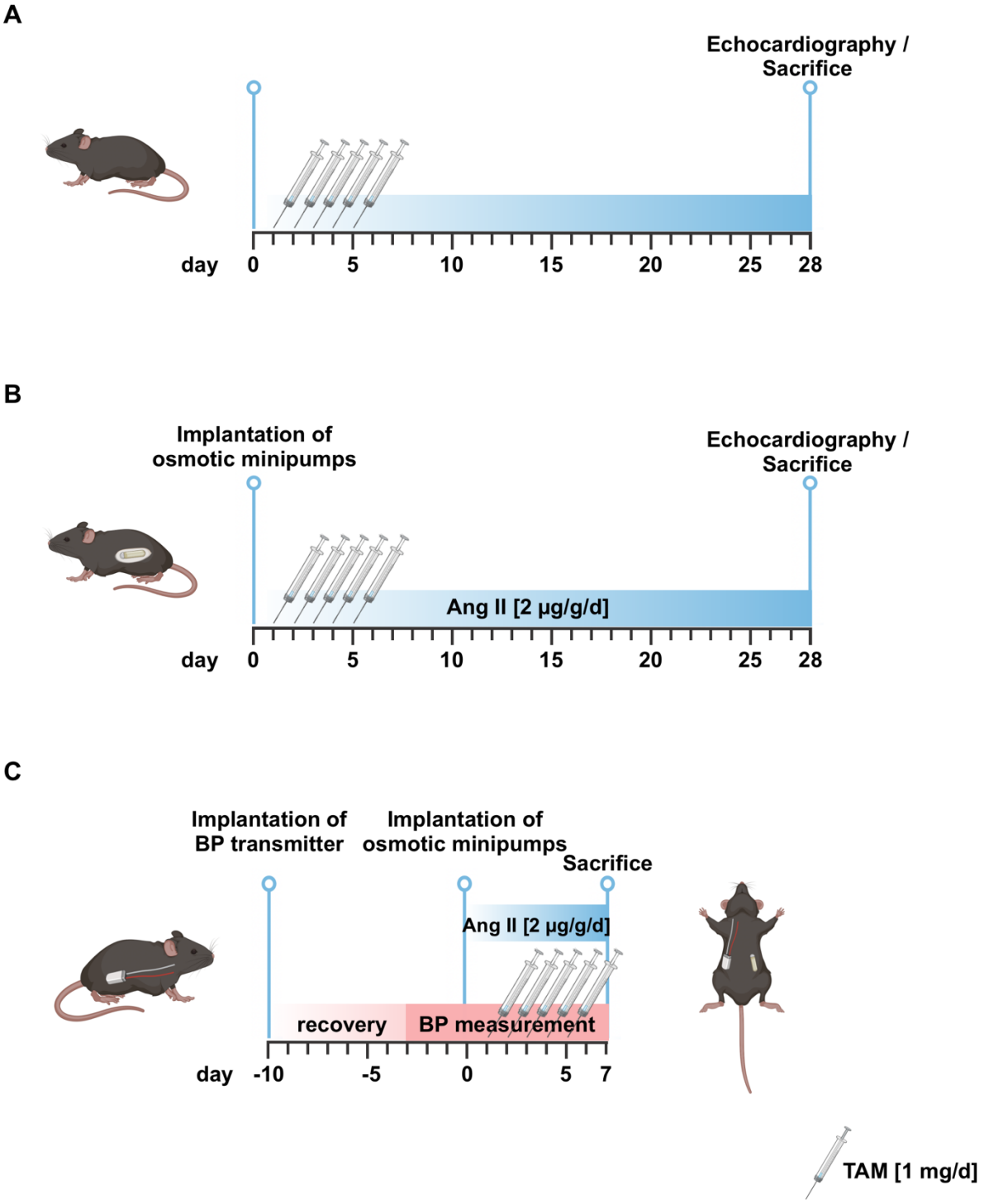

Figure 11: *In vivo* experiments in chronological order
Depicted are the chronological sequence of the distinct *in vivo* experiments as a timeline. (**A**) All animals within this experimental set-up received a five-day i.p. injection of TAM (1 mg/d) in order to activate the TAM-inducible *Postn*iCre recombinase. (**B**) Osmotic minipumps releasing Ang II continuously over 28 days were implanted subcutaneously in the experimental animals on day 0 in order to induce cardiac remodeling. One day post-operatively, the five-day TAM treatment was initiated. Four weeks later, non-invasive echocardiography's were performed, and hearts were harvested from both (**A**) TAM-treated and (**B**) TAM- and Ang II-treated animals to investigate cardiac remodeling and to isolate primary CF/CMF cell culture. (**C**) Telemetric BP transmitters were implanted to examine basal BP values as well as Ang II-mediated BP elevations. Mice were given a seven-day recovery period before basal BP parameters were acquired for the next three days. Thereafter, the Ang II-filled osmotic minipumps were implanted subcutaneously and Ang II-mediated BP increases were monitored for the next seven days. One day after implantation of the osmotic minipumps, the five-day TAM treatment was initiated. Created with BioRender.com.

2.7 Organ extraction and cultivation of CF/CMF

2.7.1 Materials, Reagents and Solutions

Product / Reagent	Reference or Source	Identifier or Catalog number
2,3-Butandion-Monoxim (BDM)	Sigma-Aldrich	B0753
4-(2-Hydroxyethyl)piperazine-1-ethanesulfonic acid (HEPES)	Sigma-Aldrich	H3375
Ampuwa	Fresenius Kabi	PZN 7610894
Bovine serum albumin (BSA)	Carl Roth	8076
CLS-2 – Collagenase, Type 2	Cellsystems®	LS004177
DMEM + GlutaMAX™	Thermo Scientific	31966021
Dulbecco's Phosphate Buffered Saline (DPBS)	Thermo Scientific	14190094
Fetal bovine serum (FBS)	Thermo Scientific	26140079
Glucose	Sigma-Aldrich	G7528
Insulin-Transferrin-Selenium (ITS) (100x)	Thermo Scientific	41400045
L-glutamic acid monosodium salt	Sigma-Aldrich	G-1626
Magnesium chloride hexahydrate ($MgCl_2 \cdot 6H_2O$)	Merck Millipore	1.05833
Magnesium sulfate heptahydrate ($MgSO_4 \cdot 7H_2O$)	Sigma-Aldrich	63138
Penicillin-Streptomycin (10,000 U/ml) (PenStrep)	Thermo Scientific	15140122
Phenol red sodium salt	Sigma-Aldrich	P5530
Potassium bicarbonate ($KHCO_3$)	Sigma-Aldrich	60339
Potassium chloride (KCl)	Sigma-Aldrich	P5405
Potassium phosphate monobasic (KH_2PO_4)	Sigma-Aldrich	P5655
Sodium bicarbonate ($NaHCO_3$)	Sigma-Aldrich	S5761
Sodium chloride (NaCl)	Sigma-Aldrich	S5886
Sodium phosphate dibasic dihydrate	Sigma-Aldrich	71643
Taurine	Sigma-Aldrich	T0625
Trypan blue solution 0.4%	Thermo Scientific	15250061
Trypsin 0.5%	Thermo Scientific	15400054
Trypsin 2.5%	Thermo Scientific	15090046

Isolation and cultivation of CF/CMF

Ca^{2+}-free media	
L-glutamic acid monosodium salt	85 mM
NaCl	60 mM
HEPES	10 mM
KCl	5.6 mM
$MgCl_2 \cdot 6H_2O$	1.0 mM
dH_2O	ad 1000 ml
→ adjust to pH 7.4 with NaOH	

CF/CMF culture media	
DMEM + GlutaMAX™	500 ml
Pen-Strep	1% (v/v)

Collagenase type II-based digestion solution	
Collagenase Typ II	1 mg/ml
BSA	1 mg/ml
Ca^{2+}-free media	ad 4 ml
→ prepare freshly and stored at 4°C until used	

0.05% Trypsin	
Trypsin 0.5%	500 µl
DPBS	5 ml

PFA 4%

FCS	10% (v/v)
ITS	1% (v/v)

PFA	30 g
1x DPBS	ad 750 ml
→ Heat to 60°C until a transparent solution of obtained	

Isolation of murine CM

Perfusion buffer (Stock solution)	
NaCl	112.94 mM
Taurine	29.96 mM
HEPES	10 mM
$NaHCO_3$	12 mM
$KHCO_3$	10 mM
KCl	4.7 mM
$MgSO_4 \cdot 7H_2O$	1.2 mM
$Na_2HPO_4 \cdot 2H_2O$	601.2 µM
KH_2PO_4	602.5 µM
Phenol red sodium salt	31.9 µM
dH_2O	ad 2000 ml

BDM (500 mM)	
BDM	500 mM
dH_2O	ad 50 ml

Perfusion buffer	
Perfusion buffer stock solution	1960 ml
BDM (500 mM)	40 ml
Glucose	2 g
→ adjust to pH to 7.46	
→ 40 ml aliquots as perfusion buffer	
→ 22.6 ml aliquots for digestion buffer	
→ stored at -20°C	

$CaCl_2$ solution (100 mM)	
$CaCl_2$	100 mM
dH_2O	ad 10 ml

$CaCl_2$ solution (10 mM)	
$CaCl_2$ (100 mM)	1 ml
dH_2O	ad 10 ml

Stop 1 solution	
Perfusion buffer	2.25 ml
$CaCl_2$ (100 mM)	1.25 µl
FCS	250 µl

Digestion buffer	
Perfusion buffer	22.5 ml
$CaCl_2$ (100 mM)	2.8 µl
Trypsin 2.5% (10x)	150 µl

Stop 2 solution	
Perfusion buffer	9.5 ml
$CaCl_2$ (100 mM)	3.75 µl
FCS	500 µl

Liberase-based digestion buffer	
Liberase solution	400 µl
Digestion buffer	22.65 ml
→ add the liberase solution to the before the digestion process to the digestion buffer directly	

Liberase solution	
Liberase DH Research Grade	50 mg
Ampuwa	12 ml
→ store aliquots of 400 µl at -20°C	

2.7.2 Organ isolation and determination of cardiac hypertrophy

Experimental mice were euthanized by CO_2 and death was ensured with a cervical dislocation. The heart was harvested as quick as possible and retrogradely perfused with ice cooled DPBS via the aorta using a modified Langendorff apparatus to remove blood clots and further cellular debris. Afterwards, the remaining aorta and the surrounding tissue were excised as well as residual DPBS was extracted from the heart by placing the organ on precision wipes allowing

the determination of the exact heart weight (HW). If required, further organs including aorta, lung, liver, spleen, and kidney were collected in the meantime and washed in a petri dish with ice cooled DPBS by carefully swirling. The organs were afterwards either further processed according to chapter 2.11.2 for the preparation of cryosections or frozen in liquid nitrogen and stored at -80°C for subsequent DNA-isolation (s. chapter 2.8).
For the determination of cardiac hypertrophy, both HW / body weight (BW) ratio as well as HW / tibia length (TL) ratio were calculated, with the latter being more precise due to potential fluctuations in BW (Yin et al., 1982). Therefore, the left hindlimb was extracted by cutting the femur near to the base and stored in a 2 ml reaction tube at -20°C until required. To easily clean the tibia from surrounding tissue (skin and muscle), 1 ml of tap water was added to the reaction tube before the collected hindlimbs were boiled for 1 h at 95°C in a heating shaker. Afterwards, the tissues were carefully removed manually and the TL starting from the condyles to the end of the medial malleolus was determined by a digital caliper (Yin et al., 1980). The TL of each mouse was calculated as a mean of three independent measures.

2.7.3 Isolation and cultivation of murine CF/CMF

Once euthanized (s. chapter 2.7.2), the hearts of experimental animals were harvested as quickly as possible and placed in a petri dish filled with ice cooled DPBS. Surrounding tissues including the atria and the aorta, were removed by a transversal incision through the heart allowing the exposed ventricles to be cleared from blood debris with DPBS. The purified ventricles were transferred into a 2 ml reaction tube filled with 1 ml of DPBS and dissected into ~1 mm pieces using a spring scissors. Each of the subsequent steps were conducted under the laminar flow cabinet in the cell culture. The 80 min digestion process at 37°C in a water bath was initiated by placing the heart pieces into a 15 ml vial containing 1 ml of the collagenase type II-based digestion solution (s. chapter 2.7.1). To favor the detachment of the cells from the tissue, the heart pieces are alternately swirled carefully or homogenized in the digestion solution using a 10 ml pipette at an interval of five minutes. To further enhance the digestion process and to preserve cell viability, the supernatant containing the isolated cells was transferred into 26 ml of 37°C warmed cultured media (s. chapter 2.7.1) every 20 min. Fresh digestion solution (s. chapter 2.7.1) was added to the heart pieces that had not yet been fully digested. This process is carried out a total of four times, whereby the isolated cells were pooled in the same reaction tube containing culture media (s. chapter 2.7.1). Applying a 40 µm cell strainer and a centrifugation step (5 min at 300 rpm), non-digested tissue, cell debris and isolated CMs were separated from CF/CMF. A second centrifugation step (7 min at 1000 rpm) of the supernatant yielded a cell pellet consisting of purified CF/CMF. Afterwards, the cell pellet was resuspended in 1 ml culture media and cells were counted using a Neubauer haemocytometer in order to plate out the required cell number for each experiment. For this counting process, 10 µl of the CF/CMF cell suspension were diluted in 90 µl of Trypan blue allowing the later differentiation of vital and death cells. Finally, 10 µl of this dilution was places in the Neubauer haemocytometer and only the vital (not blue stained) cells were counted. Cells were cultured at 37°C and 5% CO_2 and the culture media was changed every two to three days unless otherwise stated in the specific *in vitro* experiment.

In order to perform both the IF-staining (s. chapter 2.11.6) as well as the nuclear staining (s. chapter 2.11.7) on isolated CF/CMFs, glass coverslips were placed individually in each well of a 24-well plate. Per well $3 \cdot 10^4$ CF/CMF were seeded and cultured for five days *in vitro* (div 5) before being fixed by replacing the culture media with 4% PFA solution (s. chapter 2.7.1) for 15 min. After several washing steps in DPBS (3·5 min), the cells were coated with DPBS and stored airtight in the refrigerator for up to seven days.

For Western Blot analysis (s. chapter 2.9), 10^6 cells were seeded in a 10 cm petri dish and cultured until 90% confluency was reached. To harvest the cells, the culture media was withdrawn, and the cells were washed twice with DPBS, before 2 ml 0.05% trypsin (s. chapter 2.7.1) was added. The cells were then incubated for 5 min at 37°C, with gentle tapping on the outside of the petri dish in the meantime to support the detachment of the cells from the bottom. The process is arrested by the administration of 6 ml culture media. To obtain the harvested CF/CMF cell pellet, the entire cell suspension was transferred into a 50 ml centrifugation tube and centrifuged for 7 min at 1000 rpm. The supernatant was removed, and the cell pellet was again resuspended in 1 ml DPBS, before the cell suspension was passed into a 2 ml reaction tube and centrifuged once more for 7 min at 1000 rpm. The supernatant was withdrawn again, and the cell pellet was shock frozen in liquid nitrogen and stored at -80°C until required.

For the performed Cre-mediated recombination analyses on CF/CMF DNA (s. chapter 2.8), the cultivation of the isolated cells was not conducted. Consequently, after resuspension in 1 ml culture media, the purified CF/CMF cell pellet was transferred directly to a 2 ml reaction tube and centrifuged for 7 min at 1000 rpm. Afterwards, the supernatant was discarded, and the cell pellet was shock frozen in nitrogen and stored at -80°C until required.

2.7.4 Isolation of murine CM

Mice were euthanized by CO_2 and death was ensured with a cervical dislocation. The heart was harvested immediately and retrogradely perfused with 37°C warmed perfusion buffer (s. chapter 2.7.1) via the aorta using a modified Langendorff apparatus with a specific flow rate of 2.5 ml/min for 3 min, as previously described (Straubinger et al., 2017). By replacing the perfusion buffer by a liberase-based digestion buffer (s. chapter 2.7.1), the heart was digested afterwards for further 12 min. Following the perfusion process, the aorta and atria were removed, the ventricle was placed into 2.5 ml digestion buffer and dissected into ~1 mm pieces using a spring scissors. Upon the addition of Stop 1-solution, heart pieces are carefully resuspended by a 5 ml pipette for another 4 min allowing the detachment of the cells from the tissue, before non-digested heart pieces were separated from the cell suspension using a 100 µm cell strainer. A subsequent 10 min sedimentation step in a 15 ml reaction tube resulted in the separation of the isolated CF remaining in the supernatant from the vital CMs pellet. The purified CM-pellet was resuspended in Stop 2 solution and treated in a petri dish with ascending Ca^{2+} concentrations stepwise, staring with the addition of 50 µl twice and 100 µl once of a 10 mM Ca^{2+} solution (s. chapter 2.7.1) and progressing to the addition of 30 µl and 50 µl of a 100 mM Ca^{2+}-solution (s. chapter 2.7.1) at four-min intervals respectively. Upon another sedimentation step for 10 min in a 15 ml reaction tube, the cell pellet was resuspended again in 1 ml DPBS, transferred to a 2 ml reaction tube,

and centrifuged at lowest level (900 rpm for 1 min). The supernatant was removed, and the purified CM cell pellet was shock frozen in nitrogen and stored at -80°C until required.

2.8 DNA extraction for PCR analysis

In order to detect the CMF-specific Cre-mediated excision of the floxed exon 10 of *PRKG1*, an allele-specific PCR was conducted. For this purpose, primary CF/CMF and further control organs (aorta, lung, liver, spleen and kidney) were harvested as already described (s. chapter 2.7.2 and 2.7.3). Following the protocol previously mentioned in section 2.5.2, the DNA was extracted from the organs and cells via a High Pure PCR Template Preparation Kit. Moreover, the concentration of the eluted DNA was measured with a photometer and adjusted to a concentration of 10 ng/µl by dilution with elution buffer. Subsequent PCR was carried out by employing the primers and the identical Mastermix already illustrated in chapter 2.5.3 as well as by running the PCR-program outlined in Table 4. Gel electrophoretic separation and visualization of the DNA-bands was performed as previously described (s. chapter 2.5.4).

Table 4: PCR program for CMF-specific cGKI$^{-/-}$ detection

cGKI		
T1	94.0°C	3 min
T2	94.0°C	30 sec
*T3	65.0°C	30 sec
T4	72.0°C	30 sec
Repeat T2-T4		10x
T5	94.0°C	30 sec
T6	55.0°C	30 sec
Repeat T5-T6		40x
*per cycle, the T continuously decreases by 1°C		

2.9 Protein analytic by semi-dry Western Blot

Western Blot analysis was performed to verify cGKI expression levels in primary CF/CMF cultures isolated from Ang II treated CTR and *cmf*KO mice. Isolation and cultivation of the cells was conducted as previously described (s. chapter 2.7.3).

2.9.1 Materials, Reagents and Solutions

Product / Reagent	**Reference or Source**	**Identifier or Catalog number**
Ammonium peroxydisulphate (APS)	Carl Roth	9592.2
BSA	Carl Roth	8076.2
Bromophenol blue	SERVA	15375
Dithiothreitol (DTT)	Carl Roth	6908.1
Ethanol (absolute)	Sigma-Aldrich	32205-M
Ethylenediaminetetraacetic acid (EDTA)	Cal Roth	8043.1
Glycerol	Carl Roth	3783.1

Glycine	Carl Roth	3908.3
Methanol (Rotipuran® ≥ 99,9 %)	Carl Roth	4627.5
Milk powdered	Carl Roth	T145.3
peqGOLD protein marker IV	VWR	27-2110
Phenylmethyl sulphonyl fluoride (PMSF)	Carl Roth	6367.2
PhosSTOP™	Sigma-Aldrich	4906845001
Pierce TM BCA Protein Assay Kit	Thermo Scientific	23225
Protease inhibitor cocktail	Sigma-Aldrich	P8340
Rotiphorese® Gel 30 (37.5:1)	Carl Roth	3029.2
Sodium azide (NaN_3)	Carl Roth	K305.1
Sodium chloride (NaCl)	Carl Roth	3957.2
Sodium dodecyl sulfate pellets (SDS)	Carl Roth	8029.3
Sodium fluoride (NaF)	Sigma-Aldrich	201154
Sodium orthovanadate (Na_3VO_4)	Sigma-Aldrich	450243
Sodium pyrophosphate tetrabasic ($Na_4P_2O_7$)	Sigma-Aldrich	P8010
Tetramethylethylenediamine (TEMED)	Carl Roth	2367.2
Tris(hydroxymethyl)-aminomethane (Tris)	Carl Roth	5429.3
Triton X-100	Carl Roth	3051.2
Tween® 20	Carl Roth	9127.1
ε-aminocaproic acid	Sigma-Aldrich	A2504

Primary antibody	Reference or Source	Identifier or Catalog number
Rabbit IgG PKG-1 (1:250 WB)	Cell Signaling Technology	3248S
Rabbit monoclonal GAPDH (1:1000)	Cell Signaling Technology	Cat#2118S

Secondary antibody	Reference or Source	Identifier or Catalog number
Rabbit IgG HRP-linked whole Ab (from donkey) (1:1000)	Merck Millipore	GENA934

Protein extraction and BCA-assay

Lysis buffer	
Tris (pH 7.4)	50 mM
NaCl	150 mM
Glycerol	10% (v/v)
EDTA	2 mM
Triton X-100	1% (v/v)
$Na_4P_2O_7$	10 mM
NaF	50 mM
Na_3VO_4	200 µM
dH_2O	ad 50 ml
→ stored at -20°C	
→ before use supplemented with:	
Protease inhibitor (1:100)	5 µl
PhosSTOP™ (1:10)	50 µl
PMSF (1:100; 200 mM in EtOH)	5 µl

BSA-standards dilution series	
BSA 1500 µg/ml	
BSA-standard (2000 µg/ml)	225 µl
dH_2O	75 µl
BSA 1000 µg/ml	
BSA-standard (2000 µg/ml)	150 µl
dH_2O	150 µl
BSA 750 µg/ml	
BSA-standard (2000 µg/ml)	112.5 µl
dH_2O	187,5 µl
BSA 500 µg/ml	
BSA-standard (2000 µg/ml)	75 µl
dH_2O	225 µl
BSA 250 µg/ml	
BSA-standard (2000 µg/ml)	37.5 µl
dH_2O	262.5 µl

Working solutions	
Reagent A	98% (v/v)
Reagent B	2% (v/v)

200 mM PMSF	
PMSF	200 mM
Ethanol (100%)	10 ml
Stored at -20°C	

BSA 125 µg/ml	
BSA-standard (2000 µg/ml)	18.75 µl
dH_2O	281.25 µl

BSA 25 µg/ml	
BSA-standard (2000 µg/ml)	3.75 µl
dH_2O	296.25 µl

SDS-PAGE

4x Laemmli	
SDS	4.5% (w/v)
Tris	198 mM
Glycerin	40% (v/v)
Bromophenol blue	0.012% (w/v)
dH_2O	ad 50 ml

4x Laemmli with DTT	
DTT (1M)	2 µl
4x Laemmli	5 µl

1.8 M Tris-HCl, pH 8.8	
Tris	1.8 M
dH_2O	ad 1000 ml
adjust pH to 8.8 with HCl	

0.6 M Tris-HCl, pH 6.8	
Tris	0.6 M
dH_2O	ad 1000 ml
adjust pH to 6.8 with HCl	

SDS (10%)	
SDS	10% (w/v)
dH_2O	ad 100 ml

APS (30%)	
APS	30% (w/v)
dH_2O	ad 10 ml

5% Stacking gel	
dH_2O	3.6 ml
Rotiphorese acrylamide-solution	0.83 ml
0.6 M Tris-HCl, pH 6.8	0.5 ml
10 % SDS	50 µl
30 % APS	16.6 µl
TEMED	10 µl

12.5% Separation gel	
dH_2O	3.15 ml
Rotiphorese acrylamide-solution	3.55 ml
1.8 M Tris-HCl, pH 8.8	1.8 ml
10 % SDS	83.5 µl
30 % APS	33.3 µl
TEMED	10 µl

10x Elphor buffer	
Tris	247.65 mM
Glycine	14.4% (w/v)
SDS	1% (w/v)
dH_2O	ad 1000 ml
adjust pH to 8.3 with HCl	
→1x Elphor buffer: 1:10 dilution in dH_2O	
→ Sterile filtration	

10x TBST	
Tris	100 mM
NaCl	1.4 M
Tween 20	0.5% (v/v)
dH_2O	ad 1000 ml
adjust pH to 8.0 with HCl	
→1x TBST buffer: 1:10 dilution in dH_2O	
→ Sterile filtration	

Semi-dry Western Blot

Anode buffer I	
Tris	300 mM

Anode buffer II	
Tris	29.72 mM

Methanol	20% (v/v)
dH_2O	ad 1000 ml
adjust pH to 10.4	

Methanol	20% (v/v)
dH_2O	ad 1000 ml
adjust pH to 10.4	

Cathode buffer	
Tris	24.76 mM
ε-aminocaproic acid	44.22 mM
Methanol	20% (v/v)
dH_2O	ad 1000 ml
adjust pH to 7.6	

Antibody dilution solution	
BSA	5% (w/v)
NaN_3	0.05% (w/v)
1x TBST	ad 100 ml

5% dry milk blocking buffer	
Dry milk	5% (w/v)
1x TBST	ad 100 ml

2.9.2 Protein extraction from cells

To extract proteins from frozen CF/CMF- and CMs-cell pellets (s. chapter 2.7.3; 2.7.4), the samples were gently thawed on ice and resuspended in 70 µl of freshly prepared lysis buffer (s. chapter 2.9.1), before being briefly vortexed and further incubated for 5 min on ice. To completely dissolve the cell pellets, the samples were homogenized using a 30 G needle and subsequently vortexed at 5 min of interval for a total of 25 min. Afterwards, the samples were centrifuged at 13 000 rpm at 4°C for 15 min, whereby the resulted pellets were discarded, and the extracted proteins were stores at -80°C until use.

2.9.3 Determination of protein concentration using BCA-assay

For accurate adjustment of the samples to the target concentration of 40 µg protein per 20 µl pocket volume (2 µg/µl), the PierceTM bicinchoninic acid (BCA) Protein Assay Kit was conducted according to the manufacturer's instructions. This assay is based on the well-known protein-induced reduction of Cu^{2+} to Cu^{+} and the subsequent specific colorimetric detection of the resulting BCA-cooper complex exhibiting an absorption at 562 nm (Huang et al., 2010). Briefly, the samples were thawed on ice and diluted 1:10 in dH_2O (3 µl protein lysates in 27 µl dH_2O). BSA based internal standard dilution series (2000 µg/ml, 1500 µg/ml, 1000 µg/ml, 750 µg/ml, 500 µg/ml, 250 µg/ml, 125 µg/ml, and 25 µg/ml - s. chapter 2.9.1) as well as the working solution (s. chapter 2.9.1) were prepared. From each sample, the BSA standard dilutions and water, with the latter serving as negative control, 12.5 µl were pipetted as duplicates into a 96 well plate. Each well was supplemented with 100 µl of working solution, before the 96-well plate was incubated for 30 min at 37°C. The absorption was measured using TECAN Sunrise plate reader. For the subsequent determination of the protein concentration, the mean absorbance values of the samples were referred to a calibration curve, generated by a polynomial regression of the mean absorbance values of the albumin standard.

2.9.4 Sodium dodecyl sulfate polyacrylamide gel electrophoresis (SDS-PAGE)

Depending on the calculated amount of protein, the samples were adjusted to the required target concentration with ddH_2O and 4x Laemmli (s. chapter 2.9.1) and heated at 95°C for 10 min. Following a short centrifugation step, the proteins were separated according to the molecular size by gel electrophoresis (Smith, 1984). For this purpose, a polyacrylamide-based gel composed of a stacking gel (s. chapter 2.9.1) and a 12.5% separation gel (s. chapter 2.9.1) was prepared. Therefore, the separating gel was initially poured into a small gap between two glass plates in a corresponding gel chamber and layered with 100% isopropanol. Once the gel was completely polymerized, the isopropanol was replaced by the stacking gel and a comb was inserted into the latter gel allowing the formation of 10 pockets. After polymerization of the stacking gel, the comb was removed, and the gel was placed in an electrophoresis chamber containing the electrophoresis buffer (s. chapter 2.9.1). The pockets of the gel were loaded with 20 µl of each sample. To visualize the separation process and to determine the molecular weight of distinct proteins, one pocket of the gel was charged with 3 µl of the protein marker IV. The initial applied voltage of 80 V was increased to 120 V as soon as the samples had migrated from the stacking gel into the separation gel.

2.9.5 Semi-dry Western Blot

The semi-dry blotting technique was subsequently used to transfer the separated proteins from the polyacrylamide gel onto the polyvinylidene fluoride (PVDF) membranes. By employing this method, protein transfer is achieved in an electric field by placing the transfer “sandwich” consisting of the gel, the membrane and filter papers soaked in transfer buffer, horizontally between two platinum-coated electrode plates. Therefore, three filter papers soaked in anode buffer I (s. chapter 2.9.1) were positioned centrally on a moistened anode plate and covered by two filter papers soaked in anode buffer II (s. chapter 2.9.1). The PVDF-membrane was shortly equilibrated in methanol, soaked in anode buffer II, and then placed on top of the previously prepared filter papers. After completion of the electrophoresis process the stacking gel is detached from the separation gel and discarded, prior to positioned the separation gel air-bubbles free on the PVDF-membrane. Afterwards, five further filter papers saturated with cathode buffer (s. chapter 2.9.1) were laid on top of the separation gel. Finally, the whole transfer-sandwich was covered by the water wetted-cathode plate and the transfer process was initiated by applying a current of 60 mA per gel. One hour later the current was increased to 90 mA per gel for further 15 min.

2.9.6 Protein detection by chemiluminescent

After completion of the protein transfer using the semi-dry western blot technique, detection of specific proteins was enabled by chemiluminescence. Therefore, unspecific binding sides were blocked by the incubation of the membranes in 5% dry milk in 1x TBST (s. chapter 2.9.1) for 1 h at RT. Afterwards, the membranes were washed thrice in TBST (3·5 min) before being loaded with the primary antibody solution against either cGKI or GAPDH (s. chapter 2.9.1) at 4°C overnight. To examine distinct protein expression patterns on the same membrane, the membrane was sectioned using a scalpel allowing the sections to be incubated in different

primary antibody solutions. Following renewed washing steps in TBST (3·10 min), the membranes were treated with the horseradish peroxidase (HRP)-coupled secondary antibody (s. chapter 2.9.1) for 1 h at RT. Membranes were washed again thrice in TBST, before immunosignals were visualized upon incubation of the membrane for 30 sec with the HRP-chemiluminescent substrate using an Amersham Imager 600. The quantification of the obtained protein bands was conducted densitometrically using ImageJ.

2.10 Gird-based proliferation assay

An in *vitro* grid-based proliferation assay was conducted in order to determine the proliferation behavior of primary CF/CMF cell cultures isolated from Ang II treated CTR and *cmf*KO mice. For this purpose, the cells were isolated and counted as previously described (s. chapter 2.7.3). In each well of the employed 8-well Grid-500 chamber, a cell suspension adjusted to $20{\cdot}10^3$ cells was seeded and allowed to adhere to the bottom of the slide for 24 h at 5% CO_2 and 37°C. Non-adherent cells as well as potentially isolated cell debris were removed by two washing steps in DPBS, bevor the starvation medium (s. chapter 2.7.1) was applied to synchronize the cell cycle for further 24 h. Afterwards, the starvation medium was replaced by the cultivation media (s. chapter 2.7.1) followed by image acquisition of four randomly chosen quadrants within each well (time point t = 0 h) using an inverted transmitted-light microscope. Proliferation rate was monitored for five consecutive days, with images taken every 24 h.

2.11 Histochemical methods

2.11.1 Materials, Reagents and Solutions

Product / Reagent	Reference or Source	Identifier or Catalog number
Acetic acid (100%)	Carl Roth	3738.5
Ammonia (30-33%)	Carl Roth	P093.2
Aquatex®	Merck Millipore	108562
Bouin solution	Sigma-Aldrich	HT101126
BSA	Carl Roth	8076
Direct Red 80	Sigma-Aldrich	365548
DPX	Sigma-Aldrich	1.00579
DPBS	Thermo Scientific	14190094
Eosin-G solution (0.5 %)	Carl Roth	X883.1
Ethanol (absolute)	Sigma-Aldrich	32205
Glycerol	Carl Roth	3738.1
Hydrogen peroxide (H_2O_2)	Carl Roth	8070.2
Harris Haematoxylin solution	Carl Roth	X903.2
Hydrogen chloride (HCl) (0.1N)	Carl Roth	6789.1
Hoechst 33432	Thermo Scientific	62249
In Situ Cell Death Detection Kit (TUNEL)	Roche	12156792910
Levamisole solution	Vector laboratories	SP-5000-18
Sodium hydroxide (NaOH)	Carl Roth	6771
Neg-50™	Epredia	6502
Ammonium chloride (NH_4Cl)	Carl Roth	5470.1
Normal goat serum (NGS)	BIOZOL Diagnostica	ENG9010
Paraformaldehyde (PFA)	Carl Roth	0335.3

PermaFluor Aqueous Mounting Medium	Thermo Scientific	TA-030-FM
Picric acid	Sigma-Aldrich	239801
Picric acid solution (saturated)	Sigma-Aldrich	6744-1GA
Sucrose	Carl Roth	4621.2
Toluol	Carl Roth	7115.1
Triton-X-100	Carl Roth	3051
Vectastain ABC-AP kit Alkaline Phosphatase (Standard)	Vector laboratories	AK 5000
Vector® Blue Substrate Kit, Alkaline Phosphatase (AP)	Vector laboratories	SK5300
Xylene	Carl Roth	9713.3
Tris	Carl Roth	3051

Fixation of tissues

PFA 4%	
PFA	30 g
1x DPBS	ad 750 ml
→ Heat to 60°C until a transparent solution of obtained	

Sucrose gradient

Sucrose solution 5%	
Sucrose	5% (w/v)
1x DPBS	ad 100 ml

Sucrose solution 10%	
Sucrose	10% (w/v)
1x DPBS	ad 100 ml

Sucrose solution 20%	
Sucrose	20% (w/v)
1x DPBS	ad 100 ml

Permeabilization solution

Triton X-100 0.3%	
Triton X-100	0.3% (v/v)
1x DPBS	500 ml

Triton X-100 0.01%	
Triton X-100	0.01% (v/v)
1x DPBS	500 ml

Immunoflourescence

Mounting medium for cell nuclei staining	
Hoechst	1/1000
PermaFluor	7.5 ml

Blocking buffer	
Glycerol	2% (v/v)
NGS	5% (v/v)
Triton-X-100	0.3% (v/v)
BSA	2% (w/v)
NH_4Cl	50 mM
DPBS	ad 100 ml

Chemical Cocktail	
H_2O_2	3% (v/v)
NaOH	50 mM

Immunohistochemistry (AP)

NGS-based blocking solution	
NGS	10% (v/v)

NGS 1.5 %	
NGS	1.5% (v/v)

DPBS	ad 10 ml

Tris-HCl pH 8.2	
Tris	0.1 M
dH_2O	ad 1000 ml
→ adjust pH to 8.2 with HCl	

AP-substrate solution	
Reagent 1	0.02% (v/v)
Reagent 2	0.02% (v/v)
Reagent 3	0.02% (v/v)
Levamisole	0.02% (v/v)
Tris-HCl	ad 5 ml

Picrosirius Red staining

Direct Red 80 1%	
Direct Red 80	1% (w/v)
dH_2O	ad 25 ml
→ filter dissolved solution	

Hematoxylin and eosin staining

Eosin-Y solution	
Eosin-G solution (0.5%)	20% (v/v)
dH2O	ad 10 ml
→ acidify with a drop 100% acetic acid	

DPBS	ad 10 ml

ABC-AP-working solution	
Reagent A	0.01% (v/v)
Reagent B	0.01% (v/v)
DPBS	ad 5 ml
→ Incubation for 30 minutes in the dark	

Sirius Red solution	
Direct Red 80 (1%)	0.1% (v/v)
Picric acid	0.02% (w/v)
Saturated picric acid	250 ml
→ add saturated picric acid via an filter to the Direct Red solution	

TUNEL-staining

TUNEL-reaction solution	
TUNEL-enzyme solution	10% (v/v)
TUNEL-label solution	ad 500 µl

Primary antibody	**Reference or Source**	**Identifier or Catalog number**
Alexa Fluor 488 Phalloidin (1:500)	Thermo Scientific	A12379
Alexa Fluor Plus 647 Phalloidin (1:500)	Thermo Scientific	A30107
Mouse monoclonal Anti-Collagen I (1:1000)	Abcam	ab6308
Rabbit IgG PKG-1 (1:1000)	Cell Signaling Technology	3248S
Rabbit monoclonal Anti-Collagen III (1:500)	Abcam	ab184993
Rabbit monoclonal Ki67 (1:1000)	Cell Signaling Technology	9129
Rabbit polyclonal Anti-Periostin (1:500)	Abcam	ab14041
Rabbit Troponin I antibody (1:100)	Cell Signaling Technology	4002S

Secondary antibody	**Reference or Source**	**Identifier or Catalog number**
Goat anti-Mouse IgG1 Alexa Fluor 488 (1:2000)	Thermo Scientific	A-21121
Goat anti-Rabbit (H+L) Alexa Fluor 488 (1:1000)	Thermo Scientific	A-11008
Goat anti-Rabbit (H+L) Alexa Fluor 555 (1:1000)	Thermo Scientific	A-21428

Goat anti-Rabbit (H+L) Alexa Fluor 647 (1:1000)	Thermo Scientific	A32733
Goat anti-Rabbit (H+L) biotinylated (1:1000)	Vector laboratories	BA-1000

2.11.2 Preparation of tissue cryosections

For the preparation of tissue cryosections, the organs were isolated and purified as previously described (s. chapter 2.7.2) and subsequently fixed in 4% PFA for 4 h at 4°C on a shaker. After three washing steps in DPBS (3x20 min), the organs were gently dehydrated using an ascending sucrose gradient by initially incubating the organs in a 5% sucrose solution (s. chapter 2.11.1) for 1 h, then in a 10% sucrose solution (s. chapter 2.11.1) overnight and finally in a 20% sucrose solution (s. chapter 2.11.1) for 24 h. Excess sucrose solution was removed by placing the organs on precision wipes. The organs were embedded in NEG-50 in previously prepared carrier molds consisting of aluminum foil and stored at -80°C.
In order to generate tissue sections, the embedded organs were first thawed at -20°C for 30 min before being cut using a cryostat. For slicing the organs, the same settings were consistently employed within the present work (s. Table 5).

Table 5: Cryostat setting

Tissue cut thickness	10 µm
Trim thickness	50 µm
Object temperature	-21°C until -23°C
Knife temperature	-23°C until -24°C
Vacutome stage	5 - 10

For the evaluation of the cell-specific *Postn*iCre$^{Tg/+}$ expression as well as of the Ang II mediated cardiac remodeling, unchallenged and Ang II-treated hearts obtained from ROSA$^{mT/mG}$, ROSA$^{mT/mG}$ x *Postn*iCre$^{Tg/+}$, CTR and *cmf*KO mice were divided into eight equidistant areas extending from the apex (section I) to the base (section VIII) of the heart. To create these sections, excess NEG-medium was trimmed until the apex was visible in the NEG-medium. Departing from this sectional plane, 250 µm of tissue were removed in 50 µm trim steps, before 10 µm transversal heart slices were obtained and attached to a microscope slide. For each section, 5 microscope slides were collected containing 2-4 heart slices respectively. Beginning with the renewed removal of 250 µm, the second section was subsequently obtained. Following this process, all eight sections were preserved.
In accordance with the preparation of the heart slices, tissue samples of additional organs (aorta, lung, liver, kidney, and spleen) from healthy and Ang II-treated ROSA$^{mT/mG}$ and ROSA$^{mT/mG}$ x *Postn*iCre$^{Tg/+}$ animals were collected. Irrespective of the organ, at least the first five sections were acquired. The largest number of sections was determined by the size of the organ, as care was taken to obtain the section with the greatest tissue cross-sectional area.
All tissue slices were stored at -20°C until the distinct staining techniques (s. chapter 2.11.3-0) were initiated by thawing the slice at RT for 30 min. Histochemical staining and quantification were performed in collaboration with Lena Ullemeyer (Department of Experimental Pharmacology, University of Tübingen) in the course of her Master's thesis.

2.11.3 Immunohistochemistry of cGKI and Periostin

Alkaline phosphatase staining (AP-staining) was conducted for the detection of specific target proteins within fibrotic regions of remodeled hearts isolated from CTR and *cmf*KO mice. Thawed cryosections (s. chapter 2.11.2) were first carefully rimmed with a hydrophobic barrier pen in order to maintain the reagents on the samples throughout the entire staining process. Tissue sections were permeabilized using 0.3% Triton-X solution for 30 min at RT. Following multiple washing steps in DPBS (3x5 min), unspecific binding of the primary antibody was prevented by incubating the samples for 1 h at RT in the blocking buffer containing 10% NGS in DPBS (s. chapter 2.11.1). Tissue sections were loaded overnight at 4°C with the respective primary antibody solutions against either cGKI (1:1000) or periostin (1:500) dissolved in 1.5% NGS in DPBS (s. chapter 2.11.1). For the validation of every staining process as well as to exclude potential background staining, a negative control lacking the primary antibody treatment was conducted equally. After several washing steps in 1.5% NGS in DPBS (5x5 min), the tissue sections were incubated in biotinylated secondary antibodies (s. chapter 2.11.1) for 1 h at RT. The samples were again rinsed in 1.5% NGS in DPBS (5x5 min) prior to incubation in ABC-AP working solution (s. chapter 2.11.1) for 30 min at RT. In accordance with the manufacturer's instruction, the freshly prepared ABC-AP reagent was pre-formed for 30 min in the dark before the application. Next, the tissue sections were once more rinsed in 1.5% NGS in DPBS to remove excess ABC-AP reagent and loaded with the AP-substrate (s. chapter 2.11.1). Under the light microscope, the conversion of the AP-substrate by the alkaline phosphatase was monitored via the formation of the blue indigo dye. Depending on the intensity of the blue staining, the phosphatase activity and thus the staining reaction was completed after 10-20 min by immersing the tissue sections in tap water (2x2 min). Air-dried samples were embedded in the aqueous mounting medium Aquatex®. Therefore, the mounting medium was applied to a coverslip using a pasteur pipette and pressed lightly onto the tissue sections to remove potential air bubbles. After curing of the mounting medium, the tissue sections were digitalized via a digital slide scanner and viewed by the software CaseViewer.

2.11.4 Picrosirius Red staining

Picrosirius Red staining (PSR) is one of the most extensively understood and commonly applied histochemical techniques allowing the visualization of extracellular matrix through the selective binding of the dye "Direct Red 80" to distinct collagen fibers (Rittié, 2017). This method was applied to localize and above all to quantify the extent of collagen deposition in both healthy and Ang II-treated CTR and *cmf*KO hearts. Thawed cryosections (s. chapter 2.11.2) were transferred to a staining trough filled with Bouin solution (chapter 2.11.1) and fixed for at least 24 h. Parafilm was additionally used to ensure an airtight seal of the staining trough with the corresponding cover. Following the subsequent airtight incubation of the tissue sections for 1 h in a further staining chamber containing Sirius Red solution (chapter 2.11.1), the excess dye solution was removed using freshly prepared 0.01 N HCl (chapter 2.11.1). For this purpose, the tissue sections were first immersed twice in 0.01 N HCl (2x10 sec), followed by two further washing steps in 0.01 N HCl for 2 min respectively. The sections were then

rinsed in ddH_2O twice for 2 min before the water was subsequently extracted by an ascending ethanol gradient (50%, 70%, 90%) for 4 min respectively. Final dehydration was achieved by immersing the tissue in 100% ethanol for 6 min followed by 100% xylene for 4 min. Finally, the stained cryosections were dried at RT and mounted in non-aqueous DPX using a coverslip as previously described (s. chapter 2.11.3). Dyed cryosections were then digitalized using a digital slide scanner and viewed by the software CaseViewer. The amount of red-labelled collagen was determined as percentage of the total area of the considered heart slice by means of the software ImageJ. Accordingly, collagen deposition was calculated as the mean value of 2-4 heart slices for each cardiac area (section I-VIII, chapter 2.11.2). For the quantification of the total collagen deposition per heart, an average value was obtained from the individual mean values of the defined eight heart areas.

2.11.5 Hematoxylin and eosin staining

For the visualization of cardiac morphology and the determination of CM cross-sectional areas of unchallenged as well as Ang II treated CTR and *cmf*KO hearts, the hematoxylin and eosin (H&E) staining was utilized. While the basic hematoxylin possesses a high affinity for nucleic acids and thus stains the cell nuclei purple - blue, the acidic eosin dye causes a pink labelling of nonspecific cytoplasmic proteins as well as of the extracellular matrix (Fischer et al., 2008). Thawed cryosections (s. chapter 2.11.2) were rehydrated with descending concentrations of ethanol (100%, 90%, 70%, 50%) for 2 min respectively in staining troughs allowing simultaneous staining of 10 slides, and then washed thrice in dH_2O (3x2 min). After immersing the tissue sections for 7 sec in the Harris Haematoxylin solution (s. chapter 2.11.1), excess dye solution was removed by two washing steps in tap water (2x2 min). In order to develop the nuclear staining, the slides were briefly (2 sec) rinsed in 0.1% ammonia solution and transferred into tap water for further 5 min. Afterwards the slides were placed in a staining trough containing Eosin-Y-solution (s. chapter 2.11.1) for 8 min, before the excess dye solution was again purged by two washing steps in tap water (2x5 min). Dehydration of the tissue sections was then conducted through an ascending ethanol gradient (80%, 100%) for 2 min per step, followed by a 5 min incubation in toluene prior to mounting the airdried tissue sections in DPX as previously described (s. chapter 2.11.3). For the evaluation of the CM cross-sectional areas, the stained tissue sections were digitalized using a digital slide scanner and visualized with the software CaseViewer. By employing the zoom function of the application, images of the heart slices in the area of the papillary muscle were generated. By randomly selecting CMs with a centrally located nucleus within this regions, longitudinal CMs at the edge of the heart were excluded from the determination of the cross-sectional areas via ImageJ. Three slides were independently stained per heart, from which a total of 3-5 image sections were analyzed to obtain an average cross-sectional area of 50 CMs.

2.11.6 Immunoflourescence

Immunoflourescence (IF) is a special immunochemical technique employing fluorophore-tagged secondary antibodies to enable the detection and the localization of target proteins within distinct types of tissue and cells (Im et al., 2019). For this purpose, thawed cardiac

cryosections (s. chapter 2.11.2) were rimmed by a hydrophobic barrier pen and rehydrated with DPBS for 5 min before being permeabilized with 0.3% Triton-X-100 for 30 min at RT. After multiple washing steps in DPBS (3x5 min), the tissue sections were incubated between two LED panels and treated with freshly prepared chemical cocktail (Meeker et al., 2021) (s chapter 2.11.1) twice for 45 min each to minimize the autofluorescence of the CMs. Following renewed rinsing of the cardiac cryosections in DPBS (3x5 min), unspecific antibody binding was prevented using a blocking buffer for 1 h at RT. The samples were then incubated with the respective primary antibodies against either collagen I (1:1000) and Ki67 (1:1000) or collagen III (1:500) diluted in blocking buffer (s. chapter 2.11.1) overnight at 4°C. In order to verify the specific binding of the secondary antibodies applied in the later process and thus to exclude possible background staining, a negative control lacking the primary antibody treatment was treated in parallel in the same way. After removing the primary antibody and several washing steps in 0.01% Triton-X-100 in DPBS (5x5 min), the secondary antibodies (Goat anti-Mouse IgG1 Alexa Fluor 488 1:2000; Goat anti-Rabbit Alexa Fluor 555 1:1000; Goat anti-Rabbit Alex Fluor 647 1:1000) and Hoechst 33432 (1:1000) (s. chapter 2.11.1) were applied for 2 h at RT. Finally, the sections were washed again in DPBS (3x5 min) before being embedded with PermaFluor aqueous mounting media as previously described (s. chapter 2.11.3). The slides were stored in the dark at 4°C until imaging with the apotome. ImageJ was used to determine the amount of Ki67 positive nuclei as well as collagen I and III deposition as a percentage of the considered heart area.

The implementation of the IF-staining on isolated, primary CF/CMF cultured *in vitro* on coverslips (s. chapter 2.7.3) demonstrated minor differences compared to the already outlined staining process for tissue sections. The PFA-fixed cells were initially warmed up to RT for 10 min before being permeabilized with 0.3% Trition-X-100 for 15 min. Due to a lack of CF/CMF autofluorescence, the exposure of the cells to the chemical cocktail was not performed. Distinct concentrations of the primary antibodies against either cGKI (1:500) or periostin (1:500) diluted in blocking buffer were employed. Following the treatment with the secondary antibodies and simultaneous staining of the cell nuclei via Hoechst as previously mentioned, the cells were washed thrice in 0.01% Triton-X-100 in DPBS and incubated in either phalloidin-488 (1:500) or phalloidin-647 (1:500) diluted in blocking buffer. The stained cells were washed again thrice in DPBS (3x5 min) before being embedded with PermaFluor. Therefore, a dot of the mounting medium was applied centrally to the microscope slide and the coverslip side containing the CF/CMF was carefully pressed onto the mounting medium to remove potential air bubbles. The visualization of the stained cells was conducted on the Apotome.

2.11.7 Nuclear staining with Hoechst

For the verification of the CMF-specific Cre-recombination, thawed tissue sections (s. chapter 2.11.2) obtained from ROSA$^{mT/mG}$ and double transgenic ROSA$^{mT/mG}$ x *Postn*iCre$^{Tg/+}$ animals were permeabilized with 0.3% Triton in DPBS for 30 min at RT. Following multiple washes in DPBS (3x5 min), the cryosections were embedded in PermaFluor containing 0.1% Hoechst. After allowing the mounting medium to dry for 24 h in the dark, the tissue sections were analyzed at the Apotome using the FITC- ($_{Ex}$ 495 nm / $_{Em}$ 517 nm), DAPI- ($_{Ex}$ 358 nm / $_{Em}$ 463 nm) and Cy3-channels ($_{Ex}$ 549 nm / $_{Em}$ 562 nm).

With the exception of a shorter permeabilization time of 15 min, the identical protocol was applied to stain PFA-fixed primary CF/CMF cell cultures (s. chapter 2.7.3) derived from Ang II treated ROSA$^{mT/mG}$ and double transgenic ROSA$^{mT/mG}$ x *Postn*iCre$^{Tg/+}$ mice.

2.11.8 TUNEL-Staining

The commonly accepted terminal deoxynucleotidyl transferase-mediated deoxyuridine triphosphate (dUTP) nick end labeling (TUNEL)-assay is suitable for the detection of apoptotic nuclei in cardiac cryosections (Mirzayans and Murray, 2020). In this context, the terminal deoxynucleotidyl transferase catalyzes the addition of TMR-labelled dUTPs to the free 3' hydroxyl termini of DNA apoptotic fragments (Kyrylkova et al., 2012, Gavrieli et al., 1992). By employing this assay, the amount of apoptotic CMs were quantified in heart cryosections (s. chapter 2.11.2) derived from CTR and *cmf*KO mice upon chronic Ang II exposure *in vivo*. Bevor initiating the actual TUNEL-staining, an IF-staining according to the protocol described in chapter 2.11.6 was performed to visualize CMs by applying a primary antibody against troponin I (1:100) diluted in blocking buffer. Following the incubation of the cardiac cryosection with the secondary antibody (Goat anti-rabbit Alexa Fluor 488; 1:1000) and Hoechst (1:1000) diluted in blocking buffer, the samples were washed thrice in DPBS (3x5 min). Remained DPBS on the microscope slides was carefully removed by precision wipes. TUNEL-staining was conducted in accordance with the manufacturer's instructions. To validate the functionality of the staining, a negative and positive control were included for each staining process. For the latter control a tissue section was exposed to 50 µl DNase I (10 000 units) at RT for 10 min. With the exception of the negative control, which was only treated with 50 µl TUNEL label solution, all tissue slices were loaded with 50 µl freshly prepared TUNEL-reaction solution (s. chapter 2.11.1). All samples were incubated in a humid dyeing chamber for 1 h at 37°C in the dark, before being washed again thrice in DPBS (3x5 min). Air-dried, stained cardiac slices were embedded in PermaFluor as already described (s. chapter 2.11.3) and visualized via an Apotome. Quantification of TUNEL-positive CMs was expressed as a percentage of the total amount of CM cell nuclei counted in the respective image section using ImageJ.

2.12 Statistics

The software GraphPad Prism 9.4.1 was applied to conduct the statistical analysis of the data. Within the present work, all data are expressed as mean values + standard error of mean (SEM). By employing the Shapiro-Wilk or Kolmogorov-Smirnov test, the normal Gaussian distribution of the data was confirmed. The unpaired student t-test ($\alpha = 0.05$) was applied for the comparison of two groups (CTR *versus cmf*KO) in the case of normal distributed data. As non-parametric test the Mann-Whitney *U* test was performed. To compare > 2 groups (CTR +TAM; CTR +TAM+Ang II; *cmf*KO +TAM; *cmf*KO +TAM+Ang II), the two-way ANOVA followed by a Šídák's, or Tukey's multiple comparison test was performed, while a Kruskal-Wallis test followed by the Dunn test for multiple comparisons was conducted as a non-parametric test. For the assessment of the survival rate, the log-rank test (Mantel-Cox test) was employed. A more detailed description of the underlying statistics for each experiment is provided in the figure legends. P-values < 0.05 were defined as statically significant with *p < 0.05, **p < 0.01

and ***p < 0.001 representing differences between the genotypes (CTR *versus cmf*KO) and †p < 0.05; §p < 0.01; #p < 0.001 indicating difference between distinct treatments (+TAM *versus* +TAM+Ang II) within the same genotype.

3 Results

3.1 Verification of the cell specific *Postn*iCre$^{Tg/+}$-recombinase expression

In order to investigate the putative function of the CMF-specific cGMP signaling cascade in Ang II-mediated cardiac remodeling, the transgenic *Postn*iCre$^{Tg/+}$ mouse line was employed (s. chapter 2.4.2.2). This mouse strain provides a temporally controlled expression of a TAM-inducible Cre recombinase controlled by the *Postn*-promotor (Kaur et al., 2016). Since the acquisition of *Postn* expression strongly correlated with an activated CF phenotype that occurs with pathophysiological stimulations such as chronic Ang II exposure or MI, this transgenic mouse allows the selective expression of Cre recombinase in CMFs (Kanisicak et al., 2016, Kaur et al., 2016).

To initially validate the cell specificity as well as inducibility of the Cre-recombinase activity under patho-/physiological conditions, transgenic *Postn*iCre$^{Tg/+}$ mice were intercrossed with the global double-fluorescent ROSA$^{mT/mG}$ Cre reporter mouse line yielding double transgenic ROSA$^{mT/mG}$ x *Postn*iCre$^{Tg/+}$ mice and ROSA$^{mT/mG}$ control littermates. By employing this global double fluorescent Cre-reporter strain, evidence of successful Cre-mediated recombination was detectable by the excision of the floxed DNA sequence encoding for a membrane-targeted red fluorescent mT protein, consequently leading to the expression of membrane-targeted green fluorescent mG protein (s. chapter 2.4.2.3) (Muzumdar et al., 2007). Activation of the Cre recombinase under physiological conditions was achieved via i.p. application of TAM (1 mg/d) on five consecutive days followed by the assessment of Cre-mediated recombination four weeks later (+TAM-treatment group; s. chapter 2.6.7). Consistent with the underlying literature indicating that less than 1% of the interstitial cells (i.e., the non-CM cell fraction of the heart) in healthy tissue expressed *Postn*, both genotypes manifested ubiquitous expression of the red fluorescent mT protein in the unchallenged myocardium as well as in distinct organs including aorta, lung, spleen, liver, and kidney (s. Figure 12A; Figure 33A) (Kanisicak et al., 2016). To further evaluate Cre recombinase expression under pathophysiological conditions, Ang II-mediated cardiac remodeling was induced via subcutaneously implanted osmotic minipumps releasing Ang II (2 µg/g/d) over 28 days. TAM-mediated activation of the Cre recombinase was initiated one day postoperatively with one i.p. injection of TAM per day for five consecutive days (+TAM + Ang II-treatment; s. chapter 2.6.7). In response to the prolonged Ang II exposure, expression of the green fluorescent mG protein was detectable exclusively in CMFs in fibrotic heart areas identified by PSR, while CMs and non-fibrotic areas revealed a persistent expression of the red fluorescent mT protein in double transgenic animals (s. Figure 12B). In turn, only the expression of the red fluorescent mT protein was detected in remodeled as well as unchallenged heart regions of the corresponding Ang II treated control group (ROSA$^{mT/mG}$) (s. Figure 12B).

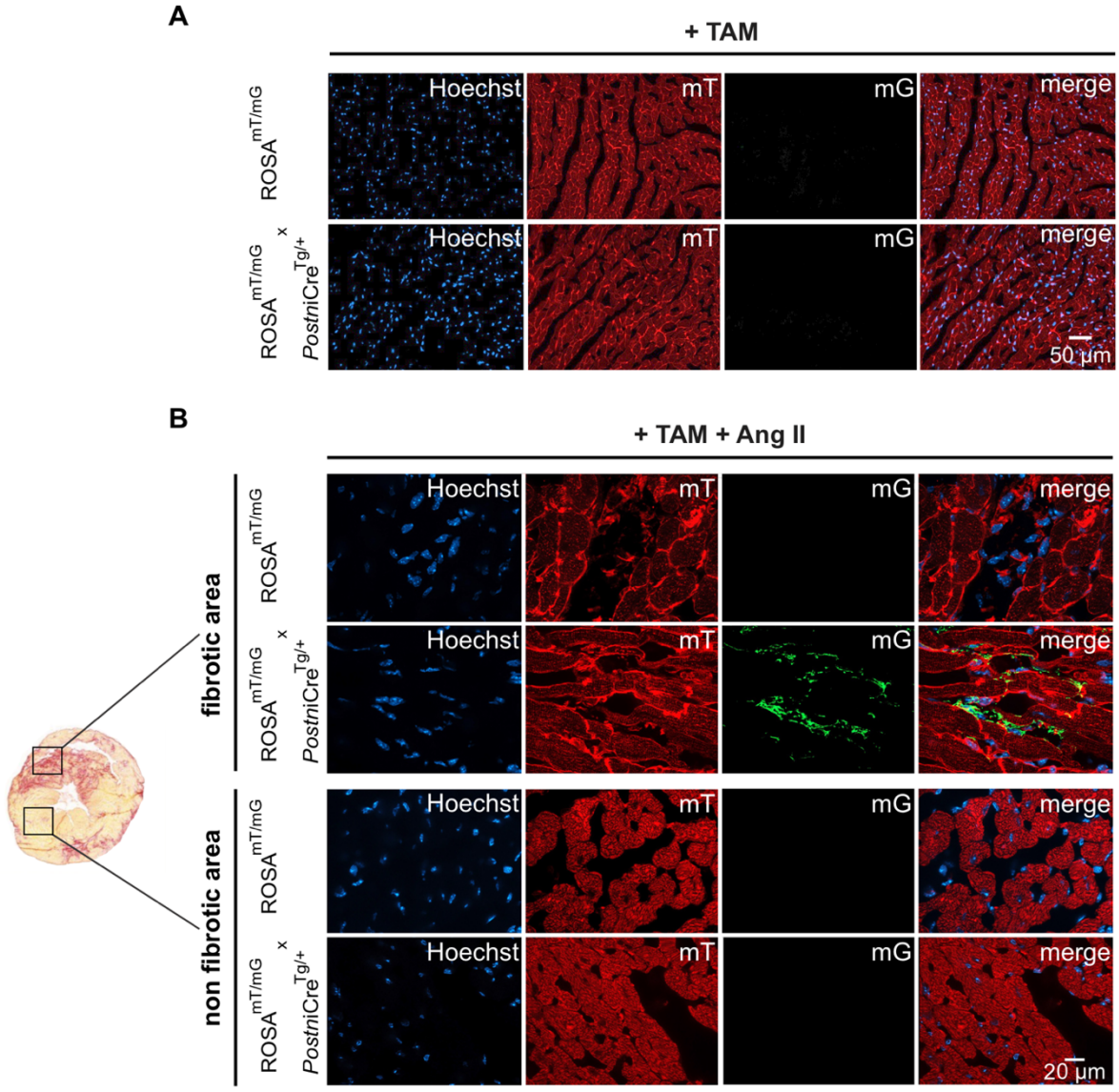

Figure 12: TAM-induced CMF-specific *Postni*Cre$^{Tg/+}$ recombination after Ang II treatment *in vivo*
Verification of cell-specific *Postni*Cre$^{Tg/+}$-mediated recombination was conducted by intercrossing the respective mouse line with the global double-fluorescent ROSA$^{mT/mG}$ Cre reporter strain. **(A)** Under physiological conditions double transgenic ROSA$^{mT/mG}$ x *Postni*Cre$^{Tg/+}$ animals undergoing TAM treatment *in vivo* revealed ubiquitous expression of the red fluorescent mT protein in unchallenged hearts. Cardiac cryosections obtained from ROSA$^{mT/mG}$ served as control. n=3 heart slices from N=3 animals per genotype. **(B)** Following TAM and chronic Ang II exposure *in vivo*, cardiac heart sections of both genotypes were stained with PSR to identify fibrotic areas. Subsequent analysis of fibrotic areas derived from double transgenic animals confirmed Cre-mediated recombination of the two loxP-sites surrounding the DNA-sequence encoding the mT protein, ultimately leading to the expression of the green fluorescent mG proteins in cells localized in the interstitial space of CMs. Importantly, non-fibrotic areas and CMs retained expression of the red fluorescent mT protein. Cardiac cryosections obtained from ROSA$^{mT/mG}$ revealed ubiquitous expression of the red fluorescent mT-protein and served as control. n=3 heart slices from N=3 animals per genotype. **(A-B)** Cell nuclei (blue) were visualized by Hoechst.

Analysis of other organ systems obtained from Ang II-treated double transgenic animals, revealed a persistent expression of the red fluorescent mT protein in the aorta, spleen, liver and kidney, with the exception of the lungs, which exhibited isolated foci of green fluorescent mG protein expression (s. Figure 13A). In ROSA$^{mT/mG}$ mice expression of the red fluorescent mT protein was still evident in all organs analyzed.

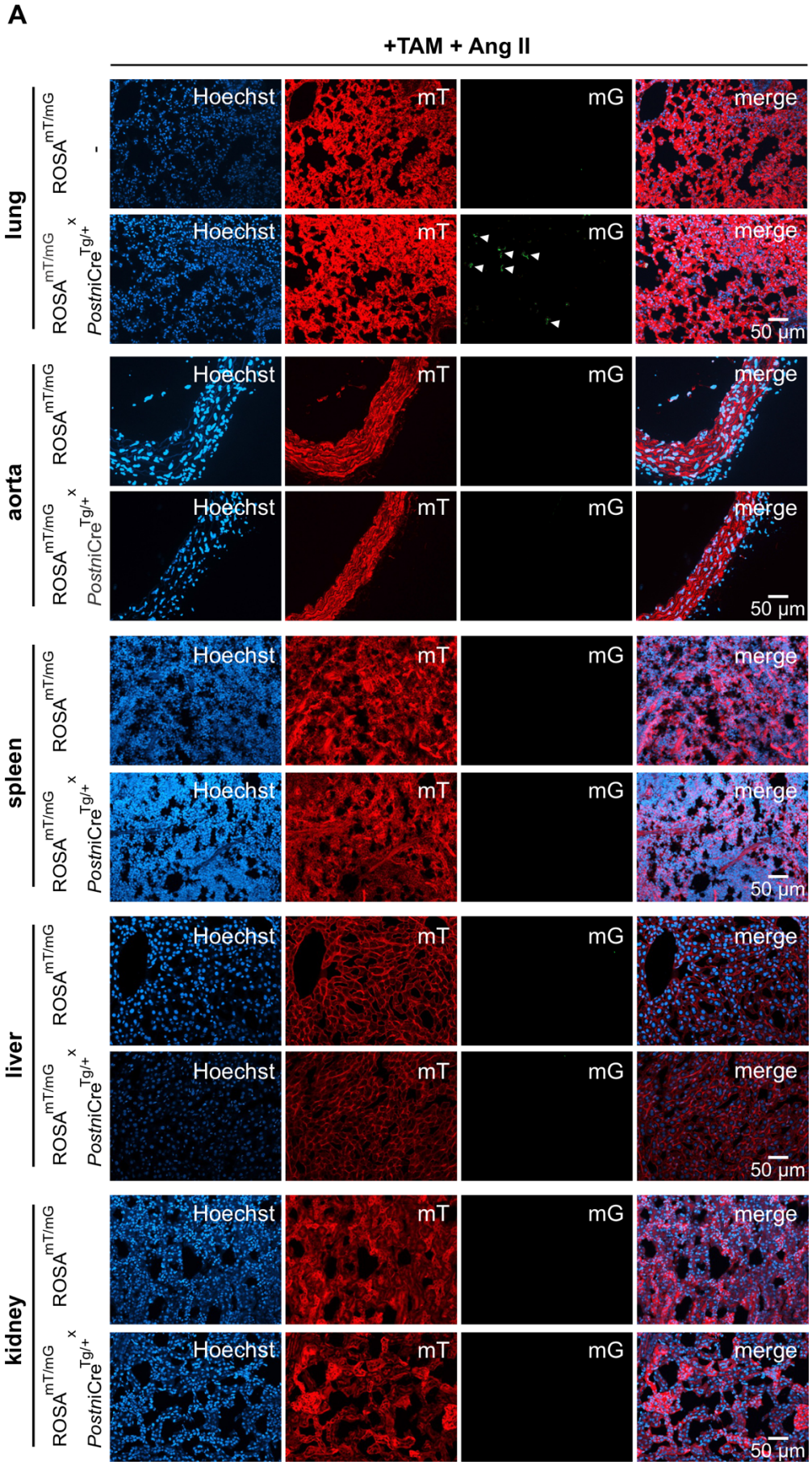

Figure 13: Extensive screening of tissue-specific *Postn*iCre$^{Tg/+}$-mediated recombination following Ang II treatment

Representative fluorescence images of distinct tissue cryosections obtained from ROSA$^{mT/mG}$ and double transgenic ROSA$^{mT/mG}$ x *Postn*iCre$^{Tg/+}$ animals. Following Ang II exposure *in vivo*, TAM-mediated activation of the Cre recombinase was observed in a minority of cells in the lung of double transgenic animals, as indicated by the expression of the green fluorescent mG protein (white arrows). Cryosections of other organs studied showed sustained expression of the red fluorescent mT protein. Respective cryosections of organs obtained from ROSA$^{mT/mG}$ revealed ubiquitous expression of the red fluorescent mT-protein and served as control. Images from n=3 tissue cryosections per organ from N=3 animals per genotype. Cell nuclei (blue) were stained throughout with Hoechst.

Aiming to verify these results at the cellular level, primary CF/CMFs were isolated from Ang II treated double transgenic ROSA$^{mT/mG}$ x *Postn*iCre$^{Tg/+}$ as well as from ROSA$^{mT/mG}$ control mice and cultured for five days *in vitro* before being fixed and stained with Hoechst for the visualization of cell nuclei (s. chapter 2.7.3). While ROSA$^{mT/mG}$-derived primary cells exhibited exclusively the expression of the red fluorescent mT protein, a mixed cell culture was obtained from double transgenic hearts. The latter cell cultures consisted of *in vivo* stimulated CMFs characterized by the expression of mG and additional CF/CMFs exhibiting solely the expression of mT (s. Figure 14A). Overall, these findings demonstrated a CMF-specific expression of the Cre recombinase in remodeled hearts, indicating the suitability of this mouse strain to investigate the function of cGMP/cGKI in CMFs during the course of Ang II-induced cardiac remodeling.

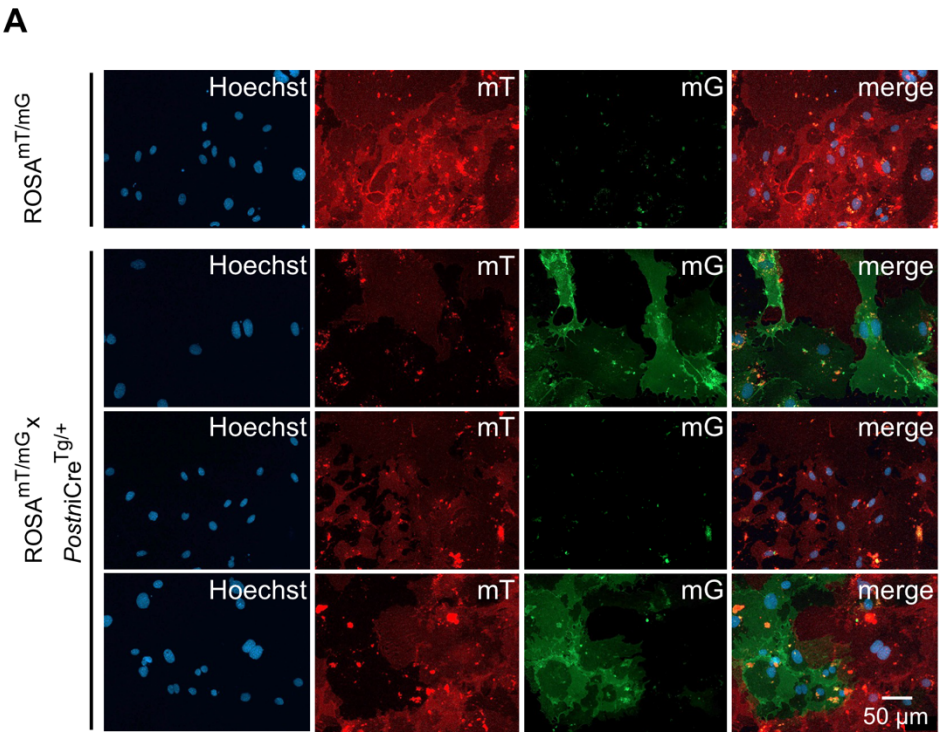

Figure 14: CMF-specific *Postn*iCre$^{Tg/+}$ recombination following TAM and Ang II treatment *in vivo*
(A) Representative fluorescent images obtained from primary, cultured CF/CMFs (div 5) isolated from global double fluorescent ROSA$^{mT/mG}$ and double transgenic ROSA$^{mT/mG}$ x *Postn*iCre$^{Tg/+}$ mice receiving TAM and Ang II *in vivo*. CF/CMF cultures derived from the Cre-reporter strain exhibited exclusively expression of the red fluorescent mT protein (top row). In contrast, CF/CMFs harvested from double transgenic hearts revealed a mixed cell culture containing *in vivo* activated CMFs expressing the green fluorescent mG protein as well as additional CF/CMFs expressing the red fluorescent mT protein (row two to four). Analysis of N=3 cell cultures per genotype. Cell nuclei (blue) were visualized by Hoechst.

3.2 Validation of the CMF-specific cGKI KO upon *Postni*Cre$^{Tg/+}$ mediated recombination

By crossbreeding the previously validated transgenic *Postn*iCre$^{Tg/+}$ mouse line with a heterozygous floxed cGKI$^{fl/+}$ mouse strain (s. chapter 2.4.2.1), both CMF-specific cGKI-deficient animals (*Postn*iCre$^{Tg/+}$ x cGKI$^{fl/fl}$; *cmf*KO) as well as corresponding littermate controls (*Postn*iCre$^{Tg/+}$ x cGKI$^{+/+}$; CTR) were generated. Application of the validated Cre/loxP system enabled a spatio-temporally controlled excision of the loxP-flanked exon 10 of the *Prkg1* gene upon TAM injection, eventually leading to the formation of the KO allele in *cmf*KO mice. The efficient cell-specific cGKI ablation in primary CF/CMFs was provided via genomic PCR analysis utilizing *cmf*KO hearts after TAM and Ang II challenge *in vivo*. Therefore, DNA samples of distinct organs (brain, liver, kidney, spleen, lung, aorta) as well as primary CF/CMFs were isolated from both genotypes. Effective Cre-mediated excision of the lox-P flanked sequences resulted in formation of the cGKI KO allele in primary CF/CMFs obtained from *cmf*KO hearts (s. Figure 15B). Apart from a reduced Cre recombination efficiency in the lung, only the expression of the floxed allele could be detected in all other organs of *cmf*KO animals. As expected, only the cGKI wild-type allele was evident in all DNA samples from CTR organs (s. Figure 15A-B). Additionally, verification of the CMF-specific cGKI ablation in *cmf*KO mice was performed at the protein level using immunoblot analysis. By employing a previously validated cGKI primary antibody capable of detecting cGKI trough a common protein region, present in cGKIα and cGKIβ (Längst et al., 2021), immunoblots showed significantly reduced cGKI abundance in protein lysates isolated from primary CF/CMFs derived from Ang II-treated *cmf*KO animals compared with CTR-derived CF/CMF lysates. Protein samples obtained from *αMHC*-Cre$^{Tg/+}$ x cGKI$^{fl/fl}$ mice, lacking cGKI specifically in CMs (s. chapter 2.4.2.4), served as negative control (s. Figure 15C-D). The CM-specific ablation of cGKI by the latter employed *αMHC*-Cre$^{Tg/+}$, is consistent with previous studies in which, for example, the BK was specifically ablated in CMs (Frankenreiter et al., 2017). Next, the expression pattern of both periostin and cGKI were explored in fibrotic regions of remodeled CTR and *cmf*KO hearts following TAM and Ang II treatment *in vivo*. In serial heart sections, periostin expression was mapped within fibrotic myocardial regions identified by PSR in both genotypes. However, while in CTR heart slices cGKI expression correlated with fibrotic areas and *Postn*$^{+}$ cells, cGKI expression levels were substantially lower in myofibroblast-rich cardiac areas of *cmf*KO hearts (s. Figure 15E). Corroborating these findings, periostin was detected by immunofluorescence in isolated CF/CMF cell cultures obtained from CTR and *cmf*KO mice following chronic Ang II exposure *in vivo*. Again, analysis of CTR-derived CF/CMFs cultures exhibited a pronounced cGKI expression (s. Figure 15F). In contrast, a mixed cell culture was obtained from Ang II-treated *cmf*KO hearts. *In vivo* activated CMFs lacking cGKI expression were observed side by side with CF/CMFs with persistent expression of the kinase protein (s. Figure 15F).

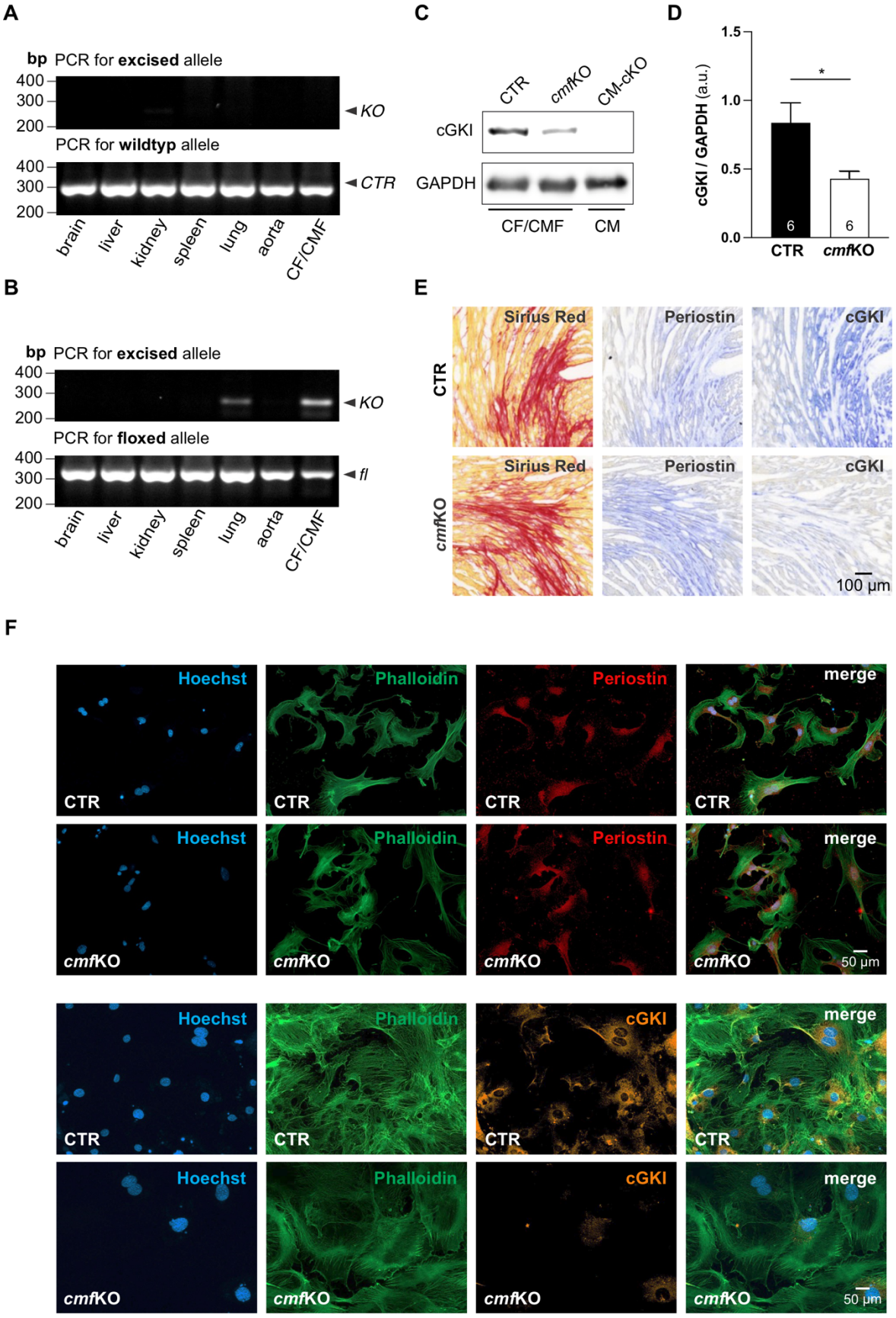

Figure 15: Characterization of the effective cGKI ablation in CMFs
DNA samples obtained from the indicated organs as well as from primary CF/CMFs derived from CTR and *cmf*KO mice upon TAM and Ang II exposure *in vivo* were amplified via PCR and separated in a 2% agarose gel. (**A**) While Cre-mediated recombination was absent in all samples obtained from CTR mice

as indicated by the ubiquitous detection of the wildtype allele ([+]; 284 bp), employment of allele-specific primers (s. chapter 2.8) revealed the (**B**) conversion of the lox-P flanked *Prkg1* allele ([fl]; 338 bp) to the KO allele ([-]; 250 bp) in primary CF/CMFs derived from *cmf*KO mice (Wegener et al., 2002, Lukowski et al., 2008). Furthermore, Cre-mediated recombination was evident to a lesser extent in the lungs, whereas all other organs exhibited the floxed allele ([fl]; 338 bp) exclusively. (**C**) Representative immunoblot of CF/CMF protein lysates derived from CTR and *cmf*KO mice upon prolonged hypertrophic stimulation with Ang II *in vivo* revealed a specific band at the indicated molecular weight of cGKI (78 kDa). CM protein lysates derived from mice lacking cGKI specifically in CMs were used as negative control. (**D**) Densitometrical quantification using ImageJ confirmed significant reduced cGKI expression levels in *cmf*KO samples in comparison to CF/CMFs obtained from CTR animals (CTR = 0.84 ± 0.15; *cmf*KO = 0.43 ± 0.05). N=6 CF/CMF protein lysates obtained per genotype. CMs samples were provided by M. Sc. Katharina Paulus (Department of Experimental Pharmacology, University of Tübingen). Western Blot was performed by Lena Ullemeyer (Department of Experimental Pharmacology, University of Tübingen) as part of her Master's thesis. (**E**) Representative PSR staining of heart slices isolated from Ang II treated CTR and *cmf*KO mice labelling fibrotic heart areas. Serial heart sections were stained by an AP-based method (s. chapter 2.11.3) against either periostin or cGKI. While cGKI expression overlapped with fibrotic and *Postn*$^{+}$ cardiac regions in CTR heart slices, *cmf*KO mice exhibited a massively reduced cGKI levels in heart areas enriched in CMFs. n=3 cryosections from N=3 animals per genotype. (**F**) Representative fluorescent images of primary CF/CMF cultures obtained from TAM and Ang II treated CTR and *cmf*KO animals. Periostin expression was evident in CF/CMF cell cultures (div 4) derived from both genotypes. Furthermore, CF/CMF cultures (div 6) isolated from CTR animals demonstrated prominent cGKI expression, while cGKI positive CF/CMFs harvested from *cmf*KO mutants were less frequently observed. Analysis of N=3-5 cell cultures per genotype. Cell nuclei (blue) were visualized by Hoechst. Statistical analyses: Unpaired student t-test (**D**).

3.3 BP independent higher susceptibility of *cmf*KO hearts exposed to Ang II

Subsequently, the consequences of CMF-specific cGKI depletion on Ang II-mediated long-term outcome, particularly in terms of survival, was explored. For this purpose, experimental animals undergoing TAM-mediated Cre-recombination both in the absence or presence of sustained Ang II stimulation were monitored and survival was estimated by plotting the data using the Kaplan-Meier method. While all experimental animals survived TAM treatment regardless of the genotype, Ang II-induced lethality was higher in both genotypes. In this context, *cmf*KO mice exhibited a significantly smaller overall survival in response to the hypertrophic and hypertensive stimulation with Ang II compared to their respective age- and littermate-matched *cmf*KO animals receiving TAM only. In total, sudden death occurred in 12 of 42 *cmf*KO mice upon neurohumoral stimulation. Besides, TAM-treated CTR animals displayed a slightly worse survival outcome in the presence of Ang II, although this trend did not reach a statistical difference compared to the corresponding CTR animals receiving TAM only (s. Figure 16A). In this context, 6 out of 39 CTR mice died in response to chronic Ang II exposure. Although the Ang II-mediated effect was clearly more prominent in the *cmf*KO group, the apparent survival disparity between genotypes failed to reach statistical significance.

Overall, these results suggest a slightly increased susceptibility of Ang II-treated CMF-specific conditional cGKI KO compared with the corresponding CTR mice.

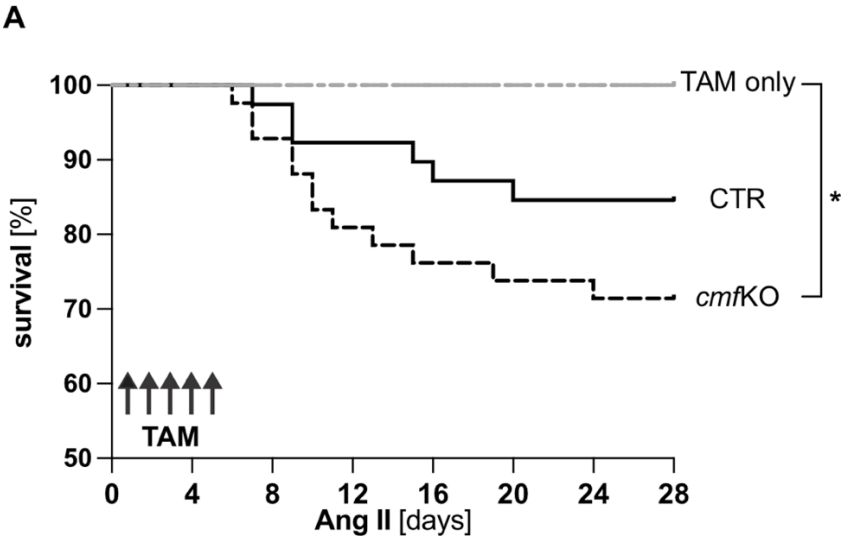

Figure 16: Higher vulnerability of *cmf*KO mice receiving Ang II
Survival rate of CTR and *cmf*KO animals upon distinct *in vivo* treatments plotted as Kaplan Meier curve. All animals receiving TAM exclusively survived the entire experimental period (CTR, N=13; *cmf*KO, N=12). TAM-treated CTR animals had a survival rate of 85% in the presence of Ang II, with no statistical difference compared to the other treatment groups (CTR, N=39). In turn, TAM-treated *cmf*KO mice presented a significantly decreased overall survival of 71% following chronic Ang II exposure *versus* the corresponding *cmf*KO group treated with TAM alone (*cmf*KO, N=42). Statistical analyses: Log-rank test was used to compare the survival distributions of the samples.

Representing a major effector molecule of the RAAS, Ang II not only affects arterial BP but also promotes cardiac remodeling and other aspects of cardiovascular diseases (Lemarié and Schiffrin, 2010). These characteristics are attributable to both its acute vasoconstrictive effects causing hypertension, and its direct modulation of CMs and CFs promoting cardiac hypertrophy and fibrosis (Sadoshima and Izumo, 1993, Crabos et al., 1994). Highlighting the importance of the NO-cGMP-cGKI signaling cascade in the regulation of BP, genetically modified mice globally lacking either NO-GC or cGKI developed hypertension (Pfeifer et al., 1998, Friebe et al., 2007). Considering the relevance of both axes on BP together with the lack of evidence for the involvement of the CMF-specific cGMP signaling cascade in BP-regulation, telemetric BP-measurements were performed. The purpose of these experiments was to find out to what extent the high vulnerability of *cmf*KO hearts is attributable to possible differences in hemodynamic parameters and their abnormal regulation in this model. For this purpose, radio-transmitters were implanted in CTR and *cmf*KO mice, providing a precise and continuous measure of systolic, diastolic, and mean arterial blood pressure (MAP) in freely moving mice under patho-/physiological conditions (s. chapter 2.6.5).

3.3.1 Telemetric BP measurements under physiological conditions

Following the implantation of the BP transmitter, the mice underwent a seven-day recovery period before measurements to monitor basal BP were started (s. chapter 2.6.7). For the acquisition of the data, values were recorded at 15 min intervals for a duration of 5 min for three consecutive days. Evaluation of systolic as well as diastolic BP and MAP yielded almost equally values for both genotypes, irrespective of the daytime (s. Figure 17A-C). The pulse pressure (PP) expressed as the difference between systolic and diastolic BP, is known to be

an major predictor of cardiovascular complications and as well revealed no genotype-specific differences (s. Figure 17D) (Benetos et al., 1997, Assmann et al., 2005). Moreover, both genotypes exhibited physiological heart rate values that were in the expected range of 550 to 600 bpm for conscious mice and they showed comparable activity patterns (s. Figure 17E-F) (Van Vliet et al., 2003, Ho et al., 2011, Kramer et al., 1993).

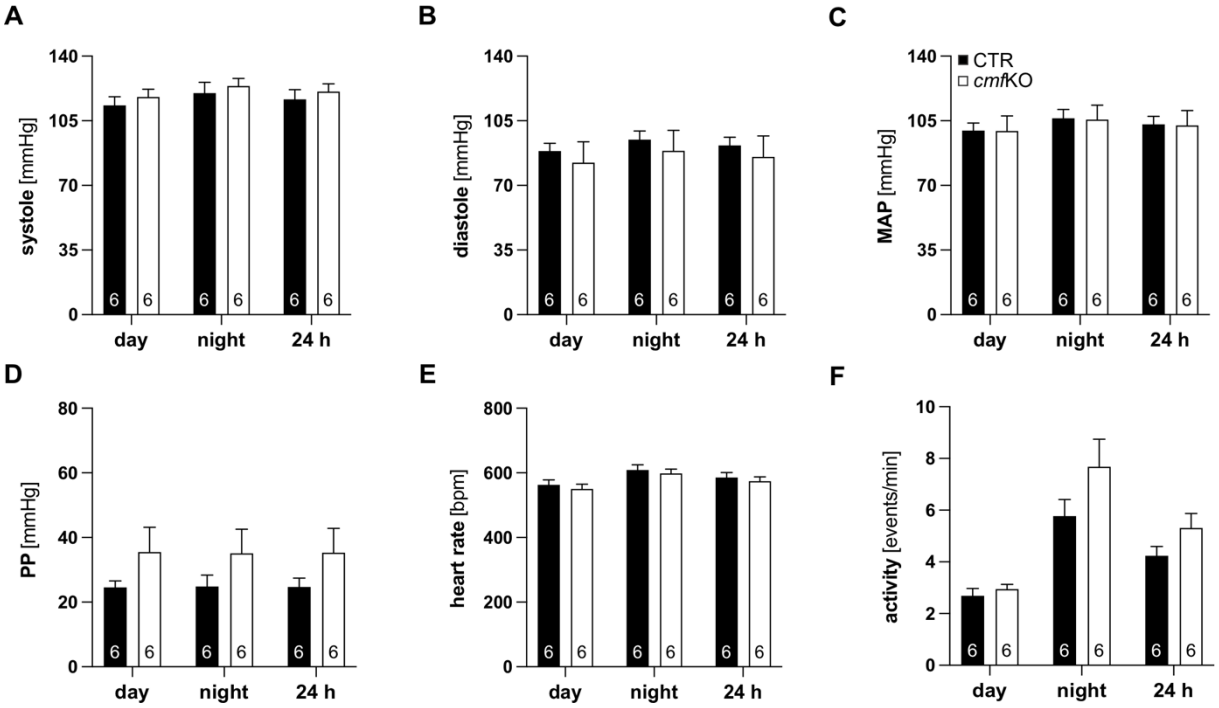

Figure 17: Exclusion of genotype-related BP differences under physiological conditions
Telemetric BP recordings of freely moving CTR and *cmf*KO mice revealed comparable (**A**) systolic BP (24 h: CTR = 116.66 ± 5.21 mmHg; *cmf*KO = 120.83 ± 4.20 mmHg), (**B**) diastolic BP (24 h: CTR = 91.66 ± 4.45 mmHg; *cmf*KO = 85.48 ± 11.24 mmHg) and concomitant (**C**) MAP values (24 h: CTR = 103.02 ± 4.40 mmHg; *cmf*KO = 102.49 ± 8.01 mmHg) prior to TAM-mediated Cre-recombination and Ang II infusion. Moreover, no genotype-related differences in (**D**) PP (24 h: CTR = 24.71 ± 2.71 mmHg; *cmf*KO = 35.31 ± 7.54 mmHg), as well as in (**E**) heart rate (24 h: CTR = 585.76 ± 15.42 bpm; *cmf*KO = 574.22 ± 13.32 bpm) and (**F**) activity pattern (24 h: CTR = 4.24 ± 0.36 events/min; *cmf*KO = 574.22 ± 13.32 events/min) were found during the day and night period. Depicted are the mean ± SEM for the day-, nighttime and the averaged 24 h values of N = 6 mice per genotype. Statistical analyses: Multiple unpaired t-test corrected for multiple comparison using the Holm-Šídák method (**A**, **B**, **C**, **E**), multiple Mann-Whitney test corrected for multiple comparison using the Holm-Šídák method (**D**, **F**). All bar diagrams presented as means + SEM. These data were acquired together with M. Sc. Pharm. Clement Kabagema-Bilan (Department of Pharmacology, Toxicology and Clinical Pharmacy, Institute of Pharmacy, University of Tübingen). Mr. Kabagema-Bilan carried out the implantation of the BP transmitter.

3.3.2 Loss of cGKI in CMFs does not alter the Ang II-induced increases in BP

Upon acquisition of basal BP readings, Ang II-mediated BP alterations in CTR and *cmf*KO mice were evaluated in the follow-up experiment. For this purpose, measurements were immediately initiated after the implantation of osmotic minipumps for the first seven days of Ang II treatment. In order to activate TAM-inducible Cre recombinase, experimental animals received a daily injection of TAM starting one day postoperatively for five consecutive days (s. chapter 2.6.7). The time-dependent progression of the MAP in response to chronic Ang II exposure was slightly slower in *cmf*KO mice compared to CTR animals, but ultimately of the

same magnitude. (s. Figure 18A). Consideration of the Ang II-mediated total BP rise, composed of the difference between basal BP and the BP values obtained after seven days of Ang II infusion, yielded no genotype-related differences for the MAP, systolic- and diastolic BP as well as PP (s. Figure 18B). Correspondingly, all investigated parameters showed nearly identical results for *cmf*KO and CTR mice for the day- and nighttime as well as for the averaged 24 h values during the seven-day neurohumoral stimulation with Ang II (s. Figure 18C-H).

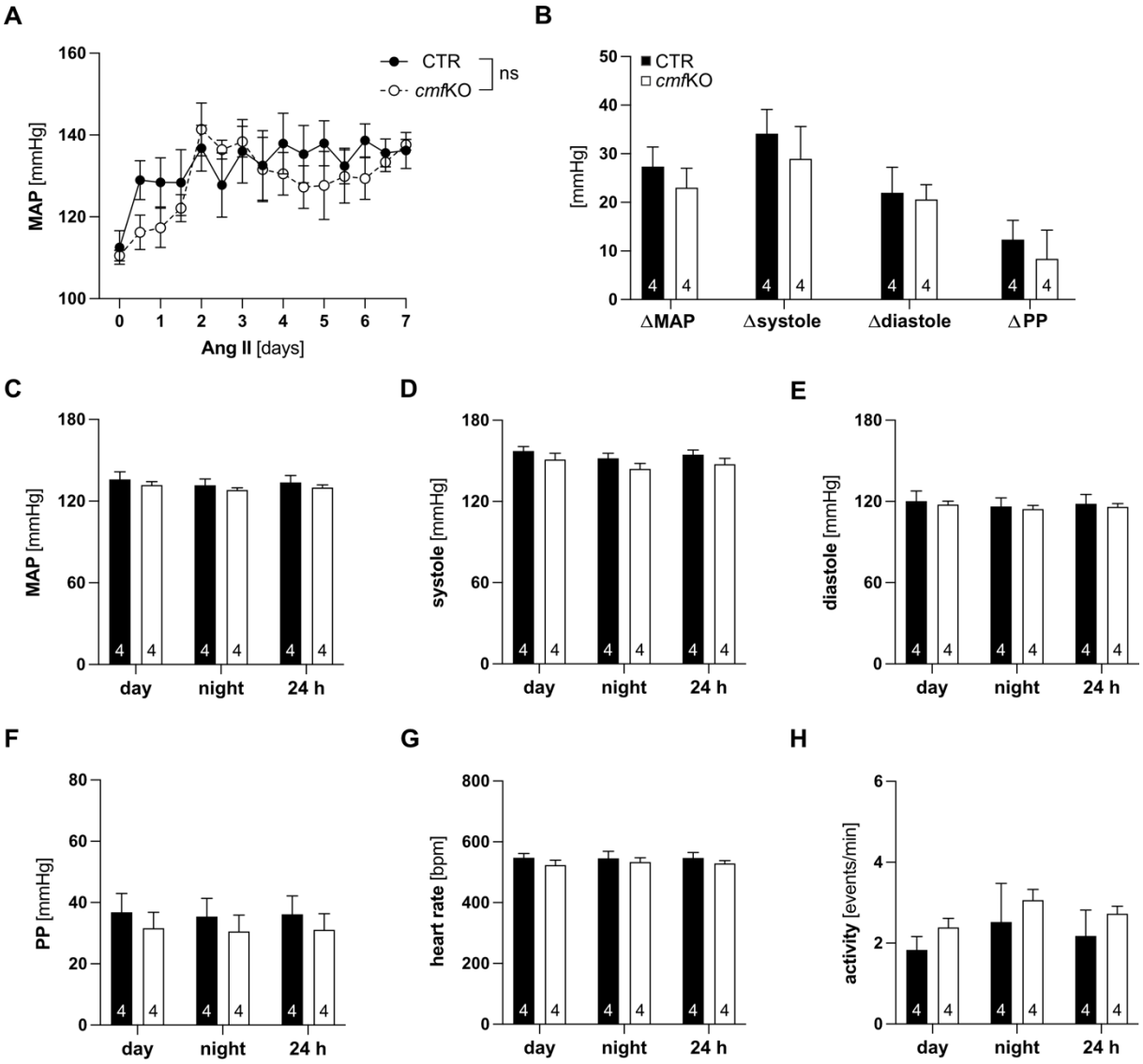

Figure 18: Comprehensive evaluation of Ang II-mediated BP-alterations
Telemetric BP measurements in freely moving TAM-treated CTR and *cmf*KO mice during sustained Ang II infusion. (**A**) Time course of Ang II-induced MAP changes exhibited no genotype-related differences within the first seven days of Ang II treatment (day 1-7). The mean values obtained from the last 24 h before the implantation of the osmotic minipump were plotted as day 0. Depicted are the mean + SEM of the day- (numerical values plotted on the X-axis) and the nighttime values (data points are located between the numerical values along the X-axis) of N=4 mice per genotype.
(**B**) Absolut increase in MAP (CTR = 27.37 ± 4.04 mmHg; *cmf*KO = 23.02 ± 4.00 mmHg), systolic BP (CTR = 34.00 ± 5.00 mmHg; *cmf*KO = 28.87 ± 6.61 mmHg), diastolic BP (CTR = 21.99 ± 5.25 mmHg; *cmf*KO = 20.61 ± 3.05 mmHg) as well as PP (CTR = 12.18 ± 3.95 mmHg; *cmf*KO = 8.28 ± 5.83 mmHg) expressed as difference between basal and the specific values obtained after seven days of Ang II infusion exhibited equivalent outcomes for both genotypes. (**C-H**) Day, night and averaged 24 h values resulting from all seven days of Ang II treatment were provided. Irrespective from the daytime neither the MAP (24 h: CTR = 133.80 ± 5.06 mmHg; *cmf*KO = 129.94 ± 2.06mmHg), systolic BP (24 h:

CTR = 154.60 ± 3.43 mmHg; *cmf*KO = 147.56 ± 4.28mmHg), diastolic BP (24 h: CTR = 118.27 ± 6.85 mmHg; *cmf*KO = 116.03 ± 2.47mmHg) nor the PP (24 h: CTR = 36.15 ± 6.01 mmHg; *cmf*KO = 31.11 ± 5.22 mmHg), heart rate (24 h: CTR = 546.71 ± 18.51 bpm; *cmf*KO = 528.87 ± 9.21 bpm) or activity patterns (24 h: CTR = 2.2 ± 0.64 events/min; *cmf*KO = 2.73 ± 0.19 events/min) were statistically different between genotypes. Statistical analyses: Two-way ANOVA followed by Šídák's multiple comparisons test **(A),** multiple unpaired t-test corrected for multiple comparison using the Holm-Šídák method (**B-G**), multiple Mann-Whitney test corrected for multiple comparison using the Holm-Šídák method (**H**). All bar diagrams presented as means + SEM with CTR: N=4, *cmf*KO: N=4. These data were acquired together with M. Sc. Pharm. Clement Kabagema-Bilan (Department of Pharmacology, Toxicology and Clinical Pharmacy, Institute of Pharmacy, University of Tübingen), who carried out the implantation of the telemetric devices.

Taken together, these results suggest that a disruption of the cGMP/cGKI-signaling cascade in CMFs exerts no effect on either physiological BP regulation or Ang II-mediated elevation of BP. Given this evidence, the augmentation of afterload was ruled out as an underlying explanation for the higher vulnerability of *cmf*KO hearts. Hence, subsequent work focused on potential local influences of Ang II on cardiac remodeling.

3.4 Sustained Ang II stimulation elicited greater cardiac remodeling in *cmf*KO mutants compared with CTR mice

As already outlined, Ang II plays a crucial role in the development of myocardial remodeling by its direct action on CMs and CFs, which may explain the enhanced susceptibility of *cmf*KO hearts (Crabos et al., 1994, Sadoshima and Izumo, 1993). To confirm this hypothesis, the extent of myocardial fibrosis and hypertrophy as well as CM cell death in response to chronic Ang II exposure were evaluated. For this purpose, hearts of both genotypes were isolated following TAM and hypertrophic stimulation with Ang II *in vivo* and divided into eight equidistant heart regions extending from the apex (section I) to the base (section VIII) of the heart (s. chapter 2.11.2) (s. Figure 19A). To exclude pre-existing genotype related differences under physiological conditions, unchallenged hearts were isolated after TAM-mediated Cre-recombination *in vivo*.

3.4.1 Increased Ang II-mediated collagen deposition in *cmf*KO mutants compared to CTR mice

In order to assess the amount of fibrosis under physiological condition, heart slices obtained from all eight sections of TAM-treated CTR and *cmf*KO mice were stained with PSR, which colors collagen fibers of the connective tissue in red (Figure 19B) (Rittié, 2017). Upon quantification, the amount of fibrosis was expressed as a percentage of the total area of the respective heart section analyzed. Unchallenged hearts exhibited comparable levels of fibrosis in each cardiac region (Figure 19C), ultimately translating into no genotype-related differences in terms of overall myocardial fibrosis (Figure 19D).

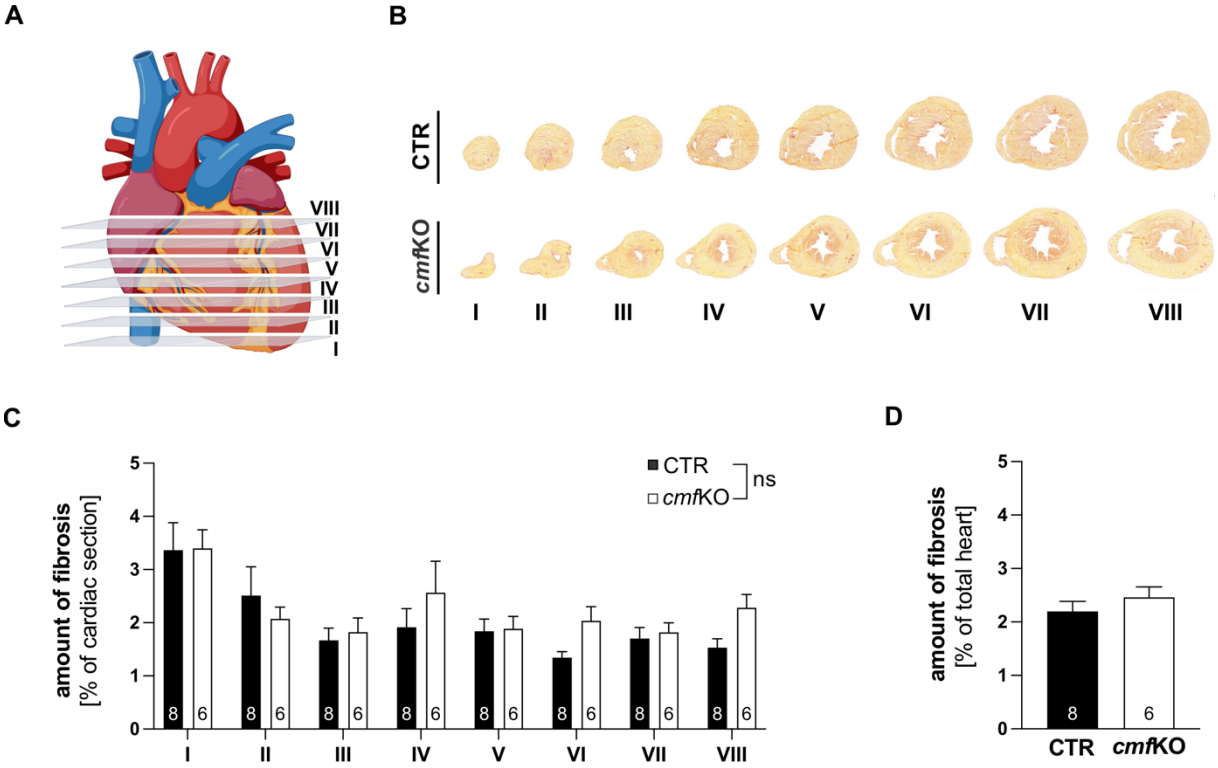

Figure 19: Similar amount of cardiac fibrosis in both genotypes under physiological conditions (**A**) Schematic representation of the division of the heart in eight equidistant regions. modified from Frankenreiter et al. (2017). Created with BioRender.com. (**B**) Representative PSR staining of heart sections of each region obtained from CTR and *cmf*KO mice following TAM-mediated Cre-recombination *in vivo*. (**C**) Quantification of the amount of cardiac fibrosis as percentage of the respective total area of the cardiac section revealed no genotype related difference. Evaluation of two heart slices per section from N=8 CTR and N=6 *cmf*KO mice. (**D**) Quantification of cardiac fibrosis as percentage of the whole heart exhibited a similar extent in fibrosis in both genotypes (CTR_{TAM} = 2.20 ± 0.19%, $cmfKO_{TAM}$ = 2.46 ± 0.19%). Statistical analyses: Two-way ANOVA followed by Šídák's multiple comparisons test (**C**), Unpaired student t-test (**D**)**.** All bar diagrams presented as means + SEM with CTR: N=8, *cmf*KO: N=6.

Next, Ang II-mediated myocardial fibrosis formation was assessed as outlined above. This approach involved the isolation of hearts from CTR and *cmf*KO mice that were subjected to TAM-mediated Cre-recombination and prolonged Ang II treatment *in vivo*. Again, hearts were divided in eight equidistant regions. Fibrotic areas were subsequently visualized in heart slices applying the PSR staining method (s. Figure 20A). Chronic hypertrophic stimulation with Ang II evoked significantly increased myocardial fibrosis in *cmf*KO hearts compared to the corresponding CTR hearts. This difference was attributable to increased collagen deposition in each individual section analyzed (s. Figure 20B-C). In addition, it was postulated that Ang II primarily drives the expression of collagen I and III in CFs (Lijnen et al., 2006, Chen et al., 2004), hence the ECM-composition in fibrotic heart areas was addressed in more detail using immunofluorescence staining technique to more directly target these collagen isoforms. Because regardless of the genotype the highest fibrosis accumulation was detected in section IV-VI these analyses were carried out in the corresponding sections. In line with the pervious findings, both collagen type I and type III depositions were increased approximately threefold and twofold, respectively, in heart slices from *cmf*KO compared to CTR hearts (s. Figure 20D-G).

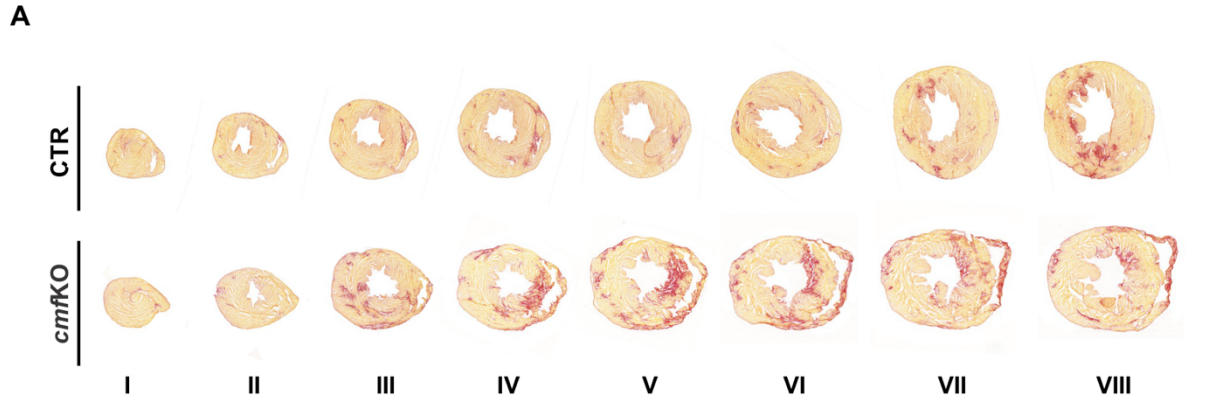
A
CTR
cmfKO
I
II
III
IV
V
VI
VII
VIII

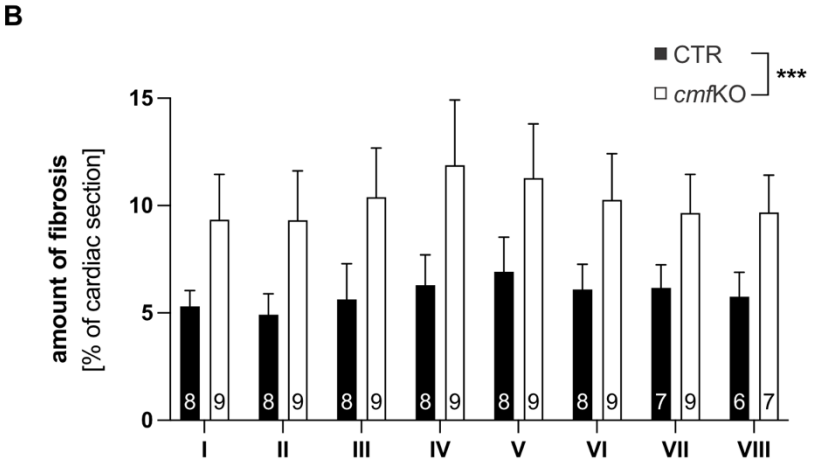
B
CTR
cmfKO
***
amount of fibrosis
[% of cardiac section]
15
10
5
0
8 9 8 9 8 9 8 9 8 9 8 9 7 9 6 7
I
II
III
IV
V
VI
VII
VIII

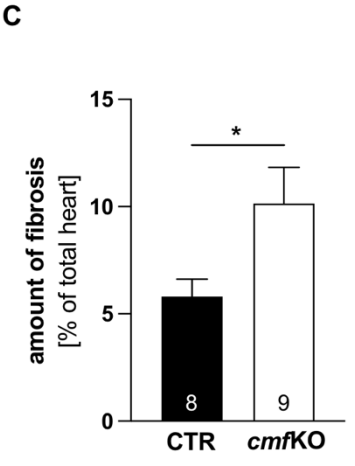
C
amount of fibrosis
[% of total heart]
*
15
10
5
0
8
9
CTR
cmfKO

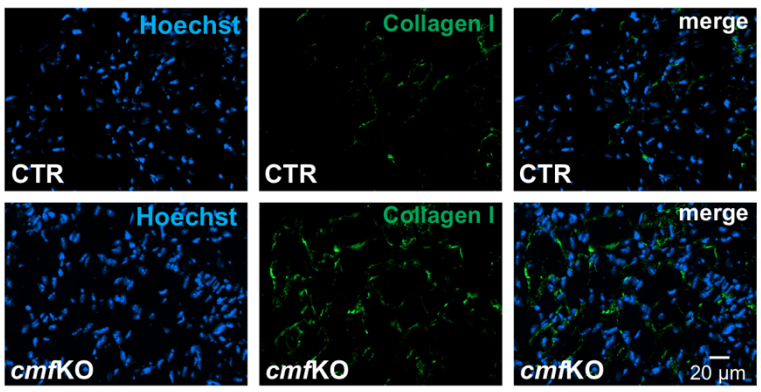
D
Hoechst
Collagen I
merge
CTR
CTR
CTR
Hoechst
Collagen I
merge
cmfKO
cmfKO
cmfKO
20 µm

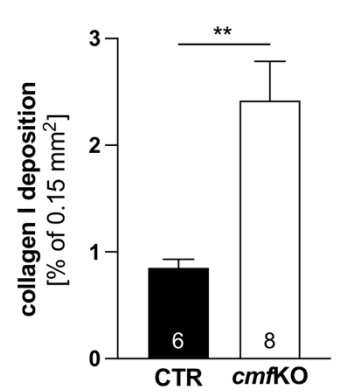
E
collagen I deposition
[% of 0.15 mm²]
**
3
2
1
0
6
8
CTR
cmfKO

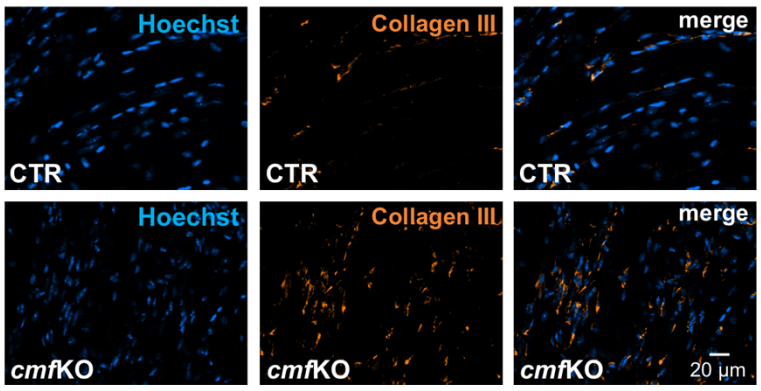
F
Hoechst
Collagen III
merge
CTR
CTR
CTR
Hoechst
Collagen III
merge
cmfKO
cmfKO
cmfKO
20 µm

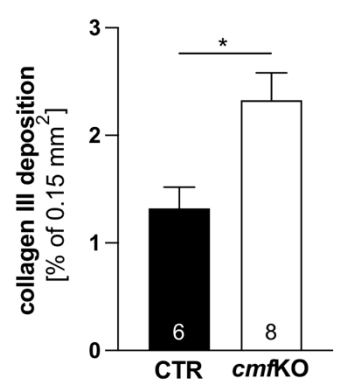
G
collagen III deposition
[% of 0.15 mm²]
*
3
2
1
0
6
8
CTR
cmfKO

Figure 20: *cmf*KO hearts displayed significantly higher collagen deposition in response to persistent Ang II exposure
(**A**) Representative PSR-stained heart slices of the indicated eight heart sections (section I to VIII) obtained from CTR (N=8) and *cmf*KO mice (N=9) after TAM and Ang II challenge *in vivo*. (**B**) Assessment of cardiac fibrosis expressed as percentage of the respective heart area revealed an enhanced accumulation of collagen in the individual sections of the *cmf*KO compared to CTR mice. (**C**) Consequently, when considering all eight sections, the *cmf*KO exhibited a significantly increased amount of myocardial fibrosis compared with the corresponding CTR group of animals ($CTR_{TAM+Ang\ II}$ = 5.80 ± 0.82%; $cmfKO_{TAM+Ang\ II}$ = 10.14 ± 1.69%). Representative collagen (**D**) type I and (**F**) type III immunofluorescence staining's of heart slices derived from Ang II and TAM-treated CTR (N=6) and *cmf*KO mice (N=8). Quantification of both collagen (**E**) type I ($CTR_{TAM+Ang\ II}$ = 0.85 ± 0.08%; $cmfKO_{TAM+Ang\ II}$ = 2.42 ± 0.37%) and (**G**) type III ($CTR_{TAM+Ang\ II}$ = 1.32 ± 0.20%; $cmfKO_{TAM+Ang\ II}$ = 2.33 ± 0.26%) specified as percentage of the respective cardiac area evidenced a substantially higher collagen deposition in *cmf*KO hearts *versus* CTR hearts. Statistical analyses: Two-way ANOVA followed by Šídák's multiple comparisons test (**B**), Mann-Whitney *U* test (**C**), Unpaired student t-test (**E**, **G**). All bar diagrams presented as means + SEM.

3.4.2 Ang II-treated *cmf*KO mutants exhibited substantially enlarged CM cross sectional areas compared to CTR mice

Cardiac hypertrophy was evaluated by normalizing HW to both BW and TL after chronic Ang II exposure *in vivo*. In particular, the latter parameter is considered to be more conclusive and reliable, as variability in BW are usually greater and are not included in the HW-to-BW calculation (Yin et al., 1982). Predictably, after TAM-mediated Cre-recombination *in vivo*, *cmf*KO mice developed normally and exhibited an equivalent cardiac phenotype compared to CTR animals, as revealed by similar BW, TL, HW as well as HW/BW and HW/TL ratios (s. Figure 34, Figure 21B, C, E). After chronic Ang II exposure, TAM-treated CTR and *cmf*KO mice developed pronounced cardiac hypertrophy. The extent of cardiac growth, compared to their corresponding unchallenged TAM-treated groups, was similar in both genotypes as indicated by HW values as well as HW/BW and HW/TL ratios (s. Figure 21A-C, E). The percentage increase in both HW/BW and mainly in HW/TL, however, pointed towards an enhanced gain of cardiac mass in the *cmf*KO mutants compared to the CTR animals, but this evaluation failed to reach statistical significance (s. Figure 21D, F). Moreover, hypertrophy was further analyzed at the cellular level by assessing the size of the CMs. To this end, CMs were visualized by H&E staining in heart sections obtained from CTR and *cmf*KO mutants either after TAM treatment alone or following TAM and Ang II exposure *in vivo*. In agreement with the increased HW, quantification of CM cross-sectional areas revealed a substantial enlargement of CMs in both genotypes upon Ang II exposure compared to the respective unchallenged groups of animals. Nevertheless, the averaged cross-sectional area of CMs in heart sections from mice specifically lacking cGKI in CMFs was markedly augmented by ~36 μm^2 compared to the size of CTR CMs (s. Figure 21G-H).

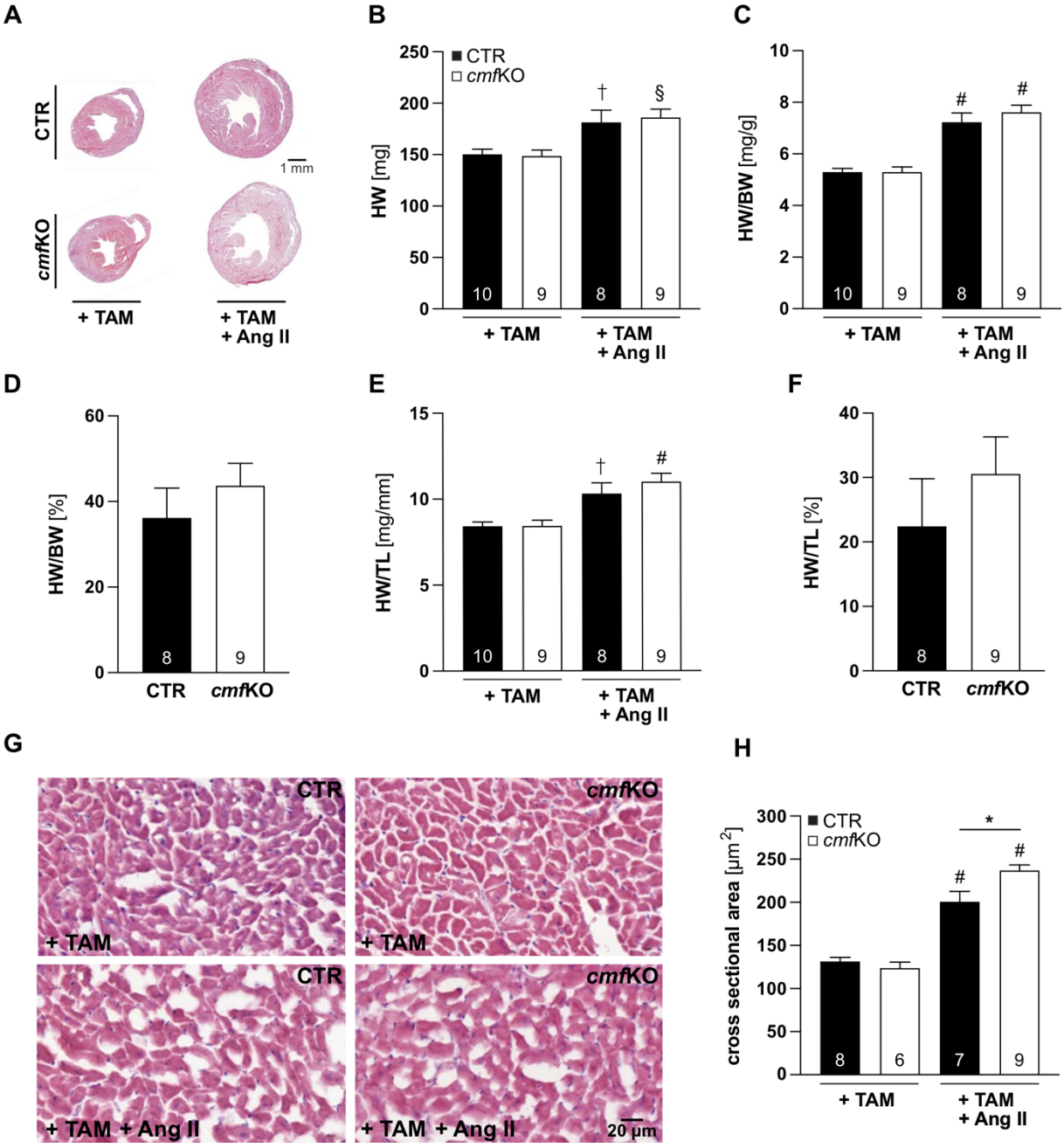

Figure 21: *cmf*KO mice displayed markedly enlarged CMs compared to CTR mice
(**A**) Representative H&E staining's of heart slices obtained from TAM-treated CTR or *cmf*KO mice in the absence (CTR: N=10, *cmf*KO: N=9) or presence of prolonged Ang II infusion (CTR: N=8, *cmf*KO: N=9). Upon 28-days of Ang II treatment both genotypes developed pronounced cardiac hypertrophy, as indicated by a significant gain in (**B**) HW (CTR_{TAM} = 150.41 ± 4.89 mg; $cmfKO_{TAM}$ = 148.58 ± 5.93 mg; $CTR_{TAM+Ang\ II}$ = 181.41 ± 11.78 mg; $cmfKO_{TAM+Ang\ II}$ = 186.2 ± 8.13 mg), (**C**) HW/BW (CTR_{TAM} = 5.30 ± 0.14 mg/g; $cmfKO_{TAM}$ = 5.30 ± 0.20 mg/g; $CTR_{TAM+Ang\ II}$ = 7.23 ± 0.36 mg/g; $cmfKO_{TAM+Ang\ II}$ = 7.61 ± 0.28 mg/g) as well as in (**D**) the percentage increase of HW/BW (CTR = 36.17 ± 6.97%; *cmf*KO = 43.69 ± 5.25%) compared to the respective group treated solely with TAM. However, the extent of Ang II-mediated hypertrophy development between genotypes attained no significant differences. Consistently, the evaluation of the (**E**) HW/TL ratio (CTR_{TAM} = 8.42 ± 0.24 mg/mm; $cmfKO_{TAM}$ = 8.43 ± 0.34 mg/mm; $CTR_{TAM+Ang\ II}$ = 10.31 ± 0.63 mg/mm; $cmfKO_{TAM+Ang\ II}$ = 11.00 ± 0.49 mg/mm) as well as the (**F**) percentage increase in HW/TL (CTR = 22.43 ± 7.41%; *cmf*KO = 30.53 ± 5.80%) tended to higher values in the *cmf*KO. (**G**) Representative H&E staining's of heart slices obtained from the indicated treatments *in vivo*. (**H**) Quantification of cross-sectional areas revealed a significant enlargement of CMs upon hypertrophic stimulation with Ang II *versus* the corresponding TAM-treated group, irrespective of the genotype analyzed (CTR_{TAM}: N=8, $cmfKO_{TAM}$: N=6, $CTR_{TAM+Ang\ II}$: N=7, $cmfKO_{TAM+Ang\ II}$: N=9). Interestingly, the

*cmf*KO myocardium exhibited significantly enhanced CM cross-sectional areas compared to the Ang II-treated CTR animals (CTR_{TAM} = 131.35 ± 4.81 µm^2; $cmfKO_{TAM}$ = 123.67 ± 7.04 µm^2; $CTR_{TAM+Ang\ II}$ = 200.61 ± 11.92 µm^2; $cmfKO_{TAM+Ang\ II}$ = 236.76 ± 6.57 µm^2). Statistical analyses: Two-way ANOVA followed by Tukey's multiple comparisons test (**B, C, E, H**), Unpaired t-test (**D**, **F**). All bar diagrams presented as means + SEM.

3.4.3 CMF-specific cGKI depletion was associated with increased CM death upon Ang II exposure

Although *cmf*KO hearts developed a higher amount of myocardial fibrosis and enlarged CMs, this adverse cardiac phenotype did not translate into aggravated cardiac hypertrophy compared to CTR mice. A potential conceivable explanation for this discrepancy involves the loss of cardiac mass due to CM cell death (Antoniak et al., 2021, Zhang et al., 2019). Ang II is widely accepted to be capable of inducing programmed CMs death, as the amount of apoptotic CMs in both the myocardium and in neonatal rat CM cultures is increased upon Ang II exposure (Diep et al., 2002, Kajstura et al., 1997, Pang et al., 2004). Another factor contributing to loss of cardiac muscle cells stems from the property of CMFs to initiate CM hypertrophy via multiple paracrine factors such as TGF-β and KLF5 causing CM damage and ultimately cell death (Piek et al., 2016, Takeda et al., 2010, Cartledge et al., 2015). To confirm this hypothesis, heart slices derived from TAM-treated CTR and *cmf*KO mice upon hypertrophic stimulation with Ang II *in vivo* were investigated using the TUNEL-assay to detect and quantify apoptotic cell death. By utilizing antibodies against Troponin T, which is a specific marker for CMs (Mingels et al., 2023), TUNEL positive cells were identified as non-/myocytes in fibrotic and non-fibrotic heart areas. While comparable amount of apoptotic CMs were identified in fibrotic cardiac regions of both genotypes, analysis of non-fibrotic cardiac areas revealed a significantly elevated amount of CM cell death in cardiac sections from *cmf*KO compared to CTR mice (s. Figure 22A-C). Taking both cardiac regions into consideration, the *Postn*iCre-driven depletion of cGKI specifically in CMFs was associated with a persistent higher CMs death compared to CTR animals (s. Figure 22D).

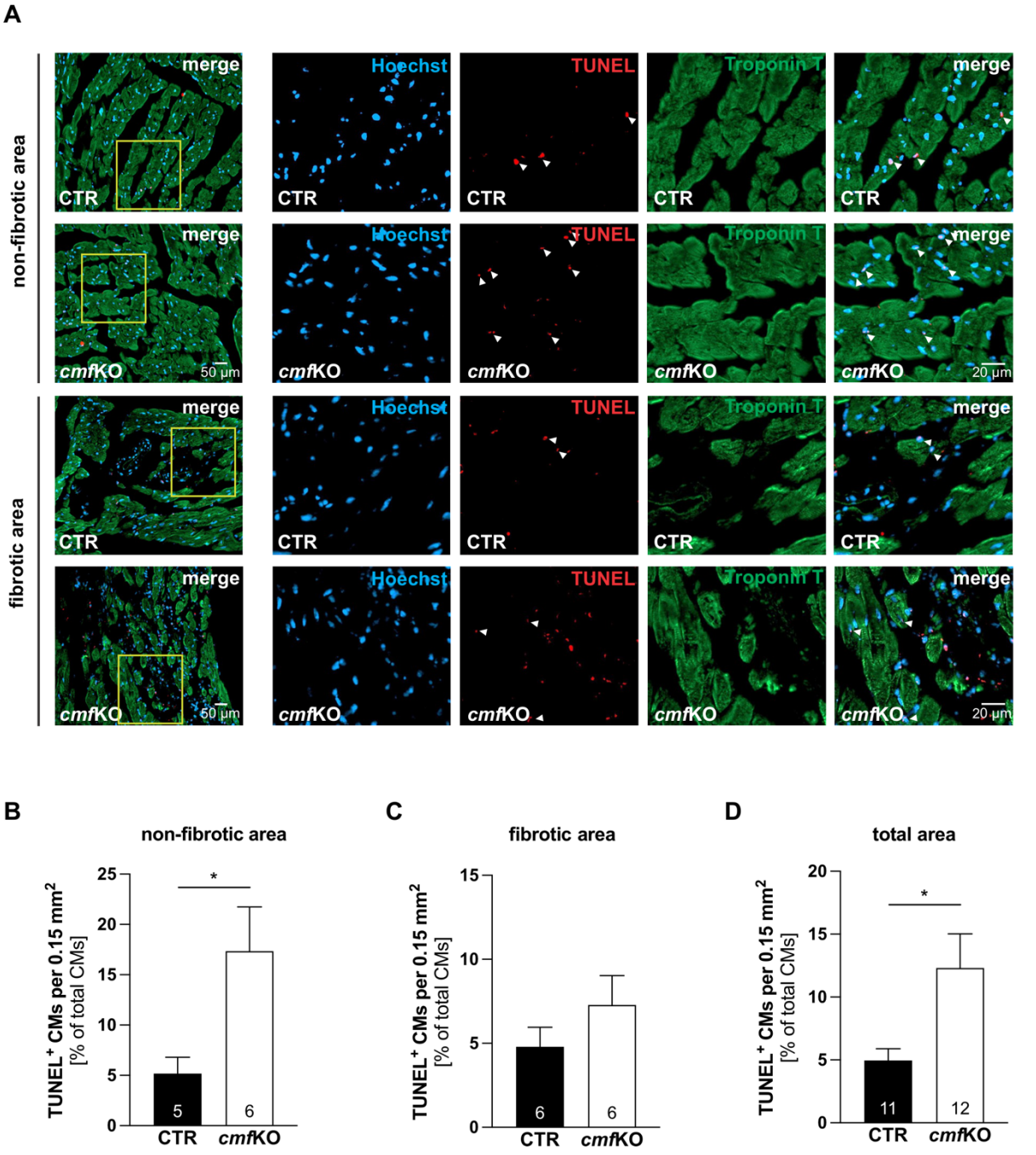

Figure 22: Enhanced CM cell death was detectable in *cmf*KO hearts upon Ang II treatment
Evaluation of CM death in TAM-treated CTR and *cmf*KO hearts upon chronic Ang II exposure *in vivo*. (**A**) Representative images of the TUNEL assay co-stained with antibodies identifying the CM marker protein troponin T (Mingels et al., 2023). Cell death was detected in both genotypes in fibrotic- as well as non-fibrotic heart areas. Quantification of apoptotic CMs expressed as percentage of the total amount of CMs exhibited (**B**) no genotype-related difference in fibrotic cardiac regions (CTR = 4.79 ± 1.16%; *cmf*KO = 7.28 ± 1.76%). However, hearts specifically lacking cGKI in CMFs presented with a significantly increased CM death compared to CTR hearts in (**C**) non-fibrotic regions (CTR = 5.17 ± 1.63%; *cmf*KO = 17.34 ± 4.40%). Evaluation of N=6 heart slices comprising an area of 0.15 mm^2 obtained from two different heart sections (section IV, VI) of n=3 animals per genotype and non-fibrotic/fibrotic area. n=3 replicates were examined from each genotype per experiment. (**D**) Both areas combined yielded pronounced CM death rates in *cmf*KO hearts compared to CTR hearts (CTR = 4.96 ± 0.92%; *cmf*KO = 12.31 ± 2.72%). Statistical analyses: Unpaired student t-test (**B-D**). All bar diagrams presented as means + SEM.

3.5 Primary CF/CMF cell cultures derived from Ang II-treated *cmf*KO mice displayed an accelerated proliferative behavior

Disruption of the cGMP/cGKI signaling cascade specifically in CMFs was herein linked to an enhanced Ang II-induced myocardial fibrosis (s. chapter 3.4.1). This prompted us to subsequently explore the role of the cGKI status on the proliferative behavior of CMFs. For this purpose, proliferation was evaluated in heart slices obtained from TAM and Ang II-treated CTR and *cmf*KO animals using immunofluorescence-based detection of Ki67, representing a nuclear protein highly expressed in proliferating cells (Sobecki et al., 2016). Since fibrotic heart areas are characterized by an augmented CMF function and the accumulation of non-myocyte cells (Kaur et al., 2016, Kanisicak et al., 2016), a collagen I antibody was co-applied to enable the localization of fibroblasts within the fibrotic areas. By correlating the increased collagen deposition with the Ki67$^+$ quantification in the latter heart regions, a threefold higher number of proliferating cells was detected in *cmf*KO compared to CTR heart slices (s. Figure 23A-B).

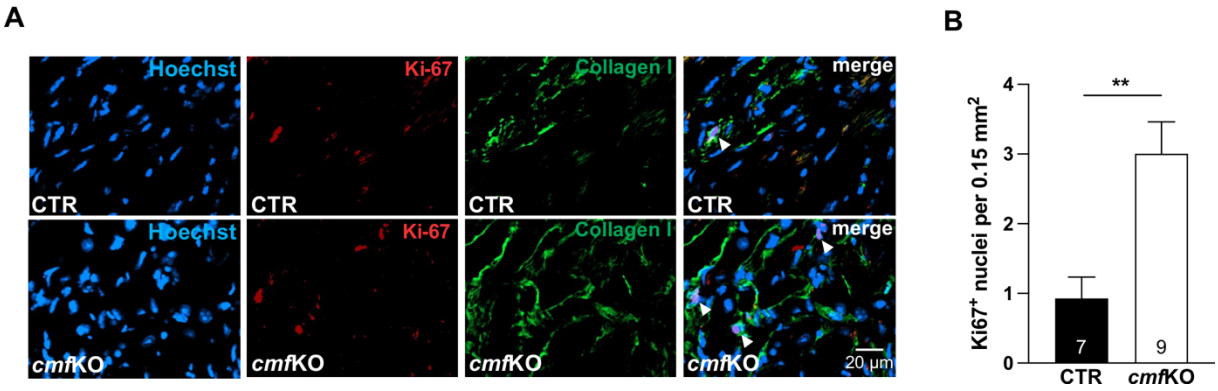

Figure 23: Elevated abundance of Ki67$^+$ cells in heart slices obtained from Ang II-treated *cmf*KO mutants
(**A**) Representative Ki67$^+$ immunofluorescence images of heart sections from TAM and Ang II-treated CTR and *cmf*KO animals. Collagen I antibodies were employed in order to localize the CMF-enriched fibrotic heart areas. (**B**) Quantification of Ki67$^+$ cells within the fibrotic heart areas exhibited a threefold higher accumulation of proliferating cells in *cmf*KO (N=7) heart sections compared to CTR (N=9) hearts ($CTR_{TAM+Ang\ II}$ = 0.93 ± 0.31; $cmfKO_{TAM+Ang\ II}$ = 3.01 ± 1.96). Per mouse, n=3 fibrotic heart areas comprising 0.15 mm^2 of distinct heart sections (section IV-VI) were randomly chosen and evaluated. Statistical analyses: Unpaired student t-test (**B**). All bar diagrams presented as means + SEM.

To provide evidence that the increased proliferation rate observed in *cmf*KO hearts was due to a disruption of the cGMP/cGKI cascade in CMFs, the proliferation behavior of primary CF/CMF cell cultures was subsequently examined. For the Grid-based proliferation assay employed, the cells were isolated from TAM- and Ang II-treated CTR and *cmf*KO animals, seeded at a cell number of $2{\cdot}10^4$ per well of an 8-well Grid-500 chamber and cultured for a period of seven days *in vitro* (s. Figure 24A; s. chapter 2.10). CF/CMF enrichment at the G_0/G_1 phase of the cell cycle was ensured by FCS deprivation for 24 h prior to the initiation of the assay (blue double arrow - s. Figure 24A). This time frame was established in preliminary experiments by assessing Ki67 expression pattern in primary CF/CMF cultures, confirming the absence of Ki67 expressing cells following FCS withdrawal for 24 h (*data not shown*). Afterwards, the cell proliferation was monitored for the next five days (t=0 h to t=120 h) (Figure 24A-B). In line with the previous results, a substantially increased proliferation rate was determined in the *cmf*KO-

derived CF/CMF primary cell culture in comparison to the CF/CMFs obtained from CTR hearts (Figure 24C). To further corroborate these findings, a predefined number of CF/CMFs ($3 \cdot 10^4$) were seeded and cultured on coverslips in a parallel approach. Applying the experimental protocol previously established, the cells were PFA fixed at the specified time points followed by the visualization of the cell nuclei using Hoechst staining (Figure 24A, D). Once again, lack of CMF-specific cGKI correlated with an increased accumulation of Hoechst$^+$ nuclei over time compared to primary CTR-derived CF/CMF cell cultures. Collectively, these results strongly imply that the endogenous CMF-specific cGMP/cGKI signaling pathway counteracts cell proliferation.

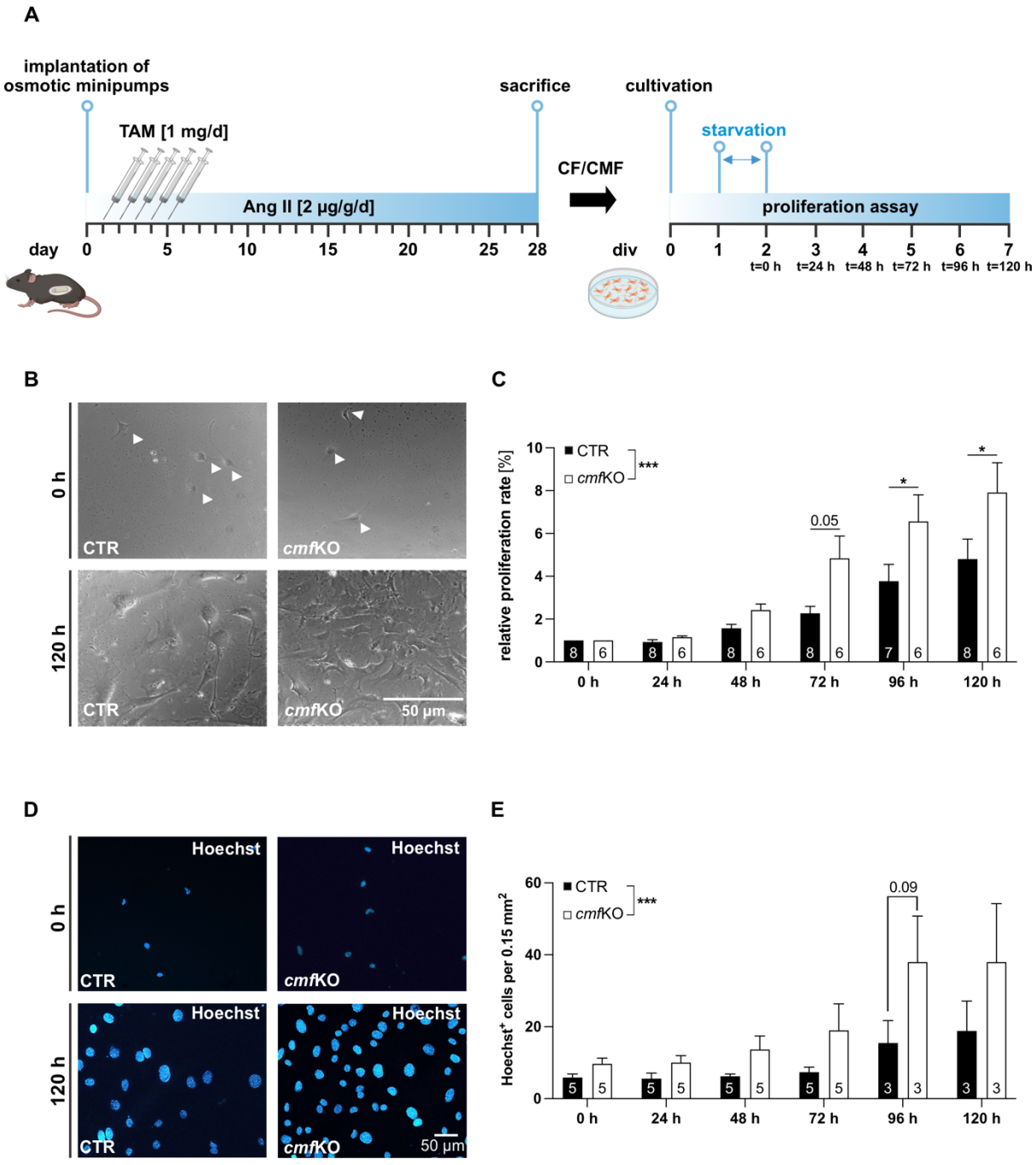

Figure 24: Primary CF/CMF cell cultures obtained from *cmf*KO mice exhibited a higher proliferation behavior compared to CF/CMFs derived from CTR animals

(**A**) Illustration of the experimental setup for monitoring the proliferation behavior of primary CF/CMF cell cultures in chronological order. CF/CMFs were isolated from TAM-treated CTR and *cmf*KO mice following 28-days of Ang II exposure *in vivo* and cultured for seven days *in vitro*. Cells were allowed to attach to the bottom of the culture surface for 24 h before replacing the culture medium (s. chapter 2.7.3) with a starvation medium for another 24 h (blue double arrow) to synchronize the cell cycle of the CF/CMFs in the G_0/G_1 phase. Proliferation rate was assessed at 24-h of intervals at the indicated time points using two distinct approaches. Created with BioRender.com. (**B**) Representative images obtained by the grid-based proliferation assay of CF/CMFs at t=0 h, representing the onset of the experiment, and after t=120 h *in vitro*. (**C**) Quantification of cell growth throughout the specified time period (t=0 h to t=120 h) revealed a significantly accelerated proliferation rate in CF/CMFs obtained from *cmf*KO mutants (N=6) *versus* CF/CMFs isolated from CTR (N=7-8) animals. n=3 replicates were examined from each genotype per experiment. (**D**) Exemplary nuclear staining of fixed primary CF/CMFs at both t=0 h and t=120 h. (**E**) Quantification of $Hoechst^+$ cell nuclei per 0.15 mm^2 coverslip area detected at the indicated time points (t=0 h to t=120 h) revealed a higher CF/CMF count in primary cell cultures obtained from *cmf*KO mice (N=3-5) in comparison to CTR (N=3-5) CF/CMFs cultures. At each time point, n=10 randomly selected areas of the coverslip containing the attached CF/CMFs of the respective genotype were evaluated per experiment. Statistical analyses: Two-way ANOVA followed by Šídák's multiple comparisons test (**C**, **E**). All bar diagrams presented as means + SEM.

3.6 *cmf*KO-mice displayed greater cardiac structural and functional alterations after Ang II treatment

Myocardial fibrosis is a crucial determinant in the clinical course of HF, as it has an unfavorable effect on the remodeling of the chambers and thus on cardiac functionality (Gyöngyösi et al., 2017, Liu et al., 2017). Indeed, excessive collagen deposition causes both cardiac stiffening and disturbance of the electro-mechanical coupling of CMs, collectively ultimately resulting in a loss of myocardial contractility and increased risk of life-threatening arrhythmias (Travers et al., 2016). Consequently, non-invasive echocardiography was conducted in CTR and *cmf*KO mice after TAM-mediated Cre-recombination and 28 days of Ang II treatment *in vivo* to investigate the impact of Ang II-mediated cardiac fibrosis on myocardial performance. In order to exclude potential cardiac abnormalities occurring under physiological conditions, a control group involving TAM-treated CTR and *cmf*KO animals were studied 28 days after the first TAM injection. Global as well as regional functional determinants were assessed using two distinct technical approaches, namely conventional and STE-based echocardiography (s. chapter 2.6.6).

3.6.1 Comprehensive assessment of global cardiac function and morphological changes using conventional M-mode echocardiography

Assessment of both global cardiac function and structural alterations were performed by the conventional echocardiography using high-resolution M-mode images obtained in the PSLAX view (s. chapter 2.6.6.1). Under physiological conditions, TAM-mediated Cre-recombination *in vivo* resulted in equivalent %EF and %FS values in CTR and *cmf*KO mutants, pointing to comparable global cardiac functions (s. Figure 25 A-C). In contrast, sustained challenge with Ang II caused a deterioration of global cardiac function in the TAM-treated *cmf*KO mutants, fitting the observed adverse cardiac phenotype (s. chapter 3.4). In detail, loss of %EF and %FS were significant compared to both the TAM and Ang II treated CTR and corresponding unchallenged *cmf*KO mice. Notably, TAM treated CTR animals exhibited equivalent %EF and %FS upon hypertrophic stimulation with Ang II compared to the corresponding unchallenged

CTR hearts, pointing to their compensatory ability to preserve cardiac function in response to Ang II induced cardiac damage (s. Figure 25 A-C).

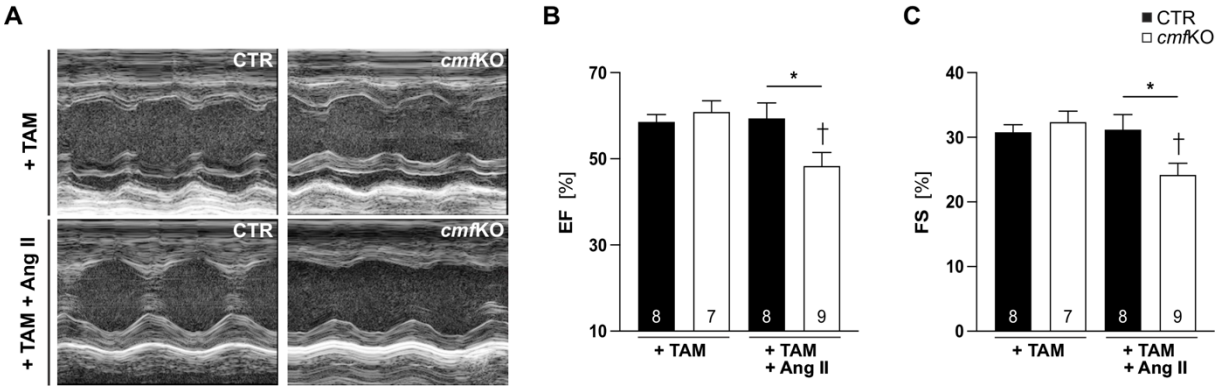

Figure 25: Ang II treated *cmf*KO mice exhibited a pronounced deterioration in global cardiac function
(**A**) Representative M-mode images acquired in the PSLAX view of CTR and *cmf*KO mice either after TAM treatment alone (CTR: N=8; *cmf*KO: N=7), or after additional 28 days of Ang II infusion (CTR: N=8; *cmf*KO: N=9) *in vivo*. Conventional quantification of cardiac function revealed no genotype-related differences in (**B**) %EF and (**C**) %FS after TAM treatment alone. Nevertheless, TAM-treated *cmf*KO mutants presented reduced %EF and %FS following hypertrophic stimulation with Ang II compared to both Ang II-treated CTR mice and corresponding unchallenged *cmf*KO animals (%EF: CTR_{TAM} = 58.56 ± 1.73; $cmfKO_{TAM}$ = 60.90 ± 2.57; $CTR_{TAM+Ang\ II}$ = 59.34 ± 3.57; $cmfKO_{TAM+Ang\ II}$ = 48.31 ± 3.15, %FS: CTR_{TAM} = 30.77 ± ;1.20; $cmfKO_{TAM}$ = 32.36 ± 1.70; $CTR_{TAM+Ang\ II}$ = 31.20 ± 2.32; $cmfKO_{TAM+Ang\ II}$ = 24.19 ± 1.79). Statistical analyses: Two-way ANOVA followed by Tukey's multiple comparisons test (**B-C**). All bar diagrams presented as means + SEM.

Next, wall dimensions, including IVS and LVPW each at the end of systole and/or diastole, were determined by conventional M-mode echocardiography. This enabled the assessment and quantification of morphological LV changes under patho-/physiological conditions. Concordant with the previously demonstrated Ang II-induced cardiac hypertrophy development (s. chapter 3.4.2), a considerable increase in $LV_{mass\text{-}corrected}$ was detected in both TAM-treated genotypes in response to prolonged Ang II stimulation compared to the corresponding control animals. However, this parameter only reached the threshold for statistical significance for the comparison among the *cmf*KO groups (s. Figure 26A). Detailed examination of wall dimensions likewise revealed a substantial increase in end-diastolic IVS and LVPW in both TAM and Ang II-treated CTR and *cmf*KO mutants compared with the respective unchallenged control animals (s. Figure 26C, I). Notably, compared to their respective control group end-systolic LVPW thickening was only detected in TAM-treated CTR animals after long-lasting Ang II stimulation and this difference also manifested in comparison to Ang II treated *cmf*KO mice (Figure 26H). In particular, the latter observed changes in Ang II-induced LVPW sizes among both genotypes contributed to the abnormal alterations in wall dimensions in the *cmf*KO mice compared to both Ang II-treated CTR and the respective unchallenged control group. In detail, *cmf*KO mice developed a smaller difference between maximal wall thickness at the end of systole and maximal relaxation during diastole (Figure 26J). Likewise, a slight decline in IVS dimensions change during the cardiac cycle was identified in Ang II-treated *cmf*KO mice, which however remained statistically insignificant compared to both Ang II-treated CTR and *cmf*KO mice after TAM treatment only (Figure 26D). Determination of ventricular dimensions yielded increased diameters in both systole and

diastole for the Ang II treated *cmf*KO mutants compared to the respective challenged CTR animals (Figure 26E-F). Examination of the difference between the largest end-diastolic ventricular dimension and the smallest end-systolic ventricular dimension revealed a reduction in ventricular changes in both Ang II-treated CTR and *cmf*KO mice, whereby only the latter genotype exhibited a significant decrease relative to its corresponding control group (Figure 26G).

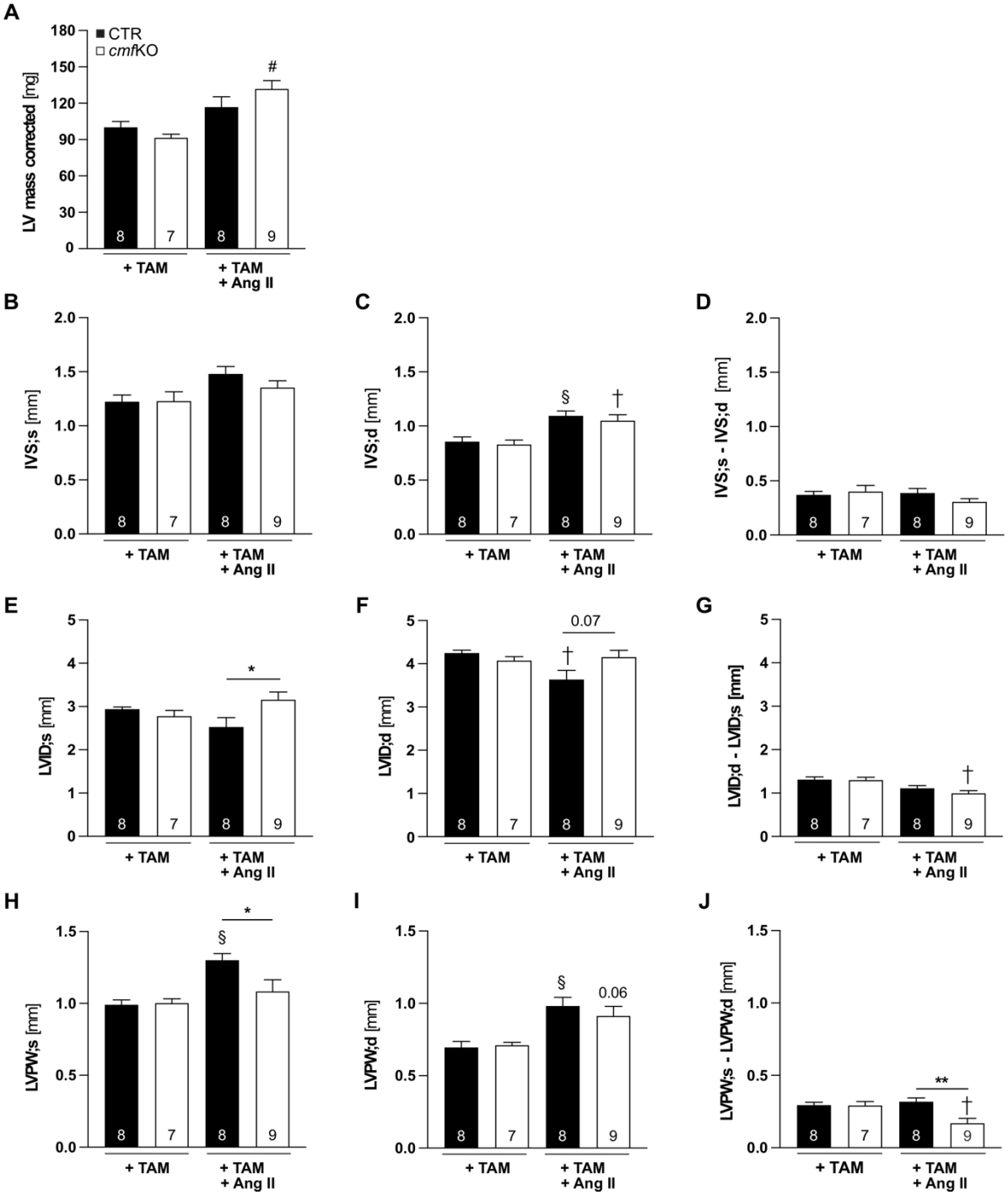

Figure 26: Changes in LV morphology in CTR and *cmf*KO mice after 28 days of Ang II infusion
LV morphological parameters were assessed by conventional M-mode echocardiography in the PSLAX view of TAM-treated animals in the absence (CTR: N=8, *cmf*KO: N=7) or after additional 28 days of Ang II stimulation (CTR: N=8, *cmf*KO: N=9). (**A**) Although an increase in $LV_{mass\ corrected}$ was detected in both genotypes following Ang II infusion compared to the corresponding unchallenged hearts, statistical

significance level was only achieved among the *cmf*KO treatment groups (CTR_{TAM} = 100 ± 4.9 mg; $cmfKO_{TAM}$ = 91 ± 2.9 mg; $CTR_{TAM+Ang\ II}$ = 117 ± 8.6 mg; $cmfKO_{TAM+Ang\ II}$ = 132 ± 6.8 mg). (**B**) End-systolic measurements of the IVS thickness yielded neither genotype-related nor treatment-dependent differences (CTR_{TAM} = 1.23 ± 0.06 mm; $cmfKO_{TAM}$ = 1.23 ± 0.09 mm; $CTR_{TAM+Ang\ II}$ = 1.48 ± 0.07 mm; $cmfKO_{TAM+Ang\ II}$ = 1.35 ± 0.63 mm). (**C**) However, TAM and Ang II-treated CTR and *cmf*KO mice displayed a significant gain in end-diastolic IVS thickness to a similar extent compared to the corresponding TAM-treated groups (CTR_{TAM} = 0.86 ± 0.04 mm; $cmfKO_{TAM}$ = 0.83 ± 0.04 mm; $CTR_{TAM+Ang\ II}$ = 1.09 ± 0.05 mm; $cmfKO_{TAM+Ang\ II}$ = 1.05 ± 0.06 mm). (**D**) The range between the maximal IVS thickness during systole and maximal relaxation during the diastole remained unaffected by the hypertrophic stimulation with Ang II as indicated by nearly identical values for the four groups investigated (CTR_{TAM} = 0.37 ± 0.03 mm; $cmfKO_{TAM}$ = 0.40 ± 0.06 mm; $CTR_{TAM+Ang\ II}$ = 0.39 ± 0.04 mm; $cmfKO_{TAM+Ang\ II}$ = 0.31 ± 0.03 mm). (**E**) Upon prolonged Ang II infusion *cmf*KO mice demonstrated an enlarged end-systolic LVID *versus* Ang II-treated CTR mice, whereby both genotypes exhibited similar values compared to the corresponding TAM treated groups (CTR_{TAM} = 2.9 ± 0.05 mm; $cmfKO_{TAM}$ = 2.8 ± 0.13 mm; $CTR_{TAM+Ang\ II}$ = 2.5 ± 0.22 mm; $cmfKO_{TAM+Ang\ II}$ = 3.2 ± 0.18 mm). (**F**) End-diastolic measurements confirmed pronounced diminished LVID in Ang II-treated CTR animals relative to the corresponding TAM-treated group, accompanied by a lack of difference to Ang II-treated *cmf*KO mutants (CTR_{TAM} = 4.2 ± 0.07 mm; $cmfKO_{TAM}$ = 4.1 ± 0.09 mm; $CTR_{TAM+Ang\ II}$ = 3.6 ± 0.21 mm; $cmfKO_{TAM+Ang\ II}$ = 4.2 ± 0.16 mm). (**G**) Considering the difference between the largest LVID determined at the end of diastole and the smallest LVID measured at the end of systole, only the TAM and Ang II treated *cmf*KO mutants presented a substantial reduction of this LVID range compared to the control group treated with TAM alone (CTR_{TAM} = 1.3 ± 0.06 mm; $cmfKO_{TAM}$ = 1.3 ± 0.07 mm; $CTR_{TAM+Ang\ II}$ = 1.1 ± 0.06 mm; $cmfKO_{TAM+Ang\ II}$ = 0.99 ± 0.06 mm). (**H**) While the end-systolic LVPW thickness was increased in TAM and Ang II-treated CTR animals in comparison to the unchallenged respective control group, (**I**) the Ang II mediated augmentation of the end-diastolic LVPW thickness was observed in both genotypes ($LVPW_s$: CTR_{TAM} = 0.99 ± 0.03 mm; $cmfKO_{TAM}$ = 1.0 ± 0.03 mm; $CTR_{TAM+Ang\ II}$ = 1.3 ± 0.05 mm; $cmfKO_{TAM+Ang\ II}$ = 1.1 ± 0.08 mm, $LVPW_d$: CTR_{TAM} = 0.70 ± 0.04 mm; $cmfKO_{TAM}$ = 0.71 ± 0.02 mm; $CTR_{TAM+Ang\ II}$ = 0.98 ± 0.06 mm; $cmfKO_{TAM+Ang\ II}$ = 0.91 ± 0.07 mm). (**J**) The differences between the maximal thickening of the LVPW during the systole and the maximal relaxation during the diastole demonstrated unchanged values in Ang II-treated CTR animals compared to the untreated corresponding control group. Consequently, Ang II-treated *cmf*KO mice exhibited a significantly reduced range of LVPW thickness in systole and maximal relaxation in diastole compared to both the Ang II-treated CTR and their untreated control group (CTR_{TAM} = 0.29 ± 0.02 mm; $cmfKO_{TAM}$ = 0.29 ± 0.03 mm; $CTR_{TAM+Ang\ II}$ = 0.32 ± 0.03 mm; $cmfKO_{TAM+Ang\ II}$ = 0.17 ± 0.04 mm). Statistical analyses: Two-way ANOVA followed by Tukey's multiple comparison except of panel G, which was evaluated via the Kruskal-Wallis test followed by the Dunn test for multiple comparison. All bar diagrams presented as means + SEM.

3.6.2 Evaluation of global and regional LV functions using STE-based echocardiography

STE-based echocardiography was performed, providing more detailed information of regional LV deformation capabilities and wall motion along with the acquisition of additional global LV functions (s. chapter 2.6.6.2) (Bauer et al., 2011). Focusing initially on the global functional performance, high-resolution B-mode images obtained in the PSLAX view of CTR and *cmf*KO animals under both patho-/physiological conditions were examined. Visualization of LV wall motion was accomplished by velocity vectors according to a semi-automatic acquisition of the LV endocardium and epicardium. The visual appearance of endocardial LV wall movement already indicated reduced systolic and diastolic vector lengths in *cmf*KO mice after hypertrophic stimulation with Ang II compared to equally treated CTR mice, suggesting an impaired wall motion (s. Figure 27A). In line with the latter observation, global longitudinal strain (GLS), referring to LV wall shortening and thickening throughout an entire cardiac cycle along the longitudinal direction, exhibited significantly impaired LV deformation capacity in *cmf*KO mice. Compromised LV deformation and thus LV contractility was not observed in CTR mice subjected to the prolonged Ang II treatment (s. Figure 27B).

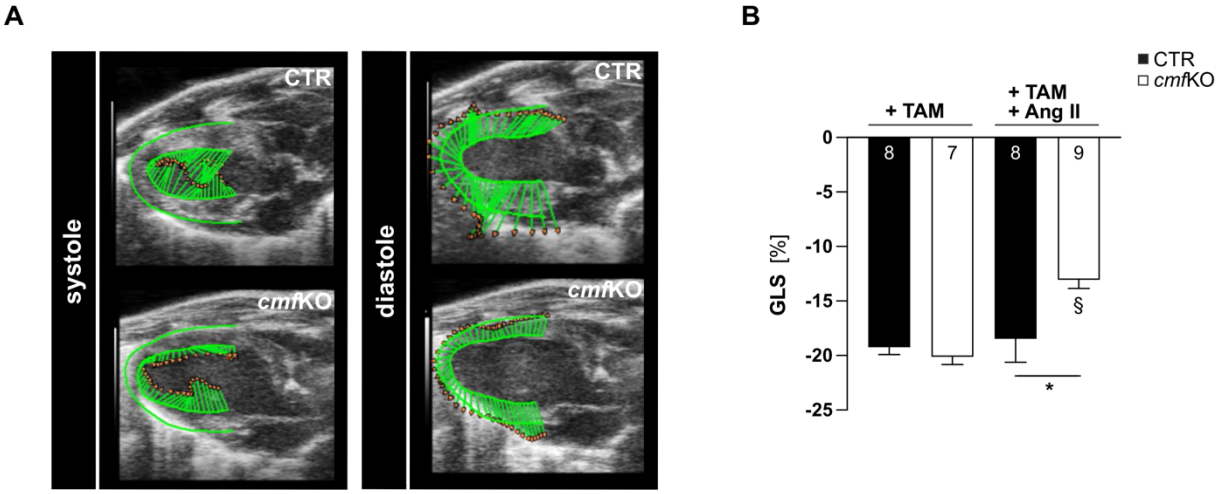

Figure 27: Sustained Ang II infusion resulted in decreased LV contractility in *cmf*KO mutants
(**A**) Representative B-mode images in PSLAX view of CTR and *cmf*KO-mutants following prolonged Ang II treatment depicting ventricular wall motion expressed as velocity vectors. During both systole and diastole, a reduced extension of the vectors in *cmf*KO *versus* CTR hearts, indicated an impaired ventricular wall motion. (**B**) Evaluation of the global longitudinal strain (GLS) exhibited markedly increased values for the Ang II-treated *cmf*KO mice compared to both the unchallenged corresponding control group and Ang II-treated CTR mice (CTR_{TAM} = -19.25 ± 0.67%; $cmfKO_{TAM}$ = -20.12 ± 0.70%; $CTR_{TAM+Ang\ II}$ = -18.47 ± 2.20%; $cmfKO_{TAM+Ang\ II}$ = -13.05 ± 0.79%). Statistical analyses: Two-way ANOVA followed by Tukey's multiple comparisons test (B). All bar diagrams presented as means + SEM with CTR_{TAM}: N=8, $cmfKO_{TAM}$: N=7, $CTR_{TAM+Ang\ II}$: N=8, $cmfKO_{TAM+Ang\ II}$: N=9.

3.6.3 Regional assessment of LV deformation and wall motion

Building on the results of globally reduced LV deformation capacity and wall motion in *cmf*KO mice after Ang II stimulation, these parameters were next comprehensively investigated in distinct cardiac muscle regions. For this purpose, the software Vevo Strain 2100 automatically divided the LV into an anterior and posterior segment, which in turn were subdivided into a base-, mid- and apex-segment (s. Figure 29A). Muscle contraction during the systole involves in a highly sophisticated way, the LV deformation in three distinct directions – i.) longitudinal shortening ii.) circumferential shortening and iii.) radial thickening (Mora et al., 2018, Scatteia et al., 2017). Based on the assessment of B-mode images obtained in the PSLAX view, quantification of the endocardial and epicardial LV deformation were restricted to the radial and longitudinal direction. The latter movement direction implies the change in the myocardial length extending along the long axis from the base to the apex. Thus, the longitudinal deformation indicated the shortening of the LV during contraction (end-systolic peak) relative to the baseline state of maximum relaxation, yielding negative strain values (Johnson et al., 2019, Flachskampf et al., 2019). Representative curvilinear recordings of endocardial LV deformation within three consecutive cardiac cycles obtained from CTR and *cmf*KO animals under patho-/physiological conditions are presented in Figure 28. Besides the individual curves representing the deformation within the six distinct LV regions, the averaged curve (black) resulting from the mean values of all segment values at the respective time points is plotted. The physiological waveform describes the longitudinal shortening of the LV ventricle until the end-systolic peak value is reached. This phase is followed by the closure of the aortic valve initiating the filling phase of the cardiac cycle as indicated by an increase in values back to the baseline level (El-Khuffash et al., 2018). After TAM-mediated Cre recombination, both

genotypes showed synchronous curve trajectories for all six segments, indicating uniform contraction and relaxation of the LV during a cardiac cycle. In contrast, the sustained Ang II stimulation provoked pronounced regional heterogeneity of myocardial contraction, characterized within these exemplary traces by systolic longitudinal elongation (strain values > 0) of the anterior base (AA) in both genotypes. Yet, heterogeneity of LV deformation was associated with impaired contractility exclusively in Ang II treated *cmf*KO mice, as evidenced by increased end-systolic mean longitudinal strain (Figure 28D, Figure 29A-C).

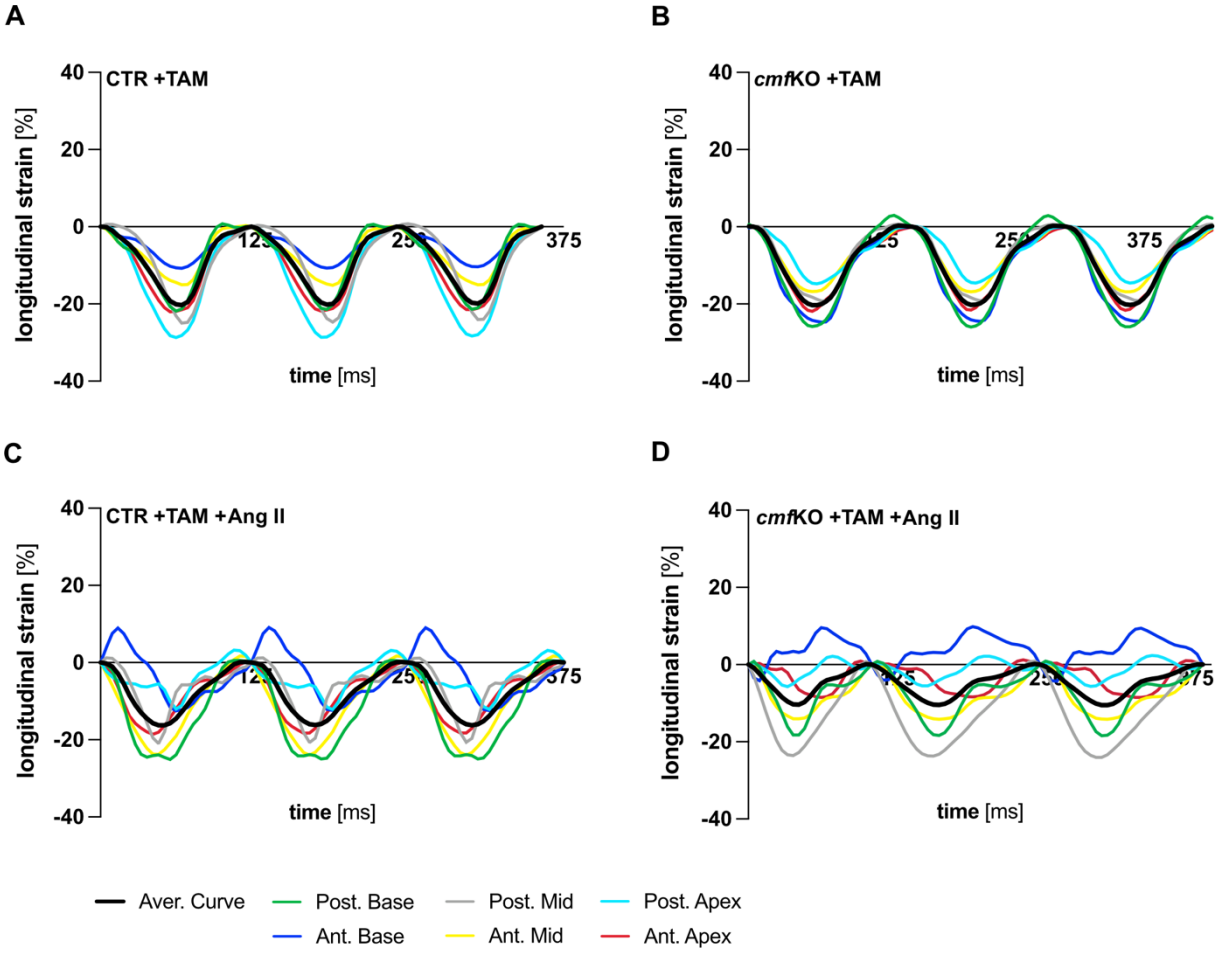

Figure 28: Ang II-treated *cmf*KO mice revealed impaired endocardial longitudinal deformation
Data were acquired using STE-based echocardiography in the B-mode view in PSLAX. Visualization of the longitudinal strain over three cardiac cycles of CTR and *cmf*KO mice after TAM treatment alone or additional sustained stimulation with Ang II. Longitudinal strain of the distinct segments was displayed with the following color pattern: green (posterior base [PB]), grey (posterior mid [PM]), turquoise (posterior apex [PA]), blue (anterior base [AB]), yellow (anterior mid [AM]), red (anterior apex [AA]), black (averaged curve).

Quantification of the peak values of each individual segment averaged over three consecutive cardiac cycles were subsequently performed to define LV deformation capacity in longitudinal direction (s. Figure 29). Following Ang II stimulation, a reduction in longitudinal peak strain was observed in each cardiac segment of *cmf*KO mice, reaching, in particular, the statistical significance level in the anterior apex (AA) compared to both the Ang II-treated CTR animals and the respective unchallenged control group (s. Figure 29B). This observation was corroborated when evaluating the averaged longitudinal deformation, revealing a substantially

reduced endocardial LV contractility only in Ang II-treated *cmf*KO mice compared to the previously outlined genotypes (s. Figure 29C). Accordingly, pathophysiological stimulation provoked a limitation of the longitudinal deformation relative to time in *cmf*KO mice compared to both Ang II-treated CTR and unchallenged hearts of respective control mice (s. Figure 29D-E). In contrast, a slight decrease in longitudinal deformation velocity was detected in *cmf*KO hearts after Ang II induced cardiac remodeling, but this trend failed to reach statistical significance compared to Ang II-treated CTR mice or the corresponding unchallenged *cmf*KO mutants (s. Figure 29F-G). Representative curves of the longitudinal strain rate and velocity are provided in the appendix (s. Figure 35).

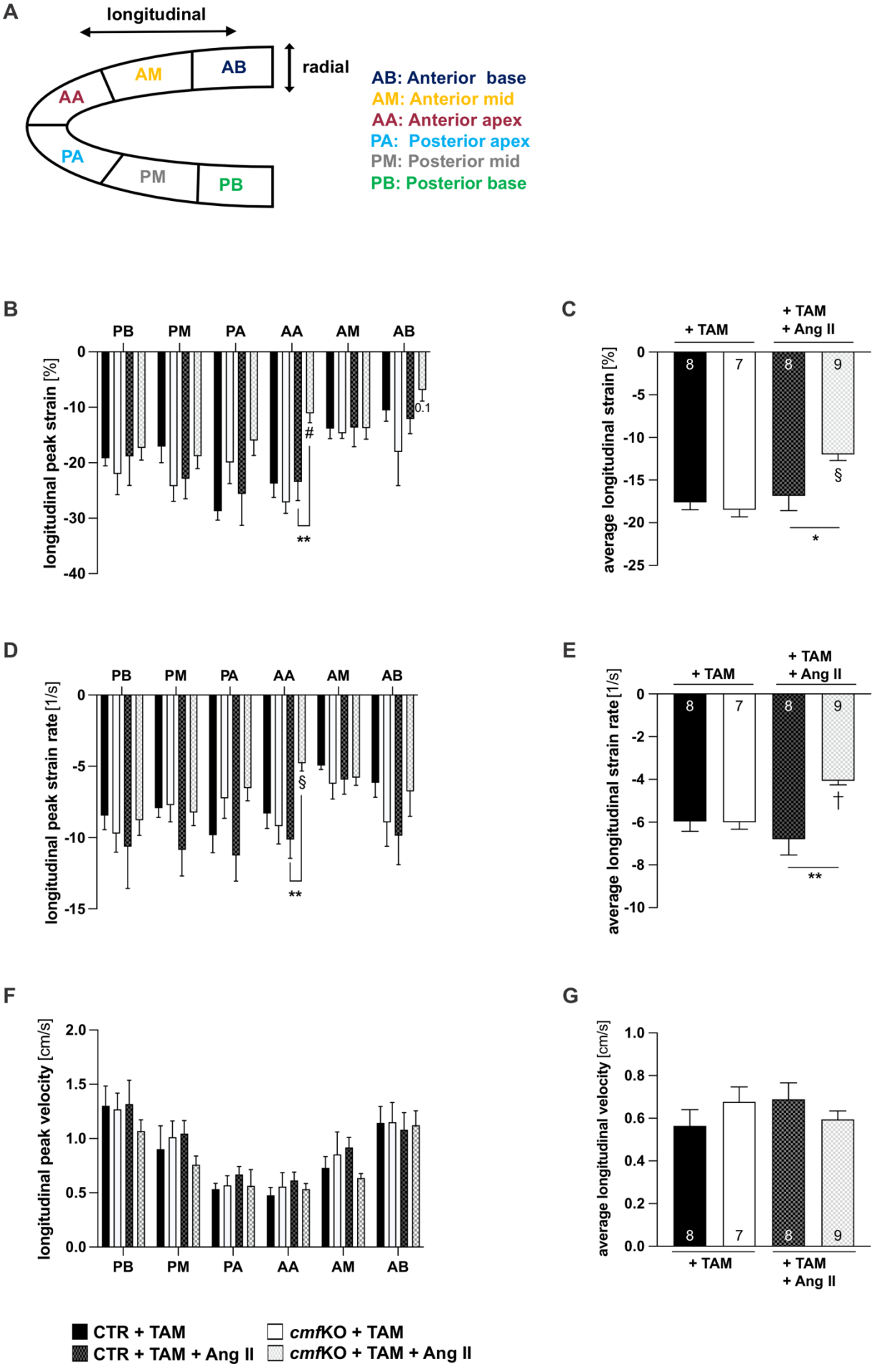
A
longitudinal
radial
AB
AM
AA
PA
PM
PB
AB: Anterior base
AM: Anterior mid
AA: Anterior apex
PA: Posterior apex
PM: Posterior mid
PB: Posterior base
B
longitudinal peak strain [%]
PB PM PA AA AM AB
0
-10
-20
-30
-40
0.1
#
**
C
average longitudinal strain [%]
+ TAM
+ TAM + Ang II
0
-5
-10
-15
-20
-25
8
7
8
9
§
*
D
longitudinal peak strain rate [1/s]
PB PM PA AA AM AB
0
-5
-10
-15
§
**
E
average longitudinal strain rate [1/s]
+ TAM
+ TAM + Ang II
0
-2
-4
-6
-8
-10
8
7
8
9
†
**
F
longitudinal peak velocity [cm/s]
2.0
1.5
1.0
0.5
0.0
PB PM PA AA AM AB
G
average longitudinal velocity [cm/s]
1.0
0.8
0.6
0.4
0.2
0.0
8
7
8
9
+ TAM
+ TAM + Ang II
CTR + TAM
CTR + TAM + Ang II
cmfKO + TAM
cmfKO + TAM + Ang II

Figure 29: Ang II stimulation led to profound deterioration of endocardial longitudinal deformation ability in *cmf*KO mutants
Evaluation of regional LV endocardial deformation capacity in the longitudinal direction of wall motion using STE-based echocardiography. For this purpose, the LV was automatically divided into six equivalent segments by the software as representatively illustrated in (**A**). Schematic representation modified from Frankenreiter et al. (2017). (**B**) Longitudinal peak strain was decreased in nearly all cardiac segments in *cmf*KO mutants subjected to chronic Ang II stimulation compared to both Ang II-treated CTR mice and their respective TAM-treated control group. (**C**) In consequence, the averaged consideration of all individual segments reflected a significantly impaired longitudinal deformation capacity in the Ang II treated *cmf*KO mutants in comparison to the previously mentioned distinct groups (CTR_{TAM} = -17.61 ± 0.87%; $cmfKO_{TAM}$ = -18.47 ± 0.83%; $CTR_{TAM+Ang\ II}$ = -16.84 ± 1.74%; $cmfKO_{TAM+Ang\ II}$ = -11.99 ± 0.70%). (**D-E**) Accordingly, quantification of the strain rate in *cmf*KO mice after prolonged Ang II infusion revealed a substantially worsened cardiac performance compared to the Ang II-treated CTR mice as well as to the TAM-treated corresponding control group, evident in both each individual heart segment and in the overall average analysis (CTR_{TAM} = -5.96 ± 0.46 1/s; $cmfKO_{TAM}$ = -6.00 ± 0.33 1/s; $CTR_{TAM+Ang\ II}$ = -6.79 ± 0.74 1/s; $cmfKO_{TAM+Ang\ II}$ = -4.06 ± 0.19 1/s). (**F**) Summary data of the longitudinal deformation velocity. (**G**) Evaluation of the average deformation velocity exhibited neither a treatment- nor a genotype-specific effect (CTR_{TAM} = 0.56 ± 0.08 cm/s; $cmfKO_{TAM}$ = 0.68 ± 0.07 cm/s; $CTR_{TAM+Ang\ II}$ = 0.69 ± 0.08 cm/s; $cmfKO_{TAM+Ang\ II}$ = 0.59 ± 0.04 cm/s). All bar diagrams presented as means + SEM with CTR_{TAM}: N=8, $cmfKO_{TAM}$: N=7, $CTR_{TAM+Ang\ II}$: N=8, $cmfKO_{TAM+Ang\ II}$: N=9. Statistical analyses: Two-way ANOVA followed by Tukey's multiple comparisons test (B [PB, PM, AA, AB], C, D [PM, AM, AB], E, F [AA, AM, AB]), Kruskal-Wallis test followed by the Dunn test for multiple comparisons (B [PA, AM], D [PB, PA, AA], F [PB, PM, PA]).

Another valuable indicator for the evaluation of LV contractility is the radial gain in wall thickness during the systole (Dandel et al., 2009). Thus, radial motion describes the thickening of the myocardial wall diameter during a contraction that is perpendicular to the longitudinal axis and directed towards the LV lumen, resulting in a positive strain value (Johnson et al., 2019, Bansal and Kasliwal, 2013). Evaluation of the distinct parameters including radial strain, strain rate and velocity remained unchanged under physiological conditions in CTR and *cmf*KO animals after TAM-mediated Cre-recombination, indicating comparable LV functions (s. Figure 30A-F). In line with previous results, neurohumoral stimulation with Ang II caused a considerable diminution of LV deformation capacity in both genotypes as compared to the corresponding TAM-treated control group (s. Figure 30A-B). Concomitant, an impairment in the rate of deformation relative to time was observed in animals following sustained Ang II stimulation, albeit only the comparison between the Ang II-treated CTR mice and the respective unchallenged control group yielded a significant difference (s. Figure 30C-D). Quantification of the radial deformation velocity exhibited a slightly impaired wall motion in Ang II-treated *cmf*KO mice compared to both Ang II-treated CTR and the corresponding TAM-treated control group (s. Figure 30E-F). Representative curves of the radial strain, strain rate and velocity are provided in the appendix (s. Figure 36, Figure 37).

In conclusion, accompanying the exacerbated Ang II-mediated histomorphological changes, *cmf*KO mice displayed an enhanced decline in cardiac function as evident by a loss of %EF, %FS as well as regional dysregulation of LV motion.

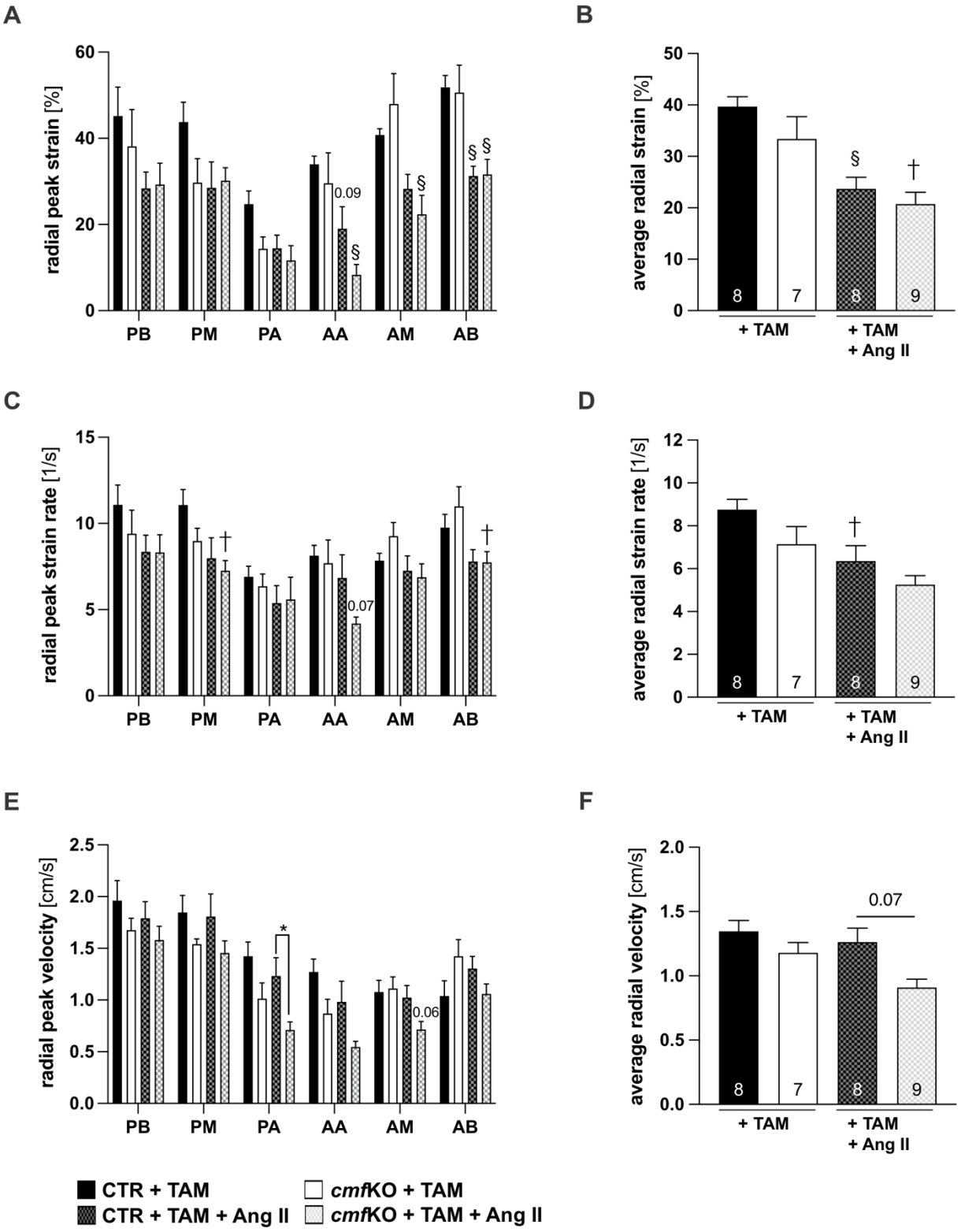

Figure 30: CTR and *cmf*KO mice exhibited comparable radial LV deformation capacity following Ang II treatment

STE-based assessment of radial LV function within the six designated regions. (**A**) In almost all segments, both genotypes exhibited reduced radial strain after chronic Ang II exposure, (**B**) cumulating in a significant deterioration of radial LV deformation capacity compared to the respective unchallenged control group (CTR_{TAM} = 39.68 ± 1.92%; *cmf*KO_{TAM} = 33.41 ± 4.34%; $CTR_{TAM+Ang\ II}$ = 23.70 ± 2.25%; *cmf*$KO_{TAM+Ang\ II}$ = 20.72 ± 2.28%). (**C**) Summary data of the region-specific radial peak strain rates. (**D**) Depiction of average radial strain rates demonstrated a pronounced reduction in both Ang II-treated

genotypes in comparison to the respective TAM treated control group, with only the comparison between the two CTR groups reaching statistical significance (CTR_{TAM} = 8.75 ± 0.48 1/s; *cmf*KO_{TAM} = 7.14 ± 0.83 1/s; $CTR_{TAM+Ang\ II}$ = 6.36 ± 0.72 1/s; *cmf*$KO_{TAM+Ang\ II}$ = 5.25 ± 0.42 1/s). (**E**) Detailed examination of the regional radial deformation velocity showed slightly reduced values for the Ang II-treated *cmf*KO mutants compared to the Ang II-treated CTR mice, (**F**) which ultimately failed to reach statistical significance in the average overall observation (CTR_{TAM} = 1.35 ± 0.09 cm/s; *cmf*KO_{TAM} = 1.18 ± 0.08 cm/s; $CTR_{TAM+Ang\ II}$ = 1.26 ± 0.11 cm/s; *cmf*$KO_{TAM+Ang\ II}$ = 0.91 ± 0.07 cm/s). All bar diagrams presented as means + SEM with CTR_{TAM}: N=8, *cmf*KO_{TAM}: N=7, $CTR_{TAM+Ang\ II}$: N=8, *cmf*$KO_{TAM+Ang\ II}$: N=9. Statistical analyses: Two-way ANOVA followed by Tukey's multiple comparisons test (A, B, C [PB, PA, AA, AM, AB], D, E), Kruskal-Wallis test followed by the Dunn test for multiple comparisons (C [PM], F)

4 Discussion

As major pathological hallmark of the failing heart, targeting myocardial fibrosis is becoming increasingly important to guide patient's therapy and consequently improve prognosis. Studies assessing myocardial fibrosis demonstrated a pronounced correlation between the occurrence of collagen deposition and adverse cardiac remodeling and outcome in asymptomatic hypertensive patients (Iyer et al., 2022). The phenotypic transition of resident CFs into CMFs in response to pathophysiological stimuli like Ang II is considered to be the critical event accelerating pathophysiological remodeling, in particular cardiac fibrosis (Liu et al., 2021b). CMFs represent a highly specialized cell type, characterized on the one hand by contractile properties obtained by de novo expression of α-SMA, and on the other hand by the amplified expression of ECM proteins (e.g., fibronectin, type I and III collagen) and matricellular proteins such as periostin (Davis and Molkentin, 2014, Frangogiannis, 2020). In particular, the expression of periostin, which is mainly enriched in collagen-rich connective tissue and is involved in the organization of the ECM, is increased in patients with HF and has been considered a potential biomarker of cardiac remodeling in this context (Zhao et al., 2014, Katsuragi et al., 2004, Stansfield et al., 2009, Dorafshan et al., 2022, Snider et al., 2008). Despite the long-standing recognition of CMFs as a critical factor in the clinical course of HF, the specific analysis and manipulation of this cell type has been challenging due to the lack of specific markers. (Alexanian and Haldar, 2018). Interestingly, *Postn* gene expression was highly associated with an activated CF phenotype and identified as a ubiquitous marker for CMFs, irrespective of their origin (Kanisicak et al., 2016, Kaur et al., 2016). By employing the innovative TAM-inducible Cre recombinase under the control of the *Postn* promoter (Kaur et al., 2016), we generated CMF-specific cGKI-deficient mice and corresponding CTR littermates to explore whether the previously established antifibrotic effects of the cGMP/cGKI cascade *in vivo* are conveyed via the *Postn*$^{+}$ CMFs.

4.1 Targeted modulation of CMF functions by *Postn*iCre$^{Tg/+}$-recombinase

A global double fluorescent ROSA$^{mT/mG}$ Cre reporter strain was employed to verify the temporally controlled, cell-specific *Postn*iCre$^{Tg/+}$-mediated recombination under both physiological and pathological conditions (Muzumdar et al., 2007). Multiple tissues and organs including aorta, lung, liver, spleen and kidney, obtained from unchallenged double transgenic ROSA$^{mT/mG}$ x *Postn*iCre$^{Tg/+}$ mice exhibited ubiquitous expression of the red fluorescent mT protein exhibiting a similar expression profile as ROSA$^{mT/mG}$ littermate control animals, indicating tight regulation of recombinase activity (s. Figure 12A, Figure 33). However, hypertrophic stimulation with Ang II and a five-day TAM treatment *in vivo* elicited Cre-mediated excision of the loxP-flanked DNA sequences encoding mT, resulting in mG expression in the interstitial space of fibrotic heart regions and to a lesser extent in the lung. In both CMs and non-fibrotic cardiac regions, the red fluorescent mT protein was persistently present in double transgenic animals (s. Figure 12, Figure 13).

Congruent with these findings, a lineage tracing analysis involving an alternative TAM-inducible mouse model based on MerCreMer, a Cre fusion protein containing two modified ER ligand binding domains, demonstrated less than 1% of *Postn* expression in interstitial cells of healthy tissue (Kanisicak et al., 2016). This confirms the highly CMF-specific expression of the MerCreMer recombinase. Furthermore, multiple studies indicate an accumulation of *Postn*$^+$ cells triggering cardiac fibrosis upon distinct pathophysiological stimuli like MI and hypertrophic stimulation with Ang II (Kaur et al., 2016, Kanisicak et al., 2016). Thus, it was shown that a targeted ablation of *Postn*$^+$ cells was beneficial for cardiac outcome after MI or prolonged stimulation with Ang II (Kaur et al., 2016). Besides the heart, *Postn* expressing cells play a crucial role in the response to acute injuries in many organs including skeletal muscle, skin, and lungs (Kanisicak et al., 2016). Especially in the context of the idiopathic pulmonary fibrosis (IPF), periostin is considered to be a potential biomarker for predicting the clinical course of the disease as well as the therapeutic outcome, and its expression was ultimately traced back to activated lung fibroblasts (Alzobaidi et al., 2022, Yamato et al., 2021, O'Dwyer and Moore, 2017). Moreover, Ang II alone or in synergy with TGF-β elicited cell proliferation, collagen production and deposition as well as fibroblast to myofibroblast differentiation in human lung fibroblasts, implicating its actions in lung fibrogenesis (Marshall et al., 2000, Marshall et al., 2004, Abdul-Hafez et al., 2009, Uhal et al., 2012). Based on the available data, the observed Cre-mediated recombination in the lungs and hearts of Ang II treated double transgenic animals was expected.

Further confirmation of these results at the cellular level was provided by isolated primary CF/CMF cell cultures deriving from double transgenic animals. These cultures presented as mixed population of cells consisting of both *in vivo* activated CMFs labelled by the expression of mG and further CF/CMFs expressing the mT protein (s. Figure 14). These mixed cultures were likely the result of the short-term TAM application *in vivo* (s. chapter 2.6.7). Provided this is true, the Cre recombinase in CF, which upregulate *Postn* expression, did not maintained an active Cre recombinase. Moreover, the isolation technique employed did not permit differential separation of CF and CMFs, always yielding a mixed culture of both cell types. Thus, these results confirmed that a five-day TAM treatment at the onset of the sustained Ang II exposure (Kaur et al., 2016), was sufficient for the pathophysiological phenotype switch from CFs to CMFs as well as for the activation of Cre recombinase.

In conclusion, these findings validate CMF-specific expression of the *Postn*iCre-recombinase in remodeled hearts, indicating the suitability of the mouse line to specifically address the function of the cGMP/cGKI cascade in CMFs during the progression of Ang II-induced cardiac remodeling.

4.2 Verification of CMF-specific cGKI deletion

The functionally crucial role of the GMP/cGKI axis has previously been established in various cell types of the cardiac system ranging from CMs, VSMCs to EC (Hofmann, 2020). Likewise, analysis of the CF transcriptome provided evidence for the expression of different components of the NO/cGMP pathway, in particular the NO-GC subunits α1 and β1, as well as the cGKI in

CF. In this respect, the cGKI/cGMP axis is considered to exert an inhibitory effect on CF proliferation (Bork and Nikolaev, 2018, Smolenski et al., 2004). In murine CMF, cGKI expression was previously verified at the protein level and reconfirmed by the published compendium of single-cell transcriptomic data obtained from the model organism mouse (Lukowski et al., 2010, Tabula Muris et al., 2018). Interestingly, this repository identified the second highest expression level of cGKI within the cardiac system in CMFs. Indeed, this levels were higher only in VSMCs and strikingly lower in CMs and CFs (Tabula Muris et al., 2018). Consistent with these previous findings, the present work validated the expression of cGKI in CMFs using a conditional KO mouse model. In this context, immunoblots confirmed high cGKI abundance in primary CF/CMFs isolated from TAM and Ang II treated CTR hearts, while this expression level was markedly reduced in *cmf*KO-derived CF/CMFs protein lysates (s. Figure 15C-D).

Moreover, efficient cell-specific *Postn*iCre-recombination was verified by examining distinct organ systems (brain, lung, aorta, liver, spleen, kidney) as well as primary CF/CMFs using genomic PCR analysis. Consistent with the results obtained in the double transgenic mice, *Postn*iCre-mediated conversion of the loxP-flanked exon 10 of the *Prkg1* allele to the KO allele, was detected exclusively in CF/CMFs and to a lesser extent in the lungs isolated from TAM and Ang II challenged *cmf*KO mice (s. Figure 15A-B).
Interestingly, further results indicated that *Postn* expression was restricted to fibrotic cardiac regions of CTR and *cmf*KO hearts following TAM and Ang II treatment *in vivo*. Especially in this collagen-rich regions, we observed a strong correlation between the cGKI expression and *Postn*$^+$ cells in CTR hearts, while this cGKI expression pattern was efficiently ablated in fibrotic areas of *cmf*KO hearts (s. Figure 15C). Hence, *Postn*$^+$ cells may represent the major source of cGKI expression in fibrotic cardiac regions, highlighting the potential importance of the CMF-specific cGMP/cGKI cascade in mediating the antifibrotic effects of this pathway.

4.3 Comprehensive characterization of CMF-specific cGKI function in Ang II-induced cardiac remodeling

In the absence of a pathophysiological stimuli, detailed investigation of CTR and *cmf*KO mice yielded no differences in survival (s. Figure 16), as well as cardiac performance (s. Figure 25-30) and morphological chamber characteristics (s. Figure 19; Figure 21) after TAM-induced *Postn*iCre-recombination. This outcome was in accordance with our expectations, since the expression of *Postn*$^+$ cells was exclusively observed in double-transgenic mice upon Ang II mediated organ injury (s. Figure 12-13; Figure 33). Conversely, TAM-treated *cmf*KO mice exhibited increased vulnerability (s. Figure 16) following sustained Ang II exposure *in vivo*, which was associated with an adverse cardiac remodeling phenotype manifested by exaggerated myocardial fibrosis (s. Figure 20) as well as CM hypertrophy and death (s. Figure 21-22) compared to respective CTR animals. Additionally, these structural abnormalities were associated with a pronounced deterioration of global cardiac function as evidence by a decline in %EF as well as compromised deformation capacity (s. Figure 25-30).

4.3.1 Impact of CMF-specific cGKI deletion on Ang II induced BP

Ang II is generally considered as the principal mediator of the RAAS system, occupying a vital role in the modulation of physiological BP through the regulation of both the salt/water homeostasis and vasoconstriction (Mehta and Griendling, 2007, Domenighetti et al., 2005). In contrast, chronically elevated circulating Ang II levels are associated with the development of cardiac remodeling due to i) the vasoconstrictive capacity leading to chronic hypertension and ii) the potential to modulate CM and CF/CMFs properties independently or in synergy with the TGF-β signaling pathway (Murphy et al., 2015, Sadoshima and Izumo, 1993, Crabos et al., 1994). The involvement of the NO/cGMP/cGKI signaling cascade in the regulation of the contractile function of VSMCs and thus in BP has been extensively explored in various genetically modified mouse strains (Ma et al., 2023). Endothelial NOS was identified as the major source of vascular NO, as mice with homozygous disruption of the eNOS gene developed profound hypertension (Shesely et al., 1996, Gödecke et al., 1998, Ataabadi et al., 2020). Moreover, NO-mediated vasodilation was abrogated in mice lacking either NO-GC or cGKI globally, resulting again in a hypertensive phenotype (Friebe et al., 2007, Pfeifer et al., 1998). Reconstitution of cGKI expression in SM22a expressing cells, including predominantly VSMCs and activated CMFs, restored the NO/cGMP-mediated vasodilation (Weber et al., 2007, Patrucco et al., 2014). However, while this pathway was extensively elucidated in VSMCs, the contribution of CMFs to BP regulation remained uncertain. As a consequence, it was important to clarify the extent to which the increased susceptibility of *cmf*KO hearts was due to possible differences in hemodynamic parameters. To this end, we performed BP measurements in freely moving CTR and *cmf*KO mice before and during the TAM and Ang II treatment according to the protocol outlined previously (s. chapter 2.6.7). Due to the absence of obvious differences in physiological BP levels (s. Figure 17) or Ang II-mediated BP elevations (s. Figure 18) between both genotypes, the higher susceptibility for cardiac damages and dysfunction was related to the local effects of Ang II promoting CM growth and death as well as pro-fibrotic signaling in CF/CMFs.

4.3.2 *cmf*KO mice exhibited increased collagen deposition in response to chronic Ang II stimulation

In the present work, disruption of the CMF-specific cGMP signaling cascade resulted in increased Ang II-mediated myocardial fibrosis, particularly associated with elevated collagen type I and III accumulations in comparison to the corresponding CTR mice (s. Figure 20). In line with these findings, two weeks of Ang II exposure in NO-GC1-deficient mice induced a comparable phenotype, which was also characterized by elevated myocardial fibrosis as well as increased mRNA levels of collagen I, periostin and TGF-β (Broekmans et al., 2020). Supporting the latter findings, pharmacological modulation of NO-GC exhibited cardioprotective functions in distinct mouse models and cardiac pathologies. Thus, treatment of animals with the NO-GC stimulator BAY 41-2272 during chronic Ang II exposure *in vivo* revealed a substantial decline in cardiac fibrosis accompanied by the downregulation of collagen I and TGF-β mRNA levels. These results were further related to a reduced abundance of *α-SMA*$^{+}$ cells, in turn suggesting a NO-GC activation-mediated suppression of CFs

differentiation to CMFs (Masuyama et al., 2006). Oral therapy with the NO-GC stimulator riociguat provided a comparable outcome, showing a reduction in TAC-induced interstitial fibrosis as well as collagen I expression. Once again, these effects were attributed to CFs, as *in vitro* findings pointed to a marked suppression of the proliferative behavior of CF treated concomitantly with Ang II and riociguat, in contrast to those exclusively exposed to Ang II (Rüdebusch et al., 2022). In summary, these multiple evidences along with our results strongly suggest an anti-fibrotic effect of the cGMP signaling cascade, especially attributable to the modulation of the pro-fibrotic characteristics of CF/CMFs.

The crucial nature of the cGMP cascade in CFs to counteract pathophysiological remodeling was further emphasized in a recent publication by Werner et al. (2023). In this context, specific ablation of GC-B in *Col1a2*$^{+}$ CFs evoked exacerbated cardiac fibrosis in response to chronic Ang II stimulation *in vivo* compared to corresponding control mice. In parallel, exogenous stimulation with CNP attenuated the fibrotic and hypertrophic response in WT animals during sustained Ang II treatment and reduced CF proliferation behavior *in vitro*, collectively leading to the conclusion that CNP mediates cardioprotective effects via the GC-B/cGMP axis in *Col1a2*$^{+}$ CFs (Werner et al., 2023). Although *Col1a2* is a frequently used marker for CFs, its specificity has been critically discussed (Umbarkar et al., 2021). For instance, RNA transcriptome analysis revealed a high *Col1a2* expression in both CFs and CMFs. The latter expression pattern was further confirmed by Kaur et al. (2016), demonstrating a strong correlation between *Postn* and *Col1a2* expression in activated CFs (Tabula Muris et al., 2018, Kaur et al., 2016). However, this wide Cre recombinase expression in different fibroblast subtypes was circumvented by employing a TAM-inducible transgenic mouse line (*Col1a2-Cre*^{ERT2}*)* in conjunction with a refined protocol of Cre recombinase activation at two weeks prior to the pathophysiological stimuli (Werner et al., 2023). Consequently, this study does not allow conclusions to be drawn regarding the antifibrotic efficacy of the GC-B/cGMP signaling cascade in CMFs. Nonetheless, in combination with our results, this study supports the notion that the cGMP/cGKI signaling cascade in distinct CF/CMF populations opposes the fibrotic response of the heart muscle induced by chronic Ang II exposure. In order to further validate this hypothesis, it would be highly interesting to elucidate the role of cGKI in *Col1a2*$^{+}$ cells and, *vice versa*, the GC-B function in *Postn*$^{+}$ cells in follow-up experiments.
Conversely, others proposed that the antifibrotic effect of CNP is conveyed predominantly via the NPR-C receptor. Mice with a specific ablation of the latter receptor displayed aggravated pressure overload-induced cardiac fibrosis, which was not ameliorated by exogenous CNP treatment as compared with the corresponding control animals (Moyes et al., 2020). Since the NPR-C receptor lacks the GC-domain, it could be assumed that the antifibrotic effect of CNP occurs independently of cGMP i.e., through a non-canonical signaling pathway (Moyes and Hobbs, 2019, Lorigo et al., 2022). However, the interaction between CNP and NPR-C has also been associated with an activation of the Ca^{2+}-calmodulin dependent eNOS, culminating in increased NO synthesis and thus exerting influence on cGMP signaling (Caniffi et al., 2010, Costa et al., 2007). Considering this interaction together with the missing quantification of cGMP levels in the hearts derived from NPR-C KO and control animals by Moyes et al. (2020),

an involvement of the cGMP/cGKI cascade in mediating the antifibrotic effect upon exogenous CNP treatment cannot be excluded.

4.3.3 Accelerated proliferative behavior of CMFs accounts for a higher collagen deposition in *cmf*KO mice

As previously outlined, a prominent characteristic of the Ang II-mediated adverse cardiac phenotype was the significant increase in collagen deposition in the absence of CMF-specific cGKI. In this sense, it was essential to subsequently clarify the kinase-mediated effects in *Postn*$^{+}$ CMFs that could counteract Ang II-mediated cardiac remodeling. Based on the current findings, three distinct mechanisms can be proposed by which cGMP elevations can convey antifibrotic actions comprising i.) the downregulation of ECM production, ii.) altered fibroblast to myofibroblast differentiation and iii.) inhibition of cell proliferation (Sandner and Stasch, 2017).

Focusing on the latter aspect, we identified a significantly increased abundance of proliferating cells, labelled by the nuclear expression of Ki67, in CMF-enriched myocardial areas from Ang II treated *cmf*KO mice compared to corresponding CTR hearts (s. Figure 23). This observation was additionally corroborated in primary CF/CMF cultures, which demonstrated an accelerated proliferation rate in cell cultures obtained from Ang II-treated *cmf*KO mice compared to CTR-derived CF/CMFs (s. Figure 24). Overall, these findings suggest a regulatory role of cGKI on cell proliferation, as the presence of the kinase prevented an excessive expansion of *Postn*$^{+}$ CMFs under both Ang II stimulation conditions *in vivo* as well as *in vitro*. Thus, it is concluded that the increased extent of myocardial fibrosis in *cmf*KO mice can be explained by an accelerated CMF proliferation behavior in the absence of cGKI.

Supporting our results, stimulation with either ANP or BNP was able to attenuate Ang II-induced proliferation of rat CF via the generation of intracellular cGMP (Fujisaki et al., 1995). Conversely, specific suppression of GC-A in CFs by siRNA-based approach caused an accelerated Ang II-induced proliferation response and upregulation of distinct collagen isoforms (type I and type III) relative to CFs derived from WT rats. Moreover, cGMP elevation by simultaneous treatment with 8-Br-cGMP counteracted the Ang II induced proliferation rate and collagen synthesis in GC-A deficient CF, suggesting an antiproliferative and thus antifibrotic effect of the ANP/GC-A/cGMP signaling cascade (Parthasarathy et al., 2013). The maladaptive response of CF to Ang II stimulation *in vitro* was further diminished by activation of the NO-GC/cGMP signaling cascade using riociguat, as suggested by a decreased proliferation rate compared to CF exclusively treated with Ang II (Rüdebusch et al., 2022).

Evidence for a conceivable downstream mechanism counteracting exaggerated CMF proliferation in a cGKI-dependent manner is provided in a publication by Li et al. (2008). In this study, mice lacking globally ANP (*Nppa*$^{-/-}$) exhibited a worser cardiac phenotype characterized by an enhanced hypertrophy development as well as increased myocardial fibrosis in response to pressure overload compared with WT animals. Additional stimulation of isolated murine CF with cGMP-elevating agents prevented TGF-β induced collagen synthesis as well as cell proliferation. As an underlying mechanism, Li et al. (2008) identified the ANP/cGMP-dependent

activation of cGKI ultimately leading to the phosphorylation of the serine^{309} and threonine^{388} residues of SMAD3 in CF. This event abrogated the translocation of pSMAD3 into the nucleus, thereby disrupting the TGF-β induced pro-fibrotic gene expression (Li et al., 2008). Whether the signaling cascade outlined contributes to the herein observed cGKI-mediated antifibrotic effects in *Postn*$^{+}$ CMFs *in vivo* needs to be investigated in future studies.

In conjunction with the present evidence, our results support that cGKI activation counteracts Ang II-mediated accelerated proliferation response of CF/CMFs, thereby explaining the antifibrotic action of both NP/cGMP and NO/cGMP signaling cascades. However, the effect of cGKI on the collagen-producing properties of CMFs and how this would contribute to the observed phenotype in *cmf*KO mice remains unclear. Additional analyses of the collagen expression patterns and ECM production profile of *Postn*$^{+}$ CMFs are required to answer this question.

4.3.4 Enlarged CM cross sectional areas in *cmf*KO mice upon Ang II treatment

In response to chronic Ang II exposure, both CTR and *cmf*KO mice developed enlarged CM cross sectional areas compared to the respective unchallenged control group. This pathophysiological cell growth was highly exacerbated in *cmf*KO mice (s. Figure 21G-H). Because genetic modulation of CMs by the Cre recombination system employed was ruled out (s. Figure 12), the enlarged CM cross-sectional areas were considered to be a consequence of both the underlying adverse cardiac remodeling associated with enhanced cardiac fibrosis and the extensive cross talk between CMs and CF/CMFs (Piek et al., 2016).

Emerging evidence suggests a cardioprotective effect of the cGMP/cGKI signaling cascade in CMs, particularly in the context of Ang II mediated cardiac hypertrophy. One focus of attention represents the cGKI-dependent phosphorylation of regulators of G protein signaling 2 (RGS2), which releases RGS2 activity leading to translocation of the protein to the plasma membrane. RGS2 acts as a GTPase-accelerating protein, thereby increasing the hydrolysis of GTP to guanosine diphosphate (GDP) and thus to a more rapid termination of the Gαq-dependent hypertrophic Ang II stimulation (Francis et al., 2010, Klaiber et al., 2010, Roman and Traynor, 2011). The involvement of this cascade is postulated to be mainly responsible for the cardioprotective effects of the ANP/GC-A/cGMP pathway, which counteracts Ang II-induced myocardial injury (Klaiber et al., 2010). Transient receptor potential canonical (TRPC) channels represent another common intersection point at which cGKI interferes with the pro-hypertrophic action of Ang II. It is widely accepted that Ang II promotes the production of diacylglycerol (DAG) in a phospholipase C (PLC)-dependent manner resulting in the activation of DAG-sensitive TRPC channels, in particular TRPC3 and TRPC6. In turn, these channels, by increasing the Ca^{2+} influx into the cell, promote the translocation of nuclear factor of activated T-cells (NFAT) into the nucleus, thus facilitating the expression of pro-hypertrophic genes (Onohara et al., 2006). Interestingly, both TRPC channels have already been identified as potential cGKI downstream targets (Koitabashi et al., 2010). For instance, in a work by Koitabashi et al. (2010), a cGKI-dependent phosphorylation of the TRPC6 channel was associated with a downregulation of the channel activity, resulting in suppressed channel

current and consequently reduced activation of Ca^{2+}-calmodulin dependent calcineurin (Cn). This in turn prevented the dephosphorylation of NFAT via Cn and thus its translocation into the nucleus (Koitabashi et al., 2010).

A recent study using a knock-in mouse model expressing a FRET-based cGMP indicator unequivocally demonstrated that neither NO, NO-GC stimulators, nor activators are able to increase cGMP levels in isolated CMs. However, following the stimulation with the above-mentioned compounds, the authors identified a strong increase in cGMP levels in CF, which was transferred via gap junctions to CMs (Menges et al., 2019). Confirmation of the latter cGMP transport was obtained shortly afterwards in living cardiac slices derived from mice with CM-specific expression of a FRET-based cGMP indicator in response to NPs or upon stimulation of NO-GC (Menges et al., 2023). Interestingly, this set of experiments identified *Tcf21*$^+$ CF as the main source of cGMP synthesis, which are widely accepted to be the principal progenitor cells of *Postn*$^+$ CMFs (Kanisicak et al., 2016). Thus, it could be speculated that the cGMP transfer via the CF/CMF-CM crosstalk was responsible for the antihypertrophic and antifibrotic effects of the cGMP cascade in Ang II-induced cardiac remodeling, although this interesting hypothesis requires experimental verification. Nevertheless, even if the cGMP transfer can be stimulated in a NO-GC- or NPs-dependent manner under pathophysiological conditions, a contribution of cGKI to the transfer seems to be unlikely, since the kinase acts downstream of the cGMP production. Interestingly, however, there is sporadic evidence implicating cGKI-dependent regulation of intracellular cGMP levels. Thus, it has been suggested that cGKI-dependent phosphorylation at serine^{64} of the NO-GC α-subunit leads to both an inhibition of the NO-GC activity as well as diminished response to endogenous NO production, thereby mediating a negative feedback mechanism (Zhou et al., 2008). However, this study is at odds with a recent publication by Dao et al. (2020), demonstrating no cGMP/cGKI-mediated regulation of NO-GC activity. In this respect, neither the stimulation of isolated pulmonary EC with 8-Br-cGMP *in vitro* was able to induce changes in NO-GC activity, nor global cGKI KO mice exhibited any changes in NO-GC expression patterns or activity *in vivo* compared to WT mice (Dao et al., 2020). Furthermore, cGKI was shown to phosphorylate the cGMP-hydrolyzing PDE5 at serine^{92} in smooth muscle cells (SMC), resulting in an increase in catalytic activity by the phosphodiesterase (Rybalkin et al., 2002). Indeed, these PDE5/cGKI interactions contributed to desensitization of the platelet NO/cGMP response (Mullershausen et al., 2003, Münzel et al., 2003). Bringing these different aspects together, it is hypothesized that cGKI may affect the amplitude as well as the distribution of cGMP within a cell system and between distinct cell types. Although there is evidence of PDE5 expression in *α-SMA*$^+$ CF (Lukowski et al., 2010) supporting the hypothesis, the signaling pathway would be in direct contradiction to the known and comprehensively investigated cardioprotective effect of cGMP in CMs (Frantz et al., 2011, Frankenreiter et al., 2017). Thus, cGKI-mediated PDE5 phosphorylation in CMFs would lead to a higher cGMP degradation resulting in a lower cGMP transfer into CMs. *Vice versa*, *cmf*KO mice would exhibit a reduced cGMP degradation allowing increased cGMP transport into CMs, which would consequently exert an antihypertrophic and cardioprotective effect and thus completely contradicting our observed phenotype. Therefore, we assume that even if the cGMP transfer in hypertensive hearts conveys cardioprotective role, this occurs independently of cGKI.

The connection between myocardial fibrosis leading to heart stiffening as well as conductivity abnormalities and decreased oxygen diffusion has already been widely accepted (Cowling et al., 2019, Kong et al., 2014, Daskalopoulos et al., 2012). Collectively, these factors contribute to an augmented workload for CMs within an unfavorable physiological environment resulting in CM hypertrophy and cell death (Piek et al., 2016). Hence, the increased collagen deposition in the *cmf*KO animals may explain the elevated CM cross-sectional indirectly i.e., through the abovementioned link between fibrosis and workload. However, besides the formation of connective tissue, the production and secretion of various cytokines and growth factors including ET-1, tumor necrosis factor α (TNFα), FGF-2 and TGF- β by CMFs may promote the development of CMs hypertrophy (Piek et al., 2016, Bogoyevitch et al., 1994). Particularly, Takeda et al. (2010) demonstrated the crucial role of CMFs to affect the growth of CMs in a paracrine manner using genetically modified mice. In this context, global loss of KLF5, an important regulator of development and cellular differentiation as well as pathogenic element in various diseases, was associated with an attenuated Ang II-induced cardiac hypertrophy and fibrosis. In search of the cellular origin of KLF5, CM-specific deletion of the indicated factor failed to ameliorate the pressure overload-induced cardiac hypertrophy. Conversely, the lack of KLF5 specifically in *Postn*$^{+}$ CMFs exhibited a beneficial cardiac outcome characterized by reduced collagen deposition, HW/BW ratios, CM cross sectional areas as well as suppressed expression of hypertrophy-associated genes such as *Nppa* and *Myh7*. In conclusion, this present investigation highlighted the important role of CMFs in conveying pro-hypertrophic signals to CMs (Takeda et al., 2010). In another mouse model, transgenic mice carrying a global deletion of FGF-2, were protected from Ang II-induced cardiac hypertrophy, which was correlated with an attenuated stimulation of MAPK activity (JNK, ERK and p38 kinase) compared to WT mice. Further, *in vitro* assays identified Ang II stimulated CF as the principal source of FGF-2 secretion and demonstrated the crucial role of this paracrine mediator in the activation of the MAPK signaling pathway in CMs (Pellieux et al., 2001). Collectively, these results reinforced the hypothesis that CF/CMFs integrate hypertrophic stimuli in CMs through the secretion of autocrine and paracrine factors (Piek et al., 2016). Currently, no conclusions can be drawn about the extent to which the disruption of the cGMP signaling pathway in CMFs has an impact on the release of paracrine mediators and thus on the CM enlargement observed in our study. Nevertheless, we expect a higher accumulation of CMFs in remodeled *cmf*KO hearts due to their accelerated proliferation behavior observed *in vitro*. This in turn enables the enhanced secretion of cytokines and growth factors responsible for the induction of CM hypertrophy, a paracrine mechanism which may explain the greater CM enlargement in *cmf*KO mice.

4.3.5 Disruption of the cGMP signaling cascade in CMFs is associated with higher CM cell death

Cardiac hypertrophy is largely defined as a complex compensatory mechanism involving the growth of CMs without concomitant increase in the cell number, the deposition of ECM proteins and proliferation of other cell populations to distinct stress-induced damages (Aoki and Izumo, 2001, Moukette et al., 2021). In this context, however, the pronounced increase in myocardial fibrosis (s. Figure 20), the elevated CMF proliferation rate (s. Figure 24), as well as the

enlarged CM cross-sectional areas (s. Figure 21G-H) in *cmf*KO hearts resulted neither in a substantially higher HW nor HW/TL ratio compared with Ang II treated CTR hearts (s. Figure 21A-F). This divergence might be due to the opposing effects of Ang II on CMs, which includes the induction of both hypertrophic, necrotic and apoptotic signaling pathways (Diep et al., 2002, Kajstura et al., 1997, Tan et al., 1991), with the latter two culminating in the loss of CMs and thus cardiac mass (Antoniak et al., 2021, Zhang et al., 2019). Consistently, the number of $TUNEL^+$ CMs in *cmf*KO hearts upon Ang II challenge *in vivo* was massively increased as compared with the corresponding CTR hearts (s. Figure 22).

There is evidence suggesting a pro-apoptotic property of Ang II conveyed via its interaction with the AT_1-receptor on CMs. Chronic activation has been postulated to trigger a $G\alpha_{12/13}$-mediated Rac1 activation, which subsequently promotes reactive oxygen species (ROS) production ultimately leading to the activation of JNK/p38 MAPK (Nishida et al., 2005, Xia et al., 2016). Likewise, a p38 MAPK-dependent signaling pathway was implicated in Ang II-mediated TGF-β expression in CMs (Wenzel et al., 2001). Through an autocrine loop, TGF-β itself is capable of inducing apoptosis in CMs via the activation of both the SMAD signaling pathway and the p38 MAPK cascade (Schröder et al., 2006, Euler, 2015). In the context of CM cell death during ischemia/reperfusion (I/R) injury, an effective interaction with the cardioprotective cGMP cascade and the pro-apoptotic p38 MAPK signaling pathway was reported. Herein, cGMP-activated cGKI has been shown to bind to p38 MAPK consequently preventing TGF-β activated protein kinase 1-binding protein 1 (TAB1) mediated p38 MAPK autophosphorylation and thus protecting CMs from apoptosis (Fiedler et al., 2006). Thus, the Ang II-mediated CM death and TGF-β synthesis might be beneficially modulated by cGMP/cGKI via the p38 MAPK cascade. Because a genetic disruption of the cGMP pathway in CMs by the *Postn*-driven Cre recombinase employed was excluded (s. Figure 12), the debate about a possible impaired cGMP transfer from CMFs to CMs as a contributor to the increased CM mortality in *cmf*KO hearts must be revisited. Nevertheless, for the reasons already stated in detail in chapter 4.3.4, the cGMP transfer conveying cardioprotective effects during Ang II-mediated cardiac injury, likely occurs independently of cGKI.

It is much more likely that the increased abundance of CMFs in the *cmf*KO hearts resulted in an amplified secretion of cytokines and growth factors, which ultimately exerted a direct impact on the functionality and viability of the CMs. This hypothesis was further strengthened by a publication from Cartledge et al. (2015), in which the intimate cross-talk between both cell populations was comprehensively investigated in a co-culture model. In the latter cultures, CMs exhibited a major enlargement of their dimensions as well as a substantial decline in viability compared to pure CM culture systems. By employing a particular co-culture technique which only allowed paracrine communication between both cell systems due to a physical separation of CM and CMFs, this pathophysiological response of CMs was attributed to the release of TGF-β from CMFs. Furthermore, CM death was prevented by simultaneous stimulation with a TGF-β inhibitor, again highlighting the crucial role of TGF-β in the interaction between both cell types (Cartledge et al., 2015). Interestingly, p38 MAPK was also identified as a potential downstream target of cGKI in kidney fibroblast cell line 293T, as evidenced by an NO/cGMP-cGKI mediated phosphorylation of the kinase (Browning et al., 2000). Transgenic

mice with a specific deletion of *Mapk14* (p38-MAPK) in *Postn*$^{+}$ CMFs were protected from Ang II and phenylephrine (PE) mediated cardiac remodeling, as demonstrated by the absence of a hypertrophic response as well as a substantial decline in collagen deposition in comparison to the corresponding control mice. *Vice versa*, a significant increase in cardiac hypertrophy and myocardial fibrosis was observed in mice with a sustained expression of active mitogen-activated protein kinase kinase 6 (MKK6), representing a well-known activator of p38-MAPK (Molkentin et al., 2017). Overall, these data indicated a pro-fibrotic action of the MKK6-p38 MAPK signaling cascade and strongly encourage consideration of p38 MAPK inhibition to explain mechanistically cGMP/cGKI function and the therapeutic significance of the cascade in cardiac fibrosis. This hypothesis and the details of p38 MAPK and cGKI must be subject of future investigations.

Apart from the already enlightened CMF-CM interactions, the increased CM cell death rate could also be a consequence of the greater structural modification encountered in the *cmf*KO hearts. In this context, the localization as well as the extent of fibrosis in particular play a critical role. Thus, an accumulation of ECM proteins diffusely surrounding the CMs are responsible for the LV stiffness, which ultimately provokes cardiac dysfunctions and restricts myocardial blood flow. Consequently, this is linked to a markedly compromised nutrient supply to the myocardium (Bernardo et al., 2010, Piek et al., 2016). Moreover, collagen fibers located around intracoronary arterioles decrease the oxygen availability of CMs as well as coronary reserves, collectively leading to ischemic injury of CMs (Brown et al., 2005, Segura et al., 2014). Likewise, the markedly enlarged CM cross-sectional areas observed in *cmf*KO mice may be associated with the higher incidence of CMs death. In this regard, it was previously postulated that enlarged CM dimensions extends the diffusion distance of oxygen from the adjacent capillaries through the concentration gradient to the mitochondria in the cell interior. This results in mitochondria ischemia as pathological consequence, leading in turn to a lower adenosine triphosphate (ATP)-forming capacity (Diwan and Gerald W. Dorn, 2007). Overall, these structural abnormalities in the myocardium create an unfavorable physiological environment, further promoting hypertrophy development and eventually contributing to cell death (Piek et al., 2016).

4.3.6 *cmf*KO mice exhibited reduced LVEF and impaired deformation capacity

Cardiac remodeling is characterized by LV morphological changes involving CMs-growth and -death as well as myocardial fibrosis, ultimately resulting in loss of cardiac function (Leancă et al., 2022). In more detail, excessive collagen deposition leads to both increased ventricular stiffness associated with loss of elasticity and disruption of electrical connectivity between CMs, in turn promoting the development of life-threatening arrhythmias (Piek et al., 2016, Verheule and Schotten, 2021). Echocardiographic assessment of global cardiac function revealed a consistent %EF and %FS in the TAM-treated CTR mice after chronic Ang II exposure *in vivo* compared to the corresponding untreated control animals, indicating their compensatory ability to preserve cardiac function during Ang II treatment (s. Figure 25). This myocardial outcome can be explained by the rather moderate Ang II infusion protocol employed here, involving the administration of 2 mg/kg/d Ang II over a period of four weeks.

Consistent with our findings, a study by Straubinger et al. (2017) reported pro-hypertrophic and pro-fibrotic actions of the latter Ang II concentration infused to WT mice for one week , in the concomitant absence of cardiac dysfunctions. Confirming our observed phenotype, another publication demonstrated that even lower Ang II concentrations (1.44 mg/kg/d for over four weeks) in WT animals also resulted in a collagen deposition of approximately 5% relative to the total cardiac area, which was once again not linked to functional impairment (Alghamri et al., 2013). In contrast, harsher Ang II infusion protocols (2.5 mg/kg/d for four weeks or 3.5 mg/kg/d for two weeks) caused greater myocardial remodeling associated with a decline in cardiac function in WT mice and primarily designed to test different therapeutic approaches (Lee et al., 2023, Ni et al., 2020). While CTR mice were able to compensatory maintain myocardial performance, TAM-treated *cmf*KO mice exhibited a severe structure-related deterioration of global cardiac function in response to sustained Ang II exposure *in vivo*, as evidence by a decline in %EF and %FS (s. Figure 25).

Moreover, STE-based echocardiography enabled the quantification of GLS, an important measure of longitudinal orientated fibers, which are particularly vulnerable to wall stress and represent an early marker of cardiac dysfunction (Brady et al., 2023, Liu et al., 2021a). Consistent with previous decline in cardiac function, *cmf*KO mice exhibited a pronounced impairment in global longitudinal LV deformation capacity compared with the respective unchallenged control group and Ang II treated CTR mice (s. Figure 27B). In addition, GLS proved to be an excellent predictor of myocardial fibrosis and adverse cardiac outcomes, as evidenced in recent studies involving both rat models and patients with heart failure (Cameli et al., 2016, Zhu et al., 2022, Fu et al., 2022). Consistent with the reduction in GLS, quantitative segmental analysis again revealed a pronounced limitation of LV deformation capacity in the longitudinal direction in *cmf*KO mice following Ang II exposure compared to the respective CTR group of mice and corresponding unchallenged control mice, further confirming their pro-fibrotic phenotype (Figure 29A-D). Furthermore, STE-based examinations of hypertensive patients demonstrated an association of changes in global radial deformation with the presence of LV concentric hypertrophy (Imbalzano et al., 2011, Oh and Park, 2022). Concordantly, quantitative segmental analyses revealed a markedly worsened LV deformation capacity in radial direction in both CTR and *cmf*KO mice, each accompanied by a significant pressure overload-induced increase in HW in comparison with the respective unchallenged control group (s. Figure 30A-D).

4.4 Limitation and outlook

The present work provides profound evidence for a cardioprotective role of the cGMP/cGKI cascade in CMFs during Ang II-mediated adverse cardiac remodeling. So far, the antifibrotic properties of cGKI were attributable to the tight regulation of CMF expansion. However, the underlying cellular mechanism by which the kinase modulates the deleterious CMF properties in the studied cardiac pathology model remains elusive so far.

One limitation of the current study is the pending verification of the functional cGMP signaling pathway in CMFs. In this respect, biochemical investigations of the cGKI-dependent

phosphorylation of VASP (serine^{239}) upon stimulation with distinct cGMP-modulating drugs (8-Br-cGMP, cinaciguat) can be exploited as a biomarker for the intracellular activity of the cGMP/cGKI cascade (Smolenski et al., 1998). To clarify this, determination of pVASP/VASP ratios in CMFs isolated from TAM and Ang II-treated *cmf*KO mice provides a reliable method to confirm the disruption of the cGMP signaling cascade, in particular the loss of cGKI function, compared with CTR-derived CMFs (*ongoing*). A complementary approach to monitor the cellular cGMP response can be enabled by the cGi500-L2 transgenic mouse strain (R26-CAG-cGi500(L2)), which, after mating with an appropriate Cre mouse line, allows the expression of FRET-based cGMP sensor (cGi500) according to the cell specific Cre-mediated recombination (Thunemann et al., 2013, Wen et al., 2018). Thus, crossing the transgenic *Postn*iCre$^{Tg/+}$ with the latter cGMP biosensor mouse line (*ongoing*) opens the possibility to specifically identify *in vivo* activated CMFs within primary CF/CMF cell cultures and to selectively monitor the cGMP dynamics in these cell population. Observation of intracellular changes in cGMP levels using various cGMP-enhancing compounds (ANP, CNP, cinaciguat, 8-Br-cGMP) could also shed more light on the expression and involvement of additional components of the NP/cGMP and NO/cGMP cascade in CMFs as well as the pharmacological responses of these cells to different cGMP elevating drugs.

Another open question concerns the activation of the catalytic activity of cGKI in CMFs. To investigate this aspect cardiac fibrosis, hypertrophy development, and function should be assessed in genetically modified mice lacking GC-activity (NO-GC, GC-A or GC-B) in *Postn*$^{+}$ CMFs. Moreover, the current evidence does not allow conclusions to be drawn on the extent to which the antifibrotic role of cGKI in CMFs is transferable to other cardiac pathologies / disease models such as fibrogenesis after MI or in HFpEF (Heinzel et al., 2020). For the latter disease model, a novel mouse model based on a high-fat diet (HFD) and inhibition of NOS by the application of N[w]-nitro-l-arginine methyl ester (L-NAME) was developed that recapitulated the various cardiovascular hallmarks of patients with HFpEF (Schiattarella et al., 2019). Following MI, CMFs serve a double-edged role, exhibiting both beneficial and detrimental properties depending on their spatial and temporal location (Turner and Porter, 2013). While CMFs are initially protective by replacing dead CMs through the deposition of collagen fibers, thereby protecting the heart from rupture, sustained activation of this cell type leads to deleterious myocardial fibrosis (Hall et al., 2021). Interference with CMF function or recruitment in the early phase of MI has been associated with ventricular wall thinning and propensity to late ruptures (Turner and Porter, 2013). Thus, mice with a specific deletion of SMAD3 in CMFs, generated by the employment of another *Postn* mouse model based on a constitutively active Cre recombinase, demonstrated a higher incidence for later rupture following non-reperfused infarction (Kong et al., 2018). *Vice versa*, ablation of *Postn*$^{+}$ cell in the subacute phase of MI was associated with a reduces myocardial fibrosis without compromising scar resistance (Kaur et al., 2016). In this context, it would be of utmost interest to explore the relevance of the cGMP signaling pathway in CMFs at the different stages after MI, which is enabled by the use of a TAM-inducible *Postn*iCre-recombinase.

Within the present work, the TAM application regime was chosen according to Kaur et al. (2016), describing the generation and functionality of the employed inducible Cre mouse line.

Verification of the protocol, comprising five days of TAM treatment initiated one day after the onset of sustained Ang II exposure, was performed using the double-transgenic ROSA$^{mT/mG}$ x *Postn*iCre$^{Tg/+}$ mice. Although we successfully confirmed the activation of the Cre recombinase by the expression of the green fluorescent mG protein (s. Figure 12-14), we cannot draw any conclusions on the recombination efficiency. In order to further characterize the degree of *Postn*iCre recombination, primary CF/CMF cell cultures from TAM and Ang II treated double transgenic animals should be separated according to the *Postn* expression to achieve a purified CMF culture. Subsequently, it would be necessary to determine the amount of *Postn*$^{+}$ cells expressing mG via fluorescence activated cell sorting (FACS) analysis. Moreover, the efficient clearance of TAM (100 mg/kg on three consecutive days) from the blood was described to occur already seven days after the i.p. application of the compound (Jahn et al., 2018). Transferring these outcomes to our study, a strong decline in plasma concentration after the restricted five-day TAM application is expected, which in turn strongly limits the time period of Cre activation during the 28-days of Ang II exposure. One consideration for further experiments would be to ensure the activation of the Cre recombinase throughout the entire Ang II treatment period by means of TAM food pellets or TAM diluted in drinking water, provided the latter is possible (Whitfield et al., 2015).

Interestingly, the observed antifibrotic actions of the CMF-specific cGKI were already established in the absence of pharmacological activation of the cGMP cascade. Consequently, the next major question arises whether the therapeutic potential of cGMP pathway activation is capable of attenuating or even reversing the Ang II-induced myocardial fibrosis by the cGMP/cGKI axis in CMFs *in vivo*. One possible approach represents the treatment of CTR and *cmf*KO mice with the sGC stimulator riociguat, which has previously been shown to reverse TAC-induced cardiac remodeling in WT mice (Rüdebusch et al., 2022).

Disruption of the cGMP signaling cascade was associated with an accelerated CMF proliferation rate, thus revealing an important anti-fibrotic function of the cGMP signaling pathway. Additional proliferation experiments involving treatment of primary CF/CMF cell cultures derived from TAM and Ang II-treated CTR and *cmf*KO mice with cGMP-elevating drugs in the presence or absence of Ang II or TGF-β should provide further insight into the anti-proliferative effect of the cGMP pathway activation in CMFs (*ongoing*).

Further studies are necessary to elucidate the potential downstream targets of cGKI in CMFs in order to gain a deeper understanding of the antifibrotic mechanisms induced by cGMP. First evidence for an interaction partner of cGKI was provided by a previous study by Li et al. (2008) demonstrating that cGKI-mediated phosphorylation of SMDA3 at serine^{309} and threonine^{388} prevents the TGF-β induced translocation of SMAD3 into the nucleus. However, examination of this cGKI-mediated phosphorylation in CMFs becomes challenging due to the unavailability of an antibody targeting the cGKI-specific SMAD3 phosphorylation sites.

5 Summary

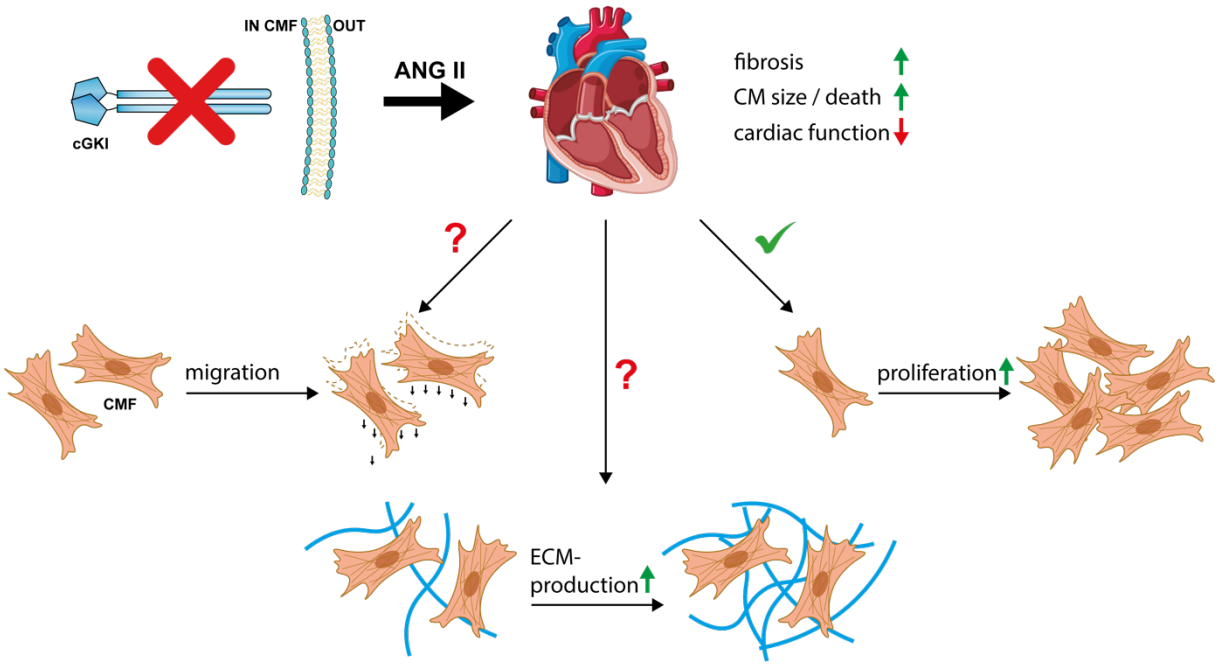

Figure 31: CMF-specific cGKI counteracts Ang II-mediated cardiac remodeling
The schematic depiction summarizes the consequences of a disruption of the cGMP/cGKI axis specifically in cardiac myofibroblasts (CMFs) in Ang II-induced cardiac remodelling. The present work focused on the investigation of the putative role of cGKI in *Postn*$^{+}$ CMFs in mediating the well-known antifibrotic actions of the NO/cGMP and NP/cGMP signaling cascade(s). To address this question, we generated mice with a specific deletion of cGKI in CMFs (*Postn*iCre$^{Tg/+}$ x cGKI$^{fl/fl}$; *cmf*KO) and corresponding littermate control animals (*Postn*iCre$^{Tg/+}$ x cGKI$^{+/+}$; CTR) by using a transgenic *Postn*iCre$^{Tg/+}$ mouse line expressing the tamoxifen (TAM)-inducible Cre recombinase controlled by the *Postn*-Promotor (Kaur et al., 2016). To induce cardiac remodeling, osmotic minipumps releasing Ang II over 28 days were implanted subcutaneously. CMF-specific Cre-recombination resulted in a pronounced reduction of cGKI expression levels in fibrotic heart areas as well as in primary CF/CMF cell cultures derived from TAM and Ang II-treated *cmf*KO mice. Interestingly, although both genotypes responded identically to Ang II in terms of blood pressure and heart weight, *cmf*KO mice exhibited a slightly increased myocardial vulnerability compared to Ang II-treated CTR animals. In line with this adverse outcome, Ang II challenged *cmf*KO mice displayed a significantly increased collagen deposition as well as cardiomyocyte (CM) cross sectional areas and cell death *versus* corresponding CTR animals. Furthermore, *cmf*KO mice showed a structure-related decline in global cardiac performance (%EF, %FS) and muscle deformation capacity following prolonged Ang II stimulation compared to corresponding CTR mice. Consistent with the observed phenotype *in vivo*, primary cardiac fibroblasts (CF)/CMFs isolated from Ang II-treated *cmf*KO mice exhibited accelerated proliferation behavior compared with CTR-derived CF/CMFs. Future studies are still required to address how cGKI contributes to further CMF characteristics including ECM-production and migration. Overall, the present work provides evidence for a cardioprotective role of the cGMP/cGKI cascade in CMF during Ang II-mediated cardiac remodeling, with these antifibrotic effects attributable to tight regulation of CMF expansion.

6 Zusammenfassung

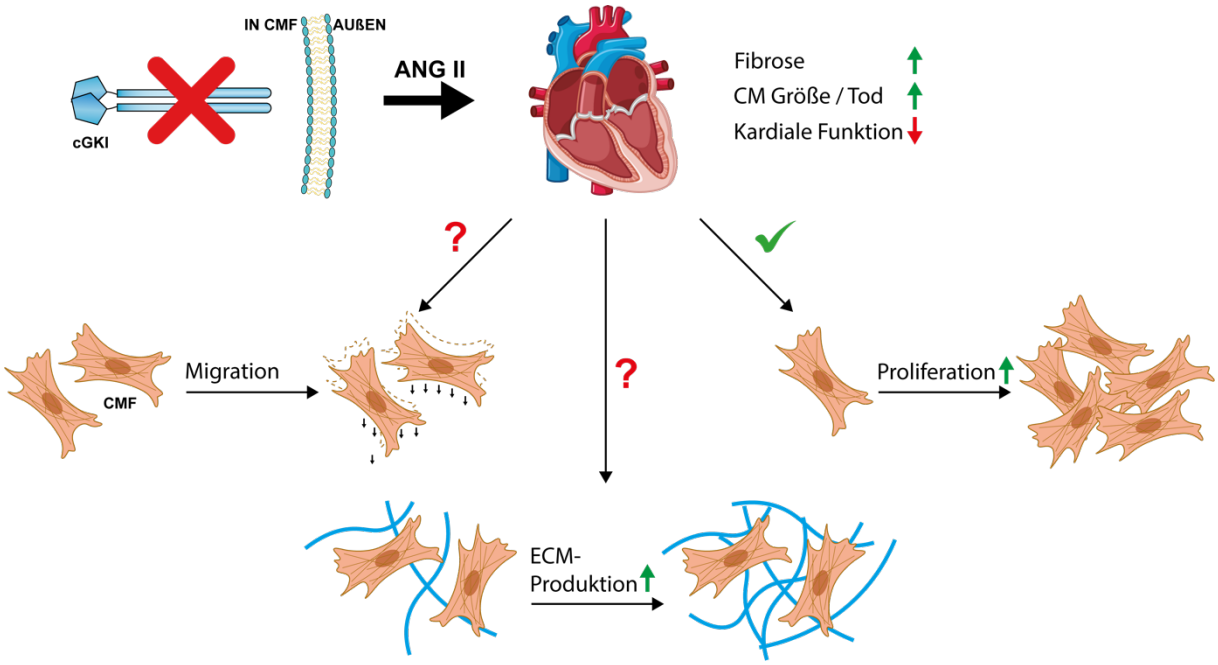

Figure 32: Die CMF-spezifische cGKI wirkt dem Ang II-vermittelten kardialen Remodeling entgegen
Die schematische Darstellung veranschaulicht die Auswirkungen einer Unterbrechung der cGMP/cGKI Signalkaskade in kardialen Myofibroblasten (CMFs) auf die Ang II vermittelten kardialen Umbauprozesse. Die vorliegende Arbeit konzentrierte sich auf die Untersuchung der mutmaßlichen Rolle der cGKI in *Postn*$^{+}$ CMFs bei der Vermittlung der allgemein anerkannten antifibrotischen Wirkung der NO/cGMP- und NP/cGMP-Signalkaskade. Um diese Fragestellung zu untersuchen, generierten wir Mäuse mit einer spezifischen Deletion der cGKI in CMFs (*Postn*iCre$^{Tg/+}$ x cGKI$^{fl/fl}$) und entsprechende Kontrolltiere (*Postn*iCre$^{Tg/+}$ x cGKI$^{+/+}$), indem wir die transgene Mauslinie *Postn*iCre$^{Tg/+}$, die die Tamoxifen (TAM) induzierte Cre Rekombinase unter der Kontrolle des *Postn* Promotors exprimiert (Kaur et al., 2016), verwendeten. Zur Induktion des kardialen Remodelings kamen subkutan implantierbare osmotische Minipumpen, die über 28 Tage hinweg kontinuierliche Ang II freisetzen, zur Anwendung. Die CMF-spezifische Rekombination führte zu einer deutlichen Senkung des cGKI-Expressionslevels sowohl in fibrotischen Herzarealen als auch in primären CF/CMF-Zellkulturen, die aus TAM- und Ang II behandelten *cmf*KO Mäuse isoliert wurden. Obwohl beide Genotypen hinsichtlich der Blutdruckerhöhung und Herzgewichtzunahme identisch auf die chronische Ang II Stimulation reagierten, wiesen *cmf*KO Mäuse interessanterweise eine leicht erhöhte Vulnerabilität im Vergleich zu den entsprechenden CTR-Tieren auf. In Übereinstimmung mit diesem Ergebnis, zeigten die Ang II behandelten *cmf*KO-Mäuse erhöhte kardiale Umbauprozesse, die durch eine erhöhte Fibroseentwicklung, sowie Kardiomyozyten (CM)-Querschnittsflächen, als auch durch einen Anstieg der CM-Zelltodrate zum Vorschein kamen. Darüber hinaus war in *cmf*KO-Mäusen im Vergleich zu den mit Ang II-behandelten CTR-Mäusen eine strukturbedingte Verschlechterung der globalen Herzleistung und der Muskeldeformationsfähigkeit erkennbar. Zugleich wiesen die primären kardialen Fibroblasten (CF)/CMFs, die aus Ang II behandelten *cmf*KO Mäusen isoliert wurden, ein schnelleres Proliferationsverhalten in Relation zu den CF/CMFs, die aus entsprechenden CTR-Tieren gewonnen wurden, auf. Um ferner ein Einfluss der cGKI auf weitere CMF-Eigenschaften zu analysieren sind weitere Untersuchungen hinsichtlich des Migrationsverhaltens sowie der ECM-Produktion vonnöten. Zusammenfassend lässt sich sagen, dass wir im Rahmen des Ang II-induzierten kardialen Umbauprozesses eine kardioprotektive Wirkung der cGMP/cGKI-Kaskade in CMFs nachweisen konnten. In diesem Zusammenhang waren die cGKI vermittelten antifibrotischen Effekte auf eine enge Regulierung der CMF-Expansion zurückzuführen.

7 Supplement

7.1 Comprehensive characterization of tissue-specific *Postn*iCre$^{Tg/+}$ mediated recombination under physiological conditions

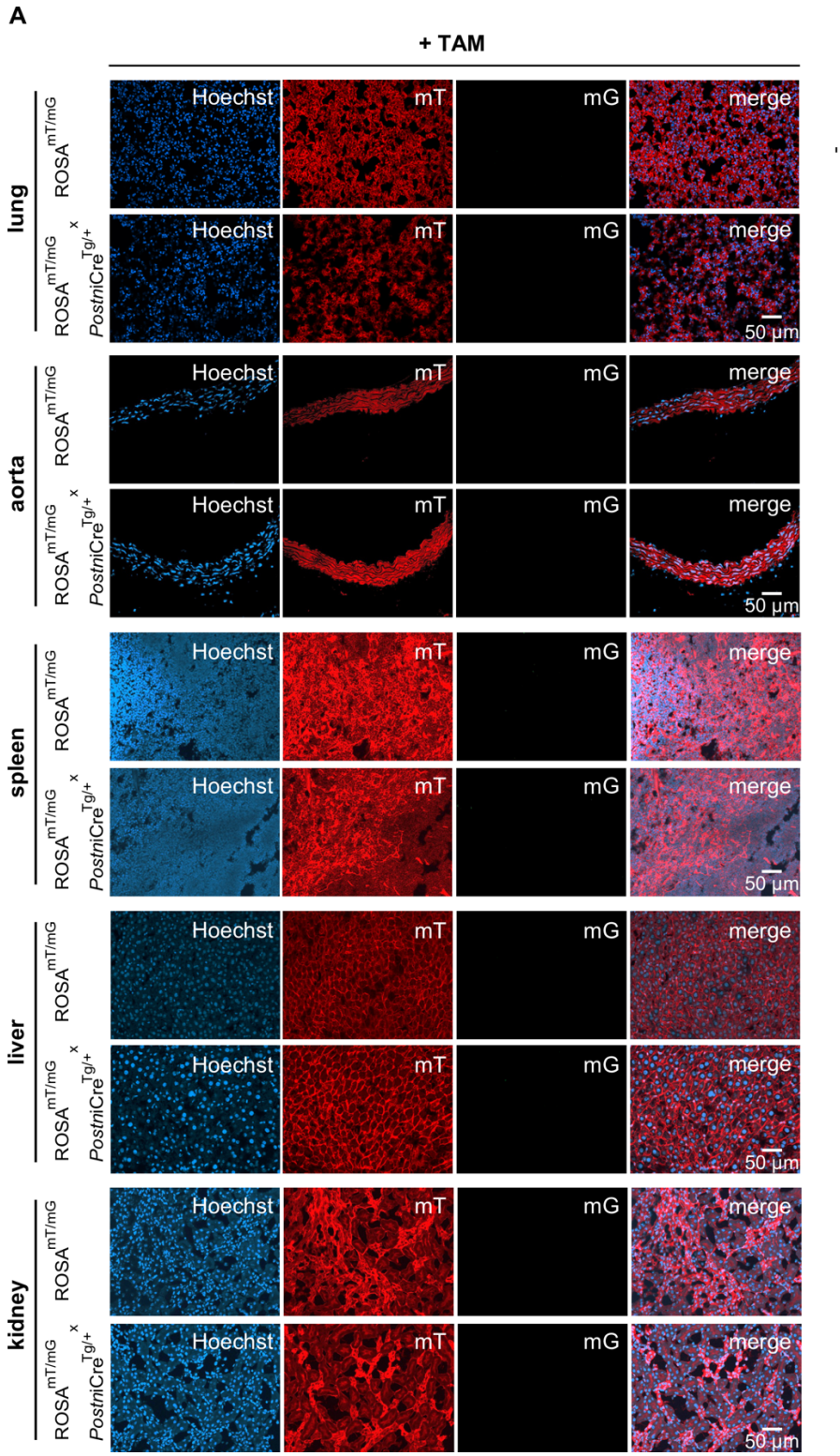

Figure 33: Lack of *Postn*iCre$^{Tg/+}$ recombinase expression in the absence of Ang II
Representative fluorescence images of distinct organs obtained from TAM-treated ROSA$^{mT/mG}$ and double transgenic ROSA$^{mT/mG}$ x *Postn*iCre$^{Tg/+}$ animals. Both genotypes demonstrated a ubiquitous

expression of the red fluorescent mT protein under physiological conditions. Analysis of n=3 tissue cryosections per organ derived from N=3 animals per genotype. Cell nuclei (blue) were stained by Hoechst.

7.2 TAM mediated Cre-recombination has no impact on BW and TL

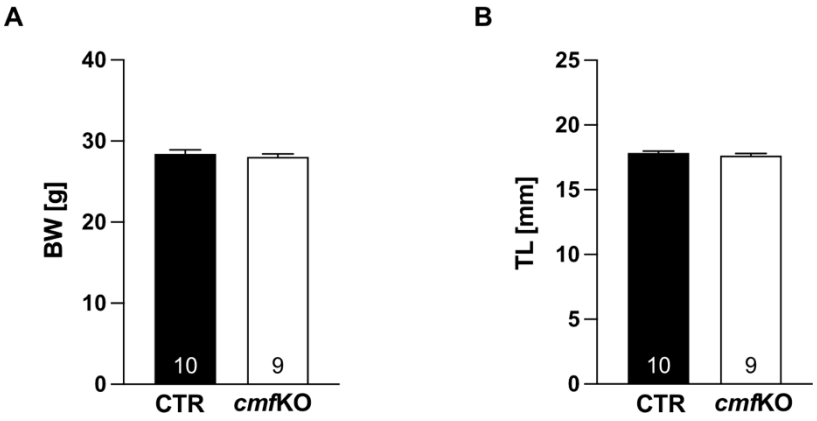

Figure 34: Normal development of *cmf*KO mutants following TAM-mediated Cre-recombination *in vivo*
Upon TAM-mediated Cre-recombination *in vivo*, *cmf*KO mutants developed normally compared to CTR mice as indicated by both (**A**) equivalent BW (CTR = 28.41 ± 0.52 g; *cmf*KO = 28.04 ± 0.39 g) and (**B**) TL (CTR = 17.84 ± 0.14 mm; *cmf*KO = 17.64 ± 0.16 mm). Statistical analyses: Unpaired t-test (**A, B**). All bar diagrams presented as means + SEM with CTR_{TAM}: N=10, *cmf*KO_{TAM}: N=9.

7.3 Exemplary representation of the longitudinal deformation rate and velocity under patho-/physiological conditions

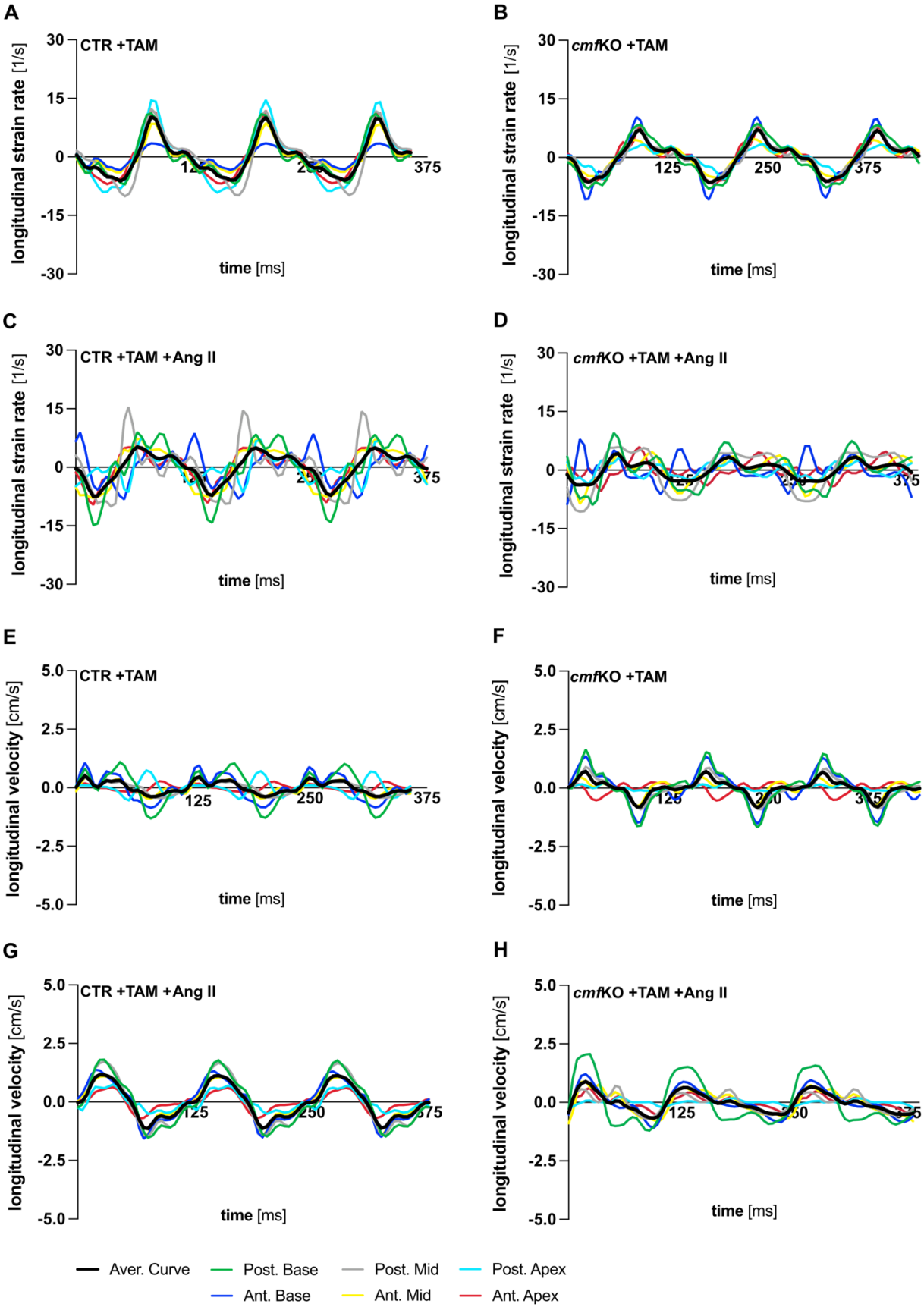

Figure 35: Exemplary graphical representation of curvilinear data on longitudinal strain rate and velocity of LV endocardial deformation
Data were acquired using STE-based echocardiography in the B-mode view in PSLAX. Visualization of the (**A-D**) strain rate and (**E-H**) velocity over three cardiac cycles of CTR and *cmf*KO mice after TAM treatment alone or additional sustained stimulation with Ang II. Longitudinal strain of the distinct segments was displayed with the following color pattern: green (posterior base), grey (posterior mid), turquoise (posterior apex), blue (anterior base), yellow (anterior mid), red (anterior apex), black (averaged curve).

7.4 Exemplary representation of the radial strain, strain rate and velocity under patho-/physiological conditions

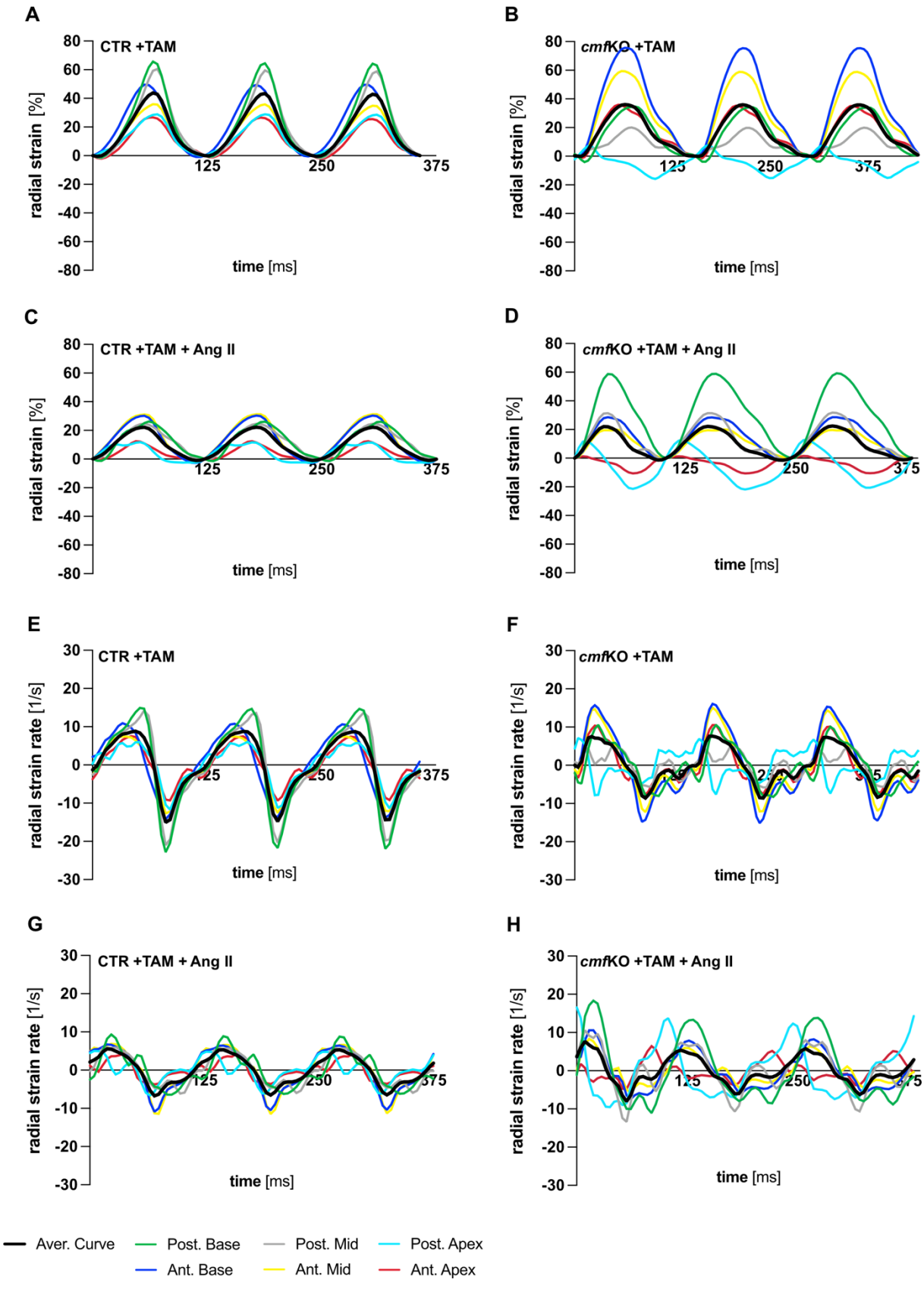

Figure 36: Exemplary graphical representation of curvilinear data on radial strain and strain rate of LV endocardial deformation
Data were acquired using STE-based echocardiography in the B-mode view in PSLAX. Visualization of the (**A-D**) strain and (**E-H**) strain rate over three cardiac cycles of CTR and *cmf*KO mice after TAM treatment alone or additional sustained stimulation with Ang II. Radial strain of the distinct segments was displayed with the following color pattern: green (posterior base), grey (posterior mid), turquoise (posterior apex), blue (anterior base), yellow (anterior mid), red (anterior apex), black (averaged curve).

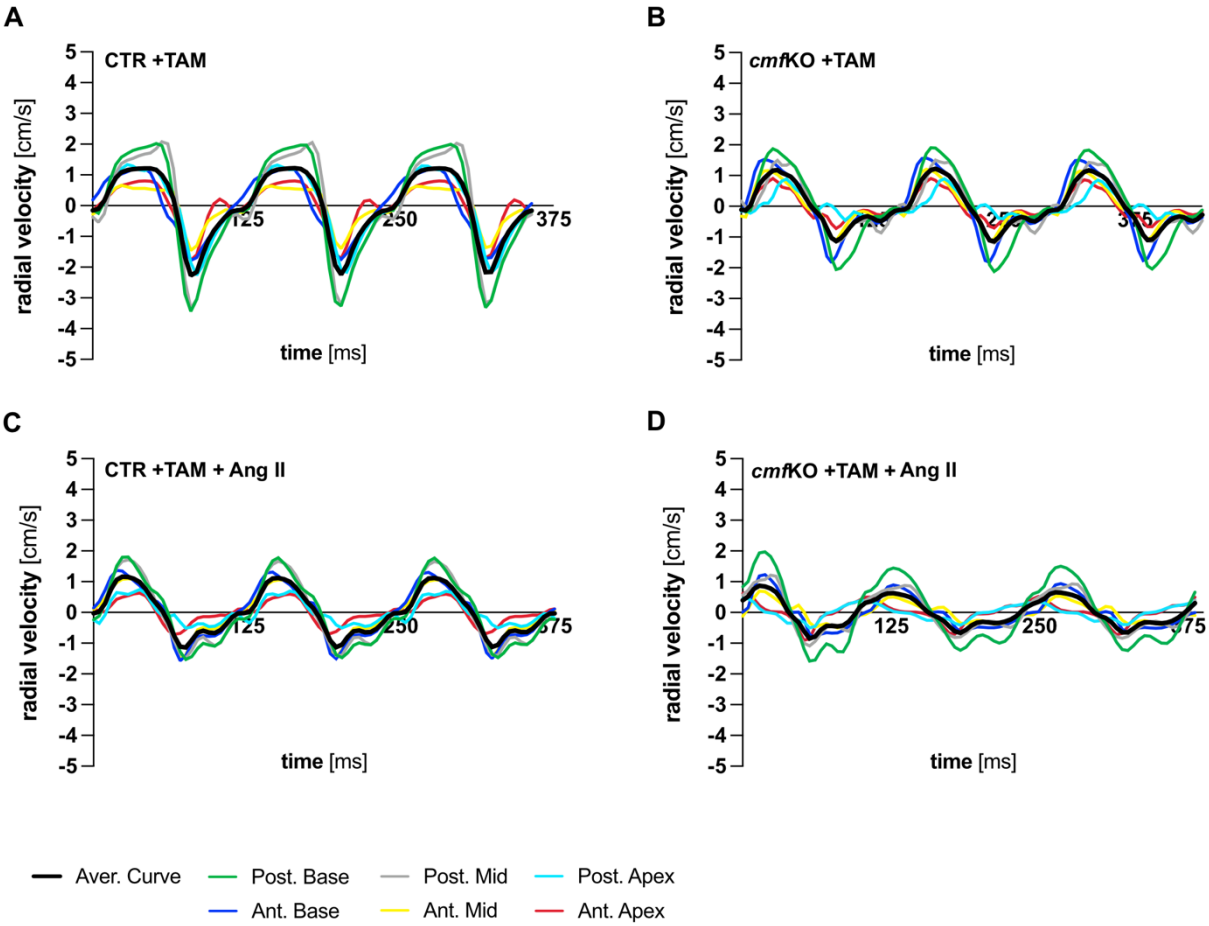

Figure 37: Exemplary graphical representation of curvilinear data on radial velocity of LV endocardial deformation
Data were acquired using STE-based echocardiography in the B-mode view in PSLAX. Visualization of the radial velocity over three cardiac cycles of CTR and *cmf*KO mice after TAM treatment alone or additional sustained stimulation with Ang II. Radial velocity of the distinct segments was displayed with the following color pattern: green (posterior base), grey (posterior mid), turquoise (posterior apex), blue (anterior base), yellow (anterior mid), red (anterior apex), black (averaged curve).

8 Bibliography

ABDELAZIZ, N., COLOMBO, F., MERCIER, I. & CALDERONE, A. 2001. Nitric Oxide Attenuates the Expression of Transforming Growth Factor-β₃ mRNA in Rat Cardiac Fibroblasts via Destabilization. *Hypertension,* 38, 261-266.

ABDUL-HAFEZ, A., SHU, R. & UHAL, B. D. 2009. JunD and HIF-1alpha mediate transcriptional activation of angiotensinogen by TGF-beta1 in human lung fibroblasts. *Faseb j,* 23, 1655-62.

AGAH, R., FRENKEL, P. A., FRENCH, B. A., MICHAEL, L. H., OVERBEEK, P. A. & SCHNEIDER, M. D. 1997. Gene recombination in postmitotic cells. Targeted expression of Cre recombinase provokes cardiac-restricted, site-specific rearrangement in adult ventricular muscle in vivo. *J Clin Invest,* 100, 169-79.

AKTAN, F. 2004. iNOS-mediated nitric oxide production and its regulation. *Life Sciences,* 75, 639-653.

ALEXANIAN, M. & HALDAR, S. M. 2018. The Cardiac Myofibroblast. *Circ Res,* 123, 1258-1260.

ALGHAMRI, M. S., WEIR, N. M., ANSTADT, M. P., ELASED, K. M., GURLEY, S. B. & MORRIS, M. 2013. Enhanced Angiotensin II-Induced Cardiac and Aortic Remodeling in ACE2 Knockout Mice. *Journal of Cardiovascular Pharmacology and Therapeutics,* 18, 138-151.

ALVAREZ, D., BRIASSOULI, P., CLANCY, R. M., ZAVADIL, J., REED, J. H., ABELLAR, R. G., HALUSHKA, M., FOX-TALBOT, K., BARRAT, F. J. & BUYON, J. P. 2011. A Novel Role of Endothelin-1 in Linking Toll-like Receptor 7-mediated Inflammation to Fibrosis in Congenital Heart Block*. *Journal of Biological Chemistry,* 286, 30444-30454.

ALZOBAIDI, N., REHMAN, S., NAQVI, M., GULATI, K. & RAY, A. 2022. Periostin: A Potential Biomarker and Therapeutic Target in Pulmonary Diseases. *J Pharm Pharm Sci,* 25, 137-148.

ANDERSEN, M. J., ERSBØLL, M., AXELSSON, A., GUSTAFSSON, F., HASSAGER, C., KØBER, L., BORLAUG, B. A., BOESGAARD, S., SKOVGAARD, L. T. & MØLLER, J. E. 2013. Sildenafil and Diastolic Dysfunction After Acute Myocardial Infarction in Patients With Preserved Ejection Fraction. *Circulation,* 127, 1200-1208.

ANDERSON, K. R., SUTTON, M. G. & LIE, J. T. 1979. Histopathological types of cardiac fibrosis in myocardial disease. *J Pathol,* 128, 79-85.

ANTONIAK, S., PHUNGPHONG, S., CHENG, Z. & JENSEN, B. C. 2021. Novel Mechanisms of Anthracycline-Induced Cardiovascular Toxicity: A Focus on Thrombosis, Cardiac Atrophy, and Programmed Cell Death. *Front Cardiovasc Med,* 8, 817977.

AOKI, H. & IZUMO, S. 2001. CHAPTER 58 - Signal Transduction of Cardiac Myocyte Hypertrophy. *In:* SPERELAKIS, N., KURACHI, Y., TERZIC, A. & COHEN, M. V. (eds.) *Heart Physiology and Pathophysiology (Fourth Edition).* San Diego: Academic Press.

ARMSTRONG, P. W., LAM, C. S. P., ANSTROM, K. J., EZEKOWITZ, J., HERNANDEZ, A. F., O'CONNOR, C. M., PIESKE, B., PONIKOWSKI, P., SHAH, S. J., SOLOMON, S. D., VOORS, A. A., SHE, L., VLAJNIC, V., CARVALHO, F., BAMBER, L., BLAUSTEIN, R. O., ROESSIG, L. & BUTLER, J. 2020a. Effect of Vericiguat vs Placebo on Quality of Life in Patients With Heart Failure and Preserved Ejection Fraction: The VITALITY-HFpEF Randomized Clinical Trial. *Jama,* 324, 1512-1521.

ARMSTRONG, P. W., PIESKE, B., ANSTROM, K. J., EZEKOWITZ, J., HERNANDEZ, A. F., BUTLER, J., LAM, C. S. P., PONIKOWSKI, P., VOORS, A. A., JIA, G., MCNULTY, S. E., PATEL, M. J., ROESSIG, L., KOGLIN, J. & O'CONNOR, C. M. 2020b. Vericiguat in Patients with Heart Failure and Reduced Ejection Fraction. *N Engl J Med,* 382, 1883-1893.

ASSMANN, G., CULLEN, P., EVERS, T., PETZINNA, D. & SCHULTE, H. 2005. Importance of arterial pulse pressure as a predictor of coronary heart disease risk in PROCAM. *European Heart Journal,* 26, 2120-2126.

ATAABADI, E. A., GOLSHIRI, K., JÜTTNER, A., KRENNING, G., DANSER, A. H. J. & ROKS, A. J. M. 2020. Nitric Oxide-cGMP Signaling in Hypertension. *Hypertension,* 76, 1055-1068.

AUJLA, P. K. & KASSIRI, Z. 2021. Diverse origins and activation of fibroblasts in cardiac fibrosis. *Cellular Signalling,* 78, 109869.

BAGEGHNI, S. A., HEMMINGS, K. E., ZAVA, N., DENTON, C. P., PORTER, K. E., AINSCOUGH, J. F. X., DRINKHILL, M. J. & TURNER, N. A. 2018. Cardiac fibroblast-specific p38α MAP kinase promotes cardiac hypertrophy via a putative paracrine interleukin-6 signaling mechanism. *Faseb j,* 32, 4941-4954.

BAI, J., ZHANG, N., HUA, Y., WANG, B., LING, L., FERRO, A. & XU, B. 2013. Metformin inhibits angiotensin II-induced differentiation of cardiac fibroblasts into myofibroblasts. *PLoS One,* 8, e72120.

BANSAL, M. & KASLIWAL, R. R. 2013. How do I do it? Speckle-tracking echocardiography. *Indian Heart J,* 65, 117-23.

BAUDINO, T. A., CARVER, W., GILES, W. & BORG, T. K. 2006. Cardiac fibroblasts: friend or foe? *American Journal of Physiology-Heart and Circulatory Physiology,* 291, H1015-H1026.

BAUER, M., CHENG, S., JAIN, M., NGOY, S., THEODOROPOULOS, C., TRUJILLO, A., LIN, F. C. & LIAO, R. 2011. Echocardiographic speckle-tracking based strain imaging for rapid cardiovascular phenotyping in mice. *Circ Res,* 108, 908-16.

BAUM, J. & DUFFY, H. S. 2011. Fibroblasts and myofibroblasts: what are we talking about? *J Cardiovasc Pharmacol,* 57, 376-9.

BAYNE, K. 2018. Environmental enrichment and mouse models: Current perspectives. *Animal Model Exp Med,* 1, 82-90.

BENETOS, A., SAFAR, M., RUDNICHI, A., SMULYAN, H., RICHARD, J.-L., DUCIMETIÈRE, P. & GUIZE, L. 1997. Pulse Pressure. *Hypertension,* 30, 1410-1415.

BERNARDO, B. C., WEEKS, K. L., PRETORIUS, L. & MCMULLEN, J. R. 2010. Molecular distinction between physiological and pathological cardiac hypertrophy: Experimental findings and therapeutic strategies. *Pharmacology & Therapeutics,* 128, 191-227.

BIEL, M. & MICHALAKIS, S. 2009. Cyclic nucleotide-gated channels. *Handb Exp Pharmacol*, 111-36.

BIEL, M., SAUTTER, A., LUDWIG, A., HOFMANN, F. & ZONG, X. 1998. Cyclic nucleotide-gated channels--mediators of NO:cGMP-regulated processes. *Naunyn Schmiedebergs Arch Pharmacol,* 358, 140-4.

BOGOYEVITCH, M. A., GLENNON, P. E., ANDERSSON, M. B., CLERK, A., LAZOU, A., MARSHALL, C. J., PARKER, P. J. & SUGDEN, P. H. 1994. Endothelin-1 and fibroblast growth factors stimulate the mitogen-activated protein kinase signaling cascade in cardiac myocytes. The potential role of the cascade in the integration of two signaling pathways leading to myocyte hypertrophy. *J Biol Chem,* 269, 1110-9.

BONDERMAN, D., GHIO, S., FELIX, S. B., GHOFRANI, H.-A., MICHELAKIS, E., MITROVIC, V., OUDIZ, R. J., BOATENG, F., SCALISE, A.-V., ROESSIG, L. & SEMIGRAN, M. J. 2013. Riociguat for Patients With Pulmonary Hypertension Caused by Systolic Left Ventricular Dysfunction. *Circulation,* 128, 502-511.

BONDERMAN, D., PRETSCH, I., STERINGER-MASCHERBAUER, R., JANSA, P., ROSENKRANZ, S., TUFARO, C., BOJIC, A., LAM, C. S. P., FREY, R., OCHAN KILAMA, M., UNGER, S., ROESSIG, L. & LANG, I. M. 2014. Acute hemodynamic effects of riociguat in patients with pulmonary hypertension associated with diastolic heart failure (DILATE-1): a randomized, double-blind, placebo-controlled, single-dose study. *Chest,* 146, 1274-1285.

BOOZ, G. W. & BAKER, K. M. 1996. Role of Type 1 and Type 2 Angiotensin Receptors in Angiotensin II–Induced Cardiomyocyte Hypertrophy. *Hypertension,* 28, 635-640.

BORK, N. I. & NIKOLAEV, V. O. 2018. cGMP Signaling in the Cardiovascular System-The Role of Compartmentation and Its Live Cell Imaging. *International journal of molecular sciences,* 19, 801.

BOZKURT, B., COATS, A. J. S., TSUTSUI, H., ABDELHAMID, M., ADAMOPOULOS, S., ALBERT, N., ANKER, S. D., ATHERTON, J., BÖHM, M., BUTLER, J., DRAZNER, M. H., FELKER, G. M., FILIPPATOS, G., FONAROW, G. C., FIUZAT, M., GOMEZ-MESA, J. E., HEIDENREICH, P., IMAMURA, T., JANUZZI, J., JANKOWSKA, E. A., KHAZANIE, P., KINUGAWA, K., LAM, C. S. P., MATSUE, Y., METRA, M., OHTANI, T., FRANCESCO PIEPOLI, M., PONIKOWSKI, P., ROSANO, G. M. C., SAKATA, Y., SEFEROVIĆ, P., STARLING, R. C., TEERLINK, J. R., VARDENY, O., YAMAMOTO, K., YANCY, C., ZHANG, J. & ZIEROTH, S. 2021. Universal Definition and Classification of Heart Failure: A Report of the Heart Failure Society of America, Heart Failure Association of the European Society of Cardiology, Japanese Heart Failure Society and Writing Committee of the Universal Definition of Heart Failure. *Journal of Cardiac Failure,* 27, 387-413.

BOZKURT, B., NAIR, A. P., MISRA, A., SCOTT, C. Z., MAHAR, J. H. & FEDSON, S. 2023. Neprilysin Inhibitors in Heart Failure: The Science, Mechanism of Action, Clinical Studies, and Unanswered Questions. *JACC Basic Transl Sci,* 8, 88-105.

BRADY, B., KING, G., MURPHY, R. T. & WALSH, D. 2023. Myocardial strain: a clinical review. *Ir J Med Sci,* 192, 1649-1656.

BROEKMANS, K., GIESEN, J., MENGES, L., KOESLING, D. & RUSSWURM, M. 2020. Angiotensin II-Induced Cardiovascular Fibrosis Is Attenuated by NO-Sensitive Guanylyl Cyclase1. *Cells,* 9.

BROWN, R. D., AMBLER, S. K., MITCHELL, M. D. & LONG, C. S. 2005. The cardiac fibroblast: therapeutic target in myocardial remodeling and failure. *Annu Rev Pharmacol Toxicol,* 45, 657-87.

BROWNING, D. D., MCSHANE, M. P., MARTY, C. & YE, R. D. 2000. Nitric oxide activation of p38 mitogen-activated protein kinase in 293T fibroblasts requires cGMP-dependent protein kinase. *J Biol Chem,* 275, 2811-6.

BUGLIONI, A. & JR., J. C. B. 2016. New Pharmacological Strategies to Increase cGMP. *Annual Review of Medicine,* 67, 229-243.

BUYS, E. & SIPS, P. 2014. New insights into the role of soluble guanylate cyclase in blood pressure regulation. *Curr Opin Nephrol Hypertens,* 23, 135-42.

CAMELI, M., MONDILLO, S., RIGHINI, F. M., LISI, M., DOKOLLARI, A., LINDQVIST, P., MACCHERINI, M. & HENEIN, M. 2016. Left Ventricular Deformation and Myocardial Fibrosis in Patients With Advanced Heart Failure Requiring Transplantation. *J Card Fail,* 22, 901-907.

CANIFFI, C., ELESGARAY, R., GIRONACCI, M., ARRANZ, C. & COSTA, M. Á. 2010. C-type natriuretic peptide effects on cardiovascular nitric oxide system in spontaneously hypertensive rats. *Peptides,* 31, 1309-1318.

CAREY, R. M. 2005. Angiotensin type-2 receptors and cardiovascular function: are angiotensin type-2 receptors protective? *Current Opinion in Cardiology,* 20, 264-269.

CAREY, R. M. & PARK, J. 2006. Role of Angiotensin Type 2 Receptors in Vasodilation of Resistance and Capacitance Vessels. *Hypertension,* 48, 824-825.

CARTLEDGE, J. E., KANE, C., DIAS, P., TESFOM, M., CLARKE, L., MCKEE, B., AL AYOUBI, S., CHESTER, A., YACOUB, M. H., CAMELLITI, P. & TERRACCIANO, C. M. 2015. Functional crosstalk between cardiac fibroblasts and adult cardiomyocytes by soluble mediators. *Cardiovascular Research,* 105, 260-270.

CHEN, K., CHEN, J., LI, D., ZHANG, X. & MEHTA, J. L. 2004. Angiotensin II Regulation of Collagen Type I Expression in Cardiac Fibroblasts. *Hypertension,* 44, 655-661.

CLAYTON, S. W., BAN, G. I., LIU, C. & SERRA, R. 2020. Canonical and noncanonical TGF-β signaling regulate fibrous tissue differentiation in the axial skeleton. *Scientific Reports,* 10, 21364.

COLUCCI, W. S. 2001. Nesiritide for the treatment of decompensated heart failure. *J Card Fail,* 7, 92-100.

CONOLE, D. & SCOTT, L. J. 2013. Riociguat: first global approval. *Drugs,* 73, 1967-75.

COSTA, M. A., ELESGARAY, R., CANIFFI, C., FELLET, A. & ARRANZ, C. 2007. Role of cardiovascular nitric oxide system in C-type natriuretic peptide effects. *Biochem Biophys Res Commun,* 359, 180-6.

COWLING, R. T., KUPSKY, D., KAHN, A. M., DANIELS, L. B. & GREENBERG, B. H. 2019. Mechanisms of cardiac collagen deposition in experimental models and human disease. *Translational Research,* 209, 138-155.

CRABOS, M., ROTH, M., HAHN, A. W. & ERNE, P. 1994. Characterization of angiotensin II receptors in cultured adult rat cardiac fibroblasts. Coupling to signaling systems and gene expression. *J Clin Invest,* 93, 2372-8.

DALLA COSTA, A. P., CLEMENTE, C. F. M. Z., CARVALHO, H. F., CARVALHEIRA, J. B., NADRUZ, W., JR & FRANCHINI, K. G. 2009. FAK mediates the activation of cardiac fibroblasts induced by mechanical stress through regulation of the mTOR complex. *Cardiovascular Research,* 86, 421-431.

DANDEL, M., LEHMKUHL, H., KNOSALLA, C., SURAMELASHVILI, N. & HETZER, R. 2009. Strain and strain rate imaging by echocardiography - basic concepts and clinical applicability. *Curr Cardiol Rev,* 5, 133-48.

DAO, V. T.-V., ELBATREEK, M. H., DEILE, M., NEDVETSKY, P. I., GÜLDNER, A., IBARRA-ALVARADO, C., GÖDECKE, A. & SCHMIDT, H. H. H. W. 2020. Non-canonical chemical feedback self-limits nitric oxide-cyclic GMP signaling in health and disease. *Scientific Reports,* 10, 10012.

DARBY, I., SKALLI, O. & GABBIANI, G. 1990. Alpha-smooth muscle actin is transiently expressed by myofibroblasts during experimental wound healing. *Lab Invest,* 63, 21-9.

DASKALOPOULOS, E. P., JANSSEN, B. J. A. & BLANKESTEIJN, W. M. 2012. Myofibroblasts in the Infarct Area: Concepts and Challenges. *Microscopy and Microanalysis,* 18, 35-49.

DAVIS, J., BURR, A. R., DAVIS, G. F., BIRNBAUMER, L. & MOLKENTIN, J. D. 2012. A TRPC6-dependent pathway for myofibroblast transdifferentiation and wound healing in vivo. *Dev Cell,* 23, 705-15.

DAVIS, J. & MOLKENTIN, J. D. 2014. Myofibroblasts: trust your heart and let fate decide. *J Mol Cell Cardiol,* 70, 9-18.

DESMOULIÈRE, A., REDARD, M., DARBY, I. & GABBIANI, G. 1995. Apoptosis mediates the decrease in cellularity during the transition between granulation tissue and scar. *Am J Pathol,* 146, 56-66.

DÍAZ-ARAYA, G., VIVAR, R., HUMERES, C., BOZA, P., BOLIVAR, S. & MUÑOZ, C. 2015. Cardiac fibroblasts as sentinel cells in cardiac tissue: Receptors, signaling pathways and cellular functions. *Pharmacological Research,* 101, 30-40.

DIEP, Q. N., MABROUK, M. E., YUE, P. & SCHIFFRIN, E. L. 2002. Effect of AT1 receptor blockade on cardiac apoptosis in angiotensin II-induced hypertension. *American Journal of Physiology-Heart and Circulatory Physiology,* 282, H1635-H1641.

DIWAN, A. & GERALD W. DORN, I. 2007. Decompensation of Cardiac Hypertrophy: Cellular Mechanisms and Novel Therapeutic Targets. *Physiology,* 22, 56-64.

DOBACZEWSKI, M., GONZALEZ-QUESADA, C. & FRANGOGIANNIS, N. G. 2010. The extracellular matrix as a modulator of the inflammatory and reparative response following myocardial infarction. *J Mol Cell Cardiol,* 48, 504-11.

DOMENIGHETTI, A. A., WANG, Q., EGGER, M., RICHARDS, S. M., PEDRAZZINI, T. & DELBRIDGE, L. M. D. 2005. Angiotensin II–Mediated Phenotypic Cardiomyocyte Remodeling Leads to Age-Dependent Cardiac Dysfunction and Failure. *Hypertension,* 46, 426-432.

DORAFSHAN, S., RAZMI, M., SAFAEI, S., GENTILIN, E., MADJD, Z. & GHODS, R. 2022. Periostin: biology and function in cancer. *Cancer Cell International,* 22, 315.

DUANGRAT, R., PARICHATIKANOND, W., LIKITNUKUL, S. & MANGMOOL, S. 2023a. Endothelin-1 Induces Cell Proliferation and Myofibroblast Differentiation through the ETAR/Gαq/ERK Signaling Pathway in Human Cardiac Fibroblasts. *International Journal of Molecular Sciences,* 24, 4475.

DUANGRAT, R., PARICHATIKANOND, W. & MANGMOOL, S. 2023b. Dual Blockade of TGF-β Receptor and Endothelin Receptor Synergistically Inhibits Angiotensin II-Induced Myofibroblast Differentiation: Role of AT(1)R/G(αq)-Mediated TGF-β1 and ET-1 Signaling. *Int J Mol Sci,* 24.

DUANGRAT, R., PARICHATIKANOND, W., MORALES, N. P., PINTHONG, D. & MANGMOOL, S. 2022. Sustained AT(1)R stimulation induces upregulation of growth factors in human cardiac fibroblasts via G(αq)/TGF-β/ERK signaling that influences myocyte hypertrophy. *Eur J Pharmacol,* 937, 175384.

EL-KHUFFASH, A., SCHUBERT, U., LEVY, P. T., NESTAAS, E. & DE BOODE, W. P. 2018. Deformation imaging and rotational mechanics in neonates: a guide to image acquisition, measurement, interpretation, and reference values. *Pediatr Res,* 84, 30-45.

EULER, G. 2015. Good and bad sides of TGFβ-signaling in myocardial infarction. *Front Physiol,* 6, 66.

FAN, D., TAKAWALE, A., LEE, J. & KASSIRI, Z. 2012. Cardiac fibroblasts, fibrosis and extracellular matrix remodeling in heart disease. *Fibrogenesis Tissue Repair,* 5, 15.

FATIMA, N., PATEL, S. N. & HUSSAIN, T. 2021. Angiotensin II Type 2 Receptor: A Target for Protection Against Hypertension, Metabolic Dysfunction, and Organ Remodeling. *Hypertension,* 77, 1845-1856.

FAUL, C. 2017. Cardiac actions of fibroblast growth factor 23. *Bone,* 100, 69-79.

FIEDLER, B., FEIL, R., HOFMANN, F., WILLENBOCKEL, C., DREXLER, H., SMOLENSKI, A., LOHMANN, S. M. & WOLLERT, K. C. 2006. cGMP-dependent Protein Kinase Type I Inhibits TAB1-p38 Mitogen-activated Protein Kinase Apoptosis Signaling in Cardiac Myocytes *. *Journal of Biological Chemistry,* 281, 32831-32840.

FISCHER, A. H., JACOBSON, K. A., ROSE, J. & ZELLER, R. 2008. Hematoxylin and eosin staining of tissue and cell sections. *CSH Protoc,* 2008, pdb.prot4986.

FLACHSKAMPF, F. A., BLANKSTEIN, R., GRAYBURN, P. A., KRAMER, C. M., KWONG, R. Y. K., MARWICK, T. H., NAGEL, E., SENGUPTA, P. P., ZOGHBI, W. A. & CHANDRASHEKHAR, Y. 2019. Global Longitudinal Shortening: A Positive Step Towards Reducing Confusion Surrounding Global Longitudinal Strain. *JACC Cardiovasc Imaging,* 12, 1566-1567.

FÖRSTERMANN, U. & SESSA, W. C. 2012. Nitric oxide synthases: regulation and function. *Eur Heart J,* 33, 829-37, 837a-837d.

FOUNTAIN, J. H., KAUR, J. & LAPPIN, S. L. 2023. Physiology, Renin Angiotensin System. *StatPearls.* Treasure Island (FL): StatPearls Publishing

Copyright © 2023, StatPearls Publishing LLC.

FRANCIS, S. H., BUSCH, J. L., CORBIN, J. D. & SIBLEY, D. 2010. cGMP-dependent protein kinases and cGMP phosphodiesterases in nitric oxide and cGMP action. *Pharmacol Rev,* 62, 525-63.

FRANCIS, S. H., TURKO, I. V. & CORBIN, J. D. 2001. Cyclic nucleotide phosphodiesterases: relating structure and function. *Prog Nucleic Acid Res Mol Biol,* 65, 1-52.

FRANGOGIANNIS, N. G. 2020. Cardiac fibrosis. *Cardiovascular Research,* 117, 1450-1488.

FRANKENREITER, S., BEDNARCZYK, P., KNIESS, A., BORK, N. I., STRAUBINGER, J., KOPROWSKI, P., WRZOSEK, A., MOHR, E., LOGAN, A., MURPHY, M. P., GAWAZ, M., KRIEG, T., SZEWCZYK, A., NIKOLAEV, V. O., RUTH, P. & LUKOWSKI, R. 2017. cGMP-Elevating Compounds and Ischemic Conditioning Provide Cardioprotection Against Ischemia and Reperfusion Injury via Cardiomyocyte-Specific BK Channels. *Circulation,* 136, 2337-2355.

FRANTZ, S., KLAIBER, M., BABA, H. A., OBERWINKLER, H., VÖLKER, K., GABNER, B., BAYER, B., ABEBER, M., SCHUH, K., FEIL, R., HOFMANN, F. & KUHN, M. 2011. Stress-dependent dilated cardiomyopathy in mice with cardiomyocyte-restricted inactivation of cyclic GMP-dependent protein kinase I. *European Heart Journal,* 34, 1233-1244.

FRIEBE, A., MERGIA, E., DANGEL, O., LANGE, A. & KOESLING, D. 2007. Fatal gastrointestinal obstruction and hypertension in mice lacking nitric oxide-sensitive guanylyl cyclase. *Proc Natl Acad Sci U S A,* 104, 7699-704.

FU, L., RUAN, Q., YOU, Z., HUANG, H., CHEN, Y., CHENG, S., YAN, L., CAI, H., CHEN, Y., LIN, D., CHEN, H. & HUANG, C. 2022. Investigation of Left Ventricular Strain and Its Morphological Basis During Different Stages of Diastolic and Systolic Dysfunction in Spontaneously Hypertensive Rat. *Am J Hypertens,* 35, 423-432.

FUJISAKI, H., ITO, H., HIRATA, Y., TANAKA, M., HATA, M., LIN, M., ADACHI, S., AKIMOTO, H., MARUMO, F. & HIROE, M. 1995. Natriuretic peptides inhibit angiotensin II-induced proliferation of rat cardiac fibroblasts by blocking endothelin-1 gene expression. *J Clin Invest,* 96, 1059-65.

GALIÈ, N., HUMBERT, M., VACHIERY, J. L., GIBBS, S., LANG, I., TORBICKI, A., SIMONNEAU, G., PEACOCK, A., VONK NOORDEGRAAF, A., BEGHETTI, M., GHOFRANI, A., GOMEZ SANCHEZ, M. A., HANSMANN, G., KLEPETKO, W., LANCELLOTTI, P., MATUCCI, M., MCDONAGH, T., PIERARD, L. A., TRINDADE, P. T., ZOMPATORI, M. & HOEPER, M. 2016. 2015 ESC/ERS Guidelines for the diagnosis and treatment of pulmonary hypertension: The Joint Task Force for the Diagnosis and Treatment of Pulmonary Hypertension of the European Society of Cardiology (ESC) and the European Respiratory Society (ERS): Endorsed by: Association for European Paediatric and Congenital Cardiology (AEPC), International Society for Heart and Lung Transplantation (ISHLT). *Eur Heart J,* 37, 67-119.

GAO, X., HE, X., LUO, B., PENG, L., LIN, J. & ZUO, Z. 2009. Angiotensin II increases collagen I expression via transforming growth factor-beta1 and extracellular signal-regulated kinase in cardiac fibroblasts. *European Journal of Pharmacology,* 606, 115-120.

GARIBYAN, L. & AVASHIA, N. 2013. Polymerase chain reaction. *J Invest Dermatol,* 133, 1-4.

GAVRIELI, Y., SHERMAN, Y. & BEN-SASSON, S. A. 1992. Identification of programmed cell death in situ via specific labeling of nuclear DNA fragmentation. *J Cell Biol,* 119, 493-501.

GIBB, A. A., LAZAROPOULOS, M. P. & ELROD, J. W. 2020. Myofibroblasts and Fibrosis. *Circulation Research,* 127, 427-447.

GÖDECKE, A., DECKING, U. K. M., DING, Z., HIRCHENHAIN, J., BIDMON, H.-J., GÖDECKE, S. & SCHRADER, J. 1998. Coronary Hemodynamics in Endothelial NO Synthase Knockout Mice. *Circulation Research,* 82, 186-194.

GORDON, B., GONZÁLEZ-FERNÁNDEZ, V. & DOS-SUBIRÀ, L. 2022. Myocardial fibrosis in congenital heart disease. *Front Pediatr,* 10, 965204.

GRAY, M. O., LONG, C. S., KALINYAK, J. E., LI, H.-T. & KARLINER, J. S. 1998. Angiotensin II stimulates cardiac myocyte hypertrophy via paracrine release of TGF-β1 and endothelin-1 from fibroblasts. *Cardiovascular Research,* 40, 352-363.

GUO, D. F., SUN, Y. L., HAMET, P. & INAGAMI, T. 2001. The angiotensin II type 1 receptor and receptor-associated proteins. *Cell Research,* 11, 165-180.

GYÖNGYÖSI, M., WINKLER, J., RAMOS, I., DO, Q.-T., FIRAT, H., MCDONALD, K., GONZÁLEZ, A., THUM, T., DÍEZ, J., JAISSER, F., PIZARD, A. & ZANNAD, F. 2017. Myocardial fibrosis: biomedical research from bench to bedside. *European Journal of Heart Failure,* 19, 177-191.

HAFIZI, S., WHARTON, J., MORGAN, K., ALLEN, S. P., CHESTER, A. H., CATRAVAS, J. D., POLAK, J. M. & YACOUB, M. H. 1998. Expression of functional angiotensin-converting enzyme and AT1 receptors in cultured human cardiac fibroblasts. *Circulation,* 98, 2553-9.

HAKAM, A. C. & HUSSAIN, T. 2005. Renal Angiotensin II Type-2 Receptors Are Upregulated and Mediate the Candesartan-Induced Natriuresis/Diuresis in Obese Zucker Rats. *Hypertension,* 45, 270-275.

HALL, C., GEHMLICH, K., DENNING, C. & PAVLOVIC, D. 2021. Complex Relationship Between Cardiac Fibroblasts and Cardiomyocytes in Health and Disease. *Journal of the American Heart Association,* 10, e019338.

HATZIMOURATIDIS, K., AMAR, E., EARDLEY, I., GIULIANO, F., HATZICHRISTOU, D., MONTORSI, F., VARDI, Y. & WESPES, E. 2010. Guidelines on male sexual dysfunction: erectile dysfunction and premature ejaculation. *Eur Urol,* 57, 804-14.

HEINZEL, F. R., HEGEMANN, N., HOHENDANNER, F., PRIMESSNIG, U., GRUNE, J., BLASCHKE, F., DE BOER, R. A., PIESKE, B., SCHIATTARELLA, G. G. & KUEBLER, W. M. 2020. Left ventricular dysfunction in heart failure with preserved ejection fraction—molecular mechanisms and impact on right ventricular function. *Cardiovascular Diagnosis and Therapy,* 10, 1541-1560.

HINDERER, S. & SCHENKE-LAYLAND, K. 2019. Cardiac fibrosis – A short review of causes and therapeutic strategies. *Advanced Drug Delivery Reviews,* 146, 77-82.

HO, D., ZHAO, X., GAO, S., HONG, C., VATNER, D. E. & VATNER, S. F. 2011. Heart Rate and Electrocardiography Monitoring in Mice. *Curr Protoc Mouse Biol,* 1, 123-139.

HOFMANN, F. 2020. The cGMP system: components and function. *Biological Chemistry,* 401, 447-469.

HOFMANN, F., AMMENDOLA, A. & SCHLOSSMANN, J. 2000. Rising behind NO: cGMP-dependent protein kinases. *Journal of Cell Science,* 113, 1671-1676.

HOFMANN, F., DOSTMANN, W., KEILBACH, A., LANDGRAF, W. & RUTH, P. 1992. Structure and physiological role of cGMP-dependent protein kinase. *Biochim Biophys Acta,* 1135, 51-60.

HOFMANN, F. & WEGENER, J. W. 2013. cGMP-dependent protein kinases (cGK). *Methods Mol Biol,* 1020, 17-50.

HUANG, T., LONG, M. & HUO, B. 2010. Competitive Binding to Cuprous Ions of Protein and BCA in the Bicinchoninic Acid Protein Assay. *Open Biomed Eng J,* 4, 271-8.

IM, K., MARENINOV, S., DIAZ, M. F. P. & YONG, W. H. 2019. An Introduction to Performing Immunofluorescence Staining. *Methods Mol Biol,* 1897, 299-311.

IMBALZANO, E., ZITO, C., CARERJ, S., ORETO, G., MANDRAFFINO, G., CUSMÀ-PICCIONE, M., DI BELLA, G., SAITTA, C. & SAITTA, A. 2011. Left Ventricular Function in Hypertension: New Insight by Speckle Tracking Echocardiography. *Echocardiography,* 28, 649-657.

IRVINE, J. C., GANTHAVEE, V., LOVE, J. E., ALEXANDER, A. E., HOROWITZ, J. D., STASCH, J.-P., KEMP-HARPER, B. K. & RITCHIE, R. H. 2012. The Soluble Guanylyl Cyclase Activator Bay 58-2667 Selectively Limits Cardiomyocyte Hypertrophy. *PLOS ONE,* 7, e44481.

IYER, N. R., LE, T. T., KUI, M. S. L., TANG, H. C., CHIN, C. T., PHUA, S. K., BRYANT, J. A., PUA, C. J., ANG, B., TOH, D. F., AW, T. C., LEE, C. H., COOK, S. A., UGANDER, M. & CHIN, C. W. L. 2022. Markers of Focal and Diffuse Nonischemic Myocardial Fibrosis Are Associated With Adverse Cardiac Remodeling and Prognosis in Patients With Hypertension: The REMODEL Study. *Hypertension,* 79, 1804-1813.

JABŁOŃSKA-TRYPUĆ, A., MATEJCZYK, M. & ROSOCHACKI, S. 2016. Matrix metalloproteinases (MMPs), the main extracellular matrix (ECM) enzymes in collagen degradation, as a target for anticancer drugs. *J Enzyme Inhib Med Chem,* 31, 177-183.

JAHN, H. M., KASAKOW, C. V., HELFER, A., MICHELY, J., VERKHRATSKY, A., MAURER, H. H., SCHELLER, A. & KIRCHHOFF, F. 2018. Refined protocols of tamoxifen injection for inducible DNA recombination in mouse astroglia. *Sci Rep,* 8, 5913.

JOHNSON, C., KUYT, K., OXBOROUGH, D. & STOUT, M. 2019. Practical tips and tricks in measuring strain, strain rate and twist for the left and right ventricles. *Echo Res Pract,* 6, R87-r98.

KAJSTURA, J., CIGOLA, E., MALHOTRA, A., LI, P., CHENG, W., MEGGS, L. G. & ANVERSA, P. 1997. Angiotensin II induces apoptosis of adult ventricular myocytes in vitro. *J Mol Cell Cardiol,* 29, 859-70.

KANISICAK, O., KHALIL, H., IVEY, M. J., KARCH, J., MALIKEN, B. D., CORRELL, R. N., BRODY, M. J., SC, J. L., ARONOW, B. J., TALLQUIST, M. D. & MOLKENTIN, J. D. 2016. Genetic lineage tracing defines myofibroblast origin and function in the injured heart. *Nat Commun,* 7, 12260.

KATSURAGI, N., MORISHITA, R., NAKAMURA, N., OCHIAI, T., TANIYAMA, Y., HASEGAWA, Y., KAWASHIMA, K., KANEDA, Y., OGIHARA, T. & SUGIMURA, K. 2004. Periostin as a Novel Factor Responsible for Ventricular Dilation. *Circulation,* 110, 1806-1813.

KAUPP, U. B. & SEIFERT, R. 2002. Cyclic Nucleotide-Gated Ion Channels. *Physiological Reviews,* 82, 769-824.

KAUR, H., TAKEFUJI, M., NGAI, C. Y., CARVALHO, J., BAYER, J., WIETELMANN, A., POETSCH, A., HOELPER, S., CONWAY, S. J., MÖLLMANN, H., LOOSO, M., TROIDL, C., OFFERMANNS, S. & WETTSCHURECK, N. 2016. Targeted Ablation of Periostin-Expressing Activated Fibroblasts Prevents Adverse Cardiac Remodeling in Mice. *Circ Res,* 118, 1906-17.

KEILBACH, A., RUTH, P. & HOFMANN, F. 1992. Detection of cGMP dependent protein kinase isozymes by specific antibodies. *European Journal of Biochemistry,* 208, 467-473.

KHALIL, H., KANISICAK, O., PRASAD, V., CORRELL, R. N., FU, X., SCHIPS, T., VAGNOZZI, R. J., LIU, R., HUYNH, T., LEE, S. J., KARCH, J. & MOLKENTIN, J. D. 2017. Fibroblast-specific TGF-β-Smad2/3 signaling underlies cardiac fibrosis. *J Clin Invest,* 127, 3770-3783.

KLAIBER, M., KRUSE, M., VÖLKER, K., SCHRÖTER, J., FEIL, R., FREICHEL, M., GERLING, A., FEIL, S., DIETRICH, A., LONDOÑO, J. E. C., BABA, H. A., ABRAMOWITZ, J., BIRNBAUMER, L., PENNINGER, J. M., PONGS, O. & KUHN, M. 2010. Novel insights into the mechanisms mediating the local antihypertrophic effects of cardiac atrial natriuretic peptide: role of cGMP-dependent protein kinase and RGS2. *Basic Research in Cardiology,* 105, 583-595.

KOITABASHI, N., AIBA, T., HESKETH, G. G., ROWELL, J., ZHANG, M., TAKIMOTO, E., TOMASELLI, G. F. & KASS, D. A. 2010. Cyclic GMP/PKG-dependent inhibition of TRPC6 channel activity and expression negatively regulates cardiomyocyte NFAT activation Novel mechanism of cardiac stress modulation by PDE5 inhibition. *J Mol Cell Cardiol,* 48, 713-24.

KONG, P., CHRISTIA, P. & FRANGOGIANNIS, N. G. 2014. The pathogenesis of cardiac fibrosis. *Cell Mol Life Sci,* 71, 549-74.

KONG, P., SHINDE, A. V., SU, Y., RUSSO, I., CHEN, B., SAXENA, A., CONWAY, S. J., GRAFF, J. M. & FRANGOGIANNIS, N. G. 2018. Opposing Actions of Fibroblast and Cardiomyocyte Smad3 Signaling in the Infarcted Myocardium. *Circulation,* 137, 707-724.

KRAEHLING, J. R. & SESSA, W. C. 2017. Contemporary Approaches to Modulating the Nitric Oxide–cGMP Pathway in Cardiovascular Disease. *Circulation Research,* 120, 1174-1182.

KRAMER, K., VAN ACKER, S. A. B. E., VOSS, H.-P., GRIMBERGEN, J. A., VAN DER VIJGH, W. J. F. & BAST, A. 1993. Use of telemetry to record electrocardiogram and heart rate in freely moving mice. *Journal of Pharmacological and Toxicological Methods,* 30, 209-215.

KUHN, M. 2016. Molecular Physiology of Membrane Guanylyl Cyclase Receptors. *Physiol Rev,* 96, 751-804.

KUKREJA, R. C., SALLOUM, F. N. & DAS, A. 2012. Cyclic guanosine monophosphate signaling and phosphodiesterase-5 inhibitors in cardioprotection. *J Am Coll Cardiol,* 59, 1921-7.

KUROSE, H. 2021. Cardiac Fibrosis and Fibroblasts. *Cells,* 10, 1716.

KYRYLKOVA, K., KYRYACHENKO, S., LEID, M. & KIOUSSI, C. 2012. Detection of apoptosis by TUNEL assay. *Methods Mol Biol,* 887, 41-7.

LANGMESSER, S., FRANKEN, P., FEIL, S., EMMENEGGER, Y., ALBRECHT, U. & FEIL, R. 2009. cGMP-dependent protein kinase type I is implicated in the regulation of the timing and quality of sleep and wakefulness. *PLoS One,* 4, e4238.

LÄNGST, N., ADLER, J., SCHWEIGERT, O., KLEUSBERG, F., CRUZ SANTOS, M., KNAUER, A., SAUSBIER, M., ZELLER, T., RUTH, P. & LUKOWSKI, R. 2021. Cyclic GMP-Dependent Regulation of Vascular Tone and Blood Pressure Involves Cysteine-Rich LIM-Only Protein 4 (CRP4). *Int J Mol Sci,* 22.

LEANCĂ, S. A., CRIȘU, D., PETRIȘ, A. O., AFRĂSÂNIE, I., GENES, A., COSTACHE, A. D., TESLOIANU, D. N. & COSTACHE, I. I. 2022. Left Ventricular Remodeling after Myocardial Infarction: From Physiopathology to Treatment. *Life,* 12, 1111.

LEE, P. Y., COSTUMBRADO, J., HSU, C. Y. & KIM, Y. H. 2012. Agarose gel electrophoresis for the separation of DNA fragments. *J Vis Exp*.

LEE, S.-J. & STULL, J. T. 1998. Calmodulin-dependent Regulation of Inducible and Neuronal Nitric-oxide Synthase*. *Journal of Biological Chemistry,* 273, 27430-27437.

LEE, S.-Y., KUO, Y.-H., DU, C.-X., HUANG, C.-W. & KU, H.-C. 2023. A novel caffeic acid derivative prevents angiotensin II-induced cardiac remodeling. *Biomedicine & Pharmacotherapy,* 162, 114709.

LEMARIÉ, C. A. & SCHIFFRIN, E. L. 2010. The angiotensin II type 2 receptor in cardiovascular disease. *J Renin Angiotensin Aldosterone Syst,* 11, 19-31.

LESLIE, K. O., TAATJES, D. J., SCHWARZ, J., VONTURKOVICH, M. & LOW, R. B. 1991. Cardiac myofibroblasts express alpha smooth muscle actin during right ventricular pressure overload in the rabbit. *Am J Pathol,* 139, 207-16.

LI, P., WANG, D., LUCAS, J., OPARIL, S., XING, D., CAO, X., NOVAK, L., RENFROW, M. B. & CHEN, Y.-F. 2008. Atrial Natriuretic Peptide Inhibits Transforming Growth Factor β–Induced Smad Signaling and Myofibroblast Transformation in Mouse Cardiac Fibroblasts. *Circulation Research,* 102, 185-192.

LI, Y., KISHIMOTO, I., SAITO, Y., HARADA, M., KUWAHARA, K., IZUMI, T., TAKAHASHI, N., KAWAKAMI, R., TANIMOTO, K., NAKAGAWA, Y., NAKANISHI, M., ADACHI, Y., GARBERS, D. L., FUKAMIZU, A. & NAKAO, K. 2002. Guanylyl cyclase-A inhibits angiotensin II type 1A receptor-mediated cardiac remodeling, an endogenous protective mechanism in the heart. *Circulation,* 106, 1722-8.

LIJNEN, P., PAPPARELLA, I., PETROV, V., SEMPLICINI, A. & FAGARD, R. 2006. Angiotensin II-stimulated collagen production in cardiac fibroblasts is mediated by reactive oxygen species. *J Hypertens,* 24, 757-66.

LIU, F., WANG, X., LIU, D. & ZHANG, C. 2021a. Frequency and risk factors of impaired left ventricular global longitudinal strain in patients with end-stage renal disease: a two-dimensional speckle-tracking echocardiographic study. *Quantitative Imaging in Medicine and Surgery,* 11, 2397-2405.

LIU, M., LÓPEZ DE JUAN ABAD, B. & CHENG, K. 2021b. Cardiac fibrosis: Myofibroblast-mediated pathological regulation and drug delivery strategies. *Advanced drug delivery reviews,* 173, 504-519.

LIU, S., SHI-WEN, X., KENNEDY, L., PALA, D., CHEN, Y., EASTWOOD, M., CARTER, D. E., BLACK, C. M., ABRAHAM, D. J. & LEASK, A. 2007. FAK Is Required for TGFβ-induced JNK Phosphorylation in Fibroblasts: Implications for Acquisition of a Matrix-remodeling Phenotype. *Molecular Biology of the Cell,* 18, 2169-2178.

LIU, T., SONG, D., DONG, J., ZHU, P., LIU, J., LIU, W., MA, X., ZHAO, L. & LING, S. 2017. Current Understanding of the Pathophysiology of Myocardial Fibrosis and Its Quantitative Assessment in Heart Failure. *Frontiers in Physiology,* 8.

LORIGO, M., OLIVEIRA, N. & CAIRRAO, E. 2022. PDE-Mediated Cyclic Nucleotide Compartmentation in Vascular Smooth Muscle Cells: From Basic to a Clinical Perspective. *Journal of Cardiovascular Development and Disease,* 9, 4.

LUKOWSKI, R., CRUZ SANTOS, M., KURET, A. & RUTH, P. 2022. cGMP and mitochondrial K(+) channels-Compartmentalized but closely connected in cardioprotection. *Br J Pharmacol,* 179, 2344-2360.

LUKOWSKI, R., RYBALKIN, S. D., LOGA, F., LEISS, V., BEAVO, J. A. & HOFMANN, F. 2010. Cardiac hypertrophy is not amplified by deletion of cGMP-dependent protein kinase I in cardiomyocytes. *Proceedings of the National Academy of Sciences,* 107, 5646-5651.

LUKOWSKI, R., WEINMEISTER, P., BERNHARD, D., FEIL, S., GOTTHARDT, M., HERZ, J., MASSBERG, S., ZERNECKE, A., WEBER, C., HOFMANN, F. & FEIL, R. 2008. Role of smooth muscle cGMP/cGKI signaling in murine vascular restenosis. *Arterioscler Thromb Vasc Biol,* 28, 1244-50.

LUO, K. & LODISH, H. F. 1996. Signaling by chimeric erythropoietin-TGF-beta receptors: homodimerization of the cytoplasmic domain of the type I TGF-beta receptor and heterodimerization with the type II receptor are both required for intracellular signal transduction. *The EMBO Journal,* 15, 4485-4496.

LYU, L., WANG, H., LI, B., QIN, Q., QI, L., NAGARKATTI, M., NAGARKATTI, P., JANICKI, J. S., WANG, X. L. & CUI, T. 2015. A critical role of cardiac fibroblast-derived exosomes in activating renin angiotensin system in cardiomyocytes. *J Mol Cell Cardiol,* 89, 268-79.

MA, J., LI, Y., YANG, X., LIU, K., ZHANG, X., ZUO, X., YE, R., WANG, Z., SHI, R., MENG, Q. & CHEN, X. 2023. Signaling pathways in vascular function and hypertension: molecular mechanisms and therapeutic interventions. *Signal Transduct Target Ther,* 8, 168.

MARKHAM, A. & DUGGAN, S. 2021. Vericiguat: First Approval. *Drugs,* 81, 721-726.

MARSHALL, R. P., GOHLKE, P., CHAMBERS, R. C., HOWELL, D. C., BOTTOMS, S. E., UNGER, T., MCANULTY, R. J. & LAURENT, G. J. 2004. Angiotensin II and the fibroproliferative response to acute lung injury. *Am J Physiol Lung Cell Mol Physiol,* 286, L156-64.

MARSHALL, R. P., MCANULTY, R. J. & LAURENT, G. J. 2000. Angiotensin II is mitogenic for human lung fibroblasts via activation of the type 1 receptor. *Am J Respir Crit Care Med,* 161, 1999-2004.

MASCHERBAUER, J., GRÜNIG, E., HALANK, M., HOHENFORST-SCHMIDT, W., KAMMERLANDER, A. A., PRETSCH, I., STERINGER-MASCHERBAUER, R., ULRICH, S., LANG, I. M., WARGENAU, M., FREY, R. & BONDERMAN, D. 2016. Evaluation of the pharmacoDYNAMIC effects of riociguat in subjects with pulmonary hypertension and heart failure with preserved ejection fraction : Study protocol for a randomized controlled trial. *Wien Klin Wochenschr,* 128, 882-889.

MASUYAMA, H., TSURUDA, T., KATO, J., IMAMURA, T., ASADA, Y., STASCH, J.-P., KITAMURA, K. & ETO, T. 2006. Soluble Guanylate Cyclase Stimulation on Cardiovascular Remodeling in Angiotensin II–Induced Hypertensive Rats. *Hypertension,* 48, 972-978.

MCCLELLAN, M., BROWN, N., CALIFF, R. M. & WARNER, J. J. 2019. Call to Action: Urgent Challenges in Cardiovascular Disease: A Presidential Advisory From the American Heart Association. *Circulation,* 139, e44-e54.

MCEWAN, P. E., GRAY, G. A., SHERRY, L., WEBB, D. J. & KENYON, C. J. 1998. Differential effects of angiotensin II on cardiac cell proliferation and intramyocardial perivascular fibrosis in vivo. *Circulation,* 98, 2765-73.

MCMURRAY, J. J. V., PACKER, M., DESAI, A. S., GONG, J., LEFKOWITZ, M. P., RIZKALA, A. R., ROULEAU, J. L., SHI, V. C., SOLOMON, S. D., SWEDBERG, K. & ZILE, M. R. 2014. Angiotensin–Neprilysin Inhibition versus Enalapril in Heart Failure. *New England Journal of Medicine,* 371, 993-1004.

MEEKER, A. K., HEAPHY, C. M., DAVIS, C. M., ROY, S. & PLATZ, E. A. 2021. Photochemical pre-bleaching of formalin-fixed archival prostate tissues significantly reduces autofluorescence to facilitate multiplex immunofluorescence staining. *bioRxiv*, 2021.11.09.467916.

MEHTA, P. K. & GRIENDLING, K. K. 2007. Angiotensin II cell signaling: physiological and pathological effects in the cardiovascular system. *American Journal of Physiology-Cell Physiology,* 292, C82-C97.

MENGES, L., GIESEN, J., YILMAZ, K., MERGIA, E., FÜCHTBAUER, A., FÜCHTBAUER, E. M., KOESLING, D. & RUSSWURM, M. 2023. It takes two to tango: cardiac fibroblast-derived NO-induced cGMP enters cardiac myocytes and increases cAMP by inhibiting PDE3. *Commun Biol,* 6, 504.

MENGES, L., KRAWUTSCHKE, C., FÜCHTBAUER, E. M., FÜCHTBAUER, A., SANDNER, P., KOESLING, D. & RUSSWURM, M. 2019. Mind the gap (junction): cGMP induced by nitric oxide in cardiac myocytes originates from cardiac fibroblasts. *Br J Pharmacol,* 176, 4696-4707.

MENK, M., GRAW, J. A., VON HAEFEN, C., SIFRINGER, M., SCHWAIBERGER, D., UNGER, T., STECKELINGS, U. & SPIES, C. D. 2015. Stimulation of the Angiotensin II AT2 Receptor is Anti-inflammatory in Human Lipopolysaccharide-Activated Monocytic Cells. *Inflammation,* 38, 1690-1699.

MINGELS, A. M., MILLS, N. L. & MUELLER, C. 2023. Cardiac troponin T and I: back to basics. *Eur Heart J Acute Cardiovasc Care,* 12, 631-632.

MIRZAYANS, R. & MURRAY, D. 2020. Do TUNEL and Other Apoptosis Assays Detect Cell Death in Preclinical Studies? *Int J Mol Sci,* 21.

MOLKENTIN, J. D., BUGG, D., GHEARING, N., DORN, L. E., KIM, P., SARGENT, M. A., GUNAJE, J., OTSU, K. & DAVIS, J. 2017. Fibroblast-Specific Genetic Manipulation of p38 Mitogen-Activated Protein Kinase In Vivo Reveals Its Central Regulatory Role in Fibrosis. *Circulation,* 136, 549-561.

MORA, V., ROLDÁN, I., ROMERO, E., ROMERO, D., BERTOLÍN, J., UGALDE, N., PÉREZ-OLIVARES, C., RODRIGUEZ-ISRAEL, M., PÉREZ-GOZALBO, J. & LOWENSTEIN, J. A. 2018. Comprehensive assessment of left ventricular myocardial function by two-dimensional speckle-tracking echocardiography. *Cardiovascular Ultrasound,* 16, 16.

MOUKETTE, B., BARUPALA, N. P., AONUMA, T., SEPULVEDA, M., KAWAGUCHI, S. & KIM, I.-M. 2021. Chapter 14 - Interactions between noncoding RNAs as epigenetic regulatory mechanisms in cardiovascular diseases. *In:* SHUKLA, A. K. (ed.) *Methods in Cell Biology.* Academic Press.

MOYES, A. J., CHU, S. M., AUBDOOL, A. A., DUKINFIELD, M. S., MARGULIES, K. B., BEDI, K. C., HODIVALA-DILKE, K., BALIGA, R. S. & HOBBS, A. J. 2020. C-type natriuretic peptide co-ordinates cardiac structure and function. *Eur Heart J,* 41, 1006-1020.

MOYES, A. J. & HOBBS, A. J. 2019. C-type Natriuretic Peptide: A Multifaceted Paracrine Regulator in the Heart and Vasculature. *Int J Mol Sci,* 20.

MULLERSHAUSEN , F., FRIEBE , A., FEIL , R., THOMPSON , W. J., HOFMANN , F. & KOESLING , D. 2003. Direct activation of PDE5 by cGMP : long-term effects within NO/cGMP signaling. *Journal of Cell Biology,* 160, 719-727.

MÜNZEL, T., FEIL, R., MÜLSCH, A., LOHMANN, S. M., HOFMANN, F. & WALTER, U. 2003. Physiology and Pathophysiology of Vascular Signaling Controlled by Cyclic Guanosine 3′,5′-Cyclic Monophosphate–Dependent Protein Kinase. *Circulation,* 108, 2172-2183.

MURPHY, A. M., WONG, A. L. & BEZUHLY, M. 2015. Modulation of angiotensin II signaling in the prevention of fibrosis. *Fibrogenesis Tissue Repair,* 8, 7.

MUZUMDAR, M. D., TASIC, B., MIYAMICHI, K., LI, L. & LUO, L. 2007. A global double-fluorescent Cre reporter mouse. *Genesis,* 45, 593-605.

NAG, S., PATEL, S., MANI, S. & HUSSAIN, T. 2019. Role of angiotensin type 2 receptor in improving lipid metabolism and preventing adiposity. *Molecular and Cellular Biochemistry,* 461, 195-204.

NAKAGAWA, H. & SAITO, Y. 2022. Roles of Natriuretic Peptides and the Significance of Neprilysin in Cardiovascular Diseases. *Biology (Basel),* 11.

NAKAYAMA, H., BODI, I., MAILLET, M., DESANTIAGO, J., DOMEIER, T. L., MIKOSHIBA, K., LORENZ, J. N., BLATTER, L. A., BERS, D. M. & MOLKENTIN, J. D. 2010. The IP3 receptor regulates cardiac hypertrophy in response to select stimuli. *Circ Res,* 107, 659-66.

NANAYAKKARA, S., BYRNE, M., MAK, V., CARTER, K., DEAN, E. & KAYE, D. M. 2020. Extended-Release Oral Milrinone for the Treatment of Heart Failure With Preserved Ejection Fraction. *J Am Heart Assoc,* 9, e015026.

NATHAN, C. & XIE, Q. W. 1994. Nitric oxide synthases: roles, tolls, and controls. *Cell,* 78, 915-8.

NI, G., WANG, K., ZHOU, Y., WU, X., WANG, J., SHANG, H., WANG, L. & LI, X. 2020. Citri reticulatae Pericarpium attenuates Ang II-induced pathological cardiac hypertrophy via upregulating peroxisome proliferator-activated receptors gamma. *Annals of Translational Medicine,* 8, 1064.

NICOLAS, D., KERNDT, C. C. & REED, M. 2023. Sacubitril-Valsartan. *StatPearls.* Treasure Island (FL): StatPearls Publishing

Copyright © 2023, StatPearls Publishing LLC.

NISHIDA, M., TANABE, S., MARUYAMA, Y., MANGMOOL, S., URAYAMA, K., NAGAMATSU, Y., TAKAGAHARA, S., TURNER, J. H., KOZASA, T., KOBAYASHI, H., SATO, Y., KAWANISHI, T., INOUE, R., NAGAO, T. & KUROSE, H. 2005. Gα12/13- and Reactive Oxygen Species-dependent Activation of c-Jun NH₂-terminal Kinase and p38 Mitogen-activated Protein Kinase by Angiotensin Receptor Stimulation in Rat Neonatal Cardiomyocytes *. *Journal of Biological Chemistry,* 280, 18434-18441.

O'DWYER, D. N. & MOORE, B. B. 2017. The role of periostin in lung fibrosis and airway remodeling. *Cell Mol Life Sci,* 74, 4305-4314.

OH, J. K. & PARK, J. H. 2022. Role of strain echocardiography in patients with hypertension. *Clin Hypertens,* 28, 6.

OLIVER, P. M., FOX, J. E., KIM, R., ROCKMAN, H. A., KIM, H. S., REDDICK, R. L., PANDEY, K. N., MILGRAM, S. L., SMITHIES, O. & MAEDA, N. 1997. Hypertension, cardiac hypertrophy, and sudden death in mice lacking natriuretic peptide receptor A. *Proc Natl Acad Sci U S A,* 94, 14730-5.

OLSON, E. R., NAUGLE, J. E., ZHANG, X., BOMSER, J. A. & MESZAROS, J. G. 2005. Inhibition of cardiac fibroblast proliferation and myofibroblast differentiation by resveratrol. *American Journal of Physiology-Heart and Circulatory Physiology,* 288, H1131-H1138.

OMLAND, T., LIE, R. T., AAKVAAG, A., AARSLAND, T. & DICKSTEIN, K. 1994. Plasma endothelin determination as a prognostic indicator of 1-year mortality after acute myocardial infarction. *Circulation,* 89, 1573-1579.

ONOHARA, N., NISHIDA, M., INOUE, R., KOBAYASHI, H., SUMIMOTO, H., SATO, Y., MORI, Y., NAGAO, T. & KUROSE, H. 2006. TRPC3 and TRPC6 are essential for angiotensin II-induced cardiac hypertrophy. *Embo j,* 25, 5305-16.

PANG, J.-J., XU, R.-K., XU, X.-B., CAO, J.-M., NI, C., ZHU, W.-L., ASOTRA, K., CHEN, M.-C. & CHEN, C. 2004. Hexarelin protects rat cardiomyocytes from angiotensin II-induced apoptosis in vitro. *American Journal of Physiology-Heart and Circulatory Physiology,* 286, H1063-H1069.

PARADIS, P., DALI-YOUCEF, N., PARADIS, F. W., THIBAULT, G. & NEMER, M. 2000. Overexpression of angiotensin II type I receptor in cardiomyocytes induces cardiac hypertrophy and remodeling. *Proc Natl Acad Sci U S A,* 97, 931-6.

PARTHASARATHY, A., GOPI, V., UMADEVI, S., SIMNA, A., SHEIK, M. J. Y., DIVYA, H. & VELLAICHAMY, E. 2013. Suppression of atrial natriuretic peptide/natriuretic peptide receptor-A-mediated signaling upregulates angiotensin-II-induced collagen synthesis in adult cardiac fibroblasts. *Molecular and Cellular Biochemistry,* 378, 217-228.

PATEL, S., RAUF, A., KHAN, H. & ABU-IZNEID, T. 2017. Renin-angiotensin-aldosterone (RAAS): The ubiquitous system for homeostasis and pathologies. *Biomedicine & Pharmacotherapy,* 94, 317-325.

PATRUCCO, E., DOMES, K., SBROGGIÓ, M., BLAICH, A., SCHLOSSMANN, J., DESCH, M., RYBALKIN, S. D., BEAVO, J. A., LUKOWSKI, R. & HOFMANN, F. 2014. Roles of cGMP-dependent protein kinase I (cGKI) and PDE5 in the regulation of Ang II-induced cardiac hypertrophy and fibrosis. *Proceedings of the National Academy of Sciences,* 111, 12925-12929.

PAVLAKI, N. & NIKOLAEV, V. O. 2018. Imaging of PDE2- and PDE3-Mediated cGMP-to-cAMP Cross-Talk in Cardiomyocytes. *J Cardiovasc Dev Dis,* 5.

PELLIEUX, C., FOLETTI, A., PEDUTO, G., AUBERT, J. F., NUSSBERGER, J., BEERMANN, F., BRUNNER, H. R. & PEDRAZZINI, T. 2001. Dilated cardiomyopathy and impaired cardiac hypertrophic response to angiotensin II in mice lacking FGF-2. *J Clin Invest,* 108, 1843-51.

PETRAINA, A., NOGALES, C., KRAHN, T., MUCKE, H., LÜSCHER, T. F., FISCHMEISTER, R., KASS, D. A., BURNETT, J. C., JR, HOBBS, A. J. & SCHMIDT, H. H. H. W. 2021. Cyclic GMP modulating drugs in cardiovascular diseases: mechanism-based network pharmacology. *Cardiovascular Research*.

PETROV, V. V., FAGARD, R. H. & LIJNEN, P. J. 2002. Stimulation of Collagen Production by Transforming Growth Factor-β₁ During Differentiation of Cardiac Fibroblasts to Myofibroblasts. *Hypertension,* 39, 258-263.

PFEIFER, A., KLATT, P., MASSBERG, S., NY, L., SAUSBIER, M., HIRNEISS, C., WANG, G. X., KORTH, M., ASZÓDI, A., ANDERSSON, K. E., KROMBACH, F., MAYERHOFER, A., RUTH, P., FÄSSLER, R. & HOFMANN, F. 1998. Defective smooth muscle regulation in cGMP kinase I-deficient mice. *Embo j,* 17, 3045-51.

PHOSRI, S., ARIEYAWONG, A., BUNRUKCHAI, K., PARICHATIKANOND, W., NISHIMURA, A., NISHIDA, M. & MANGMOOL, S. 2017. Stimulation of Adenosine A(2B) Receptor Inhibits Endothelin-1-Induced Cardiac Fibroblast Proliferation and α-Smooth Muscle Actin Synthesis Through the cAMP/Epac/PI3K/Akt-Signaling Pathway. *Front Pharmacol,* 8, 428.

PIEK, A., DE BOER, R. A. & SILLJÉ, H. H. 2016. The fibrosis-cell death axis in heart failure. *Heart Fail Rev,* 21, 199-211.

PISTNER, A., BELMONTE, S., COULTHARD, T. & BLAXALL, B. 2010. Murine echocardiography and ultrasound imaging. *J Vis Exp*.

PONIKOWSKI, P., ANKER, S. D., ALHABIB, K. F., COWIE, M. R., FORCE, T. L., HU, S., JAARSMA, T., KRUM, H., RASTOGI, V., ROHDE, L. E., SAMAL, U. C., SHIMOKAWA, H., BUDI SISWANTO, B., SLIWA, K. & FILIPPATOS, G. 2014. Heart failure: preventing disease and death worldwide. *ESC Heart Fail,* 1, 4-25.

PONIKOWSKI, P., VOORS, A. A., ANKER, S. D., BUENO, H., CLELAND, J. G. F., COATS, A. J. S., FALK, V., GONZÁLEZ-JUANATEY, J. R., HARJOLA, V.-P., JANKOWSKA, E. A., JESSUP, M.,

LINDE, C., NIHOYANNOPOULOS, P., PARISSIS, J. T., PIESKE, B., RILEY, J. P., ROSANO, G. M. C., RUILOPE, L. M., RUSCHITZKA, F., RUTTEN, F. H., VAN DER MEER, P. & GROUP, E. S. D. 2016. 2016 ESC Guidelines for the diagnosis and treatment of acute and chronic heart failure: The Task Force for the diagnosis and treatment of acute and chronic heart failure of the European Society of Cardiology (ESC)Developed with the special contribution of the Heart Failure Association (HFA) of the ESC. *European Heart Journal,* 37, 2129-2200.

POTTER, L. R. 2011. Natriuretic peptide metabolism, clearance and degradation. *Febs j,* 278, 1808-17.

POTTER, L. R. & HUNTER, T. 2001. Guanylyl cyclase-linked natriuretic peptide receptors: structure and regulation. *J Biol Chem,* 276, 6057-60.

POTTER, L. R., YODER, A. R., FLORA, D. R., ANTOS, L. K. & DICKEY, D. M. 2009. Natriuretic peptides: their structures, receptors, physiologic functions and therapeutic applications. *Handb Exp Pharmacol*, 341-66.

REDFIELD, M. M., CHEN, H. H., BORLAUG, B. A., SEMIGRAN, M. J., LEE, K. L., LEWIS, G., LEWINTER, M. M., ROULEAU, J. L., BULL, D. A., MANN, D. L., DESWAL, A., STEVENSON, L. W., GIVERTZ, M. M., OFILI, E. O., O'CONNOR, C. M., FELKER, G. M., GOLDSMITH, S. R., BART, B. A., MCNULTY, S. E., IBARRA, J. C., LIN, G., OH, J. K., PATEL, M. R., KIM, R. J., TRACY, R. P., VELAZQUEZ, E. J., ANSTROM, K. J., HERNANDEZ, A. F., MASCETTE, A. M. & BRAUNWALD, E. 2013. Effect of phosphodiesterase-5 inhibition on exercise capacity and clinical status in heart failure with preserved ejection fraction: a randomized clinical trial. *Jama,* 309, 1268-77.

RICHARDS, D. A., ARONOVITZ, M. J., LIU, P., MARTIN, G. L., TAM, K., PANDE, S., KARAS, R. H., BLOOMFIELD, D. M., MENDELSOHN, M. E. & BLANTON, R. M. 2021. CRD-733, a Novel PDE9 (Phosphodiesterase 9) Inhibitor, Reverses Pressure Overload-Induced Heart Failure. *Circ Heart Fail,* 14, e007300.

RIORDAN, J. F. 2003. Angiotensin-I-converting enzyme and its relatives. *Genome Biol,* 4, 225.

RITTIÉ, L. 2017. Method for Picrosirius Red-Polarization Detection of Collagen Fibers in Tissue Sections. *Methods Mol Biol,* 1627, 395-407.

ROMAN, D. L. & TRAYNOR, J. R. 2011. Regulators of G protein signaling (RGS) proteins as drug targets: modulating G-protein-coupled receptor (GPCR) signal transduction. *J Med Chem,* 54, 7433-40.

ROSENKRANZ, S. 2004. TGF-β1 and angiotensin networking in cardiac remodeling. *Cardiovascular Research,* 63, 423-432.

RUBIN, L. J., BADESCH, D. B., FLEMING, T. R., GALIÈ, N., SIMONNEAU, G., GHOFRANI, H. A., OAKES, M., LAYTON, G., SERDAREVIC-PEHAR, M., MCLAUGHLIN, V. V. & BARST, R. J. 2011. Long-term treatment with sildenafil citrate in pulmonary arterial hypertension: the SUPER-2 study. *Chest,* 140, 1274-1283.

RÜDEBUSCH, J., BENKNER, A., NATH, N., FLEUCH, L., KADERALI, L., GRUBE, K., KLINGEL, K., ECKSTEIN, G., MEITINGER, T., FIELITZ, J. & FELIX, S. B. 2022. Stimulation of soluble guanylyl cyclase (sGC) by riociguat attenuates heart failure and pathological cardiac remodelling. *British Journal of Pharmacology,* 179, 2430-2442.

RYBALKIN, S. D., RYBALKINA, I. G., FEIL, R., HOFMANN, F. & BEAVO, J. A. 2002. Regulation of cGMP-specific Phosphodiesterase (PDE5) Phosphorylation in Smooth Muscle Cells*. *Journal of Biological Chemistry,* 277, 3310-3317.

SADOSHIMA, J. & IZUMO, S. 1993. Molecular characterization of angiotensin II--induced hypertrophy of cardiac myocytes and hyperplasia of cardiac fibroblasts. Critical role of the AT1 receptor subtype. *Circulation Research,* 73, 413-423.

SANDNER, P. & STASCH, J. P. 2017. Anti-fibrotic effects of soluble guanylate cyclase stimulators and activators: A review of the preclinical evidence. *Respiratory Medicine,* 122, S1-S9.

SANDNER, P., ZIMMER, D. P., MILNE, G. T., FOLLMANN, M., HOBBS, A. & STASCH, J. P. 2021. Soluble Guanylate Cyclase Stimulators and Activators. *Handb Exp Pharmacol,* 264, 355-394.

SANO, M., FUKUDA, K., KODAMA, H., PAN, J., SAITO, M., MATSUZAKI, J., TAKAHASHI, T., MAKINO, S., KATO, T. & OGAWA, S. 2000. Interleukin-6 family of cytokines mediate angiotensin II-induced cardiac hypertrophy in rodent cardiomyocytes. *J Biol Chem,* 275, 29717-23.

SANTIAGO, J. J., MCNAUGHTON, L. J., KOLEINI, N., MA, X., BESTVATER, B., NICKEL, B. E., FANDRICH, R. R., WIGLE, J. T., FREED, D. H., ARORA, R. C. & KARDAMI, E. 2014. High molecular weight fibroblast growth factor-2 in the human heart is a potential target for prevention of cardiac remodeling. *PLoS One,* 9, e97281.

SATO, K., CHAN, J., APPADURAI, V., OBONYO, N., SEE HOE, L., SUEN, J. Y. & FRASER, J. F. 2022. Exploration of the Utility of Speckle-Tracking Echocardiography During Mechanical Ventilation and Mechanical Circulatory Support. *Crit Care Explor,* 4, e0666.

SCATTEIA, A., BARITUSSIO, A. & BUCCIARELLI-DUCCI, C. 2017. Strain imaging using cardiac magnetic resonance. *Heart Failure Reviews,* 22, 465-476.

SCHIATTARELLA, G. G., ALTAMIRANO, F., TONG, D., FRENCH, K. M., VILLALOBOS, E., KIM, S. Y., LUO, X., JIANG, N., MAY, H. I., WANG, Z. V., HILL, T. M., MAMMEN, P. P. A., HUANG, J., LEE, D. I., HAHN, V. S., SHARMA, K., KASS, D. A., LAVANDERO, S., GILLETTE, T. G. & HILL, J. A. 2019. Nitrosative stress drives heart failure with preserved ejection fraction. *Nature,* 568, 351-356.

SCHLOSSMANN, J. & HOFMANN, F. 2005. cGMP-dependent protein kinases in drug discovery. *Drug Discovery Today,* 10, 627-634.

SCHMIDT, H. H., HOFMANN, F. & STASCH, J. P. 2009. Handbook of Experimental Pharmacology 191. cGMP: generators, effectors and therapeutic implications. Preface. *Handb Exp Pharmacol*, v-vi.

SCHRÖDER, D., HEGER, J., PIPER, H. M. & EULER, G. 2006. Angiotensin II stimulates apoptosis via TGF-β1 signaling in ventricular cardiomyocytes of rat. *Journal of Molecular Medicine,* 84, 975-983.

SCOTT, J. D. 1991. Cyclic nucleotide-dependent protein kinases. *Pharmacol Ther,* 50, 123-45.

SEGURA, A. M., FRAZIER, O. H. & BUJA, L. M. 2014. Fibrosis and heart failure. *Heart Failure Reviews,* 19, 173-185.

SHAHIM, B., KAPELIOS, C. J., SAVARESE, G. & LUND, L. H. 2023. Global Public Health Burden of Heart Failure: An Updated Review. *Cardiac Failure Review 2023;9:e11.*

SHESELY, E. G., MAEDA, N., KIM, H. S., DESAI, K. M., KREGE, J. H., LAUBACH, V. E., SHERMAN, P. A., SESSA, W. C. & SMITHIES, O. 1996. Elevated blood pressures in mice lacking endothelial nitric oxide synthase. *Proc Natl Acad Sci U S A,* 93, 13176-81.

SHIMIZU, T. & LIAO, J. K. 2016. Rho Kinases and Cardiac Remodeling. *Circ J,* 80, 1491-8.

SHUM, M., PINARD, S., GUIMOND, M.-O., LABBÉ, S. M., ROBERGE, C., BAILLARGEON, J.-P., LANGLOIS, M.-F., ALTERMAN, M., WALLINDER, C., HALLBERG, A., CARPENTIER, A. C. & GALLO-PAYET, N. 2013. Angiotensin II type 2 receptor promotes adipocyte differentiation and restores adipocyte size in high-fat/high-fructose diet-induced insulin resistance in rats. *American Journal of Physiology-Endocrinology and Metabolism,* 304, E197-E210.

SMITH, B. J. 1984. SDS Polyacrylamide Gel Electrophoresis of Proteins. *Methods Mol Biol,* 1, 41-55.

SMOLENSKI, A., BACHMANN, C., REINHARD, K., HÖNIG-LIEDL, P., JARCHAU, T., HOSCHUETZKY, H. & WALTER, U. 1998. Analysis and Regulation of Vasodilator-stimulated Phosphoprotein Serine 239 Phosphorylation in Vitro and in Intact Cells Using a Phosphospecific Monoclonal Antibody *. *Journal of Biological Chemistry,* 273, 20029-20035.

SMOLENSKI, A., SCHULTESS, J., DANIELEWSKI, O., GARCIA ARGUINZONIS, M. I., THALHEIMER, P., KNEITZ, S., WALTER, U. & LOHMANN, S. M. 2004. Quantitative analysis of the cardiac fibroblast transcriptome-implications for NO/cGMP signaling. *Genomics,* 83, 577-87.

SNIDER, P., HINTON, R. B., MORENO-RODRIGUEZ, R. A., WANG, J., ROGERS, R., LINDSLEY, A., LI, F., INGRAM, D. A., MENICK, D., FIELD, L., FIRULLI, A. B., MOLKENTIN, J. D., MARKWALD, R. & CONWAY, S. J. 2008. Periostin Is Required for Maturation and Extracellular Matrix Stabilization of Noncardiomyocyte Lineages of the Heart. *Circulation Research,* 102, 752-760.

SOBECKI, M., MROUJ, K., CAMASSES, A., PARISIS, N., NICOLAS, E., LLÈRES, D., GERBE, F., PRIETO, S., KRASINSKA, L., DAVID, A., EGUREN, M., BIRLING, M.-C., URBACH, S., HEM, S., DÉJARDIN, J., MALUMBRES, M., JAY, P., DULIC, V., LAFONTAINE, D. L. J., FEIL, R. & FISHER, D. 2016. The cell proliferation antigen Ki-67 organises heterochromatin. *eLife,* 5, e13722.

SODERLING, S. H., BAYUGA, S. J. & BEAVO, J. A. 1998. Identification and Characterization of a Novel Family of Cyclic Nucleotide Phosphodiesterases *. *Journal of Biological Chemistry,* 273, 15553-15558.

SOEKI, T., KISHIMOTO, I., OKUMURA, H., TOKUDOME, T., HORIO, T., MORI, K. & KANGAWA, K. 2005. C-type natriuretic peptide, a novel antifibrotic and antihypertrophic agent, prevents cardiac remodeling after myocardial infarction. *J Am Coll Cardiol,* 45, 608-16.

SOLOMON, S. D., MCMURRAY, J. J. V., ANAND, I. S., GE, J., LAM, C. S. P., MAGGIONI, A. P., MARTINEZ, F., PACKER, M., PFEFFER, M. A., PIESKE, B., REDFIELD, M. M., ROULEAU, J. L., VAN VELDHUISEN, D. J., ZANNAD, F., ZILE, M. R., DESAI, A. S., CLAGGETT, B., JHUND, P. S., BOYTSOV, S. A., COMIN-COLET, J., CLELAND, J., DÜNGEN, H. D., GONCALVESOVA, E., KATOVA, T., KERR SARAIVA, J. F., LELONEK, M., MERKELY, B., SENNI, M., SHAH, S. J., ZHOU, J., RIZKALA, A. R., GONG, J., SHI, V. C. & LEFKOWITZ, M. P. 2019. Angiotensin-Neprilysin Inhibition in Heart Failure with Preserved Ejection Fraction. *N Engl J Med,* 381, 1609-1620.

SONNYLAL, S., DENTON, C. P., ZHENG, B., KEENE, D. R., HE, R., ADAMS, H. P., VANPELT, C. S., GENG, Y. J., DENG, J. M., BEHRINGER, R. R. & DE CROMBRUGGHE, B. 2007. Postnatal induction of transforming growth factor beta signaling in fibroblasts of mice recapitulates clinical, histologic, and biochemical features of scleroderma. *Arthritis Rheum,* 56, 334-44.

SOUDERS, C. A., BOWERS, S. L. K. & BAUDINO, T. A. 2009. Cardiac Fibroblast. *Circulation Research,* 105, 1164-1176.

SOUSA, A. M., LIU, T., GUEVARA, O., STEVENS, J., FANBURG, B. L., GAESTEL, M., TOKSOZ, D. & KAYYALI, U. S. 2007. Smooth muscle α-actin expression and myofibroblast differentiation by TGFβ are dependent upon MK2. *Journal of Cellular Biochemistry,* 100, 1581-1592.

STANSFIELD, W. E., ANDERSEN, N. M., TANG, R. H. & SELZMAN, C. H. 2009. Periostin is a novel factor in cardiac remodeling after experimental and clinical unloading of the failing heart. *Ann Thorac Surg,* 88, 1916-21.

STRAUBINGER, J., BOLDT, K., KURET, A., DENG, L., KRATTENMACHER, D., BORK, N., DESCH, M., FEIL, R., FEIL, S., NEMER, M., UEFFING, M., RUTH, P., JUST, S. & LUKOWSKI, R. 2017. Amplified pathogenic actions of angiotensin II in cysteine-rich LIM-only protein 4-negative mouse hearts. *Faseb j,* 31, 1620-1638.

TABULA MURIS, C., OVERALL, C., LOGISTICAL, C., ORGAN, C., PROCESSING, LIBRARY, P., SEQUENCING, COMPUTATIONAL DATA, A., CELL TYPE, A., WRITING, G., SUPPLEMENTAL TEXT WRITING, G. & PRINCIPAL, I. 2018. Single-cell transcriptomics of 20 mouse organs creates a Tabula Muris. *Nature,* 562, 367-372.

TAI, Y., WOODS, E. L., DALLY, J., KONG, D., STEADMAN, R., MOSELEY, R. & MIDGLEY, A. C. 2021. Myofibroblasts: Function, Formation, and Scope of Molecular Therapies for Skin Fibrosis. *Biomolecules,* 11, 1095.

TAKEDA, N. & MANABE, I. 2011. Cellular Interplay between Cardiomyocytes and Nonmyocytes in Cardiac Remodeling. *Int J Inflam,* 2011, 535241.

TAKEDA, N., MANABE, I., UCHINO, Y., EGUCHI, K., MATSUMOTO, S., NISHIMURA, S., SHINDO, T., SANO, M., OTSU, K., SNIDER, P., CONWAY, S. J. & NAGAI, R. 2010. Cardiac fibroblasts are essential for the adaptive response of the murine heart to pressure overload. *J Clin Invest,* 120, 254-65.

TAKIMOTO, E., CHAMPION, H. C., LI, M., BELARDI, D., REN, S., RODRIGUEZ, E. R., BEDJA, D., GABRIELSON, K. L., WANG, Y. & KASS, D. A. 2005. Chronic inhibition of cyclic GMP phosphodiesterase 5A prevents and reverses cardiac hypertrophy. *Nature Medicine,* 11, 214-222.

TALLQUIST, M. D. & MOLKENTIN, J. D. 2017. Redefining the identity of cardiac fibroblasts. *Nat Rev Cardiol,* 14, 484-491.

TAN, L. B., JALIL, J. E., PICK, R., JANICKI, J. S. & WEBER, K. T. 1991. Cardiac myocyte necrosis induced by angiotensin II. *Circ Res,* 69, 1185-95.

THUNEMANN, M., WEN, L., HILLENBRAND, M., VACHAVIOLOS, A., FEIL, S., OTT, T., HAN, X., FUKUMURA, D., JAIN, R. K., RUSSWURM, M., DE WIT, C. & FEIL, R. 2013. Transgenic mice for cGMP imaging. *Circ Res,* 113, 365-71.

TRAVERS, J. G., KAMAL, F. A., ROBBINS, J., YUTZEY, K. E. & BLAXALL, B. C. 2016. Cardiac Fibrosis. *Circulation Research,* 118, 1021-1040.

TRAVERS, J. G., THARP, C. A., RUBINO, M. & MCKINSEY, T. A. 2022. Therapeutic targets for cardiac fibrosis: from old school to next-gen. *J Clin Invest,* 132.

TSUTAMOTO, T., WADA, A., MAEDA, K., MABUCHI, N., HAYASHI, M., TSUTSUI, T., OHNISHI, M., SAWAKI, M., FUJII, M., MATSUMOTO, T., HORIE, H., SUGIMOTO, Y. & KINOSHITA, M. 2000. Transcardiac extraction of circulating endothelin-1 across the failing heart. *Am J Cardiol,* 86, 524-8.

TURNER, N. A. & PORTER, K. E. 2013. Function and fate of myofibroblasts after myocardial infarction. *Fibrogenesis Tissue Repair,* 6, 5.

TUTEJA, N., CHANDRA, M., TUTEJA, R. & MISRA, M. K. 2004. Nitric Oxide as a Unique Bioactive Signaling Messenger in Physiology and Pathophysiology. *J Biomed Biotechnol,* 2004, 227-237.

UHAL, B. D., LI, X., PIASECKI, C. C. & MOLINA-MOLINA, M. 2012. Angiotensin signalling in pulmonary fibrosis. *Int J Biochem Cell Biol,* 44, 465-8.

UMBARKAR, P., EJANTKAR, S., TOUSIF, S. & LAL, H. 2021. Mechanisms of Fibroblast Activation and Myocardial Fibrosis: Lessons Learned from FB-Specific Conditional Mouse Models. *Cells,* 10, 2412.

VADUGANATHAN, M., MENSAH, G. A., TURCO, J. V., FUSTER, V. & ROTH, G. A. 2022. The Global Burden of Cardiovascular Diseases and Risk. *Journal of the American College of Cardiology,* 80, 2361-2371.

VALLUR, R., KALBACHER, H. & FEIL, R. 2014. Catalytic Activity of cGMP-Dependent Protein Kinase Type I in Intact Cells Is Independent of N-Terminal Autophosphorylation. *PLOS ONE,* 9, e98946.

VAN VLIET, B. N., CHAFE, L. L. & MONTANI, J. P. 2003. Characteristics of 24 h telemetered blood pressure in eNOS-knockout and C57Bl/6J control mice. *J Physiol,* 549, 313-25.

VERDECCHIA, P., ANGELI, F., MAZZOTTA, G., GENTILE, G. & REBOLDI, G. 2008. The renin angiotensin system in the development of cardiovascular disease: role of aliskiren in risk reduction. *Vasc Health Risk Manag,* 4, 971-81.

VERHEULE, S. & SCHOTTEN, U. 2021. Electrophysiological Consequences of Cardiac Fibrosis. *Cells,* 10, 3220.

WALKER, G. A., MASTERS, K. S., SHAH, D. N., ANSETH, K. S. & LEINWAND, L. A. 2004. Valvular myofibroblast activation by transforming growth factor-beta: implications for pathological extracellular matrix remodeling in heart valve disease. *Circ Res,* 95, 253-60.

WEBER, S., BERNHARD, D., LUKOWSKI, R., WEINMEISTER, P., WÖRNER, R., WEGENER, J. W., VALTCHEVA, N., FEIL, S., SCHLOSSMANN, J., HOFMANN, F. & FEIL, R. 2007. Rescue of cGMP Kinase I Knockout Mice by Smooth Muscle–Specific Expression of Either Isozyme. *Circulation Research,* 101, 1096-1103.

WEGENER, J. W., NAWRATH, H., WOLFSGRUBER, W., KÜHBANDNER, S., WERNER, C., HOFMANN, F. & FEIL, R. 2002. cGMP-Dependent Protein Kinase I Mediates the Negative Inotropic Effect of cGMP in the Murine Myocardium. *Circulation Research,* 90, 18-20.

WEN, L., FEIL, S., WOLTERS, M., THUNEMANN, M., REGLER, F., SCHMIDT, K., FRIEBE, A., OLBRICH, M., LANGER, H., GAWAZ, M., DE WIT, C. & FEIL, R. 2018. A shear-dependent NO-cGMP-cGKI cascade in platelets acts as an auto-regulatory brake of thrombosis. *Nature Communications,* 9, 4301.

WENZEL, S., TAIMOR, G., PIPER, H. M. & SCHLÜTER, K. D. 2001. Redox-sensitive intermediates mediate angiotensin II-induced p38 MAP kinase activation, AP-1 binding activity, and TGF-beta expression in adult ventricular cardiomyocytes. *Faseb j,* 15, 2291-3.

WERNER, F., PRENTKI SANTOS, E., MICHEL, K., SCHRADER, H., VÖLKER, K., POTAPENKO, T., KREBES, L., ABESSE, M., MÖLLMANN, D., SCHLATTJAN, M., SCHMIDT, H., SKRYABIN, B. V., ŠPIRANEC SPES, K., SCHUH, K., DENTON, C. P., BABA, H. A. & KUHN, M. 2023. Ablation of C-type natriuretic peptide/cGMP signaling in fibroblasts exacerbates adverse cardiac remodeling in mice. *JCI Insight,* 8.

WHITFIELD, J., LITTLEWOOD, T. & SOUCEK, L. 2015. Tamoxifen administration to mice. *Cold Spring Harb Protoc,* 2015, 269-71.

WILLEMS, I. E., HAVENITH, M. G., DE MEY, J. G. & DAEMEN, M. J. 1994. The alpha-smooth muscle actin-positive cells in healing human myocardial scars. *Am J Pathol,* 145, 868-75.

WONG, T. C., PIEHLER, K., MEIER, C. G., TESTA, S. M., KLOCK, A. M., ANEIZI, A. A., SHAKESPRERE, J., KELLMAN, P., SHROFF, S. G., SCHWARTZMAN, D. S., MULUKUTLA, S. R., SIMON, M. A. & SCHELBERT, E. B. 2012. Association between extracellular matrix expansion quantified by cardiovascular magnetic resonance and short-term mortality. *Circulation,* 126, 1206-16.

XIA, P., LIU, Y. & CHENG, Z. 2016. Signaling Pathways in Cardiac Myocyte Apoptosis. *Biomed Res Int,* 2016, 9583268.

YAMATO, H., KIMURA, K., FUKUI, E., KANOU, T., OSE, N., FUNAKI, S., MINAMI, M. & SHINTANI, Y. 2021. Periostin secreted by activated fibroblasts in idiopathic pulmonary fibrosis promotes tumorigenesis of non-small cell lung cancer. *Sci Rep,* 11, 21114.

YANG, J., CHEN, C., REN, H., HAN, Y., HE, D., ZHOU, L., HOPFER, U., JOSE, P. A. & ZENG, C. 2012. Angiotensin II AT(2) receptor decreases AT(1) receptor expression and function via nitric oxide/cGMP/Sp1 in renal proximal tubule cells from Wistar-Kyoto rats. *J Hypertens,* 30, 1176-84.

YANG, J., YU, X., XUE, F., LI, Y., LIU, W. & ZHANG, S. 2018. Exosomes derived from cardiomyocytes promote cardiac fibrosis via myocyte-fibroblast cross-talk. *Am J Transl Res,* 10, 4350-4366.

YIN, F. C., SPURGEON, H. A., RAKUSAN, K., WEISFELDT, M. L. & LAKATTA, E. G. 1982. Use of tibial length to quantify cardiac hypertrophy: application in the aging rat. *American Journal of Physiology-Heart and Circulatory Physiology,* 243, H941-H947.

YIN, F. C., SPURGEON, H. A., WEISFELDT, M. L. & LAKATTA, E. G. 1980. Mechanical properties of myocardium from hypertrophied rat hearts. A comparison between hypertrophy induced by senescence and by aortic banding. *Circ Res,* 46, 292-300.

YOSHIMURA, M., YASUE, H., MORITA, E., SAKAINO, N., JOUGASAKI, M., KUROSE, M., MUKOYAMA, M., SAITO, Y., NAKAO, K. & IMURA, H. 1991. Hemodynamic, renal, and hormonal responses to brain natriuretic peptide infusion in patients with congestive heart failure. *Circulation,* 84, 1581-8.

ZEISBERG, M. & KALLURI, R. 2013. Cellular mechanisms of tissue fibrosis. 1. Common and organ-specific mechanisms associated with tissue fibrosis. *Am J Physiol Cell Physiol,* 304, C216-25.

ZHANG, X., ZHU, J. X., MA, Z. G., WU, H. M., XU, S. C., SONG, P., KONG, C. Y., YUAN, Y. P., DENG, W. & TANG, Q. Z. 2019. Rosmarinic acid alleviates cardiomyocyte apoptosis via cardiac fibroblast in doxorubicin-induced cardiotoxicity. *Int J Biol Sci,* 15, 556-567.

ZHAO, S., WU, H., XIA, W., CHEN, X., ZHU, S., ZHANG, S., SHAO, Y., MA, W., YANG, D. & ZHANG, J. 2014. Periostin expression is upregulated and associated with myocardial fibrosis in human failing hearts. *Journal of Cardiology,* 63, 373-378.

ZHOU, Z., SAYED, N., PYRIOCHOU, A., ROUSSOS, C., FULTON, D., BEUVE, A. & PAPAPETROPOULOS, A. 2008. Protein Kinase G Phosphorylates Soluble Guanylyl Cyclase on Serine 64 and Inhibits Its Activity. *Arteriosclerosis, Thrombosis, and Vascular Biology,* 28, 1803-1810.

ZHU, J. & CARVER, W. 2012. Effects of interleukin-33 on cardiac fibroblast gene expression and activity. *Cytokine,* 58, 368-79.

ZHU, L., WANG, Y., ZHAO, S. & LU, M. 2022. Detection of myocardial fibrosis: Where we stand. *Front Cardiovasc Med,* 9, 926378.

9 Publications and congress contributions

9.1 Publications

2023

***Cruz Santos, M.**, Birkenfeld, L., Pham, T., Maier, S., Paulus, K., Ullemeyer, L., Knauer, A., Kabagema-Bilan, C., Längst, N., Roslan, A., Wettschureck, N., Gawaz, M., Ichinose, F., Lukowski, R. (202x). Angiotensin II-induced cardiac fibrosis and dysfunction are attenuated by myofibroblast-specific cGKI. (**submitted – JCI Insight**)*

*Roslan, A., Paulus, K., Matt, L., Bischof, H., Längst, N., Schanz, S., Luczak, A., Yang, J., **Cruz Santos, M.**, Burgstaller, S., Skrabak, D., Bork, N.I., Malli, R., Schmidtko, A., Gawaz, M., Nikolaev, V.O., Ruth, P., Ehinger, R., Lukowski, R. (202x). The Kcnt1 encoded Na^+-activated K^+-channel Slack limits ischemia/reperfusion-induced cardiac injury. **(in revision – Cardiovascular Research)***

Pham, T., Hussein, T., Calis, D., Bischof, H., Skrabak, D., **Cruz Santos, M.**, Maier, S., Spähn, D., Kalina, D., Simonsig, S., Ehinger, R., Groschup, B., Knipper, M., Plesnila, N., Ruth, P., Lukowski, R., Matt, L. (2023). BK channels sustain neuronal Ca^{2+} oscillations to support hippocampal long-term potentiation and memory formation. *Cell Mol Life Sci, 80(12), 369.*

2022

Lukowski, R., **Cruz Santos, M.**, Kuret, A., & Ruth, P. (2022). cGMP and mitochondrial K^+channels-Compartmentalized but closely connected in cardioprotection. *Br J Pharmacol*, *179*(11), 2344-2360.

2021

Längst, N., Adler, J., Schweigert, O., Kleusberg, F., **Cruz Santos, M.**, Knauer, A., Sausbier, M., Zeller, T., Ruth, P., & Lukowski, R. (2021). Cyclic GMP-Dependent Regulation of Vascular Tone and Blood Pressure Involves Cysteine-Rich LIM-Only Protein 4 (CRP4). *International journal of molecular sciences*, *22*(18).

Bork, N. I., Kuret, A., **Cruz Santos, M.**, Molina, C. E., Reiter, B., Reichenspurner, H., Friebe, A., Skryabin, B. V., Rozhdestvensky, T. S., Kuhn, M., Lukowski, R., & Nikolaev, V. O. (2021). Rise of cGMP by partial phosphodiesterase-3A degradation enhances cardioprotection during hypoxia. *Redox Biol*, *48*, 102179.

9.2 Congress contributions

2023

Cruz Santos, M., Birkenfeld, L., Ullemeyer, L., Längst, N., Roslan, A., Gawaz, M., Offermanns, S., Wettschureck, N., Ichinose, F., Lukowski, L.: “Angiotensin II-induced cardiac remodeling is attenuated by myofibroblast-specific cGKI”; "Annual Meeting of the German Pharmaceutical Society (DPhG)", Tübingen, Germany, 09/23, (***Poster***)

2022

Cruz Santos, M.: “Myofibroblast cGMP-dependent protein kinase I (cGKI) opposes the adverse effects of Angiotensin II on cardiac function and remodeling”; "Annual Meeting of the German Pharmaceutical Society (DPhG)", Marburg, Germany, 09/22, (*selected abstract for **oral presentation** – Category: Young Researcher*)

Cruz Santos, M.: “Angiotensin II-induced cardiac fibrosis is attenuated by myofibroblast-specific cGKI”; 10th International Conference on cGMP, Augsburg, Germany, 06/22, (*selected abstract for **oral presentation** – Category: Emerging Fields **& Poster***)

Cruz Santos, M.: “Impact of the NO-cGMP pathway on cardiac arrest and cardiopulmonary resuscitation”; Reinhard-Frank-Mini-Symposium – organized by the trainees of the RTG 2381 Boston, USA, 04/22 (***oral presentation***)

2021

Cruz Santos, M., Birkenfeld, L., Längst, N., Kuret, A., Offermanns, S., Ichinose, F., Lukowski, R.: “Lack of cGKI in myofibroblasts amplifies cardiac fibrosis following Ang II infusion”; CanCaN2021 – International Conference organized by the trainees of the RTG 2381 Tübingen, Germany, 11/21 (***Poster***)

10 Curriculum Vitae

11 Acknowledgments